Electron spin resonance spectroscopy based on fluorescence detection at millikelvin temperature, applied to rare earth ions in scheelite

Eric Billaud

université PARIS-SACLAY

Electron spin resonance spectroscopy of rare earth ions in scheelite detected by microwave fluorescence at millikelvin temperature

Spectroscopie de résonance de spin électronique des ions de terres rares dans la scheelite détectée par fluorescence micro-ondes, à une température de l'ordre du millikelvin

Thèse de doctorat de l'université Paris-Saclay

École doctorale n◦ 564, physique en Ile-de-France (PIF)
Spécialité de doctorat : physique
Graduate School : physique, Référent : faculté des sciences d'Orsay

Thèse préparée dans l'unité de recherche **SPEC** (Université Paris-Saclay, CEA, CNRS), sous la direction de **Patrice BERTET**, directeur de recherche au CEA-Saclay, la codirection de **Denis VION**, directeur de recherche au CEA-Saclay, et le co-encadrement de **Emmanuel FLURIN**, chargé de recherche, CEA Saclay

Thèse présentée et soutenue à Paris-Saclay, le 31/01/2023, par

Eric BILLAUD

Composition du Jury

Jean-François ROCH Professeur, ENS Paris-Saclay	Président
Dieter SUTER Professeur, Université de Dortmund	Rapporteur & Examinateur
Mikael AFZELIUS Chargé de recherche, Université de Genève	Rapporteur & Examinateur
Hélène BOUCHIAT Directrice de recherche, Université Paris-Saclay	Examinatrice
Diana SERRANO Chargée de recherche, CNRS	Examinatrice
Jean-Damien PILLET Professeur assistant, Ecole Polytechnique	Examinateur

Thèse de doctorat

NNT : 2023UPASP012

Acknowledgments

First of all, I would like to thank the members of the Jury, for your work and for attending my defense: thank you Hélène, Diana, Jean François, Jean Damien, Dieter and Mikael. Thank you for reading and appreciating my thesis, at the value that will have seemed to you right.

My thanks go then naturally to the people with whom I worked during these 3 years and a half, in the Quantronics group, within the spin team. First of all, to the people who supervised me, and who taught me so much. Thanks to you Patrice for all that you taught me, for your unfailing availability. Facing such a complicated subject, it's an incredible chance to have at my side someone who understands it as well as you do. Thank you Manu, for all your explanations, thank you for having accompanied me every day to do these experiments. Thank you also for these numerous and varied discussions, on all the subjects even the most random let us say it. Thank you Denis for your sympathy, your wisdom and your rigor that you are always ready to share. Many times I went off in all directions and talking with you reassured me, and even perhaps reframed me.

My thanks go then to those who have shared my daily life as a learner, in which I include doctoral students and post-doctoral fellows. All those people who understand what it means to not understand anything on a daily basis. I am hardly exaggerating. First of all Vishal, Dan, Emanuele, Marianne who in their role as former members have helped me a lot. Boris, Yutian, Zhiren, Leo with whom we worked together on a daily basis. Then the next generation, Louis, Jaimé, Alexandre, to whom I hope I could transmit a little bit of what I know.

My thanks go then to the whole group. To the members of the other research projects. The Andreïves team: Hugues, Marcelo, Christian, Manas, Joan. The Graal team: Hélène, Philippe, Brian, Jean-come. The Dual team: Charlar, Alexander, Margaret, Ramiro. Thank you Patrick for all your technical support, especially crucial for the defense. And of course Daniel, for your comforting presence in the group. Thank you to all these people and subjects that stimulate our daily research.

All of this is part of a working framework, with a lot of support. Thanks to Pascal, and to all the mechanical workshop, for your indispensable help for our experiments. Thanks to the nanofab, Pief and sébastien, the great binomial who accompanied me in the clean room to make nanoelectronics as well as outside to repair my bike when I had small mechanical problems, two fields in which they excel. Thank you to the secretaries of the SPEC, who are always present when we need them. Thank you to the cleaning staff, for your work, always in a good mood. Thank you to the iPhT for setting up the necessary equipment to do the defense. Thank you to the lab management, for organizing the life of all these people, and thank you for accompanying them in their future evolutions. Thanks also to the carbon footprint working group, which is working on the future of the lab, and on how to make it viable.

And now comes my thanks for those who supported me in this adventure of thesis. Thanks again to all these people already mentioned, for their sympathy and the working atmosphere they maintain in the lab. A huge thank you in particular to the one who will remain forever my co-PhD student, Léo, we started at the same time and I finished before.

Without you I don't know if I would have been able to reach the end, without your daily presence, with all those moments of exchange and laughter in the office at the end of the corridor which made me willing to come to the lab everyday.

Other people were essential and made my thesis a happy moment, first of all my roommates, Guillaume and Antoine, with whom we also started our thesis at the same time, but this time it was you who finished before me. Thank you for your support in the hard moments, and thank you for your daily presence. Thanks to the roommates++, Charlotte and Capucine, with whom we shared life, a life that you made fun and joyful, even in times of confinement. Maybe even more so as we were confined, with in mind our Sunday evening parties.

Thanks to you Margaux, for being by my side while I was attacking the most difficult part of the thesis. Thank you for all that you brought me and what you continue to bring me. Support, advice of course, but also and above all emotions and happiness. My thoughts go to you.

Thank you to my brothers, my parents and my family, who have always understood and supported me, and especially my choice to do a PhD. When you are the second of your siblings to make this choice, the family starts to make up its mind.

Thank you to my long-time friends who have seen me evolve, who have accompanied me through the years of my life, until today. So many memories and beautiful moments, and this is only the beginning.

A beginning, which however corresponds to a farewell, my farewell to fundamental research. I have shared with you the wonder and excitement about knowledge, about science, about physics. And yet I can't help questioning the meaning of it. What is the point of being interested in spin, even if it is unique, if we no longer have a planet, or a society? I tried to find answers during my PhD as I computed my group carbon footprint, available here Appendix D. However the work of researcher does not suit me, so I am going to look for it elsewhere, an elsewhere perhaps not so far from the world of research, but probably not as a researcher.

Contents

List of abbreviations

- MR: Magnetic Resonance
- ESR: Electron Spin Resonance
- NSR: Nuclear Spin Resonance
- CFD: Coherent Field detection
- cQED: cavity Quantum Electrodynamics
- SMPD: Single Microwave Photon Counter
- FD: Fluorescence Detection
- REI: Rare Earth Ions
- SNR: Signal-to-Noise ratio
- ESEEM: Electron Spin Echo Envelope Modulation
- JPA: Jospheson Parametric Amplifier
- SNR: Signal-to-Noise Ratio
- FWHM: Full Width at Half Maximum
- JTWPA: Jospheson Traveling Wave Parametric Amplifier
- TLS: Two-Level System

Chapter 1

Résumé détaillé

1.1 Présentation générale

La Résonance Magnétique (RM) est une méthode de caractérisation permettant de sonder les propriétés de la matière. Cette technique est largement utilisée car sa seule condition est la présence de spins, omniprésents dans la matière tant dans les électrons que dans les noyaux. La fréquence de Larmor des spins ω_s, accordée par l'application d'un champ magnétique statique B_0, permet aux spins d'absorber un champ électromagnétique à la même fréquence ω_s. Dans la RM à Onde Continue (CW), cette absorption se manifeste par une modification du coefficient de réflexion, mesurable à l'aide d'un analyseur de réseau. En RM pulsée, la dynamique du spin est sondée en utilisant des séquences d'impulsions résonantes. La RM donne accès à toutes les propriétés intéressantes du spin : densité de spin, fréquence de résonance, temps de relaxation, fluctuations magnétiques locales... [Abr11; AB12]. Cette méthode de détection est utilisée sur une grande variété de systèmes de spin, que ce soit en Résonance de Spin Électronique (ESR) ou en Résonance Magnétique Nucléaire (RMN), et trouve des applications en biologie [Yos+96], en biochimie [Pol06] et en sciences du solide [Sli55]. Cette diversité d'application correspond à des contraintes expérimentales variées, telles que la température de l'échantillon et la fréquence ω_s.

Cette thèse traite de la spectroscopie ESR d'impuretés paramagnétiques dans un cristal, à des fréquences micro-ondes (5-10 GHz) pour des champs B_0 dans la gamme 50-500 mT. Les spins sont couplés à un résonateur micro-ondes de fréquence ω_0 avec une force g_0. La méthode habituelle de détection des spins dans l'ESR pulsé est appelée Détection Inductive (ID) [Rab+38; Blo46; PTP46]. Les spins sont sondés par des séquences d'impulsions micro-ondes qui conduisent à une polarisation transversale macroscopique transitoire $\langle S_X \rangle$. La précession de Larmor de cette aimantation induit l'émission d'une impulsion micro-ondes appelée écho de spin. Cet écho de spin est détecté par amplification et démodulation, et son amplitude et sa phase codent les propriétés du spin. Les appareils d'ID-ESR disponibles dans le commerce ne peuvent détecter que de grands ensembles de spins, supérieurs à 10^9 spins [Abh+22]. Dans ce contexte, il est très souhaitable d'augmenter la sensibilité de l'ESR tout en préservant sa variété d'application.

Plusieurs méthodes ont été proposées et mises en œuvre pour augmenter fortement la sensibilité ESR [WF16]. L'une d'entre elles consiste à utiliser la charge de l'électron porteur du spin pour se coupler au champ électrique du résonateur, ce qui permet d'obtenir un couplage généralement supérieur de plusieurs ordres de grandeur au couplage avec le champ magnétique [Xia+04]. Cette méthode utilise une structure de transistor basée sur des matériaux semi-conducteurs, ce qui limite considérablement ses possibilités d'application. Une autre approche consiste à utiliser une pointe pour focaliser le champ magnétique au-dessus d'un cantilever mécanique. Cette méthode a un très petit volume de mode, de l'ordre de nm^3, ce qui permet de balayer une surface mais reste aveugle aux propriétés

dans le volume de l'échantillon. Une autre idée consiste à contourner la limitation due à la faible énergie des micro-ondes en utilisant des systèmes de spin qui présentent également des transitions dans le domaine optique [Riz+22]. Les centres NV dans le diamant ainsi que les ions Erbium sont de tels systèmes où la sensibilité d'un seul ion a déjà été atteinte par méthode optique [Gru+97; Yin+13]. Cependant cette méthode ne s'applique qu'aux quelques systèmes de spin avec une transition optique, ce qui limite beaucoup sa variété d'application. Une méthode ESR générale et très sensible est à trouver ailleurs.

Au sein du groupe Quantronique, notre approche, dirigée par Patrice Bertet, consiste à appliquer les techniques de l'Électrodynamique de Circuit Quantique (cQED) [HR06; Wal+06] pour réaliser une ESR très sensible. La cQED utilise des circuits supraconducteurs refroidis à la température du millikelvin. Ces circuits offrent de nouveaux dispositifs utiles pour la détection des champs micro-ondes : résonateurs micro-ondes à faible volume et à facteur de qualité élevé, Amplificateurs Paramétriques Josephson à limitation quantique (JPA) et, plus récemment, détecteurs de photons micro-ondes uniques (SMPD) à base de qubits. Ces circuits peuvent être appliqués à la spectroscopie ESR. Dans nos expériences, nous utilisons des micro-résonateurs supraconducteurs pour détecter les spins: le faible volume de leur mode magnétique permet une augmentation significative du couplage spin-photon, jusqu'à $g_0/2\pi \sim 1$ kHz. Avec un couplage aussi important, les spins résonants avec la cavité ont tendance à se relaxer de manière dominante par émission spontanée d'un photon micro-onde, atteignant un nouveau régime pour la RM appelé régime de Purcell, vu pour la première fois par Audrey Bienfait [Bie+16].

En utilisant de tels micro-résonateurs combinés à des JPA pour l'amplification sans bruit du signal d'écho, l'ID-ESR s'est avéré atteindre une très haute sensibilité de ~ 10 spins dans le travail de Vishal Ranjan [Ran+20a], mais a finalement été limité par le bruit inévitable du champ du vide. En 2020, une nouvelle méthode qui permet de surmonter cette limite fondamentale a été proposée et démontrée dans notre groupe: l'ESR détectée par fluorescence ou FD-ESR [Alb+21]. L'idée est de détecter les photons micro-ondes émis spontanément par les spins lors de leur relaxation radiative. Pour cela, nous utilisons un SMPD récemment développé dans notre groupe par Emmanuel Flurin [Les+20]. La preuve de principe de la FD-ESR a été obtenue par Emanuele Albertinale en détectant des donneurs de Bismuth dans le Silicium [Alb+21; Alb21]. Cependant, la généralité des possibilités d'application de la FD-ESR restait à prouver, ainsi que son avantage en terme de sensibilité par rapport à l'ID-ESR. Ma thèse s'est déroulée en parallèle avec celle de Léo Balembois, qui a travaillé à développer une nouvelle génération de SMPDs aux caractéristiques améliorées.

Dans cette thèse, nous appliquons la FD-ESR aux ions de terres rares (REI) dans un cristal de Scheelite de $CaWO_4$, et en particulier aux ions Er^{3+}. Ce système a été caractérisé par ID-ESR dans notre groupe par Marianne le Dantec et Milos Rančić, et a montré des propriétés de long temps de cohérence prometteuses pour des applications en informatique quantique [Le +21; Le 22].

Dans cette thèse, nous prouvons que la FD-ESR est une méthode de caractérisation générale qui donne la même information sur les spins que l'ID-ESR mais avec une plus grande sensibilité pour la détection de petits ensembles de spins.

Ce manuscrit débute par trois chapitres de "contexte théorique" qui présentent au lecteur les concepts de base nécessaires à la compréhension de notre travail. Dans le Chapter 3, nous décrirons l'ESR réalisée dans le régime quantique sur un ensemble de spins. Puis dans le Chapter 4, nous expliquerons le principe et les potentialités de deux méthodes de détection: la détection en quadrature de champ et la détection de photons. Ensuite, dans le Chapter 5 nous considérerons la physique des REI dans la Scheelite et détaillerons quelques résultats de mesure obtenus avant la réalisation de cette thèse par

Marianne Le-Dantec employant l'ID-ESR appliquée aux ions Erbium .

Dans le Chapter 6, nous décrivons les systèmes expérimentaux qui ont été utilisés pour recueillir les données présentées dans cette thèse. L'échantillon étudié dans cette thèse est un cristal de $CaWO_4$ fabriqué et d'abord pré-caractérisé par ESR standard en collaboration avec d'autres laboratoires. Nous décrivons les installations à température ambiante et cryogénique permettant de réaliser l'ESR et nous présentons ensuite au lecteur des mesures ESR typiques réalisées soit avec l'ID soit avec la FD.

Nous montrons expérimentalement dans le Chapter 7 que la FD-ESR est une méthode de détection qui peut être appliquée à une grande variété d'espèces de spin et qu'elle a une plus grande sensibilité que l'ID-ESR. Nous enregistrons pour cela des spectres avec la FD-ESR sur une large gamme de champ magnétique révélant de nombreuses espèces de spin. Parmi ces spins, nous décidons de manipuler des ions Erbium pour réaliser les expériences de FD-ESR dans la suite de cette thèse. Nous étudions le signal de fluorescence de spin car une meilleure compréhension de ce nouveau type de signal donne accès à des informations supplémentaires sur le spin. Nous enregistrons le signal pour différentes forces d'excitation et le reproduisons avec des simulations, prouvant par là que notre modèle de simulation décrit bien la physique de notre expérience. L'amélioration de la sensibilité étant au cœur de notre recherche, nous comparons le rapport Signal Sur Bruit (SNR) de la FD-ESR et de l'ID-ESR et montrons un avantage pour la FD-ESR. Par conséquent, nous validons la FD-ESR comme une méthode de spectroscopie de très haute sensibilité.

Grâce à la haute sensibilité de la FD-ESR, nous remarquons un phénomène qui était resté invisible avec l'ID-ESR. Nous présentons dans le Chapter 8 la corrélation entre la fréquence de résonance et le temps de relaxation pour un sous-ensemble de spin fortement couplé au résonateur supraconducteur. Comme les simulations montrent que la contraction thermique du fil du résonateur devrait induire une déformation du réseau cristallin, nous attribuons cet effet à des contraintes mécaniques locales. Cet effet, connu pour d'autres systèmes de spin [Pla+18], a été mesuré à différentes orientations de B_0 et nécessiterait un travail théorique supplémentaire pour être compris. L'homogénéité du couplage des sous-ensembles de spin nous permet de les manipuler dans une oscillation cohérente. Par conséquent, nous démontrons que la FD-ESR est une méthode de détection prometteuse pour manipuler de manière cohérente un petit ensemble de spins.

Finalement, dans le Chapter 9, nous détectons les échos de spin avec la FD-ESR, prouvant que cette méthode de détection est adaptée à toutes les applications standard de la RSE [Bil+22]. Une séquence de pulses d'écho de Hahn suivie d'une impulsion de restauration sont employées pour convertir la composante de spin $\langle S_X \rangle$ en composante $\langle S_Z \rangle$, visible par FD-ESR [BHP73; OMG88]. Après avoir prouvé que nous sommes effectivement capables de détecter la contribution de l'écho dans le signal de fluorescence, nous utilisons la FD-ESR pour caractériser les propriétés cohérentes des spins. Nous détectons comment l'amplitude de l'écho évolue dans le temps et montrons une modulation de l'enveloppe de l'écho des spins électroniques (ESEEM) ainsi qu'un temps de cohérence d'environ 4 ms. Grâce à des mesures antérieures obtenues avec l'ID-ESR, nous savons que ce temps de cohérence est limité par un bruit de champ magnétique, nous développons donc une procédure de détection basée sur les fluctuations du signal pour accéder avec la FD-ESR au temps de cohérence intrinsèque des spins. Nous comparons le SNR des deux méthodes de détection appliquées à la détection de l'écho de spin et trouvons à nouveau un avantage pour la FD-ESR.

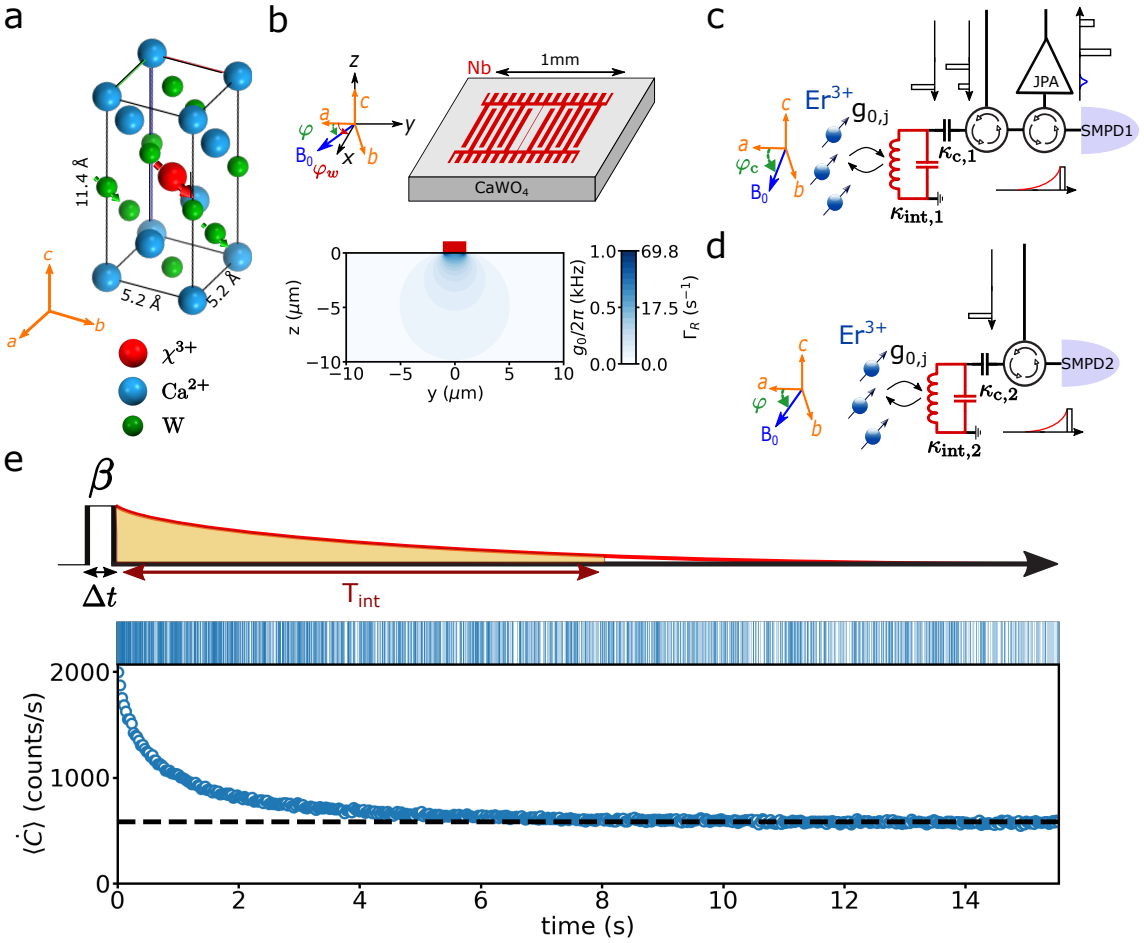

Figure 1.1: **Principe de l'expérience et signal de fluorescence de spin.** **a**. Schéma du réseau cristallin $CaWO_4$ centré sur un ion REI χ^{3+} qui a remplacé un Ca^{2+}. Les oxygènes sont supprimés pour plus de clarté. Un degré de liberté de spin est représenté pour le REI ainsi que pour certains atomes de W. La symétrie cristalline est tétragonale autour de l'axe c, ce qui signifie que les axes a et b sont équivalents. **b**. Forme du résonateur 2D de fréquence $\omega_0/2\pi \approx 7\,\mathrm{GHz}$ (rouge) fabriqué dans le plan (a, b) sur la surface de l'échantillon (gris). Le fil du résonateur est le long de l'axe x (angle $\varphi_w = 51\,^\circ$) et B_0 est dans le plan (a, b) (angle φ). La section transversale de l'échantillon sous le fil de $2\,\mu\mathrm{m}$ de largeur (rectangle rouge) présente la distribution spatiale du couplage g_0 et du taux radiatif correspondant Γ_R (lorsque $\varphi = 30\,^\circ$). **c**. Illustration du montage 1, où chaque spin j est couplé avec une force $g_{0,j}$ au résonateur avec des taux d'amortissement à la ligne $\kappa_{\mathrm{c},1}$ et aux pertes internes $\kappa_{\mathrm{int},1}$. Les circulateurs permettent d'utiliser la même ligne micro-ondes pour exciter les spins (impulsions carrées noires) et pour acheminer le signal de spin (rouge et bleu) vers l'appareil de détection. Le signal peut être détecté soit avec la FD-ESR en utilisant SMPD1, soit avec l'ID-ESR grâce à un JPA dans la ligne de détection. L'orientation de B_0 est fixée à $\varphi_\mathrm{c} = 47\,^\circ$. **d**. Illustration du montage 2, avec les caractéristiques du résonateur $\kappa_{\mathrm{c},2}$ et $\kappa_{\mathrm{int},2}$. Ce montage est adaptée uniquement pour réaliser la FD-ESR et permet de modifier l'orientation φ du champ magnétiques. **e**. Courbe de fluorescence typique prise avec le montage 2. Panneau supérieur : schéma de la séquence de détection de spin où une impulsion d'amplitude β et de durée Δt excite les spins qui se relaxent ensuite en émettant des photons de fluorescence (courbe rouge), détectés et intégrés sur une période T_int pour produire un nombre de comptes $\langle C \rangle$ (surface orange). Panneau du milieu : les clics (barres verticales) se produisent avec une probabilité plus élevée à des temps courts après l'excitation. Panneau du bas : taux de compte instantané $\langle \dot{C} \rangle$ (cercles), moyenné sur 100 itérations, qui décroît jusqu'à un taux de fond $\langle \dot{C}_\mathrm{bg.} \rangle$ (ligne noire pointillée).

1.2 Résultats de la thèse

1.2.1 Système expérimental

Dans cette thèse, nous appliquons la FD-ESR aux REIs dans un échantillon de $CaWO_4$. Les ions REI sont naturellement présents dans le $CaWO_4$ en substitution des ions Ca^{2+}. Certains ions REI, une fois insérés dans un cristal, se comportent comme des ions de Kramers [Kra30] présentant un degré de liberté de spin. Nous nous concentrons ici sur la résonance magnétique dans le cas d'un spin électronique qui se comporte comme un spin-1/2. Comme le montre Figure 2.1a, les sites Ca^{2+} ont une symétrie tétragonale qui induit la même symétrie sur les propriétés de spin [Enr71; Ber+09] : le tenseur $\mathbf{g}$ de spin est anisotrope avec $g_c \neq g_{a,b}$. La grande valeur de $\mathbf{g}$ dans le plan (a, b) pour plusieurs REIs (les ions Erbium ont $g_{a,b} = 8.38$) motive leur étude avec l'ESR car ils nécessitent un champ résonnant B_0 relativement faible et présentent un fort couplage magnétique dans ce plan. Le choix de $CaWO_4$ comme substrat est guidé par sa faible densité d'impuretés paramagnétiques, essentiellement dominée par la fraction de l'isotope ^{183}W qui possède un spin nucléaire. L'échantillon a été produit sans dopage et nous utilisons les impuretés REIs résiduelles. Une fois l'échantillon arrivé dans le Groupe Quantronique, Marianne Le Dantec, une doctorante qui a précédé ce travail de thèse, a caractérisé de manière très détaillée les propriétés des ions Erbium en utilisant l'ID-ESR [Le 22; Le +21].

Nous fabriquons sur la surface de l'échantillon dans le plan (a, b) un résonateur supraconducteur 2D en Niobium tel que représenté dans Figure 2.1b. Le résonateur est caractérisé par sa fréquence de résonance $\omega_0/2\pi$ et ses interactions avec son environnement, avec un taux d'amortissement dans la ligne κ_c et un taux d'amortissement dans ses pertes internes κ_{int} qui se combinent en un taux total $\kappa = \kappa_c + \kappa_{\text{int}}$. Le résonateur est formé par des capacités interdigitées reliées par un fil inductif de $2\,\mu$m de large. Ce fil couple magnétiquement le mode du résonateur aux spins avec une force de couplage $g_0(r)$ dépendant de la position r du spin dans le substrat. Le champ intracavité α peuplant le mode du résonateur entraîne le spin j de fréquence $\omega_j/2\pi$ à la position r avec une fréquence de Rabi $\Omega_R(r)$. En faisant varier l'amplitude du champ dans le résonateur, on peut sonder les spins à différentes distances du fil. Ensuite, les spins peuvent relaxer leur énergie soit de manière non radiative avec un taux Γ_{NR}, typiquement en émettant un phonon dans le réseau cristallin, soit de manière radiative avec un taux Γ_{R}, en émettant des photons. Dans notre système, le taux de relaxation radiatif du spin est dominé par l'influence du résonateur en raison de l'effet Purcell, ce qui donne $\Gamma_{\text{R}} = g_0^2\kappa/(\Delta\omega^2 + (\kappa/2)^2)$ avec $\Delta\omega = \omega_0 - \omega_i$ le désaccord de fréquence du résonateur avec le spin. Ce taux est crucial dans notre expérience car les photons émis radiativement par les spins sont détectables avec la FD. La section transversale dans Figure 2.1b représente la distribution spatiale de g_0 et de Γ_{R} sous le fil.

Figure 2.1c et Figure 2.1d sont les schémas des principaux composants micro-ondes mis à température cryogénique dans les 2 montages expérimentaux utilisés dans cette thèse. Dans le montage 1, l'échantillon est connecté à la fois au SMPD1, un SMPD de la première génération, et à un Amplificateur Paramétrique Josephson (JPA) et peut donc être mesuré soit avec la FD-ESR soit avec l'ID-ESR. Dans le montage 2, les mesures ne peuvent être effectuées qu'avec la FD-ESR utilisant le SMPD2, un SMPD de la deuxième génération. Dans ce 2e montage, le champ B_0 est généré par deux bobines de Helmotz qui permettent de changer la direction du champ φ dans le plan (a, b).

Une courbe typique de fluorescence de spin détectée avec la FD-ESR après une impulsion d'excitation d'amplitude β et de durée Δt appliquée à $t = 0$ est visible dans Figure 2.1e, avec une illustration de la séquence d'impulsion. Les résultats du SMPD sous forme de clics c_j, pour le cycle j se produisant à un temps de cycle t_j et dont la valeur est soit 0 soit 1, sont représentés par des barres verticales qui montrent un excès d'occurrence après l'impulsion.

Le taux de ces clics $\dot{C}$, appelé taux de compte, apparaît comme une mesure directe de la fluorescence du spin. Le signal est moyenné sur plusieurs itérations, ce qui donne $\langle \dot{C} \rangle$. Le cycle SMPD se répète pendant toute la durée T_{rep} entre deux séquences d'impulsions successives. Le taux de compte moyen décroit jusqu'au taux de fond $\langle \dot{C}_{\text{bg}} \rangle = \langle \dot{C}(t = T_{\text{rep}}) \rangle$. Pour extraire une valeur unique d'une courbe de fluorescence de spin, nous additionnons les comptes sur un temps d'intégration T_{int} pour obtenir les comptes intégrés $\langle C \rangle$. Cependant, comme une partie des photons intégrés sont des faux positifs, on peut choisir de supprimer les contributions du bruit de fond pour conserver une quantité directement proportionnelle au nombre de spins : $\langle C_{\text{spin}} \rangle$. [Alb+21; Bil+22]

1.2.2 Spectroscopie à large échelle

Dans Section 7.1, nous décrivons des spectres FD-ESR pris sur une grande échelle d'amplitude B_0 et d'orientation φ. A chaque valeur de B_0 et φ, nous envoyons une impulsion de fréquence $\omega_0/2\pi$ au résonateur et mesurons le signal de spin résultant. Nous présentons une telle spectroscopie dans le panneau de gauche Figure 2.2a avec B_0 variable, où les nombreux pics différents avec des couleurs indiquent que la FD-ESR détecte une grande variété d'espèces de spin présentes dans notre échantillon. Certains de ces pics sont directement attribués à des espèces connues, telles que Er^{3+} et Yb^{3+}, tandis que d'autres restent inconnus. Une caractéristique intéressante de la FD-ESR est d'avoir accès à la courbe de fluorescence de spin qui donne des informations supplémentaires sur le spin. Dans le panneau de droite de Figure 2.2a, nous traçons la courbe de relaxation mesurée à chaque pic et les comparons pour étayer l'attribution à des systèmes de spin.

La spectroscopie peut également être réalisée en faisant varier l'orientation du champ dans le plan (a, b), comme le montre l'illustration Figure 2.2b. Ce motif de rotation est riche en informations sur le spin car nous pouvons observer l'évolution des caractéristiques des pics avec φ telle que la largeur de ligne spectrale, l'amplitude du signal ou les courbes de relaxation. Dans le graphique, nous observons des pics qui restent fixes en B_0, comme la ligne d'Erbium à $B_0 \approx 59$ mT, et d'autres pics qui évoluent avec φ. Cette spectroscopie est cohérente avec des expériences similaires réalisées avec l'ID-ESR. [Le 22]

Dans la suite du manuscrit, nous fournissons une étude plus détaillée de Er^{3+}:$CaWO_4$ en utilisant FD-ESR. Nous montrons dans Figure 2.2c l'évolution de la largeur de raie Γ_{inh} de l'Erbium et de l'amplitude de raie à différents φ. L'amplitude atteint un maximum à $\varphi_0 = 30°$, qui est l'orientation typique utilisée pour la manipulation du spin de l'Erbium dans le montage 2 afin de maximiser le signal.

1.2.3 Le signal de fluorescence

Dans Section 7.2, nous étudions et reproduisons à l'aide de simulations la fluorescence de spin afin de mieux comprendre ce signal de spin facilement accessible avec la FD-ESR. Nous appliquons une impulsion d'excitation unique de force variable $\epsilon = \beta \times \Delta t$ aux spins et enregistrons $\langle \dot{C} \rangle$ après l'impulsion. Le résultat est comparé à la même quantité simulée avec un modèle d'équation maîtresse [Ran+20b], tel que présenté dans Figure 2.3 pour 4 valeurs de ϵ réparties sur 3 ordres de grandeur. La simulation inclut la distribution de spin inhomogène en fréquence et en couplage. La courbe de relaxation de l'ensemble des spins provient de la contribution de chaque spin j, dont la composante longitudinale $\langle S_{Z,j} \rangle$ se relaxe à la fois par rayonnement avec un taux dépendant de la position $\Gamma_{\text{R,j}}$ et de façon non radiative avec un taux constant Γ_{NR}. Comme la forme de la courbe est caractéristiques d'une force d'excitation ϵ, nous pouvons faire correspondre une forme de courbe simulée à une forme de courbe mesurée pour calibrer l'atténuation de la ligne d'entrée et trouvons $A_{\text{dB}} = 84,5$ dB. Une fois l'amplitude de l'impulsion calibrée, seule l'efficacité totale de détection du spin η reste un paramètre libre et peut être déterminée comme le rapport

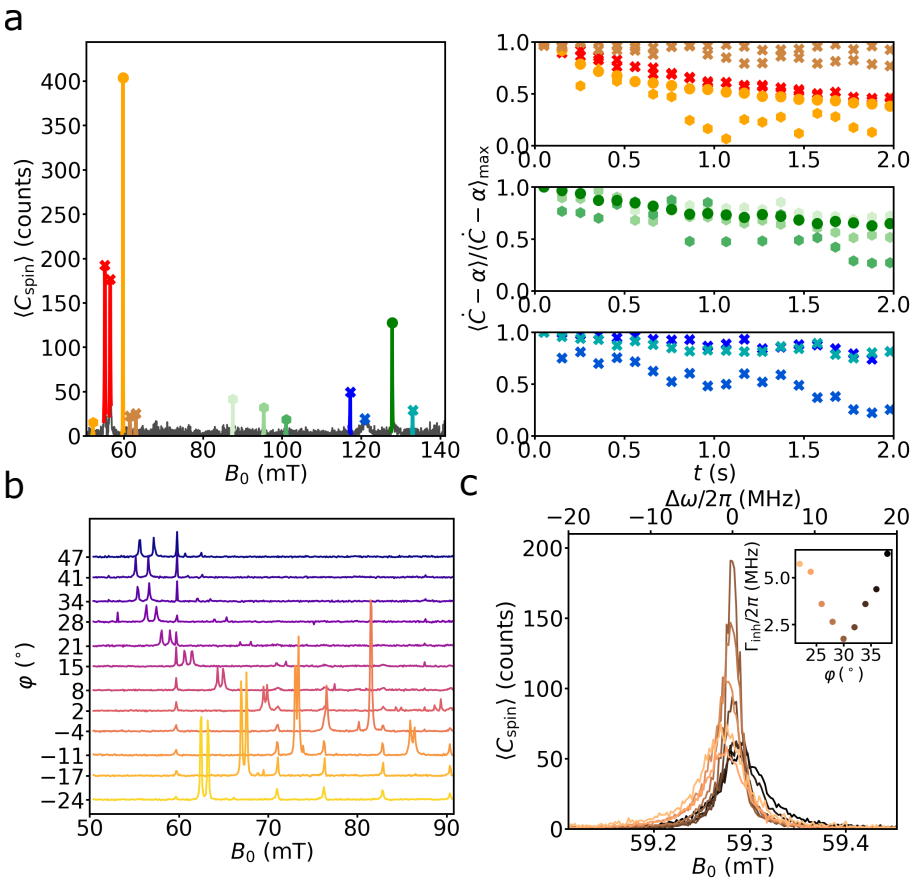

Figure 1.2: **Spectroscopie avec FD-ESR. a**. Panneau de gauche: signal de spin $\langle C_{\text{spin}} \rangle$ en fonction de l'amplitude du champ B_0 qui montre plusieurs signaux de spin (pics colorés). La position des pics permet d'attribuer Er^{3+} (orange) et Yb^{3+} (vert) avec un couplage hyperfin (symboles hexagonaux) ou sans (symboles circulaires), tandis que d'autres pics restent inconnus (symboles en croix). Panneau de droite : courbe de fluorescence normalisée avec le taux de faux positifs α soustrait pour chaque signal de spin détecté dans la spectroscopie. Les courbes de fluorescence sont regroupées entre pics de faible champ magnétique (panneau supérieur), entre pics associés à Yb^{3+} (panneau central) et entre pics inconnus (panneau inférieur). **b**. Motif de rotation où nous traçons $\langle C_{\text{spin}} \rangle$ en fonction de B_0 et φ. De nombreux pics sont visibles, certains montrant un champ résonnant indépendant de φ alors que la position d'autres pics dépend fortement de φ. La ligne d'Erbium est fixée à $B_0 \approx 59$ mT. **c**. Spectroscopie avec dépendance angulaire de la raie de l'Erbium. Les données sont ajustées avec une Lorentzienne donnant une largeur de raie inhomogène Γ_{inh} avec un minimum à $\varphi_0 = 30°$.

entre le nombre de comptes simulé et mesuré, ce qui donne $\eta = 0,15$. Cependant, nous observons des divergences entre la simulation et les données pour les faibles valeurs de ϵ que nous attribuons à l'effet des déformations du crystal, non pris en compte dans les simulations.

1.2.4 Sensibilité de la détection

Dans Section 7.3, nous avons comparé le SNR de la FD-ESR et l'ID-ESR dans des conditions d'excitation de spins très similaires afin de confirmer l'intérêt de la détection par fluorescence pour améliorer la sensibilité de la détection de spin. Pour l'ID-ESR, le signal est l'intégration de l'écho de spin X_e, exprimé dans son unité naturelle grâce à la calibration du nombre de photons de l'écho effectuée avec le SMPD. Pour la FD-ESR, le

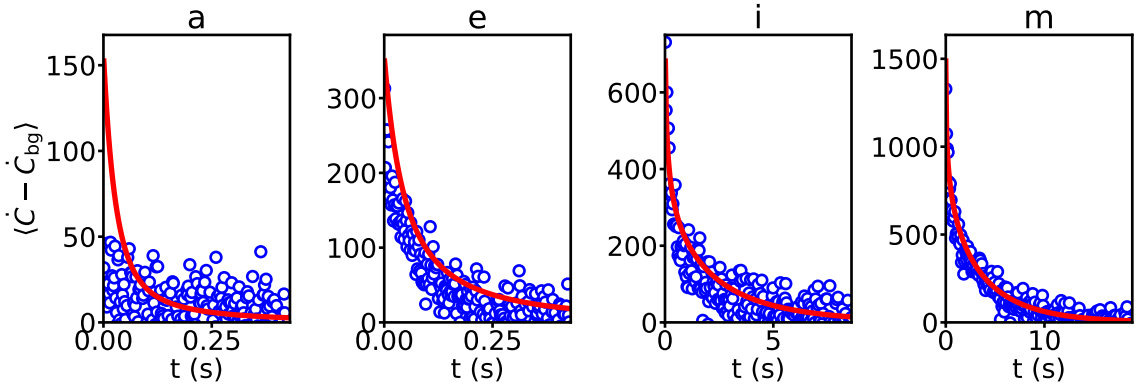

Figure 1.3: **Signal de fluorescence et simulations à différentes forces d'excitation.** Courbes de relaxation du spin avec soustraction du fond (points bleus) comparée aux simulations (courbe rouge) suite à une impulsion d'excitation unique pour différentes forces ϵ avec l'étiquette des graphiques basée sur Table 7.1 : $\epsilon = 4.9 \times 10^3\,\mathrm{ns}^{1/2}$ pour a, $\epsilon = 1.4 \times 10^4\,\mathrm{ns}^{1/2}$ pour e, $\epsilon = 1.0 \times 10^5\,\mathrm{ns}^{1/2}$ pour i, $\epsilon = 2.2 \times 10^6\,\mathrm{ns}^{1/2}$ pour m. Pour calculer ces courbes de simulation, nous avons calibré l'atténuation dans la ligne $A_{\mathrm{dB}} = 84.5$ dB et considéré une efficacité de détection totale $\eta = 0.15$.

signal est le nombre de coups intégrés sur un temps optimal T_{int} avec le fond soustrait. Les deux types de mesures sont répétés plusieurs fois afin d'obtenir des statistiques, comme le montre l'illustration Figure 2.4a. Les résultats permettent de comparer $\mathrm{SNR}_{\mathrm{ID}}$ avec $\mathrm{SNR}_{\mathrm{FD}}$ dans Figure 2.4b. Dans le régime de faible ϵ, la FD-ESR présente un gain de SNR allant jusqu'à un facteur 16 par rapport à l'ID-ESR, tandis que ce gain diminue à plus haute valeur de ϵ. Par conséquent, la FD-ESR est adaptée pour améliorer la sensibilité de l'ESR afin pour la détection de petits ensembles de spins avec une relaxation radiative rapide.

1.2.5 Spectroscopie d'ions sous contraintes méchaniques

Dans Chapter 8, nous utilisons la haute sensibilité de la FD-ESR pour mesurer un phénomène qui n'avait pas été détecté jusqu'à présent : un élargissement et une distorsion du spectre REI par déformation mécanique du crystal. Nous remarquons que le spectre de l'erbium est très différent lorsqu'il est pris à une force d'impulsion ϵ faible ou élevée, comme on peut le voir dans Figure 2.5a. Bien que le spectre à forte intensité ϵ puisse être ajusté par une Lorentzienne qui définit ce que nous appelons la ligne principale dans la suite, le spectre à faible intensité ϵ est élargi, asymétrique, et présente une corrélation entre un temps de relaxation radiative plus court et la position dans la ligne. Cela signifie que les spins plus proches du résonateur, qui se relaxent radiativement plus rapidement en raison de leur couplage plus élevé au résonateur, sont décalés en fréquence de résonance. De tels décalages ont été observés précédemment avec les ions de Bismuth dans le silicium, également mesurés par des micro-résonateurs. Ils se produisent en raison de la contraction thermique différentielle entre le fil métallique inductif et le cristal hôte [Pla+18]. Dans le cas de l'Erbium dans $CaWO_4$, la contrainte modifie le champ cristallin et donc le tenseur gyromagnétique du REI [Kie66; Mim65]. Pour explorer ce phénomène, nous mesurons les spectres d'ions Erbium avec des impulsions de faible ϵ à différents angles φ. Les résultats dans Figure 2.5b montrent comment la forme asymétrique évolue des deux côtés de la ligne principale, en fonction de φ. Nous ajustons chaque spectre avec une Lorentzienne asymétrique et trouvons que l'asymétrie $\gamma \times \Gamma_{\mathrm{inh}}$ est apparemment antisymétrique autour de φ_0. La compréhension complète de l'effet des contrainte mécaniques sur les ions Erbium nécessiterait un travail théorique plus approfondi et n'entre pas dans le cadre de cette

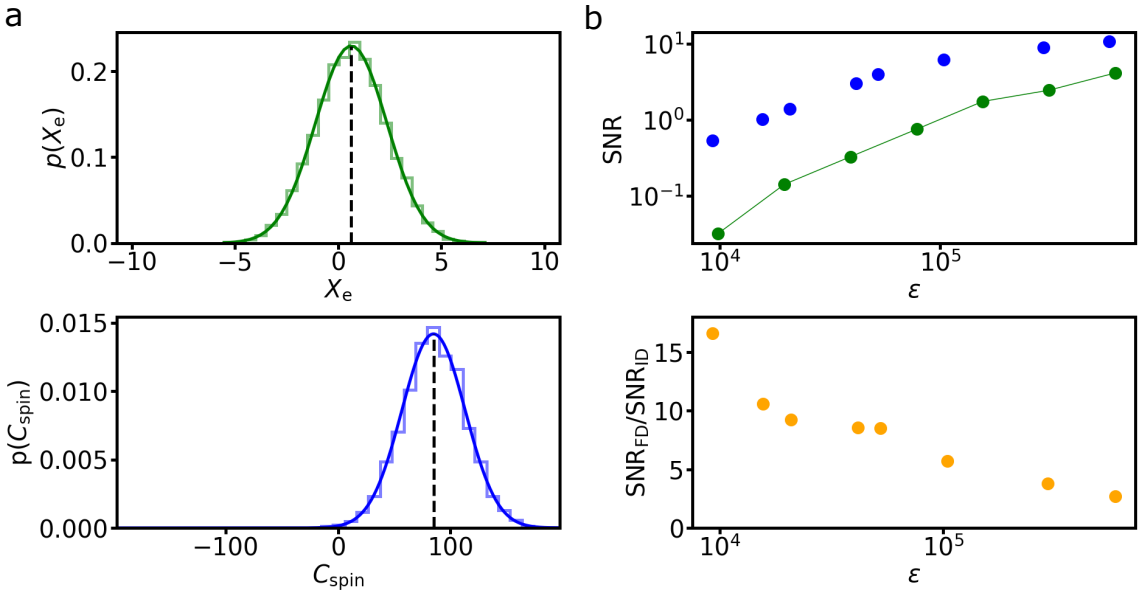

Figure 1.4: **comparaison du SNR entre l'ID et le FD**. **a**. Distribution du signal pour l'ID-ESR (panneau supérieur) et la FD-ESR (panneau inférieur) ajustée avec une fonction gaussienne (ligne solide plus foncée), montrant leur valeur moyenne (ligne pointillée noire). Les graphiques sont alignés sur 0 et ont une largeur de 14 fois l'écarts types permettant une comparaison visuelle. **b**. Panneau supérieur : $\mathrm{SNR_{ID}}$ (vert) et $\mathrm{SNR_{FD}}$ (bleu) à différents ϵ comme détaillé dans Table 7.2 et Table 7.3. Le rapport SNR est calculé en utilisant une interpolation linéaire de $\mathrm{SNR_{ID}}$ (ligne continue verte). Panneau inférieur : rapport des SNR des deux méthodes.

thèse.

Une conséquence intéressante de la contrainte mécanique est la séparation de la ligne principale d'un sous-ensemble de spins avec un couplage relativement homogène g_{eff}. En plaçant le champ magnétique à côté de la ligne principale, nous pouvons n'interagir qu'avec ces spins fortement couplés. Dans Figure 2.5c, nous fixons $B_0 = 59.7\,\mathrm{mT}$ et manipulons de manière cohérente les spins en résonance en faisant varier la durée de l'impulsion d'excitation Δt. Une oscillation cohérente est visible et est finalement amortie, probablement par l'inhomogénéité de couplage restante. En réglant le champ plus près de la ligne principale, nous pouvons sélectionner un sous-ensemble de spins avec un plus petit g_{eff} et voir effectivement un ralentissement de la fréquence de Rabi effective.

1.2.6 Détection d'écho de spin par fluorescence

Dans Chapter 9, nous présentons la détection de l'écho de spin par FD-ESR. Comme la FD-ESR est sensible à la composante de spin $\langle S_Z \rangle$, nous utilisons une séquence de trois impulsions $\epsilon/2_X - \tau - \epsilon_Y - \tau - \epsilon/2_\Phi$, qui consiste à appliquer une impulsion de restauration de phase Φ après la séquence d'écho de Hahn, pour projeter l'écho de spin sur l'axe Z. Nous confirmons dans Figure 2.6a que le signal $\langle C_{\mathrm{spin}}(\Phi) \rangle$ possède une partie incohérente constante modulée par une partie cohérente dépendant de la phase de l'impulsion de restauration Φ. Les simulations permettent de reproduire ce signal avec une bonne fidélité pour la partie incohérente et une modulation cohérente légèrement plus importante, différence que nous attribuons à l'ESEEM, la modulation du signal due à l'oscillation des spins nucléaires voisins du spin l'électronique. En mesurant l'évolution d'un signal proportionnel à l'écho de spin $C_{\mathrm{echo}} = [C(\Phi = 0) - C(\Phi = \pi)]/2$, nous observons la forme de l'écho, visible dans Figure 2.6b, ainsi que la modulation du signal ESEEM, visible

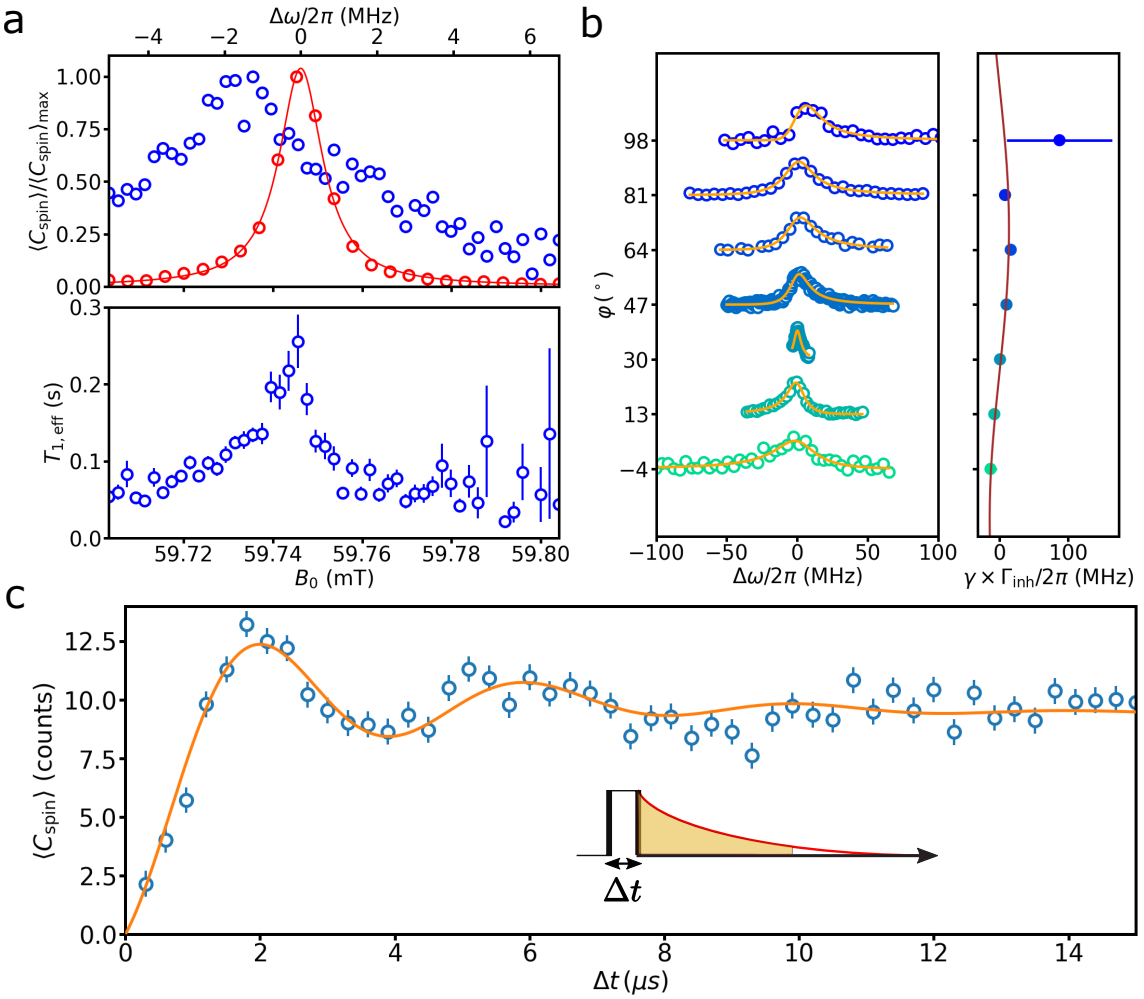

Figure 1.5: **Spectre asymétrique d'ions sous contraintes mécaniques et oscillations cohérentes.** **a**, panneau supérieur : spectroscopie normalisée de la raie de l'Erbium à haut ϵ (points rouges) ajustée avec une Lorentzienne (ligne rouge) qui définit la raie principale et une spectroscopie à bas ϵ (bleu). Panneau inférieur : $T_{1,\text{eff}}$ en fonction de B_0 déduit des ajustements exponentiels sur les courbes de relaxation des données du spectre à faible valeur de ϵ. Les barres d'erreur représentent le 1σ des ajustements. **b**, panneau de gauche : spectres à faible valeur de ϵ pour différents φ (points) et ajustement lorentzien asymétrique à l'aide de Equation 8.1 (ligne). Panneau de droite : skewness $\gamma \times \Gamma_{\text{inh}}$ (points) et ajustement en utilisant Equation 5.14 (ligne). Les barres d'erreur représentent le 1σ des ajustements. **c**. $\langle C_{\text{spin}} \rangle$ en fonction de la durée de l'impulsion Δt (points) à $B_0 = 59,7\,\text{mT}$ et $\varphi = \varphi_0$, avec la séquence d'impulsion représentée. La ligne continue est un ajustement utilisant Equation 8.3. Les barres d'erreur sont des statistiques à 1σ.

dans Figure 2.6c. Nous caractérisons également le temps de cohérence de l'Erbium mesuré par deux techniques différentes (voir dans Figure 2.6d) : par la détection du $\langle C_{\text{echo}} \rangle$, qui correspond pour l'ID-ESR à la détection d'une quadrature de champ unique, et par le calcul de l'écart type σ sur 4 phases d'impulsion de restauration différentes $\Phi_k = k\pi/2$ ($k = 0, 1, 2, 3$), qui correspond pour l'ID-ESR à la détection de l'amplitude du champ d'écho. En ajustant ces deux courbes avec une exponentielle étirée, la première technique donne un temps caractéristique relativement court $T_{2,\text{q}} = 3.6\,\text{ms}$ que nous attribuons au bruit du champ magnétique alors que la seconde technique donne le temps de cohérence intrinsèque du spin $T_{2,\text{m}} = 19\,\text{ms}$ [Le +21]. Comme la FD-ESR s'avère capable de détecter les échos de spin, nous comparons le SNR pour la détection des échos avec la FD-ESR

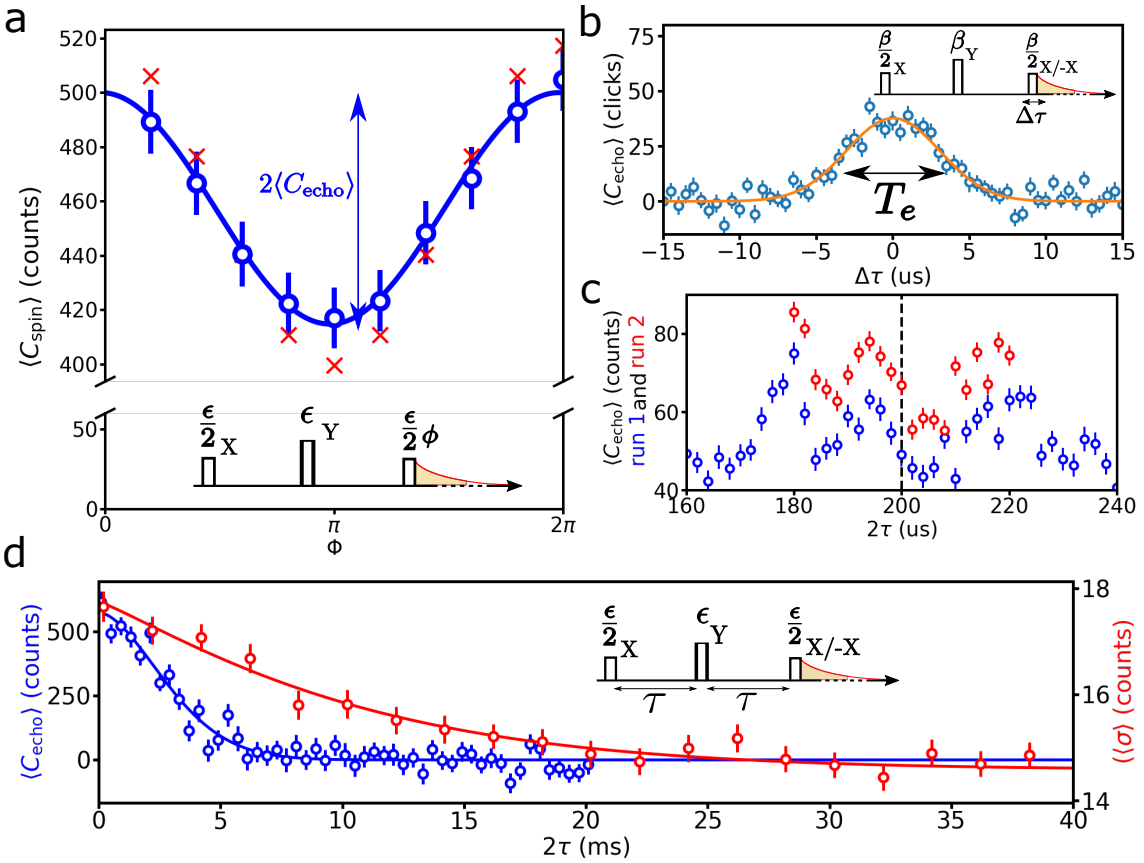

Figure 1.6: **Détection d'écho de spin par fluorescence.** Toutes les barres d'erreur sont des statistiques à 1σ. Les encarts représentent les séquences d'impulsions. **a**, $\langle C_{\text{spin}}\rangle$ en fonction de la phase de l'impulsion de restauration Φ avec des impulsions à haut ϵ, avec $B_0 = 59,7\,\text{mT}$ et $\varphi = \varphi_0$. Les points bleus (croix rouges) sont des points expérimentaux (simulés). La ligne continue est un ajustement à l'aide de Equation 9.1 sur les données, qui donne $\langle C_{\text{echo}}\rangle = 44$ points. **b**, $\langle C_{\text{echo}}\rangle$ (points bleus) en fonction du délai $\Delta\tau$ entre l'impulsion de restauration et le moment attendu pour l'écho. La ligne continue est un ajustement gaussien qui donne une largeur totale à mi-hauteur (FWHM) $T_e = 6,1\,\mu\text{s}$, correspondant à la durée de l'écho (double flèche noire). **c**, $\langle C_{\text{echo}}\rangle$ en fonction du délai 2τ de deux mesures successives (rouge et bleu), montrant l'ESEEM. La différence de signal entre les des mesures est probablement due à une différence dans la calibration du SMPD. La ligne pointillée est $\tau = 100\,\mu\text{s}$, utilisée pour les données du panneau a. **d**, courbes de relaxation de $\langle C_{\text{echo}}\rangle$ (points bleus) et σ (points rouges) en fonction du délai 2τ, toutes deux ajustées avec une exponentielle étirée Equation 9.3. Les ajustements donnent pour la relaxation $\langle C_{\text{echo}}\rangle$ une constante de temps $T_{2,\text{q}} = 3,6\,\text{ms}$ et un exposant $x_{\text{q}} = 1,7$, tandis que pour σ on obtient $T_{2,\text{m}} = 19\,\text{ms}$ et un exposant $x_{\text{m}} = 1,13$.

et l'ID-ESR dans des conditions d'excitation identiques. Nous trouvons que la FD-ESR fournit un gain d'un facteur 1.6 pour une faible impulsion d'excitation.

Chapter 2

Introduction

2.1 Overview

Magnetic resonance (MR) is a characterization method for probing the properties of matter. This technique is widely used since its only requirement is the presence of spins, ubiquitous in matter both in electrons and nuclei. The spin Larmor frequency ω_s is tuned by the application of a static magnetic field B_0, which allow the spins to absorb an electromagnetic field at the same frequency ω_s. In Continuous Wave (CW) MR, this absorption manifests itself by a change in the reflection coefficient, measurable with a network analyzer. In pulsed MR, the spin dynamics is probed by using sequences of resonant pulses. MR gives access to all the spin meaningful properties: spin density, resonant frequency, relaxation time, local magnetic fluctuations... [Abr11; AB12]. This detection method is used on a wide variety of spin system, either in Electron Spin Resonance (ESR) or Nuclear Magnetic Resonance (NMR), and finds application in biology [Yos+96], biochemistry [Pol06] and solid-state sciences [Sli55]. This diversity of application corresponds to various experimental constraints, such as the temperature of the sample and the frequency ω_s.

This thesis deals with ESR spectroscopy of paramagnetic impurities in a crystal, at microwave frequencies (5-10 GHz) for B_0 fields in the 50-500 mT range. The spins are coupled to a microwave resonator at frequency ω_0 with a strength g_0. The usual spin detection method in pulsed ESR is called the Inductive Detection (ID) [Rab+38; Blo46; PTP46]. The spins are probed by sequences of microwave pulses, which lead to the build-up of a transient macroscopic transverse polarization $\langle S_X \rangle$ at a later time. The Larmor precession of this magnetization induces the emission of a microwave pulse called a spin-echo [Hah50]. This spin-echo is detected by amplification and demodulation, and its amplitude and phase encodes the spin properties. Commercially available ID-ESR apparatus can detect only large ensemble of spins, bigger than 10^9 spins [Abh+22]. In this context, increasing the ESR sensitivity while preserving its application generality is very desirable.

Several methods have been proposed and implemented to highly increase ESR sensitivity [WF16]. One can use the charge of the electron carrying the spin to couple to the resonator electric field, yielding typically orders of magnitude greater coupling than the magnetic field coupling [Xia+04]. This method employs a transistor structure on top of semi-conducting materials, which greatly limits its generality. Another approach is to use a tip to focus the magnetic field on top of a mechanical cantilever. This method has a very small mode volume of the order nm^3, which permits to scan a surface but remains blind to bulk properties. Another idea is to get around the limitation due to the low energy microwave frequency field using spin systems that also have transitions in the optic domain [Riz+22]. NV centers in diamond as well as Erbium ions are such system where the sensitivity of a single ion has already been reached by optical method [Gru+97; Yin+13]. However this

method apply only to the few spin systems with an optical transition, which restricts a lot its generality. A general ESR method with high sensitivity is to be found somewhere else.

In the Quantronics group, our approach, led by Patrice Bertet, is to apply circuit Quantum Electrodynamics (cQED) [HR06; Wal+06] techniques to perform very sensitive ESR. cQED makes use of superconducting circuits cooled down at millikelvin temperature. These circuits offer new devices useful for microwave fields detection: low-mode-volume and high-quality-factor microwave resonators, quantum-limited Josephson Parametric Amplifiers (JPA), and more recently qubit-based Single Microwave Photon Detectors (SMPD); therefore, they can be naturally applied for ESR spectroscopy. In our experiments, we use superconducting micro-resonators to detect the spins; their specific interest is their low magnetic mode volume, which enables a significant increase in spin-photon coupling, up to $g_0/2\pi \sim 1$kHz. With such large coupling, spins resonant with the cavity tend to relax dominantly by spontaneous emission of a microwave photon, reaching a new regime for MR called the Purcell regime, first seen by Audrey Bienfait [Bie+16].

Using such micro-resonators combined with JPAs for noiseless amplification of the echo signal, ID-ESR has proven to reach very high sensitivity of ~ 10 spins in the work of Vishal Ranjan [Ran+20a], but was ultimately limited by unavoidable vacuum field noise. In 2020, a new method (called Fluorescence-Detected ESR, or FD-ESR) has been proposed and demonstrated in our group [Alb+21], which promises to overcome this fundamental limit. The idea is to detect the microwave photons spontaneously emitted by the spins during their radiative relaxation. For that, we use a SMPD recently developed in our group by Emmanuel Flurin [Les+20]. The proof of principle of FD-ESR was obtained by Emanuele Albertinale by detecting Bismuth donors in Silicon [Alb+21; Alb21]. However, the generality of FD-ESR remained to be proven as well as its advantage in term of sensitivity compared to ID-ESR. My thesis took place in parallel with the one of Leo Balembois, who worked to develop a new-generation of SMPDs with improved characteristics.

In this thesis, we apply FD-ESR to Rare-Earth Ions (REI) in a scheelite crystal of $CaWO_4$, and in particular Er^{3+} ions. This system was characterized by ID-ESR in our group by Marianne le Dantec and Milos Rančić, and have shown long coherent properties promising for quantum computing applications [Le +21; Le 22].

In this thesis, we prove that FD-ESR is a general characterization method that yields the same information on the spins than ID-ESR but with a higher sensitivity for small spin ensemble detection.

This manuscript starts with three "background" chapters that introduce the reader with the basic concepts required to understand our work. In Chapter 3, we will describe ESR performed in the quantum regime on a spin ensemble. Then in Chapter 4, we will explain the principle and potentialities of two detection methods: quadrature detection and photon detection. Next, in Chapter 5 we will consider the physics of REI in Scheelite and detail some measurement results obtained by Marianne Le-Dantec with ID-ESR applied to Erbium ions prior to this thesis .

In Chapter 6, we describe the experimental systems that have been used to collect the data presented in this thesis. The sample studied in this PhD is a $CaWO_4$ crystal fabricated and first pre-characterized with standard ESR in collaboration with other laboratories. We describe the room-temperature and cryogenic setups enabling to perform ESR and then introduce the reader to the typical ESR measurement done either with ID or with FD.

We show experimentally in Chapter 7 that FD-ESR is a detection method that can be applied to a wide variety of spin species and that it has a higher sensitivity then ID-ESR. We record large-scale spectra with FD-ESR revealing many spin species. Among those spins, we decide to manipulate Erbium ions to realize FD-ESR experiments in the rest of this thesis. We investigate the spin fluorescence signal as a better understanding of this new kind of signal gives access to additional spin information. We record the signal at

various excitation strength and reproduce it with simulations, proving that our simulation model captures most of our experiment physics. Since improving sensitivity is at the heart of our research, we compare the Signal-to-Noise Ration (SNR) of FD-ESR and ID-ESR and show an advantage for FD-ESR. Therefore, we validate FD-ESR as a very high sensitivity spectroscopic technique.

Thanks to FD-ESR high sensitivity, we notice a phenomenon that had remained invisible with ID-ESR. We present in Chapter 8 the correlation between resonant frequency and relaxation time for a small spin sub-ensemble highly coupled to the superconducting resonator. As simulations show that the resonator wire thermal contraction is expected to induce lattice deformation, we attribute this effect to local strain. This effect, known with other spin systems [Pla+18], was measured at various B_0 orientation and would need additional theoretical work to be understood. The spin sub-ensemble coupling homogeneity enables us to drive them into a coherent oscillation. Hence, we demonstrate that FD-ESR is a promising detection method to coherently manipulate a small spin ensemble.

Eventually in Chapter 9, we detect spin echoes with FD-ESR, proving that this detection method is suited for ESR standard applications [Bil+22]. A Hahn echo sequence followed by a restoring pulse is employed to convert the spin $\langle S_X \rangle$ component into the $\langle S_Z \rangle$ component, visible with FD-ESR [BHP73; OMG88]. After proving that we are indeed able to detect the echo contribution in the fluorescence signal, we use FD-ESR to characterize the spins coherent properties. We detect how the echo amplitude evolves over time and show Electron Spin Echo Envelope Modulation (ESEEM) as well as a spin coherence time of around 4 ms. From prior ID-ESR measurements, we know that this coherent time is limited by field noise, therefore we develop a detection procedure based on the signal fluctuations to access with FD-ESR the intrinsic spin coherence time. We compare the SNR of the two detection methods applied to spin echo detection and find again an advantage for FD-ESR.

2.2 Thesis Results

2.2.1 Experimental system

In this thesis, we apply FD-ESR to REIs in a sample of $CaWO_4$. REI ions are naturally present in $CaWO_4$ in substitution of Ca^{2+} ions. Some REI embedded in a crystal behave as Kramers' ions [Kra30] that present a spin degree of freedom. Here we focus on the magnetic resonance of their electron spin that behaves as a spin-1/2. As shown in Figure 2.1a, the Ca^{2+} sites have a tetragonal symmetry that induces the same symmetry on the spin properties [Enr71; Ber+09]: the spin **g**-tensor is anisotropic with $g_c \neq g_{a,b}$. The large **g**-value in the (a, b)-plane for several REIs (Erbium ions have $g_{a,b} = 8.38$) motivates their study with ESR as they require a relatively low resonant field B_0 and present a strong magnetic coupling in this plane. The choice of $CaWO_4$ as a substrate is guided by its low paramagnetic impurities density, basically dominated by the fraction of ^{183}W isotope that possess a nuclear spin. The sample was grown undoped, and we use the residual REIs impurities present in the sample. Once the sample arrived in Quantronics Group, Marianne Le Dantec, a former PhD student, has characterized in great detail the Erbium ions properties using ID-ESR [Le 22; Le +21].

We pattern on top of the sample surface in the (a, b) plane a 2D superconducting resonator made of Niobium as represented in Figure 2.1b. The resonator is characterized by its resonant frequency $\omega_0/2\pi$ and its interactions with its environment, with a damping rate in the line κ_c and a damping rate in its internal losses κ_{int} that combine in a total rate $\kappa = \kappa_c + \kappa_{\text{int}}$. The resonator lumped element design presents two capacitive interdigitated pads linked by a $2\,\mu$m-wide wire. This wire magnetically couples the resonator mode to the spins with a coupling strength $g_0(r)$ depending on the spin position r in the substrate. The intracavity field α populating the resonator mode drives the spin j of frequency $\omega_j/2\pi$ at

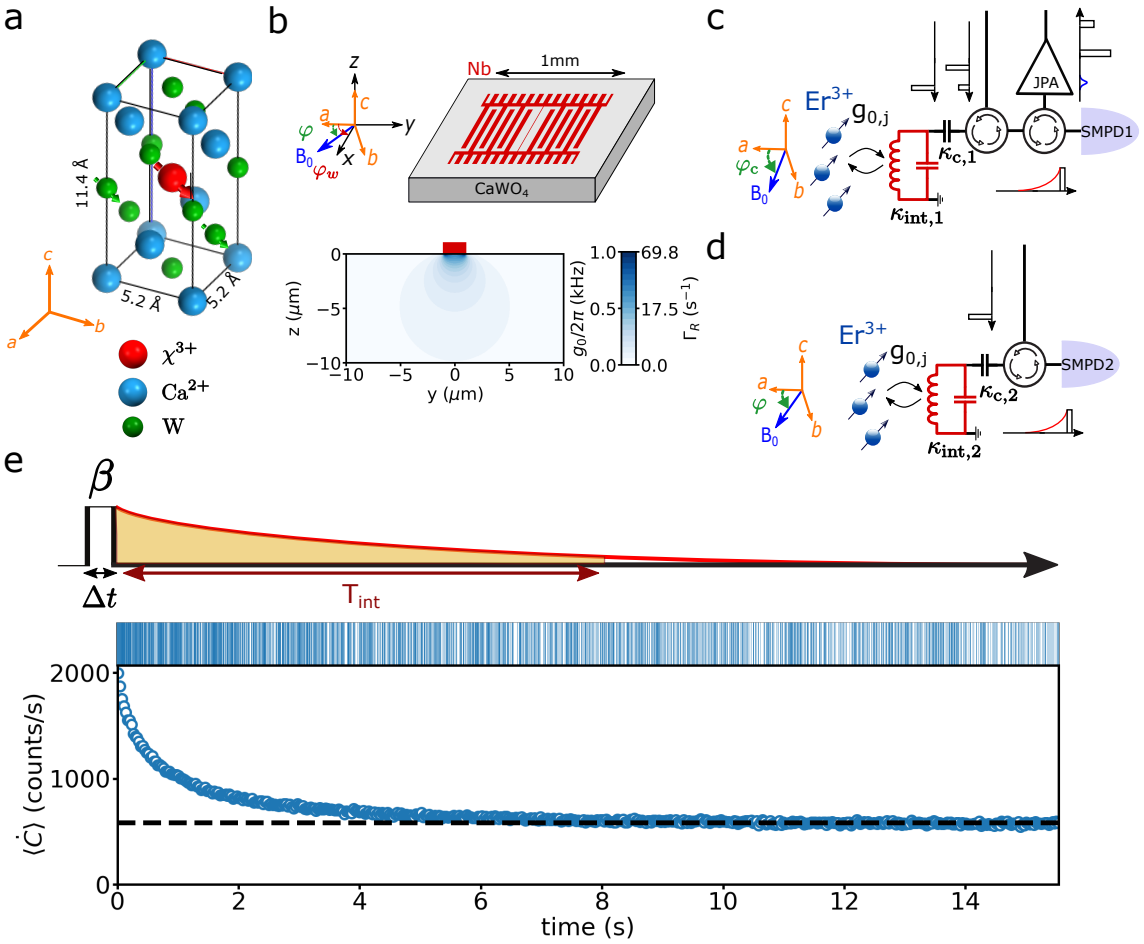

Figure 2.1: **Experiment principle and spin fluorescence signal a**. Schematic of the $CaWO_4$ lattice centered around a REI ion χ^{3+} that have replaced a Ca^{2+}. Oxygens are removed for clarity. A spin degree of freedom is represented for the REI as well as for some W atoms. The crystal symmetry is tetragonal around the axis c, which means axis a and b are equivalent. **b**. Design of the 2D resonator of frequency $\omega_0/2\pi \approx 7\,\mathrm{GHz}$ (red) patterned in the (a, b) plane on top of the sample surface (grey). The resonator wire is along the x axis (angle $\varphi_w = 51\,^\circ$) and B_0 is in the (a, b) plane (angle φ). The sample cross section below the $2\,\mu$m-wide wire (red rectangle) displays the spatial distribution of the coupling g_0 and of the corresponding radiative rate Γ_R (when $\varphi = 30\,^\circ$). **c**. Illustration of setup 1, where each spin j is coupled with a strength $g_{0,j}$ to the resonator with damping rates to the line $\kappa_{\mathrm{c},1}$ and to its internal losses $\kappa_{\mathrm{int},1}$. Circulators allow to use the same microwave line to excite the spins (black square pulses) and to route the spin signal (red and blue) to the detection apparatus. The signal can be detected either with FD-ESR using SMPD1, or with ID-ESR thanks to a JPA in the detection line. B_0 orientation is fixed at $\varphi_\mathrm{c} = 47\,^\circ$ **d**. Illustration of setup 2, with resonator characteristics $\kappa_{\mathrm{c},2}$ and $\kappa_{\mathrm{int},2}$. This setup is adapted only to perform FD-ESR and has a tunable field orientation φ. **e**. Typical fluorescence curve taken in setup 2. Top panel: schematic of the spin detection sequence where a pulse of amplitude β and duration Δt excites the spins that then relax by emitting fluorescence photons (red curve), detected and integrated over a period T_int to produce a number of counts $\langle C \rangle$ (orange surface). Middle panel: clicks (vertical bars) occur with a higher probability at short times after the excitation. Bottom pannel: instantaneous count rate $\langle \dot{C} \rangle$ (circles), averaged over ≈ 100 iterations, that decays down to a background rate $\langle \dot{C}_\mathrm{bg} \rangle$ (dashed black line).

position r with a Rabi frequency $\Omega_R(r)$. Varying the amplitude of the driving field in the resonator means probing spins at various distance from the wire. Afterward, the spins can relax their energy either non-radiatively with a rate Γ_{NR}, typically by emitting a phonon in the crystal lattice, or radiatively with a rate Γ_{R}, by emitting photons. In our system, the spin radiative relaxation rate is dominated by the influence of the resonator due to the so-called Purcell effect, yielding $\Gamma_{\mathrm{R}} = g_0^2\kappa/(\Delta\omega^2 + ((\kappa/2)^2)$ with $\Delta\omega = \omega_0 - \omega_i$ the spin resonator detuning. This rate is crucial in our experiment as the photons radiatively emitted by the spins are detectable with FD. The cross section in Figure 2.1b represents the spatial distribution of g_0 and Γ_{R} below the wire.

Figure 2.1c and Figure 2.1d are schematics of the main microwave components put at cryogenic temperature in the 2 experimental setups used in this thesis. In setup 1, the sample is connected both to the SMPD1, a SMPD from the first generation, and to a Josephson Parametric Amplifier (JPA) and thus can be measured either with FD-ESR or ID-ESR. In setup 2, measurements can only be done with FD-ESR with SMPD2, a SMPD from the second generation. B_0 is generated by two Helmotz coils that allow to change the field direction φ within the (a, b)-plane.

A typical spin fluorescence trace detected with FD-ESR following an excitation pulse of amplitude β and duration Δt applied at $t = 0$ is shown in Figure 2.1e along with the sequence representation. The SMPD clicks outputs c_j, from cycle j occurring at a cycle time t_j whose value is either 0 or 1, are represented by vertical bars and they show an excess in occurrence following the pulse. The rate of those clicks $\dot{C}$, named count rate, appears as a direct measurement of the spin fluorescence. The signal is averaged over several iterations, yielding $\langle\dot{C}\rangle$. The SMPD cycle keeps on going for the whole duration T_{rep} between two successive pulse sequence. The average count rate relaxes down to the background rate $\langle\dot{C}_{\mathrm{bg}}\rangle = \langle\dot{C}(t = T_{\mathrm{rep}})\rangle$. To extract a single value from a spin fluorescence curve, we sum the counts over an integration time T_{int} to obtain the integrated counts $\langle C\rangle$. However, since part of the photons integrated are dark counts, one can choose to remove the background contributions to keep a quantity directly proportional to the number of spins: $\langle C_{\mathrm{spin}}\rangle$. [Alb+21; Bil+22]

2.2.2 Large range spectroscopy

In Section 7.1, we describe FD-ESR spectra taken over a large scale of B_0 amplitude and orientation φ. At each value of B_0 and φ, we send a pulse with frequency $\omega_0/2\pi$ to the resonator and measure the resulting spin signal. We present such a spectroscopy in Figure 2.2a left panel with varying B_0, where the many different peaks with colors indicate that FD-ESR detects a wide variety of spin species present in our sample. Some of these peaks are straightforwardly attributed to known species, such as Er^{3+} and Yb^{3+}, whereas others remain unknown. An interesting feature of FD-ESR is to have access to the spin fluorescence curve that gives meaningfull spin information. In Figure 2.2a right panel, we plot the relaxation curve measured at each peak and compare them to deduce information on the spin system attribution.

The spectroscopy can also be taken varying the field orientation in the (a, b)-plane, as is shown in Figure 2.2b. This rotation pattern is rich in spin information as we can extract the peaks characteristics such as φ dependence, linewidth, signal amplitude or relaxation curves. In the graph, we observe peaks that remain fixed in B_0, such as the Erbium line at $B_0 \approx 59$ mT, and other peaks that evolve with φ. This spectroscopy is consistent with similar experiments done with ID-ESR. [Le 22]

In the rest of the manuscript, we provide a more detailed study of Er^{3+}:$CaWO_4$ using FD-ESR. We show in Figure 2.2c the evolution of the Erbium line linewidth Γ_{inh} and amplitude at various φ. The amplitude is reaching a maximum at $\varphi_0 = 30°$, which is the

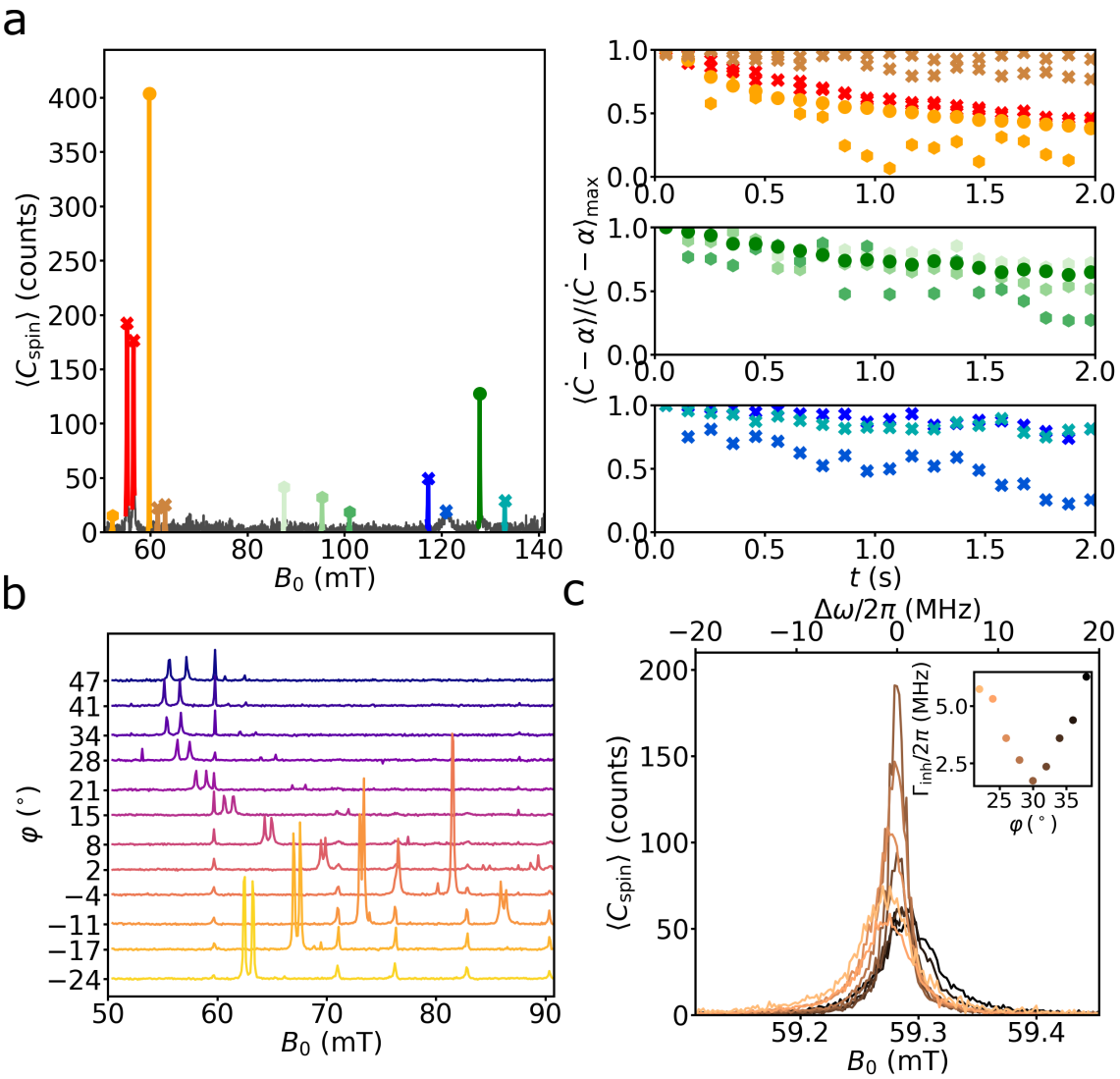

Figure 2.2: **FD-ESR spectroscopy in setup 2 a**. Left panel: spin signal $\langle C_{\text{spin}}\rangle$ as a function of the field amplitude B_0 that shows a wide variety of spin signals (colored peaks). The peaks position allows to attribute Er^{3+} (orange) and Yb^{3+} (green) with hyperfine coupling (hexagon symbols) or without (circle symbols), whereas other peaks remain unknown (cross symbols). Right panel: normalized fluorescence curve with dark count α subtracted for each spin signal detected in the spectroscopy. The fluorescence curves are grouped considering the low magnetic field peaks (top panel), the peaks associated to Yb^{3+} (middle panel) and the rest of the unknown peaks (bottom panel). **b**. Rotation pattern where we plot $\langle C_{\text{spin}}\rangle$ as a function of B_0 and φ. Many peaks are visible, with some peaks showing a resonant field independent from φ while other peaks position strongly depends on φ. The Erbium line is fixed at $B_0 \approx 59$ mT. **c**. Spectroscopy with angular dependence of the Erbium line. The data is fitted with a Lorentzian yielding the inhomogeneous linewidth Γ_{inh} with a minima at $\varphi_0 = 30°$.

typical orientation used for Erbium spin manipulation in setup 2 in order to maximize the signal.

2.2.3 Fluorescence signal

In Section 7.2, we study and reproduce with simulations the spin fluorescence in order to better understand this spin signal readily available with FD-ESR. We apply a single

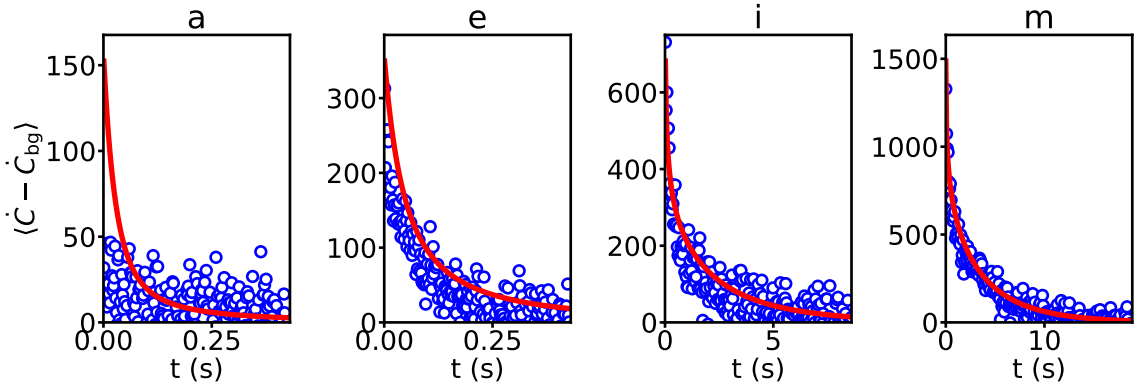

Figure 2.3: **Fluorescence signal and simulations at various excitation strength.** Spin relaxation with background subtracted (blue dots) matched with simulations (red curve) following a single pulse excitation with various strength ϵ with the graphs label based on Table 7.1: $\epsilon = 4.9 \times 10^3\,\mathrm{ns}^{1/2}$ for a, $\epsilon = 1.4 \times 10^4\,\mathrm{ns}^{1/2}$ for e, $\epsilon = 1.0 \times 10^5\,\mathrm{ns}^{1/2}$ for i, $\epsilon = 2.2 \times 10^6\,\mathrm{ns}^{1/2}$ for m. To compute these simulation curves, we have calibrated the attenuation in the line $A_{\mathrm{dB}} = 84.5$ dB and considered a total detection efficiency $\eta = 0.15$.

excitation pulse with various strength $\epsilon = \beta \times \Delta t$ to the spins and record $\langle \dot{C} \rangle$ following the pulse. The result is compared to the same quantity simulated with a master equation model [Ran+20b], as presented in Figure 2.3 for 4 values of ϵ spread over 3 orders of magnitude. The simulation includes the inhomogeneous spin distribution in frequency and coupling. The spin ensemble relaxation curve comes from the contribution of each spin j, whose longitudinal component $\langle S_{Z,j} \rangle$ relaxes both radiatively at the position dependent rate $\Gamma_{\mathrm{R,j}}$ and non-radiatively at constant rate Γ_{NR}. Since the curve shape corresponds uniquely to an excitation pulse ϵ, we can match a simulated shape with a measured shape to calibrate the input line attenuation and find $A_{\mathrm{dB}} = 84.5$ dB. Once the pulse amplitude calibrated, only the total spin detection efficiency η remains as a free parameter and can be determined as the ratio of the simulated to measured number of counts, yielding $\eta = 0.15$. However, we observe disrepancies between simulation and data at low-ϵ that we attribute to strain effect, not considered in the simulations.

2.2.4 Detection sensitivity

In Section 7.3, we have compared the SNR of FD-ESR and ID-ESR in very similar spins excitation conditions in order to confirm the interest of fluorescence detection to improve the spin detection sensitivity. For ID-ESR, the signal is the integration of the spin echo X_{e}, expressed in its natural unit thanks to the calibration of the echo photon number done with the SMPD. For FD-ESR, the signal is the counts integrated over an optimal time T_{int} with the background subtracted. Both type of measurements are reproduced many times to obtain some statistics, as is shown in Figure 2.4a. The resulting $\mathrm{SNR}_{\mathrm{ID}}$ is compared to $\mathrm{SNR}_{\mathrm{FD}}$ in Figure 2.4b. In the low-ϵ regime, FD-ESR presents a SNR gain by up to a factor 16 compared to ID-ESR, whereas the gain shrinks at high-ϵ. Therefore, FD-ESR is suited to bring an improvement in ESR sensitivity to detect small spin ensemble with fast radiative relaxation.

2.2.5 Spectroscopy of strain shifts

In Chapter 8, we then use the high sensitivity of FD-ESR to measure a phenomenon that was not detected so far: a broadening and distorsion of the REI spectrum by mechanical strain. We notice that erbium spectrum looks very different when taken at low or high

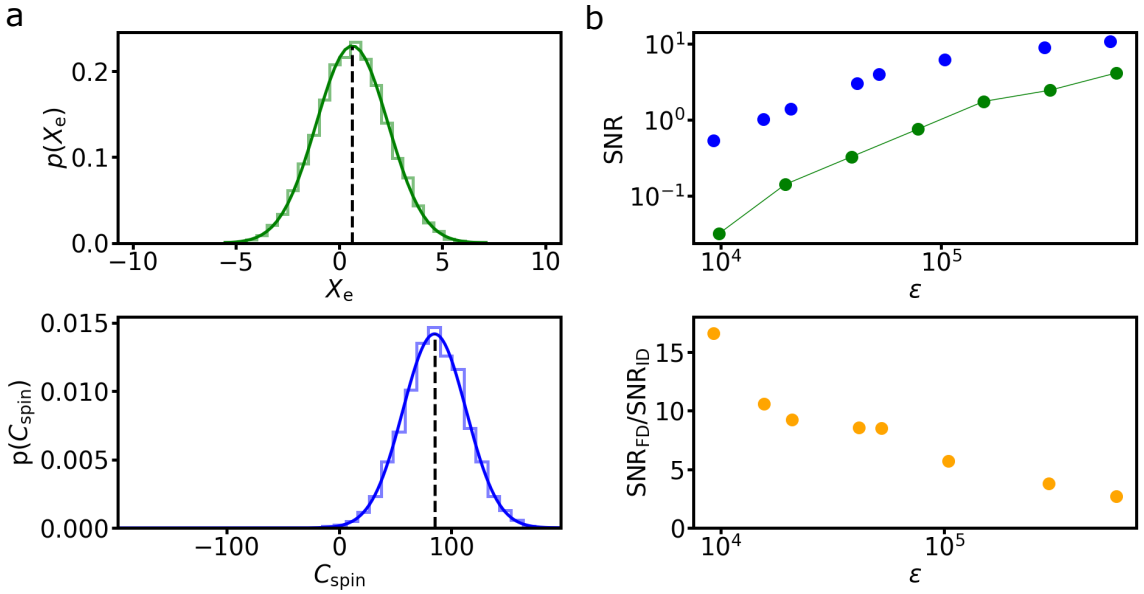

Figure 2.4: **SNR comparison between ID and FD**. **a**. Signal distribution for ID (top panel) and FD (bottom panel) fitted with a gaussian function (darker solid line), showing their mean value (black dashed line). Graphs are aligned on 0 and are 14 standard deviation large allowing visual comparison. **b**. Top panel: $\mathrm{SNR_{ID}}$ (green) and $\mathrm{SNR_{FD}}$ (blue) at various ϵ as detailed in Table 7.2 and Table 7.3. The SNR ratio is computed using a linear interpolation of $\mathrm{SNR_{ID}}$ (green solid line). Bottom panel: ratio of the two methods SNRs.

pulse strength ϵ, as can be seen in Figure 2.5a. Although the high ϵ spectrum can be fitted by a Lorentzian that sets what we call the main line in the following, the low-ϵ spectrum is broadened, asymmetrical, and displays a correlation between a shorter radiative relaxation time and the position in the line. This means that spins closer to the resonator, which relax radiatively faster due to their higher coupling to the resonator, are shifted in resonant frequency. Such shifts were previously observed in Bismuth donors in silicon also measured by micro-resonators. They occur because of the differential thermal contraction between the inductive metallic wire and the host crystal [Pla+18]. In the case of Erbium in $CaWO_4$, strain modifies the crystal field and therefore the REI gyromagnetic tensor [Kie66; Mim65]. To explore this phenomenon, we measure Erbium ions spectra with low ϵ pulses and various angle φ. The results in Figure 2.5b show how the asymmetric shape evolves on both sides of the main line, as a function of φ. We fit each spectrum with a skewed Lorentzian and find that the Skewness $\gamma \times \Gamma_{\mathrm{inh}}$ is apparently anti-symmetric around φ_0. The full understanding of the strain effect on the Erbium ions would require further theoretical work and is out of the scope of this thesis.

An interesting consequence of the strain is the detuning from the main line of a spin sub-ensemble with a relatively homogeneous coupling g_{eff}. Setting the magnetic field on the side of the main line, we can interact only with those highly coupled spins. In Figure 2.5c, we set $B_0 = 59.7\,\mathrm{mT}$ and coherently drive the spins on resonance by varying the excitation pulse duration Δt. A coherent oscillation is visible and is eventually damped, likely by the remaining inhomogeneity in coupling. By setting the field closer to the main line, we can select a spin sub-ensemble with a smaller g_{eff} and see indeed a slowdown in the effective Rabi frequency.

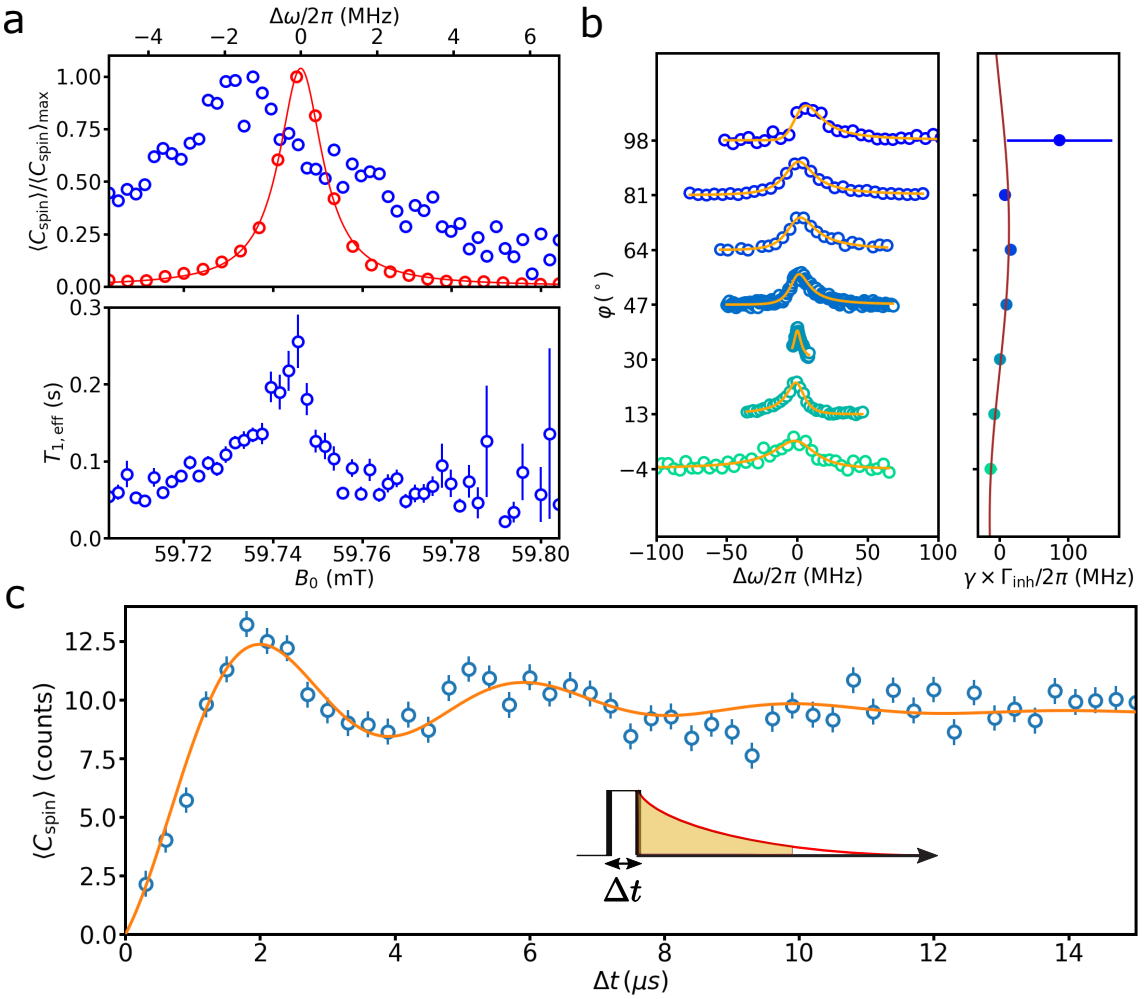

Figure 2.5: **Asymmetry spectrum of strained ions and coherent oscillations. a**, top panel: normalized spectroscopy of the Erbium line at high-ϵ (red dots) fitted with a Lorentzian (red line) that defines the main line and a spectroscopy at low-ϵ (blue). Bottom panel: $T_{1,\text{eff}}$ as a function of B_0 deduced from exponential fits on the low-ϵ spectrum. Error bars are 1σ from the fits. **b**, left panel: Low-ϵ spectra at various φ (dots) and skewed Lorentzian fit using Equation 8.1 (line). Right panel: Skewness $\gamma \times \Gamma_{\text{inh}}$ (dots) and fit using Equation 5.14 (line). Error bars are 1σ from the fits. **c**. $\langle C_{\text{spin}} \rangle$ as a function of pulse duration Δt (dots) at $B_0 = 59.7\,\text{mT}$ and $\varphi = \varphi_0$, with the pulse sequence illustrated in the inset. The solid line is a fit using Equation 8.3. Error bars are 1σ statistical.

2.2.6 Fluorescence detection of spin echoes

In Chapter 9, we report spin echo detection using FD-ESR. As FD-ESR is sensitive to the spin $\langle S_Z \rangle$ component, we use a three pulse sequence $\epsilon/2_X - \tau - \epsilon_Y - \tau - \epsilon/2_\Phi$, that consists in applying a restoring pulse of phase Φ after the Hahn echo sequence, to project the spin echo onto the Z-axis. We confirm in Figure 2.6a that the signal $\langle C_{\text{spin}}(\Phi) \rangle$ has a constant incoherent part modulated by a coherent part depending on the restoring pulse phase Φ. Simulations are used to reproduce this signal with a good reproduction of the incoherent part and a slightly larger coherent modulation, a difference that we attribute to ESEEM, the signal modulation due to the oscillation of the electron spin neighboring nuclear spins. Measuring the evolution of a signal proportional to the spin echo $C_{\text{echo}} = [C(\Phi = 0) - C(\Phi = \pi)]/2$, we observe the echo shape, visible in Figure 2.6b, as well as the ESEEM signal modulation, visible in Figure 2.6c. We also characterize

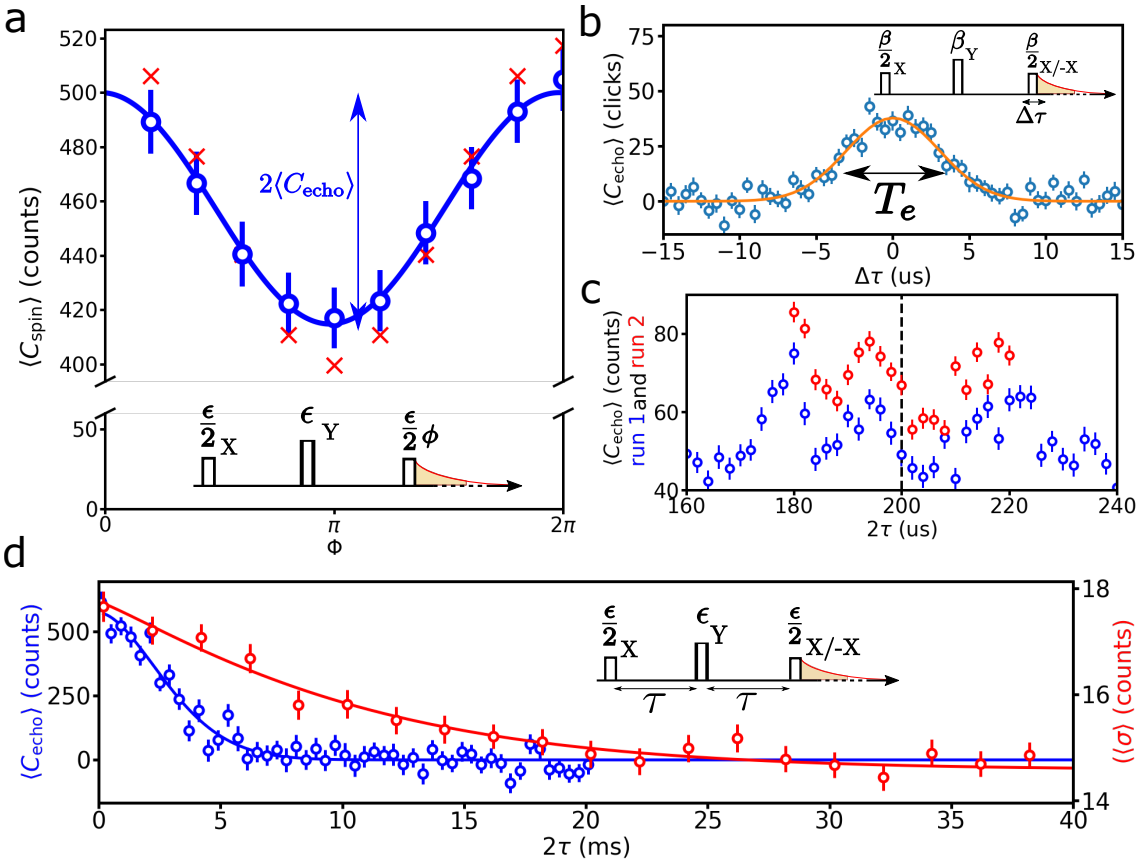

Figure 2.6: **Fluorescence detection of spin echoes.** All error bars are 1σ statistical. The insets represent the pulse sequence. **a**, $\langle C_{\text{spin}} \rangle$ as a function of the restoring pulse phase Φ with high-ϵ pulses, at $B_0 = 59.7\,\text{mT}$ and $\varphi = \varphi_0$. Blue dots (red crosses) are experimental (simulated) points. The solid line is a fit using Equation 9.1 on the data yielding $\langle C_{\text{echo}} \rangle = 44$ counts. **b**, $\langle C_{\text{echo}} \rangle$ (blue dots) as a function of the delay $\Delta\tau$ between the restoring pulse and the expected echo time. The solid line is a Gaussian fit yielding a Full Width at Half Maximum (FWHM) $T_e = 6.1\,\mu\text{s}$, corresponding to the echo duration (black double arrow). **c**, $\langle C_{\text{echo}} \rangle$ as a function of the delay 2τ of two successive runs (red and blue), showing ESEEM. The difference of signal between the runs is likely due to difference in the SMPD calibration. The dashed line is $\tau = 100\,\mu\text{s}$, used for the data of panel a. **d**, relaxation curves of $\langle C_{\text{echo}} \rangle$ (blue dots) and σ (red dots) as a function of the delay 2τ, both fitted with a stretched exponential Equation 9.3. The fits yield for $\langle C_{\text{echo}} \rangle$ relaxation a time constant $T_{2,\text{q}} = 3.6\,\text{ms}$ and exponent $x_{\text{q}} = 1.7$, whereas for σ it gives $T_{2,\text{m}} = 19\,\text{ms}$ and exponent $x_{\text{m}} = 1.13$.

the Erbium coherence time measured by two different techniques (see in Figure 2.6d): by the detection of $\langle C_{\text{echo}} \rangle$, which in ID-ESR corresponds to the detection of a single field quadrature, and by computing the standard deviation σ over 4 different refocusing pulse phase $\Phi_k = k\pi/2$ $(k = 0, 1, 2, 3)$, which in ID-ESR corresponds to the detection of the echo field magnitude. As we fit those two curves with a stretched exponential, the first technique yields a relatively short characteristic time $T_{2,\text{q}} = 3.6\,\text{ms}$ that we attribute to field noise whereas the second technique gives the intrinsic spin coherence time $T_{2,\text{m}} = 19\,\text{ms}$ [Le +21]. As FD-ESR proves to be able to detect spin echos, we compare the SNR of echo detection with FD-ESR and ID-ESR in identical pulse excitation conditions. We find that FD-ESR provides a gain of a factor 1.6 for low excitation pulse.

Chapter 3

Spins coupled to a quantum cavity

In this chapter, we proceed with the quantum description of the interaction between spins and a microwave resonator. One key concept is the resonant enhancement of the spin radiative relaxation that occurs by Purcell effect when the spin is on resonance with the resonator frequency. Based on the Purcell effect, we provide an analytical formula that describes the microwave fluorescence from an ensemble of electron spins. Combined with numerical simulations of the spin ensemble evolution, this formula will be used extensively to quantitatively model the results of the experiments presented in this manuscript.

3.1 The Jaynes-Cummings Hamiltonian

We start with the description of the spin-resonator system. The Hamiltonian that describes this system, the so-called Jaynes-Cummings Hamiltonian, is

$$H_{\mathrm{JC}} = H_{\mathrm{reso}} + H_{\mathrm{spin}} + H_{\mathrm{coupling}}. \tag{3.1}$$

It is the sum of three terms describing the resonator alone, the spin in the applied magnetic field, and their magnetic coupling. In this part, we describe with further detail these 3 contributions.

3.1.1 Quantization of an electomagnetic resonator

A 2D superconducting lumped element resonator, consisting in two capacitive pads linked by a wire, acts as a harmonic oscillator where the energy oscillates between an electrical component (when charges Q and -Q accumulate on the pads) and a magnetic component (when the charges flow from one pad to the other through the wire). The Hamiltonian that describes properly such system is

$$H_{\mathrm{reso}} = \frac{\hat{Q}^2}{2C} + \frac{\hat{\Phi}^2}{2L} \tag{3.2}$$

where $\hat{Q}$ and $\hat{\Phi}$ are respectively the charge and flux operators within the resonator, C is its capacitance and L its inductance. $\hat{Q}$ and $\hat{\Phi}$ are conjugate variables, which means they respect the commutation rule: $[\hat{Q}, \hat{\Phi}] = i\hbar$.

Rather than operators describing the electromagnetic quantities such as $\hat{Q}$ and $\hat{\Phi}$, one might conveniently use field operators that describe the amount of photon populating the resonator. Those operators are defined as

$$\begin{aligned} \hat{a} &= \frac{1}{\sqrt{2\hbar \mathrm{Z}_0}}(\hat{\Phi} + i\mathrm{Z}_0\hat{Q}) \\ \hat{a}^\dagger &= \frac{1}{\sqrt{2\hbar \mathrm{Z}_0}}(\hat{\Phi} - i\mathrm{Z}_0\hat{Q}) \end{aligned} \tag{3.3}$$

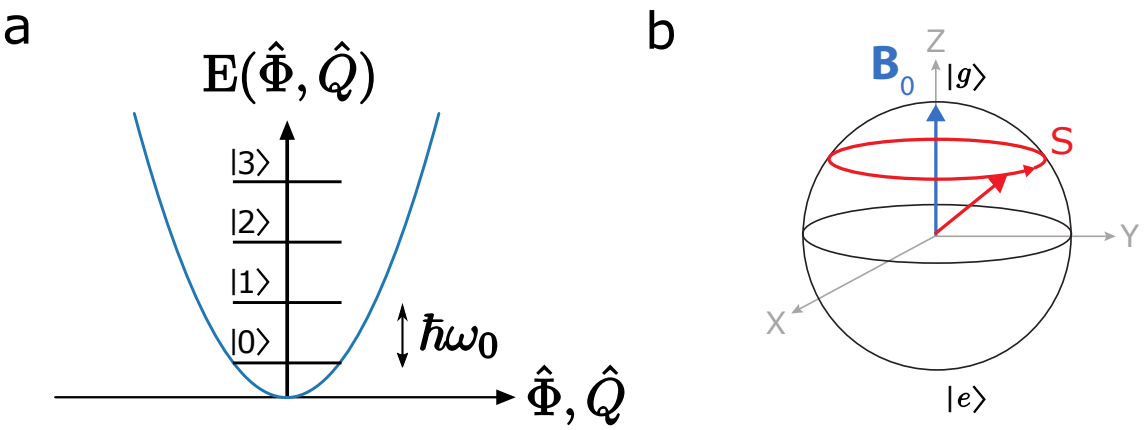

Figure 3.1: **Quantum state representation a**. Energy levels of a harmonic oscillator (black lines) confined in a quadratic potential (blue line) with the Fock states represented. **b**, Bloch sphere representation of the spin state $\boldsymbol{S}$ and its free dynamics. The spin precesses around its quantization axis, defined by $\boldsymbol{B_0}$.

where $\omega_0 = 1/\sqrt{LC}$ is the oscillator resonant angular frequency and $\mathrm{Z}_0 = \sqrt{L/C}$ its impedance. Those operators allow to express the resonator Hamiltonian

$$H_{\mathrm{reso}}/\hbar = \omega_0(\hat{a}^\dagger\hat{a} + 1/2) \tag{3.4}$$

as a function of the intra-cavity photon number operator $\hat{a}^\dagger\hat{a}$, whose eigenstates are Fock states $|n\rangle$ corresponding to n photons populating the resonator. The harmonic oscillator energy spectrum is represented in Figure 3.1a.

3.1.2 Spin Zeeman Hamiltonian

In this thesis, we will be considering paramagnetic impurities in solids. Such systems can be described by a spin operator $\hat{\boldsymbol{S}} \equiv (\hat{S}_X, \hat{S}_Y, \hat{S}_Z)$, written in this manuscript in dimensionless units. In the case of a spin-1/2 system, this operator can be defined in term of the Pauli matrices

$$\hat{\sigma}_X = \begin{pmatrix} 0 & 1 \\ 1 & 0 \end{pmatrix}, \quad \hat{\sigma}_Y = \begin{pmatrix} 0 & -i \\ i & 0 \end{pmatrix}, \quad \hat{\sigma}_Z = \begin{pmatrix} 1 & 0 \\ 0 & -1 \end{pmatrix} \tag{3.5}$$

with $\hat{\boldsymbol{S}} = 1/2\hat{\boldsymbol{\sigma}}$.

The spin is source of a magnetic moment

$$\hat{\boldsymbol{\mu}} = \hbar\mu_B \boldsymbol{g} \cdot \hat{\boldsymbol{S}} \tag{3.6}$$

where $\boldsymbol{\mu}$ is the spin magnetic moment, $\hbar$ the reduced Planck constant, μ_B the Bohr magneton and $\boldsymbol{g}$ the paramagnetic system **g**-tensor, which depends on the system itself and also of its host matrix (see Chapter 5).

In a magnetic field $\boldsymbol{B_0}$, the paramagnetic center undergoes a Zeeman effect described by the Hamiltonian

$$H_{\mathrm{spin}}/\hbar = -\hat{\boldsymbol{\mu}} \cdot \boldsymbol{B_0} = -\hbar\mu_B \boldsymbol{g}\boldsymbol{B_0} \cdot \hat{\boldsymbol{S}} = -\boldsymbol{\gamma_s}\boldsymbol{B_0} \cdot \hat{\boldsymbol{S}} \tag{3.7}$$

with $\boldsymbol{\gamma_s}$ the spin system gyromagnetic tensor. Note that we will also encounter spin systems whose Hamiltonian includes other terms, such as hyperfine interaction with nuclear spins (see Chapter 5). In that case, and in all generality, the system is described by a spin Hamiltonian $H_{\mathrm{spin}}(\boldsymbol{B_0})$, which can be diagonalized, yielding the spin energy states.

In this work, we will always focus on transitions between 2 levels of the spin system, which can be written as a ground state $|g\rangle$ and an excited state $|e\rangle$. In that basis, noting

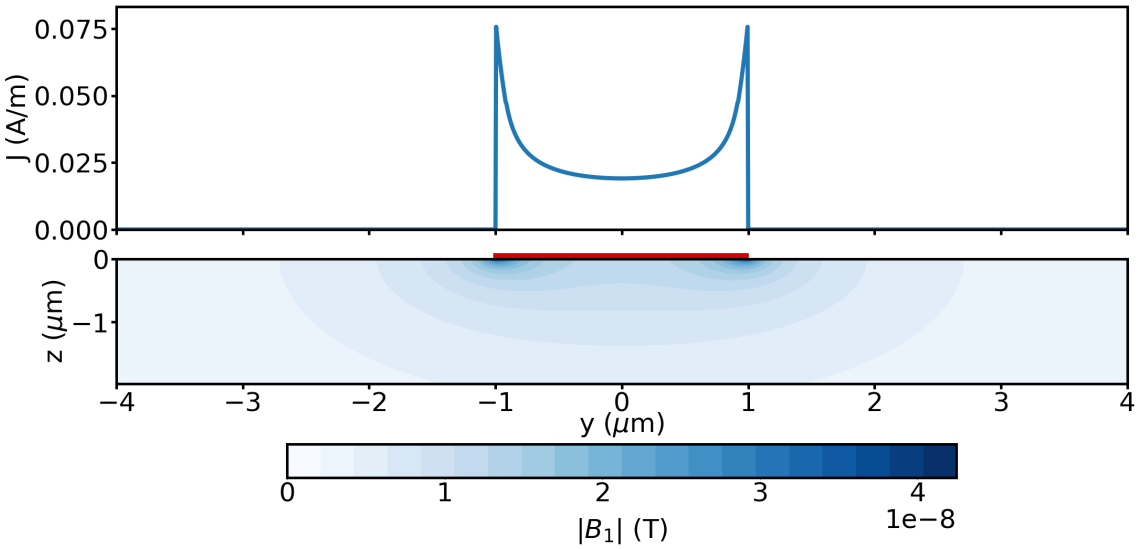

Figure 3.2: **Typical linear current distribution in the resonator wire and corresponding B_1.** Top panel: current distribution corresponding to the typical current vacuum fluctuations in our resonator, based on Equation 3.10. Bottom panel: field amplitude B_1 generated by this current simulated with a finite element software, where the red rectangle represents the wire.

$\omega_s/2\pi$ the transition frequency between these states, also called Larmor frequency, the Hamiltonian (restricted to the 2-level sub-space) is simply given by

$$H_{\text{spin}} = \frac{\hbar\omega_s}{2}\hat{\sigma}_Z. \tag{3.8}$$

The free dynamics corresponding to this Hamiltonian when the spin is not in $|g\rangle$ nor in $|e\rangle$ is a precession of its spin vector $\boldsymbol{S}$ at this Larmor frequency around its quantization axis Z set by $\boldsymbol{B_0}$, as represented in Figure 3.1b.

3.1.3 Magnetic coupling with a lumped element resonator

The resonator couples to the spin through the magnetic field $\boldsymbol{B_1}$ generated by the current flowing in the resonator wire. Since the wire constriction dominates the resonator inductance, we can express the current in the wire as

$$\hat{I} = \frac{\hat{\Phi}}{L} = \omega_0\sqrt{\frac{\hbar}{2Z_0}}(\hat{a}+\hat{a}^\dagger) = \delta I(\hat{a}+\hat{a}^\dagger). \tag{3.9}$$

From this expression, we notice that even in the field ground state $|0\rangle$ there remain zero-point quantum fluctuations of the current due to those on the field. These fluctuations are the current vacuum fluctuations: $\delta I = \sqrt{\langle 0|\,\hat{I}^2\,|0\rangle} = \omega_0\sqrt{\hbar/2Z_0}$.

The current spatial distribution within the superconducting wire is non trivial. The current penetrates the superconducting metal in such a way to expel the magnetic field from inside the superconductor, except over a thin skin. A phenomenological description of this skin effect has been proposed in [VT99], and yields the current density distribution

$$J(y) = \begin{cases} J_0(1-(2y/w)^2)^{-1/2} & \text{for } |y| \leq |w/2-\lambda^2/(2b)| \\ J(w/2)\exp(-(w/2-|y|)b/\lambda^2) & \text{for } |w/2-\lambda^2/(2b)| < |y| < w/2 \\ (1.165/\lambda)\sqrt{wb}\,J_0 & \text{for } y = w/2 \end{cases} \tag{3.10}$$

where y is the wire transversal coordinate, w the wire width, b its thickness and λ is the penetration depth of the superconducting thin film. The normalization constant J_0 allows to have $\int_{-w}^{w} J(y)dy = I$. The typical current vacuum fluctuations distribution in the resonator wire used in this thesis is shown in Figure 3.2.

From the knowledge of the current distribution, one can deduce using Faraday law the corresponding spatial distribution of the magnetic field $\boldsymbol{B_1}(I, \boldsymbol{r})$. The zero-point, or vacuum, fluctuations are thus $\hat{\boldsymbol{B_1}}(\boldsymbol{r}) = \boldsymbol{\delta B_1}(\boldsymbol{r})(\hat{a} + \hat{a}^\dagger)$ where $\boldsymbol{\delta B_1}(\boldsymbol{r})$ are the magnetic field vacuum fluctuations.

Finally, the spin-resonator coupling Hamiltonian is

$$H_{\text{coupling}} = \mu_B \boldsymbol{\delta B_1}(\boldsymbol{r}) \cdot \boldsymbol{g} \cdot \hat{\boldsymbol{S}}(\hat{a} + \hat{a}^\dagger). \tag{3.11}$$

This Hamiltonian can be projected on the spin basis. We apply the rotating wave approximation [HR06], which effectively removes the oscillating terms, and get

$$H_{\text{coupling}}/\hbar = g_0 \hat{\sigma}_+ \hat{a} + g_0^* \hat{\sigma}_- \hat{a}^\dagger \tag{3.12}$$

where $g_0 = \mu_B \boldsymbol{\delta B}_1 \cdot \boldsymbol{g} \cdot \langle e| \hat{\boldsymbol{S}} |g\rangle /\hbar$ is the spin resonator coupling field and where $\hat{\sigma}_+$ and $\hat{\sigma}_-$ are respectively the Pauli raising and lowering operators

$$\hat{\sigma}_+ = \frac{\hat{\sigma}_X + i\hat{\sigma}_Y}{2}, \quad \hat{\sigma}_- = \frac{\hat{\sigma}_X - i\hat{\sigma}_Y}{2}. \tag{3.13}$$

We thus obtain that the total Hamiltonian of the spin coupled to the resonator can be written in a Jaynes-Cummings form:

$$H_{\text{JC}}/\hbar = \omega_0(\hat{a}^\dagger \hat{a} + \frac{1}{2}) + \frac{\omega_s}{2}\hat{\sigma}_Z + g_0(\hat{\sigma}_+ \hat{a} + \hat{\sigma}_- \hat{a}^\dagger). \tag{3.14}$$

To have in mind orders of magnitude for our system, let's apply the Biot-Savard law in the case of an infinitely long and narrow wire

$$\delta B_1(r) = \mu_0 \frac{\delta I}{2\pi r} = \mu_0 \frac{\omega_0}{2\pi r}\sqrt{\frac{\hbar}{2Z_0}} \tag{3.15}$$

From the field δB_1, we deduce the expression of the coupling

$$g_0(r) = \frac{g\mu_B}{\hbar}\delta B_1(r) \langle e| \hat{S} |g\rangle = \frac{g\mu_B}{\hbar}\mu_0 \frac{\omega_0}{2\pi r}\sqrt{\frac{\hbar}{2Z_0}} 0.5. \tag{3.16}$$

where g is the spin g-factor along the direction of B_1 at position r. In the case of Er^{3+} electronic spins in a Scheelite crystal coupled to a resonator with the typical characteristics of our experiment, we have spins located at a distance $r \sim 1\mu$m from the wire and with a g-factor $g \approx 8$, coupled to a resonator of frequency $\omega_0/2\pi \approx 7$GHz and impedance $Z_0 \approx 35\,\Omega$. This yields a spin coupling $g_0/2\pi \sim 500$ Hz.

3.2 Dynamics of the spin-resonator open system

3.2.1 Input-Output theory

In reality, the spin resonator system is not isolated. The resonator is capacitively coupled to a single external line to allow spin manipulation and detection. This coupling is characterized by the rate κ_c at which the energy stored in the resonator leaks out. We model these lines by the traveling electromagnetic modes that they convey, either towards the resonator ($\hat{a}_{\text{in}}$), or away from it ($\hat{a}_{\text{out}}$). Note that whereas $\hat{a}$ has the dimension

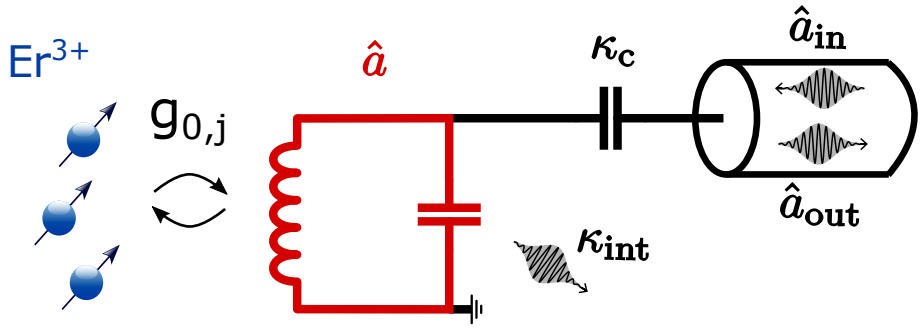

Figure 3.3: **Schematic of the spin-resonator system coupled to an external line.** The resonator of frequency $\omega_0/2\pi$ and impedance Z_0 is coupled to spin j with a strength $g_{0,j}$. It is damped via the transmission line at a rate κ_c and via internal losses at a rate κ_{int}. The traveling modes in the transmission line are either flowing in the system ($\hat{a}_{in}$) or out from the system ($\hat{a}_{out}$)

of $[\sqrt{\text{photon}}]$, $\hat{a}_{in}$ and $\hat{a}_{out}$ are expressed in $[\sqrt{\text{photon}/s}]$. The resonator also looses energy in the surrounding materials (for instance through dielectric losses or the creation of phonons) at a rate κ_{int}. In our experiment, the resonator total energy damping is $\kappa = (\kappa_c + \kappa_{int}) \sim 10^6\,\text{s}^{-1}$. Such system is represented in Figure 3.3.

The resulting evolution of the resonator field operator is based on the input-output theory [GC85] and writes as

$$\begin{aligned} \frac{d\hat{a}}{dt} &= \frac{i}{\hbar}[H,\hat{a}] - \frac{\kappa}{2}\hat{a} - \sqrt{\kappa_c}\hat{a}_{in}, \\ \sqrt{\kappa_c}\hat{a} &= \hat{a}_{out} + \hat{a_{in}}. \end{aligned} \tag{3.17}$$

To begin with, let's consider only the resonator field evolving under this equation of motion with the Hamiltonian $H = H_{reso}$, which would correspond to having the spins out of resonance. The scattering matrix of a coherent mode $a_{in} = \alpha_{in}e^{-i\omega t}$ reflecting on the resonator gives interesting insights on its properties

$$S_{11} = \frac{\alpha_{out}}{\alpha_{in}} = \frac{\sqrt{\kappa_c}\alpha - \alpha_{in}}{\alpha_{in}} = \frac{\kappa_c}{i(\omega-\omega_0)+\kappa/2} - 1. \tag{3.18}$$

According to the relative κ_c and κ_{int} amplitudes, the resonator response as a function of the incoming coherent tone frequency varies between different regimes:

- **under-coupled regime**: if $\kappa_{int} >> \kappa_c$, even an on resonance the incoming field only partially gets in the resonator where it is mostly damped, the rest is reflected with a minimal phase shift.
- **critical coupling regime**: if $\kappa_{int} \sim \kappa_c$, the field at resonance is efficiently transmitted to the resonator and then completely lost (no reflection).
- **over-coupled regime**: if $\kappa_{int} << \kappa_c$, the incoming field mostly gets in and out from the resonator, acquiring a 2π phase.

3.2.2 Spin coupled to microwave line

The spins are coupled to the lines through the resonator. According to the system characteristics, different coupling regimes are possible:

- **strong coupling regime**: if $g_0 \gg \kappa$, an excitation can be coherently exchanged back and forth between the spin and the resonator.

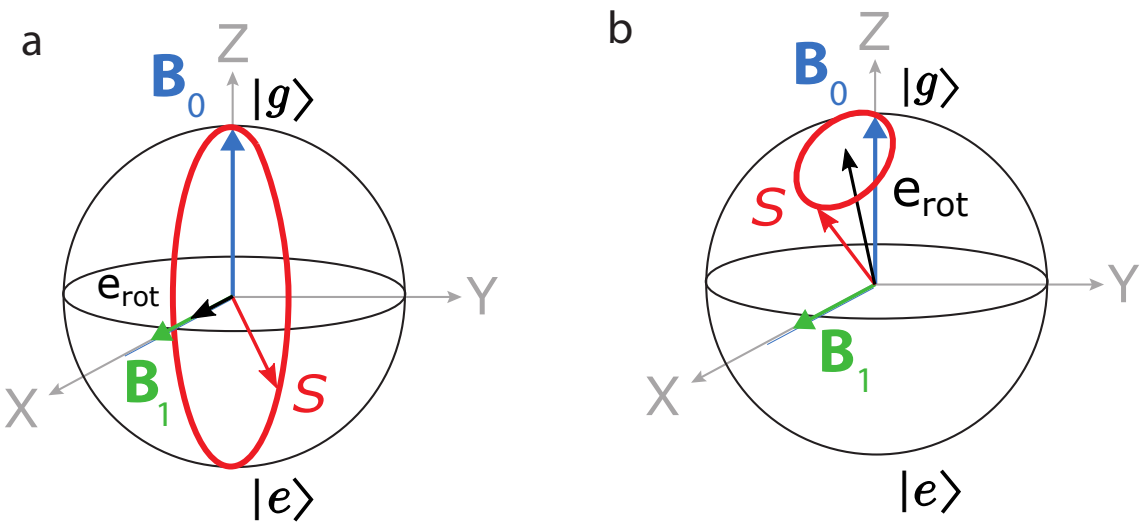

Figure 3.4: **Rabi oscillation on the Bloch sphere a**, Rabi oscillation of resonant spin around the axis $\boldsymbol{e_{rot}} = \boldsymbol{X}$ that successively gets fully polarized in excited or ground state. **b**, Rabi oscillation of a spin detuned from the resonator around the axis $\boldsymbol{e_{rot}} = 2g_0\alpha\boldsymbol{X} + \Delta\omega\boldsymbol{Z}$ that gets only partially polarized in the excited state.

- **weak coupling regime**: if $g_0 \ll \kappa$, an excitation gets damped quickly in the resonator.

In this thesis, we are in the weak coupling regime with $g_0/2\pi \sim 500\,\text{Hz} \ll \kappa/2\pi \sim 100\,\text{kHz}$. The spin dynamics considerations that will follow are valid for this regime.

3.2.2.1 Spin coherent manipulation

The weak coupling regime means that there is no entanglement between the spins and the cavity mode, therefore only the cavity field mean value is relevant in term of spin evolution. In the usual experiments, we drive the spins with a coherent tone at the resonator frequency $\omega_0/2\pi$ sent through the lines that populates the resonator mode. Neglecting the time that it takes to reach a coherent state $\hat{a} = \hat{\alpha}e^{-i\omega_0 t}$ with a constant amplitude α in the resonator, the Jaynes-Cummings Hamiltonian in the rotating frame at frequency $\omega_0/2\pi$ is

$$H/\hbar = -\frac{\Delta\omega}{2}\hat{\sigma}_z + g_0(\hat{\sigma}_+\hat{\alpha} + \hat{\sigma}_-\hat{\alpha}^*) \tag{3.19}$$

with $\Delta\omega = \omega_0 - \omega_s$.

We deduce from this Hamiltonian the evolution of the spin vector $\boldsymbol{S}$ under a drive

$$\dot{\boldsymbol{S}} = \begin{pmatrix} \dot{\hat{S}}_X \\ \dot{\hat{S}}_Y \\ \dot{\hat{S}}_Z \end{pmatrix} = \begin{pmatrix} 0 & \Delta\omega & -2g_0\,\text{Im}[\alpha] \\ -\Delta\omega & 0 & -2g_0\,\text{Re}[\alpha] \\ 2g_0\,\text{Im}[\alpha] & 2g_0\,\text{Re}[\alpha] & 0 \end{pmatrix} \boldsymbol{S}. \tag{3.20}$$

In the following, we choose the phase reference so that, in the rotating frame, $\text{Re}[\alpha] = \alpha$ and $\text{Im}[\alpha] = 0$. From this differential equation we can deduce spin trajectories in the Bloch sphere, when starting with a spin in its ground state:

- If $\Delta\omega = 0$:

$$\dot{\boldsymbol{S}} = \begin{pmatrix} 0 & 0 & 0 \\ 0 & 0 & -2g_0\alpha \\ 0 & 2g_0\alpha & 0 \end{pmatrix} \boldsymbol{S} \tag{3.21}$$

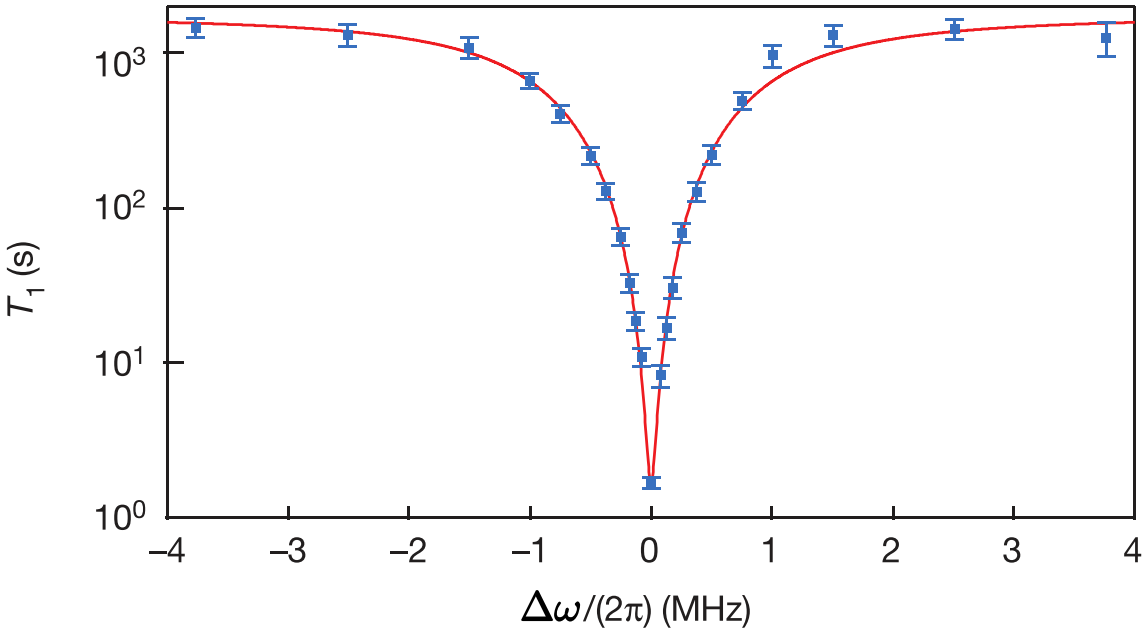

Figure 3.5: **ESR measurement of Purcell effect on Bismuth donors in silicon** [Bie+16] Spin relaxation time T_1 as a function of their detuning from the resonator $\Delta\omega$ (blue dots) and fit (red line) considering a radiative rate Γ_R and a non radiative one Γ_{NR}: $T_1^{-1} = (\Gamma_R(\Delta\omega) + \Gamma_{NR})$.

As represented in Figure 3.4a, $\boldsymbol{S}$ rotates around the axis $\boldsymbol{e_{rot}} = \boldsymbol{X}$ at a Rabi frequency $\Omega_{R0}/2\pi = 2g_0\alpha/2\pi$. Its component S_Z oscillates between $-1/2$ and $+1/2$.

- If $\Delta\omega \neq 0$:

$$\dot{\boldsymbol{S}} = \begin{pmatrix} 0 & \Delta\omega & 0 \\ -\Delta\omega & 0 & -2g_0\alpha \\ 0 & 2g_0\alpha & 0 \end{pmatrix} \boldsymbol{S} \tag{3.22}$$

As represented in Figure 3.4b, $\boldsymbol{S}$ rotates around the $\boldsymbol{e_{rot}} = 2g_0\alpha\boldsymbol{X} + \Delta\omega\boldsymbol{Z}$ at a Rabi frequency $\Omega_R/2\pi = \sqrt{\Delta\omega^2 + \Omega_{R0}^2}$. Its component S_Z oscillates between $-1/2$ and $\Omega_{R0}/(2\sqrt{\Delta\omega^2 + \Omega_{R0}^2})$.

The spin-resonator coupling Hamiltonian describes how the field drives the spin into Rabi oscillations; conversely, the Larmor precession of the spin magnetization generates a field in the cavity. In the weak coupling regime, when no tone is applied to the resonator, one can assume that $\langle d\hat{a}/dt\rangle = 0$. Then, transverse magnetization finite in average $\langle S_-\rangle$ induces an intra-cavity field

$$\langle a\rangle = \frac{ig}{\kappa}\langle S_-\rangle. \tag{3.23}$$

This field leaks into an output field $\langle \hat{a}_{out}\rangle = \sqrt{\kappa_c}\langle \hat{a}\rangle$.

3.2.2.2 Purcell effect

The presence of the spin environment, such as the crystal substrate and the resonator coupled to a line, influences the spin relaxation rate Γ_1. More precisely, when a spin is coupled to a resonator in the weak coupling regime, the resonator damping rate in the environment κ can enhance significantly the radiative relaxation rate Γ_R by the so called Purcell effect. When no drive is applied at the resonator input, one can adiabatically

eliminate the resonator [HR06], which yields for Γ_R the expression

$$\Gamma_R(\Delta\omega, g_0) = \frac{g_0^2\kappa}{\Delta\omega^2 + (\kappa/2)^2}. \tag{3.24}$$

This effect has been measured (see Figure 3.5) by a previous PhD student of the group, Audrey Bienfait, with setups very similar to those used in this work [Bie+16]. With our system characteristics, for a spin on resonance with the resonator, we estimate the order of magnitude of $\Gamma_R = 4g_0^2/\kappa \sim 50\,\mathrm{ms}^{-1}$. This rate is to be compared to the typical electron spin radiative relaxation rate in free space of around $10^{-12}\,\mathrm{s}^{-1}$, which is neglected in our experiment. Since it is the radiative decay through the resonator that provides the photons that will be detected in ESR, we understand that the enhancement of the radiative relaxation rate due to this effect is essential for this work.

3.2.3 Master equation description

To fully describe the spin evolution in an open environment, we have to take into account additional relaxation channels. We describe now the spin with its density matrix ρ_s, whose evolution is governed both by the system Hamiltonian and by the quantum jumps modeled with the Lindbladian operators L_α in the master equation:

$$\dot{\rho}_s = -\frac{i}{\hbar}[H_{JC}, \rho_s] + \sum_\alpha L_\alpha \rho_s L_\alpha^\dagger - \frac{1}{2}(L_\alpha^\dagger L_\alpha \rho_s + \rho_s L_\alpha^\dagger L_\alpha), \tag{3.25}$$

In our experiment, that takes place at cryogenic temperature $T_0 \approx 10\,\mathrm{mK}$ and at microwave frequency $\omega_0/2\pi \approx 7\,\mathrm{GHz}$, the relevant relaxation channels in our system are:

- **Radiative relaxation**: as explained in Section 3.2.2.2, the radiative relaxation rate is dominated by the Purcell rate with $L_R = \sqrt{\Gamma_R}\hat{\sigma}_-$.
- **Non radiative relaxation**: the spins can also loose energy in a non-radiative way, for instance in the lattice phonon bath, at a rate Γ_{NR} with $L_{NR} = \sqrt{\Gamma_{NR}}\hat{\sigma}_-$.
- **Pure dephasing**: fluctuations, typically in the spin magnetic environment, dephase the spin at a rate Γ_ϕ with $L_\phi = \sqrt{\Gamma_\phi/2}\hat{\sigma}_z$.

From the spin density matrix evolution, we retrieve the spin vector $\boldsymbol{S}$ with

$$\begin{aligned} \hat{\rho}_s &= \frac{1}{2}(\mathbb{1} + \hat{\boldsymbol{S}}.\hat{\boldsymbol{\sigma}}), \\ \mathrm{Tr}[\hat{\rho}_s \hat{S}_i] &= \langle \hat{S}_i \rangle. \end{aligned} \tag{3.26}$$

Altogether, it yields the complete Bloch equation

$$\langle \dot{\boldsymbol{S}} \rangle = \begin{pmatrix} \langle \dot{\hat{S}}_X \rangle \\ \langle \dot{\hat{S}}_Y \rangle \\ \langle \dot{\hat{S}}_Z \rangle \end{pmatrix} = \begin{pmatrix} 0 & \Delta\omega & 0 \\ -\Delta\omega & 0 & \Omega_{R0} \\ 0 & \Omega_{R0} & 0 \end{pmatrix} \langle \boldsymbol{S} \rangle - \begin{pmatrix} \Gamma_2 \\ \Gamma_2 \\ \Gamma_1 \end{pmatrix} \langle \boldsymbol{S} \rangle \tag{3.27}$$

where $\Gamma_1 = 1/T_1 = \Gamma_R + \Gamma_{NR}$ is the spin longitudinal relaxation rate and $\Gamma_2 = 1/T_2 = \Gamma_\phi + \Gamma_1/2$ is the spin transversal relaxation rate.

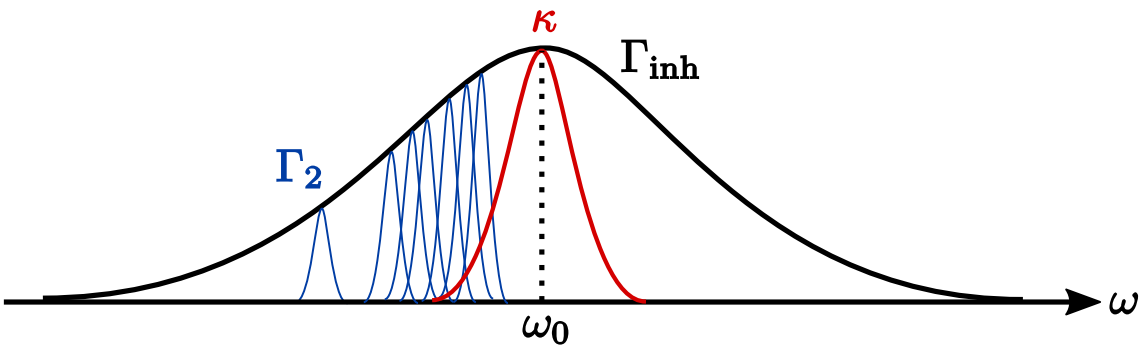

Figure 3.6: **Typical linewidths in our experiment.** Representation of the relative linewidths in our system, in increasing order: single spin linewidth $\Gamma_2/2\pi \sim 10$ kHz, resonator linewidth $\kappa/2\pi \sim 100$ kHz and ensemble of spin linewidth $\Gamma_{\text{inh}}/2\pi \sim 1$ MHz.

3.3 Dynamics of a spin ensemble in the low cooperativity regime

As detailed in the introduction, the limited sensitivity of ESR experiments requires large ensemble of spins to detect a signal. In this thesis also we are always addressing ensemble of spins, although with a moderate number of spins thanks to the high sensitivity of FD-ESR. We will now depict the dynamics of a spin ensemble coupled to a resonator and describe a simulation tool that we use to predict the spin evolution and reproduce the signal observed in the experiments.

3.3.1 Spin ensemble with frequency inhomogeneity at low cooperativity

The local environment of each spin j is crucial to determine its resonant frequency $\omega_{s,j}/2\pi$. A single spin has a linewidth Γ_2 coming from its relaxation time and from the fluctuations of its local magnetic field. Considering several spins, local magnetic impurities or local deformation of the crystal lattice can affect the spin properties such as $\omega_{s,j}/2\pi$. As a result of the spins different local environments, a spin ensemble is spread in frequency by this inhomogeneous broadening in a linewidth Γ_{inh}. These linewidths are to be compared with the resonator linewidth κ to understand which spins are contributing to the signal, as illustrated in Figure 3.6. In our experiment, the inhomogeneous linewidth $\Gamma_{\text{inh}}/2\pi \sim 1 - 10\,\text{MHz}$ largely dominates the resonator linewidth $\kappa/2\pi \sim 100\,\text{kHz}$. Therefore only a fraction of the total spin ensemble is driven and measured.

All the excited spins are coupled to the resonator mode, which means that they interact with each other through this mode. To determine whether the spin ensemble state significantly influences its own dynamics by the field it creates in the resonator, we introduce the ensemble cooperativity

$$C_p = \frac{2g_0^2 N}{\kappa \Gamma_{\text{inh}}} \tag{3.28}$$

With N the number of spins assumed to have a uniform coupling g_0 [JM12]. Two regimes of cooperativity have to be distinguished:

- **strong cooperativity regime**: if $C_p \gg 1$, the spins behave in a collective fashion. The field emitted by the spin ensemble strongly affects the spin dynamics.
- **low cooperativity regime**: if $C_p \ll 1$, the spins behave independently.

To determine in which regime we sit in our experiments, let's consider some orders of magnitude. Since in this thesis we extensively study Erbium ions, let us use the Erbium

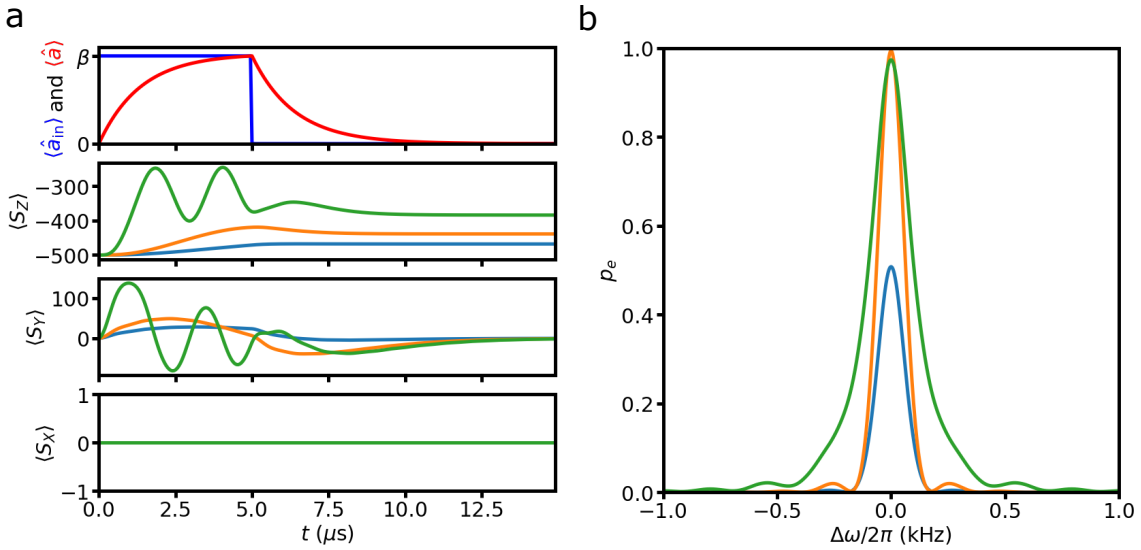

Figure 3.7: **Spin ensemble dynamics simulation with a single pulse excitation** **a**, simulation of a single pulse (upper plot) that drives the evolution of a 1000 spins with coupling $g_0/2\pi = 500$ Hz spread uniformly in frequency over $[-1, 1]$ MHz. The spin ensemble components $\langle S_X \rangle$,$\langle S_Y \rangle$,$\langle S_Z \rangle$ evolution is simulated for three different pulse amplitude β_0 (blue), $2\beta_0$ (orange) and $10\beta_0$ (green). **b**, spin excitation probability as a function of the spin detuning $\Delta\omega$ for the various pulse amplitude β_0 (blue), $2\beta_0$ (orange) and $10\beta_0$ (green). We notice that the excitation linewidth increases with the power in the so-called power broadening.

spin concentration $c \approx 0.7 \times 10^{-19}\,\mathrm{m}^{-3}$ of the sample described in Chapter 6, which has been determined from previous characterizations [Le 22]. The number N of spins with a coupling $g_0/2\pi \geq 500$ Hz corresponds roughly to those contained in a volume $l \times w \times d$ where $l = 630\,\mu$m is the wire length, $w = 2\,\mu$m is the wire width and $d = 1\,\mu$m a depth below which spin have a coupling $g_0/2\pi < 500$ Hz. This corresponds to $N \sim 10^4$. With the typical values $g_0/2\pi \sim 500$ Hz, $\kappa/2\pi \sim 100$ kHz and $\Gamma_{\mathrm{inh}}/2\pi \sim 1$ MHz, we are well in the weak cooperativity regime with $C_p \approx 0.04$.

Therefore, collective effects should be negligible in our experiments, and the spin ensemble response can be obtained by simply computing the response of each spin interacting independently with the applied field or vacuum field in the cavity.

3.3.2 Spin manipulation: the ideal case of homogeneous coupling

In order to have some insights of the spin dynamics, let us first consider a spin ensemble coupled to the resonator with a single well-defined coupling constant g_0. It's not the case in our experiment, as expected from the field inhomogeneity below the wire shown in Figure 3.2, but it is an interesting case to get a qualitative understanding of how the spin state evolves during the experiment.

3.3.2.1 Single pulse excitation

A straight forward manipulation sequence consists in sending a single excitation pulse to excite the spins. Each spin dynamics is described by Equation 3.27, a model that we have implemented into a home-made Python program. Simulation results shown in Figure 3.7 are for an ensemble of $N = 1000$ spins with coupling $g_0 = 500$ Hz uniformly spread in frequency with $\Delta\omega_j/2\pi = (\omega_0 - \omega_{s,j})/2\pi \in [-1, 1]$ MHz. A single pulse of length $\Delta t = 5\,\mu$s and of 3 different amplitudes β is used to drive the spins. This pulse induces a

rotation of about $\pi/2$, π or 5π for the spins with $\Delta\omega_i = 0$. The pulse is applied along the X axis, and the simulation considers a resonator with the typical characteristics of our experiment ($\omega/2\pi = 7$ GHz, $\kappa_c/2\pi = 130$ kHz, $\kappa_{int}/2\pi = 100$ kHz). In Figure 3.7a, we see the simulated evolution of the incoming and intra-resonator fields, as well as the the spin ensemble evolution. Right after the pulse, the oscillations in $\langle S_Z \rangle$ and $\langle S_Y \rangle$ are damped in a time $T_2^* = 1/\Gamma_{inh} \sim 5\,\mu$s, going down to 0 for the $\langle S_Y \rangle$ component. This fast decay is in practice very complicated to detect as it overlaps in time with the cavity ring down, namely the time needed for the cavity to relax the energy from the excitation pulse. On the other hand, the longitudinal component $\langle S_Z \rangle$ relaxes with a characteristic time T_1 way longer than the cavity ring down.

It's interesting to notice that the spin will rotate around different axis at different speed according to their detuning $\Delta\omega_j$, as discussed in Section 3.2.2.1. By driving stronger and stronger, we see in Equation 3.22 that we tend to drive the detuned spins around an axis closer and closer to the equatorial plane, which means they will get more and more excited. In other word, the excitation bandwidth broadens with the pulse power, a phenomenon called power broadening. We can illustrate this phenomenon by looking at the spin j excitation probability $p_{e,j}$ at the end of the simulated sequence

$$p_{e,j}(\beta, \Delta\omega_j) = \frac{1 + 2\langle S_{Z,j}(\beta, \Delta\omega_j) \rangle}{2}. \tag{3.29}$$

We plot this quantity in Figure 3.7b for the three pulse amplitudes, and clearly see the excitation linewidth broadening with the pulse excitation amplitude.

3.3.2.2 Hahn echo sequence

A widely used excitation sequence to detect the spins $\langle S_Y \rangle$ component is the Hahn echo sequence: $\beta/2_X - \tau - \beta_Y - \tau -$ echo. The idea is to project the spins on the Bloch sphere equatorial plane (at $t = -2\tau$), and to use a refocusing pulse (at $t = -\tau$) to have a coherence resurgence of $\langle S_Y \rangle$ at a given time $t = 0$, called spin echo. A simulation of such an excitation sequence and the resulting spin evolution is presented in Figure 3.8 with the same parameters as in Section 3.3.2.1. During the time of the echo, the spins refocus and redefocus emitting thus a coherent field along the X axis in a temporal mode that lasts $T_e \sim T_2^*$.

3.3.2.3 Hahn echo sequence with restoring pulse

The fluorescence detection method is sensitive to the spin longitudinal magnetization $\langle S_Z \rangle$. To detect an echo with FD, it is necessary to transfer the coherent $\langle S_Y \rangle$ component at the echo time onto the Z axis. This is achieved by a modification of the usual Hahn echo sequence, using a so-called restoring pulse. By adding a third pulse to the Hahn echo sequence, that turns it into a sequence $\beta/2_X - \tau - \beta_Y - \tau - \beta/2_\Phi$, the spin echo gets converted onto $\langle S_Z \rangle$ component. The restoring pulse has a phase Φ that determines the spin rotation axis and sets the direction towards which the coherent echo magnetization $\langle S_{coh} \rangle$ gets restored. In general, the spin longitudinal component following this excitation sequence is the sum of an incoherent component and a coherent echo component:

$$\langle S_Z(\Phi) \rangle = \langle S_{incoh} \rangle + \langle S_{coh} \rangle \cos(\Phi) \tag{3.30}$$

In Figure 3.9 are illustrated two radical cases: when $\Phi = 0$, the third pulse is aligned with the first one and the echo is projected towards the spin excited state, whereas when $\Phi = \pi$, the third pulse is anti-aligned with the first one and the echo is projected towards the spin ground state.

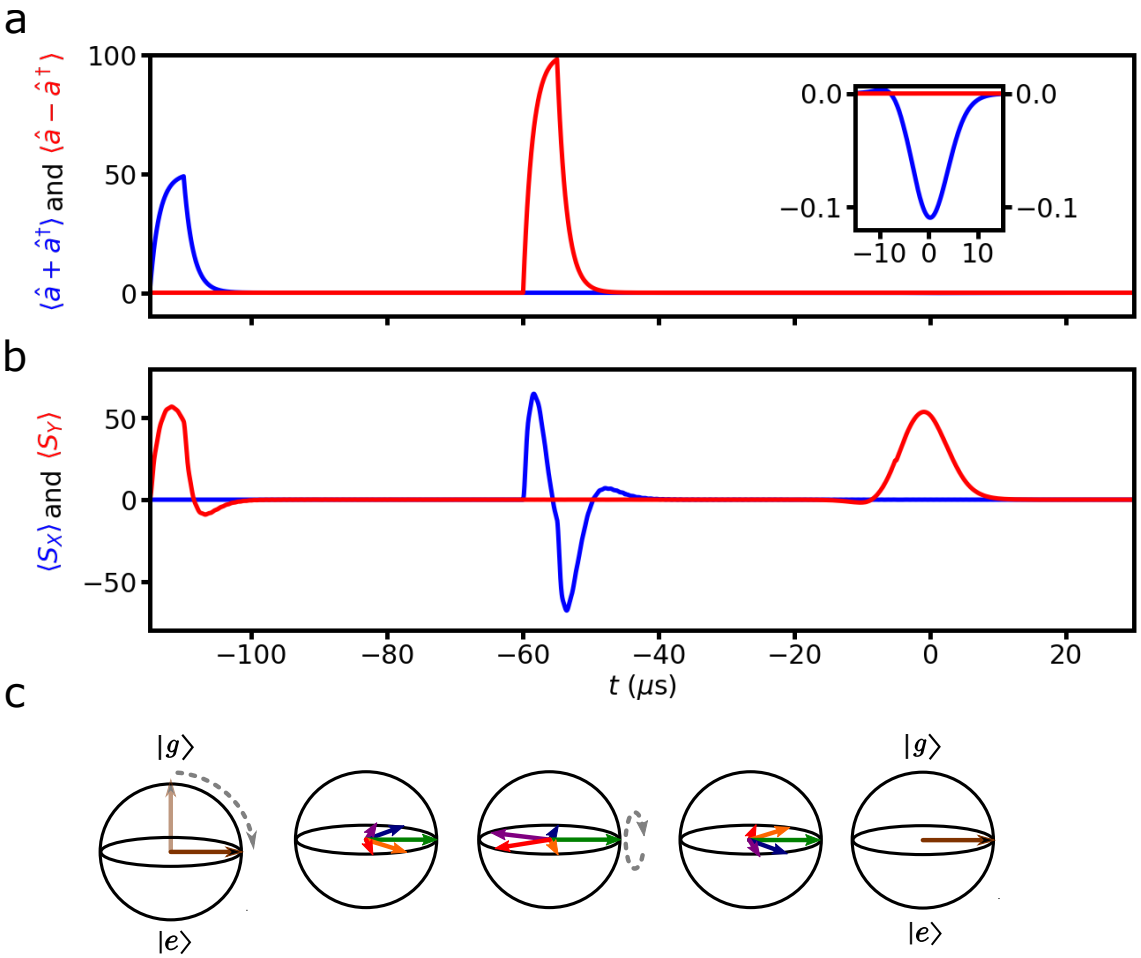

Figure 3.8: **Spin ensemble dynamics simulation with a Hahn echo excitation sequence**. **a**, time evolution of the two intra cavity quadratures. In the inset is plotted a zoom in the field resurgence due to the spin echo. **b**. Evolution of the spin ensemble transversal components where the echo appears in the $\langle S_Y \rangle$ component. **c**. Schematic of the spin orientation in the Bloch sphere during the Hahn echo sequence.

3.3.3 Spin manipulation: the real case of inhomogeneous coupling

In reality, the spin coupling to the resonator is widely spread according to the spin position in the sample. In order to quantitatively simulate both fluorescence and coherent signal, we need to accurately know the spin coupling and frequency distribution.

3.3.3.1 Coupling distribution

From the knowledge of the field below the wire presented in Figure 3.2, we compute the spatial distribution of the coupling $g_0(\boldsymbol{r})$, as shown in Figure 3.10a. The rotation angle of each spin j under an excitation pulse strongly depends on its coupling $g_{0,j}$ and its detuning $\Delta\omega_j$, as described in Equation 3.20. As the excitation pulse gets stronger, the low coupled spins far from the wire are getting noticeably excited. At the same time, the spins closer with a higher coupling undergo Rabi oscillations with the increasing pulse amplitude. The spin state depending on their position in the sample at various pulse amplitude is visible in Figure 3.10b, showing "waves" of excitation associated to Rabi oscillation in the Bloch sphere, where each maximum corresponds to a rotation of $(2k+1)\pi$ with $k \in \mathbb{N}$ from the spin ground state $|g\rangle$.

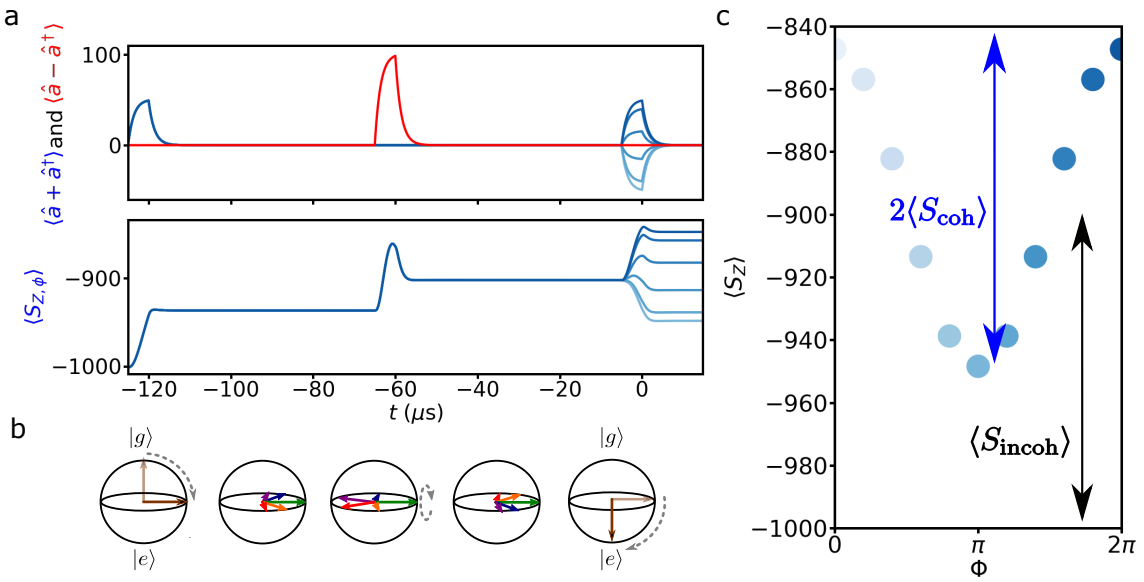

Figure 3.9: **Spin ensemble simulation with a restored Hahn echo excitation sequence a**, top panel: Evolution of the two intra cavity quadratures with a varying restoring pulse phase $\Phi \in [0 : 2\pi]$ (blue gradient for various Φ). Bottom panel: evolution of the spin ensemble longitudinal component. **b**. Schematic of the spin orientation in the Bloch sphere during the restored Hahn echo sequence for $\Phi = 0\,°$. **c**, $\langle S_Z \rangle$ at the end of the simulation according to Φ, showing the incoherent contribution (black double arrow)and the echo modulation amplitude (blue double arrow).

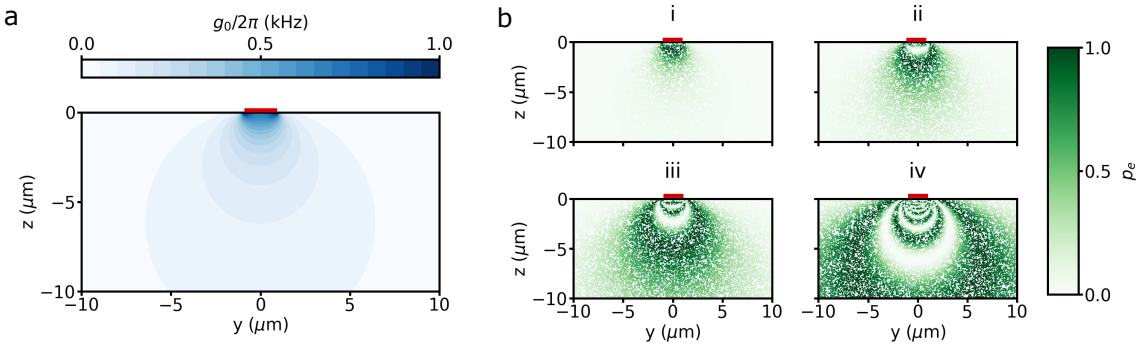

Figure 3.10: **Coupling spatial distribution and resulting spin excitation a**, Cross section below the wire (red rectangle) showing the spatial distribution of the coupling g_0 for typical experimental parameters. **b**, Representation of spins excitation probability p_e (green circle) as a function of the position below the wire (red rectangle) for 4 different pulse amplitudes: β_0 (i), $2\beta_0$ (ii), $5\beta_0$ (iii), $10\beta_0$ (iv). The computation is based on the equation Equation 3.20, with $\Delta\omega$ following a Lorentzian distribution of 1MHz linewidth and 14000 spins uniformly distributed in space.

3.3.3.2 Fluorescence formula

With all that precedes, we are now able to derive an analytical formula for the fluorescence signal evolution in time, which will be extensively used in this thesis to reproduce the experimental data. In the weak cooperative regime, the fluorescence signal of a spin ensemble is the sum of each spin individual relaxation. Following an excitation pulse sequence finishing at time $t = 0$, a spin j finishes in a state $\boldsymbol{S_j} \equiv (S_{X,j}, S_{Y,j}, S_{Z,j})$ depending on the spin characteristics $g_{0,j}$ and $\Delta\omega_j$. Then, its radiative relaxation rate $\Gamma_{R,j}$ also depends on its characteristics. As this spin can relax either in a radiative or a non

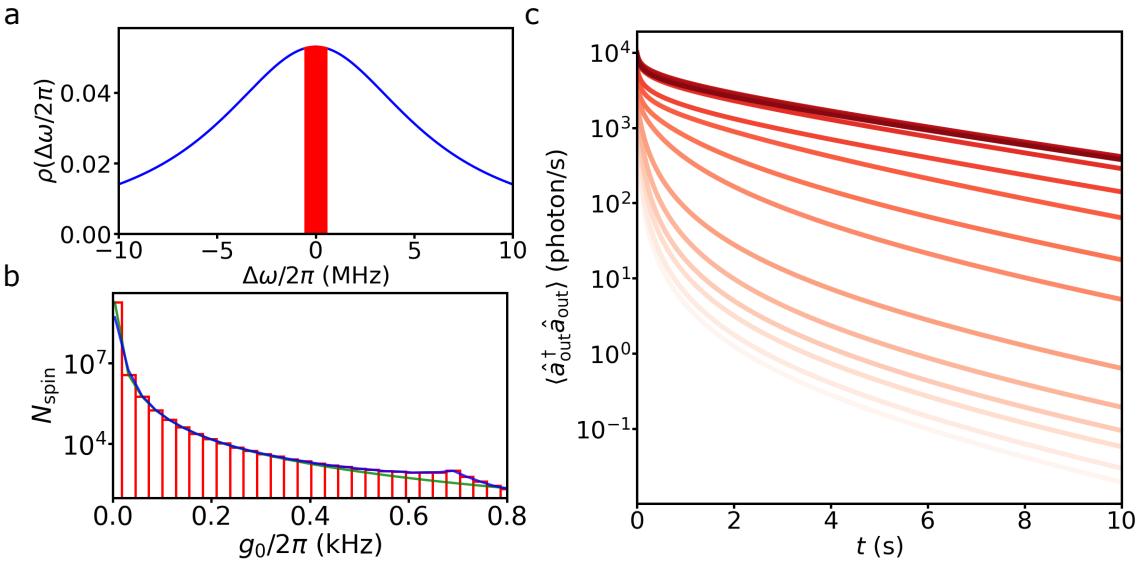

Figure 3.11: **Computation of the spin distributions and simulation of the fluorescence signal a**, Normalized spin frequency distribution of the total spin ensemble (blue) and frequency range considered in the simulations (red surface). **b**, Number of spin N_{spin} as a function of coupling g_0 used in the simulation (red histogram). The curve is a continuity between a $1/g_0^3$ fit (green line), valid far from the wire at low g_0, and the spin coupling density extracted from the simulated g_0 spatial distribution (blue line), valid close to the wire. **c**, Simulated relaxation curves at various excitation strength ϵ spread over 3 orders of magnitude (darker red means stronger excitation).

radiative way, the probability that it emits a photon after an excitation sequence is

$$p_j = \frac{\Gamma_{\mathrm{R},j}}{\Gamma_{\mathrm{R},j} + \Gamma_{NR}} \frac{1 + 2S_{Z,j}}{2}. \tag{3.31}$$

The spin relaxes exponentially with a typical rate $\Gamma_{1,j} = \Gamma_{\mathrm{R},j} + \Gamma_{\mathrm{NR}}$. The radiative relaxation triggers the emission of a photon either in the line, with a probability $\kappa_{\mathrm{c}}/\kappa$, or in the resonator losses, with a probability $\kappa_{\mathrm{int}}/\kappa$. Therefore, the emission rate of detectable photons to the line from this spin is

$$\langle \hat{a}^\dagger_{\mathrm{out},j} \hat{a}_{\mathrm{out},j} \rangle(t) = \frac{\kappa_c}{\kappa} \Gamma_{R,j} \frac{1 + 2S_{Z,j}}{2} e^{-(\Gamma_{\mathrm{R},j} + \Gamma_{\mathrm{NR}})t}. \tag{3.32}$$

The total fluorescence signal is the sum of the contributions from all the spins that writes as

$$\langle \hat{a}^\dagger_{\mathrm{out}} \hat{a}_{\mathrm{out}} \rangle(t) = \sum_j \langle \hat{a}^\dagger_{\mathrm{out},j} \hat{a}_{\mathrm{out},j} \rangle(t) = \int d\Delta\omega \int dg_0 \rho(\Delta\omega) \rho(g_0) \langle \hat{a}^\dagger_{\mathrm{out}} \hat{a}_{\mathrm{out}} \rangle(\Delta\omega, g_0, t). \tag{3.33}$$

where $\rho(\Delta\omega)$ and $\rho(g_0)$ are the spin ensemble frequency detuning and coupling distribution.

3.3.3.3 Simulations of the fluorescence signal

Using the results presented earlier in this chapter, we can effectively reproduce the fluorescence signal obtained in the data. We use the master equation based spin simulation, as introduced in Section 3.3.2, to determine the spin evolution during the excitation sequence for various spin detuning $\Delta\omega$ and g_0. The resulting spin state triggers a fluorescence that we compute using Equation 3.33. In order to have a quantitative reproduction of our data, we need to know accurately the spin frequency and coupling distribution. In

our simulations, we make the assumption that frequency and coupling distributions are not correlated and can be treated independently. The whole simulations procedure is summarized in Appendix A.

We first know from spectroscopic measurements that the frequency distribution $\rho(\Delta\omega)$ has a Lorentzian shape with a linewidth $\Gamma_{\text{inh}}/2\pi$. We integrate the spin contributions over a typical frequency range of $\Delta\omega/2\pi \in [-1, 1]$ MHz, considering that spins further away from the resonator won't contribute significantly. The proportion of spin that lies in the simulated frequency range for $\Gamma_{\text{inh}} = 12$ MHz is visible in Figure 3.11a.

In the case of the coupling distribution $\rho(g_0)$, the spatial coupling distribution below the wire, from Figure 3.10a, and the spin spatial density c enable us to compute the number of spins N_{spin} with a given coupling g_0, as shown in Figure 3.11b. At low g_0, N_{spin} evolves as the number of spin in a hemisphere centered on the wire: $N_{\text{spin}} \propto 1/g_0^3$. This is the regime far from the wire where the approximation of an infinitely long and narrow wire is valid. We observe that this model doesn't fit this distribution at high $g_0/2\pi > 500$ Hz, where the wire shape matters.

The results of fluorescence simulations following a single pulse with different strengths $\epsilon = \beta \times \Delta t$ is visible in Figure 3.11c. The curves are non exponential and behaves as expected at first sight: as ϵ increases, the fluorescence amplitude and decay time increase; at high ϵ we observe a saturation since the spins far from the wire end up relaxing mostly through their non-radiative channel. However, those curves need to be compared to the data to assert that this modeling of the spin ensemble dynamics capture all the meaningful physical phenomena, as we will verify in Chapter 7.

We notice that at high-ϵ and at time $t > 1/\Gamma_{\text{NR}}$, the curves retrieve an exponential shape, appearing as a straight line in Figure 3.11c. The spins contributing in this part of the curve have their relaxation dominated by the non-radiative relaxation, which is exponential and identical for all of them. Therefore, at high-ϵ and at time long enough, the fluorescence curve detection appears as a method to access the spin non-radiative relaxation time.

This simulation procedure is useful to extract additional information from the spin relaxation curve. Indeed, the non trivial relaxation observed in the data of Figure 3.11c is reproduced in simulations only with one value of β, which allows to calibrate it. Therefore, the simulation gives access to the attenuation in the input lines. Moreover, the experimental detection apparatus has a limited efficiency η that can be calibrated as the ratio of the photons simulated over the photons detected. All these results are discussed with further details in Chapter 7.

Chapter 4

Spin detection methods

In this chapter, we describe and analyze the two spin detection methods used in this thesis : Fluorescence-Detection (FD) ESR and Inductive Detection (ID) ESR. The difference between these two methods comes from the fact that ID-ESR measures a field quadrature, and is thus sensitive to vacuum fluctuations, whereas FD-ESR counts photons, and is thus ideally noiseless in the absence of signal. Here, we describe the detection properties of these two methods, the apparatus they require and their potential in term of sensitivity.

4.1 Quadrature detection

We start by reminding a number of useful concepts regarding the quantum description of an electromagnetic mode; for more details please see [HR06].

4.1.1 Field quadrature observable

Considering a mode with the field operator $\hat{a}$, one can decompose it on its quadratures $\hat{X}$ and $\hat{Y}$ [GK05] such that

$$\begin{aligned} \hat{X} &= \frac{\hat{a}^\dagger + \hat{a}}{2}, \\ \hat{Y} &= i\frac{\hat{a}^\dagger - \hat{a}}{2}. \end{aligned} \tag{4.1}$$

Those quadrature operators respect the commutation rule $[\hat{X}, \hat{Y}] = i/2$ and are associated to the photon number operator

$$\hat{a}^\dagger \hat{a} = \hat{X}^2 + \hat{Y}^2 - \frac{1}{2}. \tag{4.2}$$

The phase space, where each axis corresponds to a field quadrature, is a convenient way to represent a field state. In the following, we discuss several relevant states and provide their graphical phase space representation. With $\delta X^2 = \langle \hat{X}^2 \rangle - \langle \hat{X} \rangle^2$ the state variance on quadrature $\hat{X}$, we color in Figure 4.1 the position where $|X - X_{\max}| \leq \sqrt{\delta X^2}/2$ and similarly on the other quadrature $\hat{Y}$.

Vacuum state

The vacuum state $|0\rangle$ is defined as the state with no photon populating the mode. Therefore, the annihilation operator applied to this state gives a null result

$$\hat{a}\,|0\rangle = 0. \tag{4.3}$$

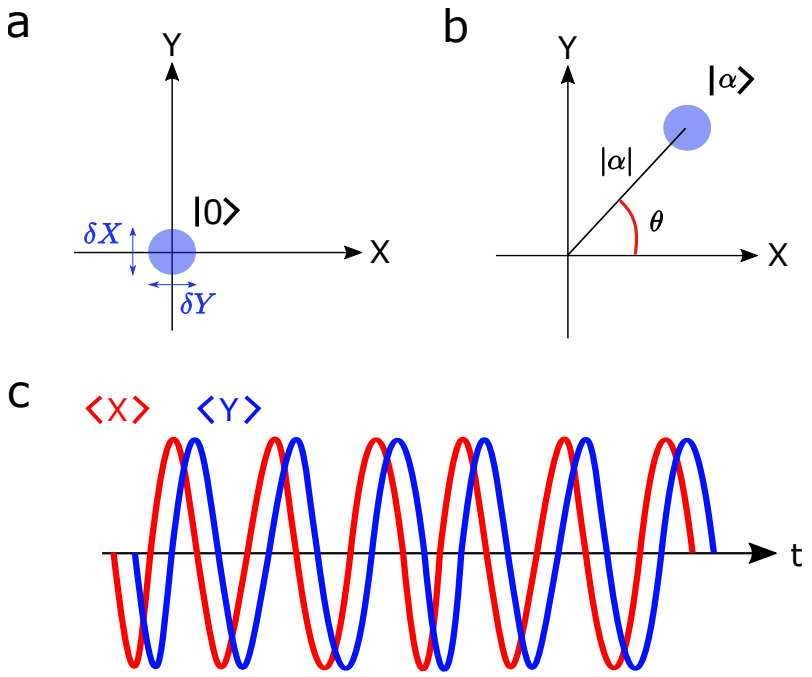

Figure 4.1: **Phase space representation of field state a**, Representation of the vacuum state $|0\rangle$ as a disk centered on the space origin. The disk diameter represents the vacuum fluctuations in each quadrature. **b**, Representation of a coherent state $|\alpha\rangle$ as a displaced vacuum state. The field amplitude α corresponds to the distance from the origin to the disk center, and its phase θ the angle with the reference quadrature X. **c**, time representation of the two coherent state quadratures.

We notice that in such a state, even though $\langle 0|\hat{X}|0\rangle = \langle 0|\hat{Y}|0\rangle = 0$, there remain fluctuations in each quadrature

$$\delta X^2 = \delta Y^2 = \frac{1}{4}. \tag{4.4}$$

In term of photon number, it means that half a photon remains in the vaccum fluctuations, represented as the state surface in Figure 4.1a.

Coherent state

A coherent state $|\alpha\rangle$ is a semi classical state with a defined phase and amplitude. This state is an eigenstate of the annihilation operator

$$\hat{a}|\alpha\rangle = \alpha|\alpha\rangle \tag{4.5}$$

where $\alpha = |\alpha|e^{i\omega t}$ is a complex number that characterizes the coherent state and $\omega/2\pi$ is the state frequency in the laboratory frame. This kind of state is represented at a given time $t_0 = \theta/\omega$ in Figure 4.1b, where we see that its quadratures write as

$$\begin{aligned} \langle\alpha|\hat{X}|\alpha\rangle &= |\alpha|\cos(\theta), \\ \langle\alpha|\hat{Y}|\alpha\rangle &= |\alpha|\sin(\theta), \\ \delta X^2 = \delta Y^2 &= \frac{1}{4}. \end{aligned} \tag{4.6}$$

This state quadratures $\langle X\rangle$ and $\langle Y\rangle$ oscillate in time at the mode frequency (see Figure 4.1c). In this thesis, as is usually done, we will use the rotating frame at ω so that the quadratures are now constant in time for a free evolution of the mode. In this frame and by choosing the appropriate phase reference, the coherent state can be all along one quadrature.

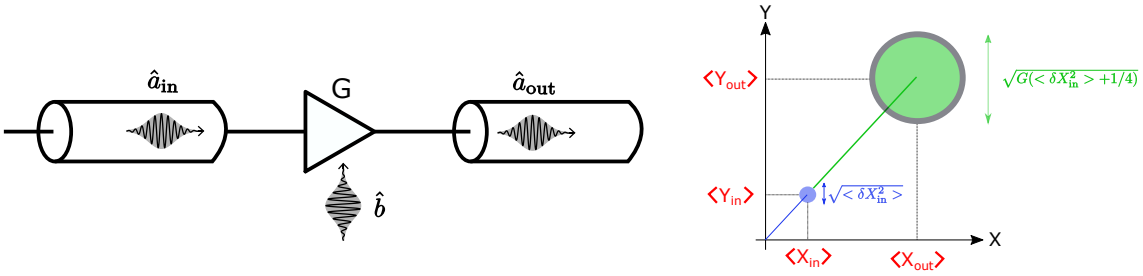

Figure 4.2: **Schematic of a coherent state amplification a**, amplifier (rectangle) of gain G amplifies the mode $\hat{a}_{\text{in}}$ and mixes it with its internal mode $\hat{b}$ to produce the mode $\hat{a}_{\text{out}}$. **b**, The incoming mode (blue) gets amplified into the outgoing mode (green). The amplification increases the mode amplitude and fluctuations by its gain G, as well as it adds its internal fluctuations (grey) to the outgoing mode.

4.1.2 Quantum limited amplifier

The spin resonant signal that we are interested in is very weak compared to the usual noise of the devices that acquire the signal at the room temperature. Therefore, we need to drastically amplify the signal so it becomes visible among this noise. Although the amplification happens all along an amplification chain, the first amplifier of such a chain is crucial in terms of the signal SNR. We focus here on the properties of our first amplifier, a parametric amplifier.

To describe an amplifier of gain G, we introduce the amplifier input and output mode, respectively $\hat{a}_{\text{in}}$ and $\hat{a}_{\text{out}}$. The amplifier applies the transfer function on each quadrature [HM62]

$$\begin{aligned} \langle \hat{X}_{\text{out}} \rangle &= \sqrt{G} \langle \hat{X}_{\text{in}} \rangle, \\ \langle \hat{Y}_{\text{out}} \rangle &= \sqrt{G} \langle \hat{Y}_{\text{in}} \rangle. \end{aligned} \tag{4.7}$$

A quantum-mechanical analysis of the amplification process [Cav82] shows that the amplifier needs to add at least half a photon noise to the signal it amplifies, such that

$$\delta X_{\text{out}}^2 + \delta Y_{\text{out}}^2 \approx G(\delta X_{\text{in}}^2 + \delta Y_{\text{in}}^2 + \frac{1}{2}), \tag{4.8}$$

as illustrated in Figure 4.2

In this thesis, we use parametric amplifiers, such as a Josephson Parametric Amplifier (JPA) and a Josephson Traveling Wave Parametric Amplifier (JTWPA), in a phase preserving amplification. The full description of those devices goes out from this thesis scope, however the reader can refer to [Flu; Cas]. Those amplifiers allow a typical gain of $G \approx 100$ and work at the quantum limit, adding only the minimal noise of half a photon.

4.2 Photon detection

4.2.1 Photon number observable

The other detection method that we use in this thesis is based on counting photons rather than detecting field quadrature. Limiting ourselves to photon numbers equal to 0 or 1, this corresponds to measuring the photon number operator $\hat{a}^\dagger \hat{a}$.

Fock state

The Fock state $|n\rangle$ is defined as the photon number operator eigenstate and describes a state populated by n photon, such that

$$\begin{aligned} \langle n|\,\hat{a}^\dagger\hat{a}\,|n\rangle &= n, \\ \delta\hat{a}^\dagger\hat{a}^2 = \langle n|\,(\hat{a}^\dagger\hat{a})^2\,|n\rangle - \langle n|\,\hat{a}^\dagger\hat{a}\,|n\rangle^2 &= 0. \end{aligned} \tag{4.9}$$

We see that the photon number fluctuation is null for any Fock state. Reminding that the vacuum state is the state without photon $|0\rangle$, this result gives a glimpse of the interest of using photon counting: there is no intrinsic fluctuation in the signal, and thus no theoretical limit in the detection SNR.

Coherent state

The SMPD can be used to detect a coherent state. In this case, the photon number observable behaves such that

$$\begin{aligned} \langle\alpha|\,\hat{a}^\dagger\hat{a}\,|\alpha\rangle &= |\alpha|^2 = n, \\ \delta a^\dagger a^2 &= |\alpha|^2 = n. \end{aligned} \tag{4.10}$$

The photon number within a coherent state follows a Poissonian statistics where its variance equals its mean value. Therefore, the direct detection of a coherent state using the SMPD has unavoidable fluctuations, called shot noise.

4.2.2 Single Microwave Photon Detector (SMPD) device

The SMPD is an apparatus that yields a click whenever a microwave photon is incoming to its input. Given that microwave photons have low energy and so are difficult to detect, the fabrication and manipulation of a photon counting device at microwave frequency is an active research field. Here we describe the photon counting principle and SMPD circuit design used in this thesis [Les+20; Alb+21]. The devices used in the measurements reported in thesis were designed and fabricated by Emanuele Albertinale and Leo Balembois, and more details can be found in their respective theses. Here we will simply give a brief account of their working principle.

4.2.2.1 SMPD principle

In order to detect photon, our SMPD implements the idea of using a Two-Level System (TLS) to catch a traveling photon into an excitation. Practically, we are using a transmon qubit as a TLS with a transition frequency in the microwave regime and a reasonably long lifetime ($T_1 \sim 10\,\mu$s). We can read out the transmon state with a very high fidelity to determine if a photon has come or not [Bla+21].

However, a direct coupling between the microwave line and the qubit would quickly damp the qubit excitation. To overcome this issue, we introduce in the SMPD additional microwave components, namely a pump, a buffer resonator and a waste resonator, in order to use a mode mixing process to catch an incoming photon. The qubit excitation occurs through a four wave mixing process that converts a photon carrying the signal from the buffer (at frequency $\omega_b/2\pi$) and a photon from the pump ($\omega_p/2\pi$) into an excitation in the qubit ($\omega_q/2\pi$) and a photon in the waste resonator ($\omega_w/2\pi$). This mode mixing requires energy conservation between the modes such that

$$\omega_b + \omega_p = \omega_q + \omega_w. \tag{4.11}$$

Thanks to the waste resonator high dissipation rate, the mode mixing process is effectively non reversible. Thus, we have enough time to read out the qubit state before it relaxes.

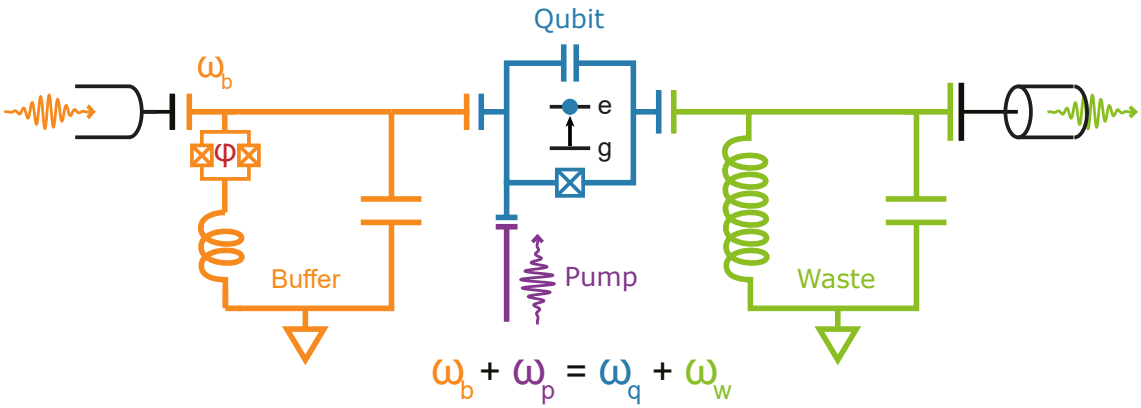

Figure 4.3: **SMPD circuit.** The signal comes from the line connected to the buffer resonator (orange). This resonator can be tune on resonance with the signal using the flux φ that thread its SQUID. The pump (violet) can convert a buffer excitation into an excitation in the qubit (blue) and in the waste resonator (green). This conversion must satisfy the energy conservation: $\omega_b + \omega_p = \omega_q + \omega_w$. The waste resonator is strongly coupled to another external line.

4.2.2.2 SMPD building blocks

Transmon qubit

The transmon qubit, in blue in Figure 4.3, is a superconducting 2D device that consists in a harmonic oscillator shunted with a Josephson junction to introduce non-linearity. This non-linearity allows to manipulate only the transmon two first energy states whose resonance frequency differs from the other transitions frequency, creating an effective TLS system. This kind of qubit can be directly driven with a coherent tone sent to a line coupled to it; in our experiment we use the same line for direct qubit manipulations as for the pump tone. The qubit read out is done thanks to its dispersive coupling to its neighboring resonators, either the waste or the resonator. The qubit non linearity is also a critical element because it mixes our SMPD four modes and therefore enables the mode conversion process.

Tunable buffer resonator

The buffer resonator, in orange in Figure 4.3, is at the SMPD input and receives the photon to be detected. Since its frequency must be tuned with this photon, the buffer resonator is designed with a SQUID loop in order to be able to adjust its resonance frequency $\omega_b/2\pi$. The SQUID is a superconducting element based on two Josephson junctions that acts as a tunable inductance according to the magnetic flux that thread it. The buffer resonator bandwidth typically corresponds to the frequency band on which photons are detected.

Dissipative waste resonator

The waste resonator, in green in Figure 4.3, is coupled to the qubit to enhance the mode conversion process as it receives an excitation along with the qubit. Once excited, our SMPD design requires the waste resonator to damp its energy faster than it would convert it back through the mode mixing. Practically, the waste resonator is strongly coupled to an external line to emit away its excitation.

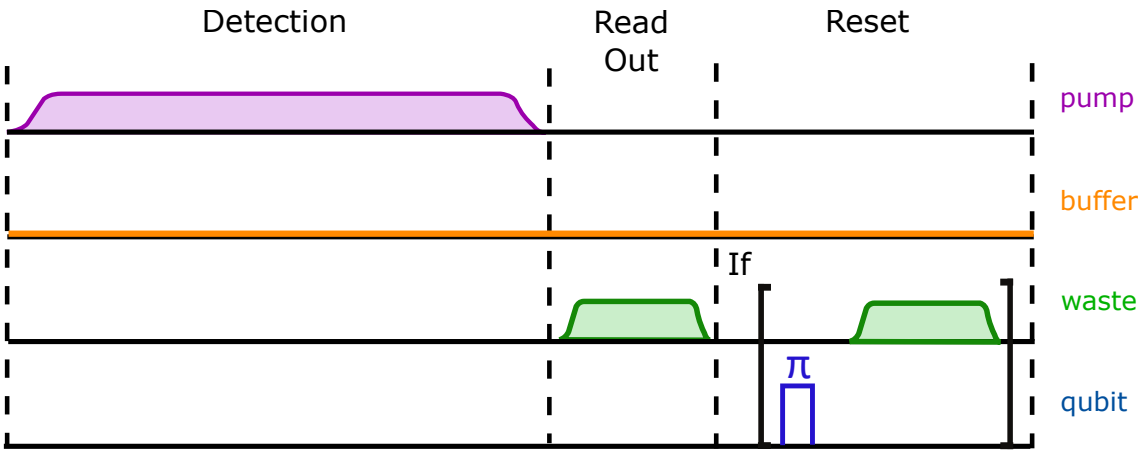

Figure 4.4: **SMPD cycling operations.** Schematic of the field amplitude reaching each SMPD port during one SMPD cycle. This sequence is repeated as long as we want to detect photons. **Detection**, the pump is ON to convert the weak signal arriving to the buffer into a qubit excitation. The signal reaching the buffer is detected only during the detection time. **Read out**, in setup 2, a coherent tone is applied to the waste to measure the qubit state. In setup 1, the read out is done through the buffer. **Reset**, as long as the qubit is found excited, we apply a π pulse on it and read out the resulting state. When the qubit is found in its ground state, we start the next cycle.

Pump tone

The pump tone, in violet in Figure 4.3, is a tunable coherent tone sent to the qubit to trigger the mode mixing process. Its frequency is chosen to satisfy the energy conservation Equation 4.11 and its amplitude determines the mode mixing rate, finding a balance so it catches the photon efficiently but lets the waste resonator relax from its excitation.

4.2.2.3 Sequence of operation

The SMPD is a device that works in a cyclic way, meaning that a basic set of operations is repeated for the whole cycling time. A single cycle is describe in Figure 4.4, showing the basic SMPD operations:

- **Detection**: during the detection time, we set the pump tone ON and enable the conversion of a photon coming to the buffer into a qubit excitation. It corresponds to the time window when the SMPD is ready to detect an incoming photon.
- **Read Out**: we probe the qubit state to determine if a photon has been detected in the detection window.
- **Reset**: if the qubit is excited, we reinitialize it with a π pulse and read out again its state. As long as the qubit is found excited by the read out, we repeat this reset operation.

This sequence has a timescale of $\sim 10\,\mu$s so it needs to be repeated many times to detect the whole spin fluorescence.

4.2.2.4 Figures of merit

From an operational point of view, the SMPD meaningful characteristics describe its sensitivity to an incoming photon. This sensitivity depends on the photon detection efficiency and on the detection noise due to dark counts.

Efficiency

The SMPD efficiency determines the proportion of incoming photons that are indeed detected by the SMPD. This efficiency is the product of two contributions:

- **Duty cycle**: η_{dc} corresponds to the ratio of the detection time over a full cycle time. Indeed a photon that arrives out of the detection window won't be detected, limiting the SMPD efficiency.
- **Conversion efficiency**: η_{SMPD} describes the probability for a photon coming during the detection window to be converted in a qubit excitation detected by the following read out.

A balance is needed in the choice of the detection window: although we would like to enlarge it to increase η_{dc}, if it becomes too long compared to the qubit T_1 then an excitation received at the beginning of the detection time window might relax before the read out step, effectively reducing η_{SMPD}. For the SMPDs used in this thesis, the typical parameters are $\eta_{\mathrm{dc}} \sim 0.75$ and $\eta_{\mathrm{SMPD}} \sim 0.5$.

Dark counts

The SMPD dark count rate α describes the rate of SMPD clicks in absence of signal. Since readout errors are negligible when the qubit is in its ground state, the false click are due to 2 main sources:

- **qubit intrinsic excitation**: superconducting qubits are in general found to have an excitation probability higher than what would be expected at a temperature of 10 mK, due to various high-energy sources of radiation (infrared photons, cosmic rays, ...). This spurious excitation can cause a SMPD click in absence of incoming photon, which is thus a dark count.
- **lines converted excitation**: it is extremely difficult to thermalize the microwave modes in the input line at 10 mK. In practice, there are always out-of-equilibrium microwave photons arriving from higher-temperature stages, which will be detected by the SMPD and that we include in the so-called "dark count rate".

For the SMPD used in this thesis, we have typically $\alpha \sim 1000$ counts/s. It is worth to mention that α fluctuates noticeably from experiment to experiment due to fluctuations in the flux threading the buffer SQUID, in the qubit T_1 and in the read out fidelity.

4.3 Spin detection methods Signal-to-Noise Ratio (SNR)

The SNR of an experiment yielding a signal s, with average value $\langle s \rangle$ and variance δs^2, is defined as

$$\mathrm{SNR} = \frac{\langle s \rangle}{\sqrt{\delta s^2}}. \tag{4.12}$$

It is a critical experimental property as it describes the amount of information extracted from a single shot experiment and therefore the number of iterations needed to detect a signal. Because an experimental system has fluctuations that prevent from averaging indefinitely, a good SNR not only reduces the acquisition time but also gives access to weak signals.

From this quantity, we can deduce an ESR experiment sensitivity, expressed in [Spins/$\sqrt{\text{Hz}}$], as the number of spins needed to have a SNR = 1 for 1 second of experiment. Although given this definition the sensitivity is a quantity that we want to minimize, we will keep referring to a gain in sensitivity as we reduce it. We extrapolate the minimal number of spins detectable N_{min} for a given experiment time $T_{\text{experiment}}$ as

$$N_{\text{min}} = \frac{\text{sensitivity}}{\sqrt{T_{\text{experiment}}}} \tag{4.13}$$

The goal of this section is to derive analytical formulas for the SNR of the 2 detection methods used in this thesis. In that goal, we will consider a somewhat idealized situation in which N spins are coupled to the detection resonator with an identical coupling constant g_0, and where they are spread in frequency in a Lorentzian distribution with an inhomogeneous linewidth Γ_{inh} much smaller than the resonator bandwidth κ, enabling the application of ideal spin driving pulses. Also the only relaxation channel considered is radiative, which sets the experiment time $T_{\text{experiment}} = T_{\text{R}} = \Gamma_{\text{R}}^{-1}$. Even though these conditions are not met in the actual experiments, the formulas derived will provide useful physical insights. Whenever quantitative comparison with the data will be needed, we will use simulations.

4.3.1 Spin signal modeling

4.3.1.1 Spin inductive detection

We first compute the spin signal contained in a spin echo detected with ID. In the ideal case studied here, the echo sequence can be defined for all spins as: $\pi/2_X - \tau - \pi_Y - \tau -$ echo.

For a single spin j with detuning $\Delta\omega_j$ and the echo occurring at a time $t = 0$, one can deduce from Equation 3.20 that the spin lowering operator is

$$\langle S_{-,j}(\Delta\omega)\rangle = -\frac{i}{4}e^{-i\Delta\omega t}. \tag{4.14}$$

As we integrate over the contributions from each spin, the spin ensemble lowering operator becomes

$$\langle S_-\rangle = \int S_-(\Delta\omega)\rho(\Delta\omega) = -\frac{iN}{4}e^{-\Gamma_{\text{inh}}|t|/2}. \tag{4.15}$$

We see in this equation that the spin operator indeed has a resurgence during the echo. Using Equation 3.23, the resulting intra-cavity field echo is

$$\langle\hat{a}\rangle(t) = -\frac{g_0 N}{\kappa}e^{-\Gamma_{\text{inh}}|t|/2}. \tag{4.16}$$

The echo is then transmitted to the line into a traveling mode $\hat{a}_{\text{out}}$. Experimentally, we measure the echo field quadrature after its propagation in the microwave lines

$$\langle\hat{X}_{\text{out}}(t)\rangle = \eta_{\text{line}}\langle\frac{\hat{a}^\dagger_{\text{out}}(t) + \hat{a}_{\text{out}}(t)}{2}\rangle \tag{4.17}$$

with η_{line} is the transmission efficiency in the lines.

The echo is described by its normalized mode temporal function $u(t)$, which allows to deduce the echo integrated amplitude

$$\langle\hat{X}_{\text{e}}\rangle = \int\langle\hat{X}_{\text{out}}(t)\rangle u(t)dt \tag{4.18}$$

where the mode normalization imposes $\int|u(t)|^2dt = 1$. As we choose a function that captures the mode shape $u(t) = \langle\hat{X}_{\text{out}}(t)\rangle/\langle\hat{X}_{\text{e}}\rangle$, we have

$$\langle\hat{X}_{\text{e}}\rangle = N\sqrt{\eta_{\text{reso}}\eta_{\text{line}}\frac{\Gamma_{\text{R}}}{2\Gamma_{\text{inh}}}} \tag{4.19}$$

where $\eta_{\text{reso}} = \kappa_c/\kappa$ is the proportion of intracavity photon emitted in the line. We see that the echo signal is proportional to the number of contributing spin N. In the low cooperativity regime, where $N\Gamma_R/\Gamma_{\text{inh}} \ll 1$, the number of photons in an echo is small compared to the spin number: $\langle \hat{X}_e \rangle^2 << N$.

4.3.1.2 Spin fluorescence detection

As discussed in Section 3.3.2.1, the typical signal detected in FD-ESR is the spin fluorescence following a single excitation pulse π. One can show with Equation 3.23 that after all the drive photons have escaped the resonator at time $t = 0$, the intracavity photon number is

$$\langle \hat{a}^\dagger \hat{a} \rangle(t) = \frac{\Gamma_R}{\kappa} N e^{-\Gamma_R t}. \tag{4.20}$$

The number of photons emitted by the spins is the integration of the intracavity photon number over the whole spin relaxation. The FD signal corresponds to the number of counts $\langle C \rangle$ detected with the SMPD, which differs from the number of photons emitted by the spins due to the limited detection efficiency η:

$$\begin{aligned} \langle C \rangle &= \eta N \\ \eta &= \eta_{\text{reso}} \eta_{\text{line}} \eta_{\text{dc}} \eta_{\text{SMPD}} \end{aligned} \tag{4.21}$$

where η_{reso} and η_{line} are considered the same as for ID detection.

We note that in our experiments

$$\frac{\langle C \rangle}{\langle X_e \rangle^2} = \frac{\eta_{dc} \eta_{SMPD}}{2C_p} \gg 1 \tag{4.22}$$

with C_p the spin ensemble cooperativity. Therefore, the amount of detectable photons is expected to be greater for FD than for ID.

4.3.2 Noise modeling in spin detection

4.3.2.1 Noise in inductive detection

As we explained in Section 4.1.1, the echo mode quadrature that we detect with ID holds fluctuations at least equal to the vacuum fluctuations. Moreover, since we use amplification to detect this signal, the parametric amplifier adds a quantum limited noise as detailed in Section 4.1.2, which yields a total fluctuation in the echo mode

$$\delta X_e^2 = \delta X_{\text{vacuum}}^2 + \delta X_{\text{amplification}}^2 = \frac{1}{2}. \tag{4.23}$$

This fluctuation is due to quantum mechanics laws that cannot be avoided with the detection scheme presented here. One can think of using a phase dependent amplifier to remove the amplifier noise contribution, but the fluctuation remains limited in the end by the vacuum fluctuations.

4.3.2.2 Noise in fluorescence detection

In FD, the noise comes from two contributions:

- **Dark counts**: SMPD false clicks are rare and independent event that follow a Poissonian distribution. It introduces therefore a fluctuation $\delta C_{\text{DC}}^2 = \alpha T_R$ in the number of counts depending on the amount of dark counts during the experiment.

- **Partition noise**: the limited detection efficiency means that the number of counts follow a binomial law with fluctuations $\delta C_\eta^2 = \eta(1-\eta)N$, the so-called partition noise.

The FD fluctuations is the sum of those contributions

$$\delta C^2 = \delta C_{\mathrm{DC}}^2 + \delta C_\eta^2 = \alpha T_{\mathrm{R}} + \eta(1-\eta). \tag{4.24}$$

We see here that FD fluctuations depend on the device parameters α and η. We can arbitrarily reduce those fluctuations if we find ways to improve the SMPD properties.

4.3.3 SNR comparison

Considering the SNR of these two detection methods, we get:

$$\begin{aligned} \mathrm{SNR}_{\mathrm{ID}} &= N\sqrt{\eta_{\mathrm{reso}}\eta_{\mathrm{line}}\frac{\Gamma_{\mathrm{R}}}{\Gamma_{\mathrm{inh}}}} \\ \mathrm{SNR}_{\mathrm{FD}} &= \frac{\eta N}{\sqrt{\alpha T_{\mathrm{R}} + \eta(1-\eta)N}} \end{aligned} \tag{4.25}$$

In ID-ESR, the SNR increases linearly with the number of spins N. It also depends on the rates ratio between the photon emission rate Γ_{R} and the echo damping rate Γ_{inh}.

In FD-ESR, we can distinguish two different fluctuation regimes:

- if $\alpha T_{\mathrm{R}} \gg \eta(1-\eta)N$: the fluctuations are dominated by the dark counts. The SNR increases linearly with the number of spins N, and it gets also larger when the spin relaxation time Γ_{R} reduces. In this thesis, we are always in this regime.
- if $\alpha T_{\mathrm{R}} \ll \eta(1-\eta)N$: the fluctuations are dominated by the partition noise. The SNR increases as the square root of N, and is now independent from Γ_{R}.

To compare the two detection methods sensitivity, we have to introduce some parameter values. To correspond to our experimental conditions, let's consider the following figures: $\eta_{\mathrm{reso}} \sim 1/2$, $\eta_{\mathrm{line}} \sim 1$, $\eta \sim 0.1$, $\Gamma_{\mathrm{R}}/2\pi \sim 3$ Hz, $\Gamma_{\mathrm{inh}}/2\pi \sim 1$ MHz, $\alpha \sim 1000$ counts/s, $N \sim 10^4$. In this condition, the ratio of SNR is

$$\frac{\mathrm{SNR}_{\mathrm{FD}}}{\mathrm{SNR}_{\mathrm{ID}}} \sim 10. \tag{4.26}$$

Therefore, this ideal model predicts a gain in sensitivity with FD-ESR compared to ID-ESR in our current experimental conditions. This gain in sensitivity is experimentally confirmed in Chapter 7.

In addition, we see that $\mathrm{SNR}_{\mathrm{FD}}$ is only limited by the detection scheme characteristics η and α that can, in principle, be arbitrarily improved. On the other hand, $\mathrm{SNR}_{\mathrm{ID}}$ is limited by the spin properties N, Γ_{R} and Γ_{inh} that depend on the spin system.

Note that the SMPD can be used for direct echo detection, as will be done in Section 7.3. In that case, the echo detection SNR is

$$\mathrm{SNR}_{\mathrm{echo,SMPD}} = \frac{\langle \hat{X}_{\mathrm{e}} \rangle^2}{\langle \hat{X}_{\mathrm{e}} \rangle} = N\sqrt{\eta_{\mathrm{reso}}\eta_{line}\eta_{\mathrm{dc}}\eta_{\mathrm{SMPD}}\frac{\Gamma_{\mathrm{R}}}{2\Gamma_{\mathrm{inh}}}}. \tag{4.27}$$

This time, the photon detection is expected to have a lower sensitivity than quadrature detection by a factor $\sqrt{2}$ even in the case of an ideal SMPD with $\eta_{\mathrm{dc}} = \eta_{\mathrm{SMPD}} = 1$. This appears as a motivation to develop a spin echo detection method based on spin fluorescence detection, as will be implemented in Chapter 9.

Chapter 5

Rare Earth Ions (REI) in Scheelite

In this thesis, we apply the FD-ESR method to REI spins in a scheelite crystal of $CaWO_4$, with a specific focus on Erbium ions Er^{3+}. In this chapter, we introduce the physics of REI embedded in a crystal of $CaWO_4$ with a particular emphasis on the magnetic properties of the ground-state doublet, which is the effective electron spin system under study in this manuscript.

Our goal is not to provide a comprehensive review of this system, but rather to give the essential elements of background needed to understand the experiments described later, as well as point to relevant references whenever needed.

5.1 Rare earth ions in a crystal

5.1.1 Ion Hamiltonian

In this thesis we focus on rare earth atoms that belong to the Lanthanides family. In a crystal, they usually become a tri-positive ion with their electronic structure becoming: $1s^2 2s^2 2p^6 3s^2 3p^6 4s^2 3d^{10} 4p^6 5s^2 4d^{10} 5p^6 4f^{N_e}$ where $N_e \in [0, 14]$ is the number of electrons sitting in the $4f$ shell. Since the $4f$ orbital is spatially closer to the nucleus than the $5s$ and $5p$ orbitals, it is shielded from external perturbations. This orbital property explains the similarity between the Lanthanides as well as the possibility to describe their electronic energy levels based on the free ion level structure.

5.1.1.1 Free ion Hamiltonian

We start the description of the rare earth electronic energy structure by considering a free ion with interactions between the electrons and the nucleus. A central field approximation allows to split the free ion Hamiltonian into 3 parts [Wei83]

$$H_{\mathrm{FI}} = H_0 + H_{\mathrm{NC}} + H_{\mathrm{SO}}, \tag{5.1}$$

where

$$H_0 = -\sum_{i=1}^{N_e} \left[\frac{\hbar^2}{2m} \nabla_i^2 + U(r_i) \right] \tag{5.2}$$

is the central field Hamiltonian with $U(r)$ a spherical potential that approximates the Coulombic potential due to the contribution of both the nucleus and the interaction with the other electrons in the mean-field approximation,

$$H_{\mathrm{NC}} = \sum_{i<j}^{N_e} \frac{e^2}{r_{ij}} - \langle \sum_{i<j}^{N_e} \frac{e^2}{r_{ij}} \rangle \tag{5.3}$$

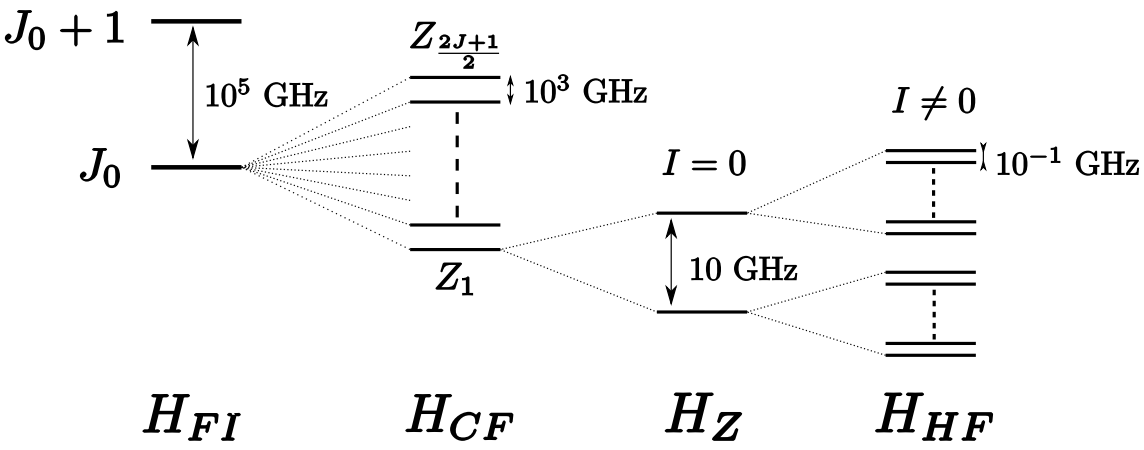

Figure 5.1: **Energy states of a REI embedded in a crystal.** The REI is described by successive Hamiltonians with different energy scale. The free ion Hamiltonian H_{FI} ($\sim 10^5$ GHz) defines electronic states characterized by the quantum number J. For Kramers ions, the crystal field Hamiltonian H_{CF} ($\sim 10^3$ GHz) splits their state into $(2J+1)/2$ doublets called Z_i. The doublet behaves as a spin 1/2 and its degeneracy is lifted under a magnetic field by the Zeeman Hamiltonian H_{Z} (~ 10 GHz). In the case of an nuclear isotope with nuclear spin $\boldsymbol{I}$, the hyperfine Hamiltonian H_{HF} ($\sim 10^{-1}$ GHz) splits each electronic spin state.

is the electron-electron Coulombic interaction beyond the mean-field approximation, and

$$H_{\mathrm{SO}} = \sum_{i=1}^{N_e} \xi(r_i) \boldsymbol{l_i}.\boldsymbol{s_i} \tag{5.4}$$

is the spin orbit coupling between the spin s_i and the angular momentum l_i of electron i.

The central field approximation allows to solve the Schrödinger equation with H_0. The description of the electronic structure is based on 4 quantum numbers (n, l, m_l, m_s): the principal quantum number n, the angular momentum quantum number l $(0 \leq l < n-1)$, the magnetic quantum number m_l $(-l \leq m_l \leq l)$ and the spin quantum number $m_s = \pm 1/2$. H_0 eigenstates depend on n and l so those are good quantum numbers to describe the electronic state. In the following, we concentrate on the $4f$ orbital with $n = 4$ and $l = 3$, which is relevant for the magnetic properties.

The Hamiltonians H_{NC} and H_{SO} can be treated together as perturbations since they both have a lower energy scale than H_0. One can use the so-called intermediate coupling scheme [JL05] where we introduce the operator $\boldsymbol{J} = \boldsymbol{L} + \boldsymbol{S}$ with $\boldsymbol{L} = \sum_i^{N_e} l_i$ and $\boldsymbol{S} = \sum_i^{N_e} s_i$. It defines another good quantum number J such that $\hbar J(J+1)$ is an eigenvalue of $\boldsymbol{J}^2$. The energy levels end up being $(2J+1)$ degenerate multiplets.

5.1.1.2 Effective spin 1/2 under crystal field interactions

For REIs in a crystal lattice, the spherical symmetry of $U(r)$ is broken by the crystal electric field following the crystal field Hamiltonian H_{CF}. The crystal influence can be treated as a perturbation that lifts the $(2J+1)$ degeneracy into crystal field states. In particular, for REIs that have an odd number of electrons N_e in their $4f$ shell, the Kramers theorem states [Kra30] that each crystal field state is at least doubly degenerate at zero magnetic field. The states are therefore grouped into series of "Kramers doublets".

The Kramers doublet degeneracy is lifted by the application of an external magnetic field B_0 through the Zeeman effect

$$H_Z = \mu_B \boldsymbol{B_0} \cdot (\boldsymbol{L} + \mathrm{g}_s \boldsymbol{S}) = \mathrm{g}_J \mu_B \boldsymbol{B_0} \cdot \boldsymbol{J}, \tag{5.5}$$

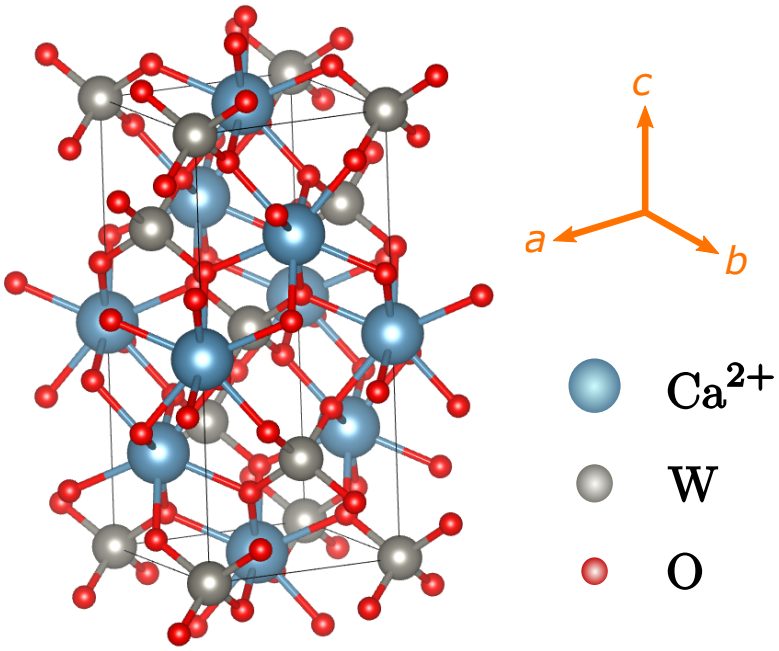

Figure 5.2: $CaWO_4$ **crystal structure.** Schematic of the $CaWO_4$ lattice showing a tetragonal structure, with a rotational symmetry around the c-axis.

where $g_s = 2$ and g_J is the Landé g-factor. In the limit where the Zeeman energy splitting of a given Kramers doublet is much smaller than the energy difference that separates it from other doublets, the Zeeman Hamiltonian can be treated as if it arises from an effective spin 1/2. This is the case in particular for the lowest-energy Kramers doublet, on which we will focus in the following. Restricting ourselves to this effective spin 1/2, the Zeeman Hamiltonian becomes

$$H_Z = \mu_B \boldsymbol{B_0} \cdot \mathbf{g} \cdot \boldsymbol{S} \tag{5.6}$$

where the **g**-tensor depends on the crystal host and reflects its symmetry.

Moreover, some REI isotopes have a non-zero nuclear spin $\boldsymbol{I}$ which induces additional terms in the spin Hamiltonian. The hyperfine Hamiltonian arising from this nuclear spin describes the interaction between electronic spin and nuclear spin as well as the nuclear spin Zeeman splitting

$$H_{HF} = \boldsymbol{S} \cdot \boldsymbol{A} \cdot \boldsymbol{I} + \mu_N \boldsymbol{B_0} \cdot g^n \cdot \boldsymbol{I} \tag{5.7}$$

where $\boldsymbol{A}$-tensor is the hyperfine tensor, proportional to the electron **g**-tensor when the Kramers doublets are non-mixed, which is the case for the REIs considered here, μ_N is the nuclear magneton and g^n is the nuclear spin g-factor.

The energy spectrum of a REI in a crystal is represented in Figure 5.1, considering only the lowest energy levels of each Hamiltonian.

5.1.2 Rare earth ions in calcium tungstate

5.1.2.1 $CaWO_4$ crystal properties

The calcium tungstate is a crystal with a tetragonal structure with lattice parameters $a = b = 0.524$ nm and $c = 1.138$ nm, as is represented in Figure 5.2. In the lattice unit cell the REI replaces Ca^{2+}. Considering the calcium site, it is identical under any combination of rotations by 90° around the c-axis and of reflections in the (a, b)-plane. This kind of symmetry, called $S4$, affects the REI crystal field Hamiltonian, which satisfies the same symmetry. Because of the crystal-field $S4$ symmetry, the **g**-tensor is diagonal in the

Isotope	Nuc. spin	Nat. abun.	$g_\parallel$	$g_\perp$	$A_\parallel/h$ (MHz)	$A_\perp/h$ (MHz)	g^n
Er ($I=0$)	0	0.77	1.247	8.38	0	0	0
^{167}Er	7/2	0.23			-130	-873	0.563
Yb ($I=0$)	0	0.7			0	0	0
^{171}Yb	1/2	0.14	1.05	3.92	788	3082	0.494
^{173}Yb	5/2	0.16			-216	-851	-0.648

Table 5.1: **Spin parameters for Er^{3+} and Yb^{3+} in $CaWO_4$.** Values for the erbium are coming from [Ber+07] whereas for the ytterbium they come from [Sto14].

crystallographic (a, b, c) axes, with identical values when the field is applied perpendicular to the c axis ($g_a = g_b = g_\perp$) and a different value when it is applied parallel to c ($g_c = g_\parallel$).

There exist 2 different types of site for Ca^{2+} that distinguish themselves by the position of the neighboring Oxygen atoms. Those two sites are related by inversion symmetry, as can be seen in Figure 5.2, meaning that a rotation by 180° around an axis in the (a, b)-plane allows to convert one site into the other. The difference between those two sites, populated by REI with equal probability, induces different electric field dependence for the ion spin [Mim64].

Since the REI substitute a 2+ ion by a 3+ ion, a charge compensation process unavoidably happens in the crystal during its growth. For instance, this can happen through the creation of calcium vacancies [MG67]. The charge compensation is a local random phenomenon which triggers inhomogeneity in the crystal electric field that potentially breaks the $S4$ symmetry of a neighboring REI site [GM64]. Nevertheless, ESR spectroscopy studies of $CaWO_4$ have shown REI lines that satisfy $S4$ symmetry, which implies that the charge compensation happens over large scales and doesn't impact the site symmetry for at least a fraction of the sites.

The choice of $CaWO_4$ as a substrate is motivated both by its crystal electrostatic field that sustains high REI **g**-tensor components as well as its low concentration of magnetic fluctuations sources. In term of crystal nuclear spin, the main contribution is the tungsten isotope ^{183}W that has a natural abundance of 0.145. Due to this low abundance combined with a relatively small gyromagnetic ratio $\gamma_W/2\pi = 1.8\,\mathrm{MHz/T}$, $CaWO_4$ is one of the most magnetically-silent materials that can be found (at least, with natural abundance elements), and is therefore well-suited to host long-coherence times electron spins [Kan+22].

5.1.2.2 REI spin properties in $CaWO_4$

As discussed before, the ions **g**-tensor in such crystal follows an axial symmetry around the c-axis. The strength of the spin coupling to the magnetic field varies from a REI specie to another, with values for the species detected in this thesis given in Table 5.1. The spin anisotropic **g**-tensor means that its polarization isn't necessarily along the external magnetic field. For a magnetic field with θ and φ in the spherical coordinates within the crystal axis (a, b, c), the electron spin Zeeman Hamiltonian is

$$H_{\text{spin}} = \mu B_0(g_\perp \sin(\theta)\cos(\varphi)S_a + g_\perp \sin(\theta)\sin(\varphi)S_b + g_\parallel \cos(\theta)S_c), \tag{5.8}$$

as illustrated in Figure 5.3. Because of the c-axis symmetry, one can choose $\varphi = 0$ and rewrite the Hamiltonian along the spin axis (X, Y, Z)

$$H_{\text{spin}} = \mathrm{g}_{\text{eff}}\mu_B B_0 \hat{S}_Z \tag{5.9}$$

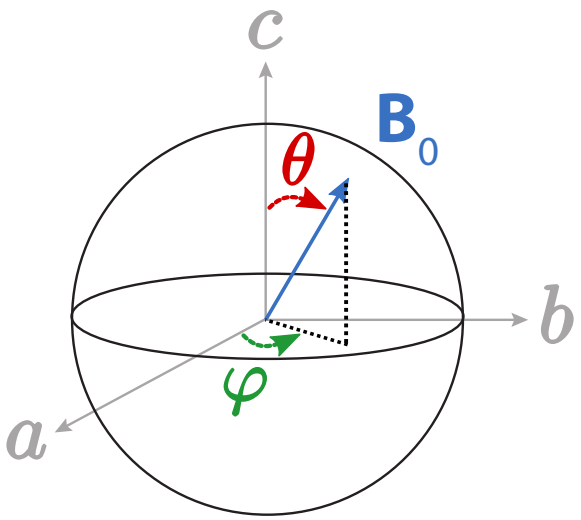

Figure 5.3: **Magnetic field orientation in the** (a, b, c) **axis**

with

$$\begin{aligned} g_{\text{eff}} &= \sqrt{(g_\perp \sin\theta)^2 + (g_\parallel \cos\theta)^2} \\ \boldsymbol{Z} &= \cos(\theta)\boldsymbol{c} + \sin(\theta)\boldsymbol{a} \\ \sin\theta' &= \sin\theta \times g_\perp / g_{\text{eff}} \\ \cos\theta' &= \cos\theta \times g_\parallel / g_{\text{eff}} \end{aligned} \tag{5.10}$$

where $\boldsymbol{Z}$ is the spin quantization axis and g_{eff} the effective gyromagnetic factor.

In addition to the Zeeman splitting, some REI isotopes have a nuclear spin that contribute to the spin Hamiltonian through the hyperfine coupling and the nuclear Zeeman effect (Equation 5.7). The hyperfine **A**-tensor depends in the **g**-tensor and presents also a parallel component $A_\parallel$ along the axis c and a perpendicular components $A_\perp$ in the (a, b) plane. The relevant values for this thesis are presented also in Table 5.1. In this thesis, we stick to the case where the Zeeman interaction dominates the hyperfine interaction. In this high field limit, the m_s and m_I are indeed good quantum numbers and the hyperfine coupling splits each Zeeman state into $(2I + 1)$ states $|m_s, m_I\rangle$.

The spin polarization depends on its ground-state manifold structure and follows a Boltzmann distribution. In the case of a $I = 0$ spin, the spin states energy difference is such that in a dilution cryostat

$$\hbar\omega_s \gg k_B T_{\text{eff}} \tag{5.11}$$

with k_B the Boltzmann constant and T_{eff} the effective spin temperature. Therefore, the spin is fully polarized in its ground state. In the case of spins with $I \neq 0$, neglecting the population of the excited manifold, the population of level k of the ground state manifold is given by Boltzmann law

$$p_k = \frac{e^{-E_k/k_B T_{\text{eff}}}}{\sum_l e^{-E_l/k_B T_{\text{eff}}}} \tag{5.12}$$

with E_k the energy level of state k.

5.2 Erbium ion spins properties in $CaWO_4$

We now focus more particularly on the case of $Er^{3+} : CaWO_4$. We review its properties as well as the measurements performed by Marianne Le Dantec during her thesis on the very same crystal as was used in this thesis, but using ID-ESR [Le 22].

5.2.1 Resonance linewidth

The interaction of the spin with its environment induces frequency shifts, which can be static (leading to inhomogeneous broadening) or dynamic (homogeneous broadening).

5.2.1.1 Homogeneous linewidth

Fluctuations in a single spin resonant frequency appears as a broadening of its linewidth. As those same fluctuations trigger the spin decoherence, the single spin linewidth is $\Gamma_2 = 1/T_2$. These fluctuations arise from the spin dipolar coupling to surrounding magnetic dipoles. In our system, the main contribution comes from the Tungsten nuclear spin bath.

5.2.1.2 Inhomogeneous linewidth

The specific environment of each REI leads to static shifts of its resonance frequency. Therefore, the ensemble linewidth appears much broader, with an inhomogeneous linewidth $\Gamma_{\text{inh}} \gg \Gamma_2$. We now discuss the physical causes of this inhomogeneous broadening

Dipolar coupling

A first cause of inhomogeneous broadening is the dipolar coupling to other magnetic moments in the ion near vicinity, which causes the local magnetic field felt by each ion to slightly vary from B_0 and from each other. Here, we consider a very dilute crystal where the distance between paramagnetic impurities is so large that the impurity to impurity coupling contribution is negligible. The inhomogeneous broadening caused by the Tungsten nuclear spins is estimated to be ~ 100 kHz for Er^{3+} ions, much lower than the values measured (see below). In summary, the magnetic contribution to inhomogeneous broadening is negligible in the crystal considered here.

Electric field inhomogeneity

At zero magnetic field, the two states of a Kramers doublet have the same energy no matter the electric field, because of time-reversal symmetry. However, the application of a magnetic field B_0 lifts this symmetry and allows a static electric field to modify the **g**-tensor [Kie66]. Therefore, the transition frequency of a Kramers' doublet can become linearly sensitive to an applied electric field. Because this energy shift is itself also proportional to B_0, it can be interpreted as a linear dependence of the **g**-tensor with an applied electric field. The inhomogeneous electric fields seen by the REIs appears as a source of inhomogeneous broadening and is in fact the dominant one, as demonstrated in [Mim65] and as seen below.

In [Mim65] is studied in detail the **g**-tensor modifications induced by the application of a static E field. In this thesis, we will restrict ourselves to application of B_0 field in the (a, b)-plane. In these conditions, it was found that an electric field in the (a, b)-plane has no first order effect on the spin frequency whereas an electric field E_c along the c direction induces a linear frequency shift through a change $\delta g_\perp$ of the **g**-tensor perpendicular component $g_\perp$. This change can be written as

$$\delta \mathrm{g}_\perp(\varphi) = \frac{\alpha \sin(2\varphi - 2\varphi_0)}{2\mathrm{g}_\perp} E_c \tag{5.13}$$

where φ_0 is the angle where the sensitivity to the electric field vanishes and α is a parameter that characterizes the spin sensitivity to the electric field. We see that $\delta g_\perp$ depends on the angle φ at which B_0 is applied, and therefore the applied electric field breaks the rotational invariance of the **g**-tensor in the (a, b)-plane into an ellipse. This ellipse intersects with the

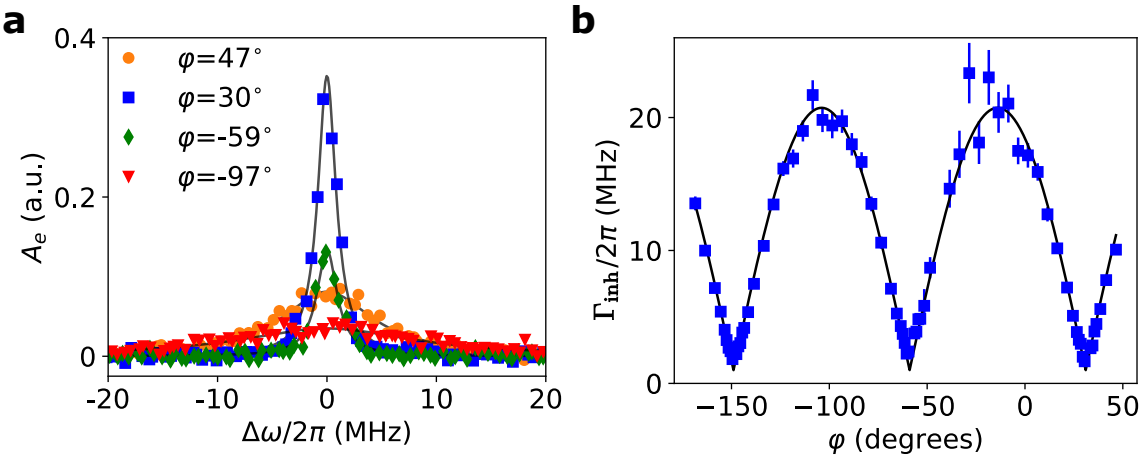

Figure 5.4: **Er^{3+} spectroscopy with ID-ESR from [Le 22]** **a**, echo amplitude A_e as a function of the detuning $\Delta\omega$ from the middle of the Erbium line at various magnetic field angle φ in the (a, b)-plane, where the symbols are data and the lines are Lorentzian fit. **b**. Full-Width-at-Half-Maximum (FWHM) linewidth $\Gamma_{inh}/2\pi$ as a function of φ, where symbols are data and the line is a fit using Equation 5.14.

original circle at an angle φ_0 where the Kramers doublet frequency becomes insensitive to an applied electric field.

For a typical electric field inhomogeneity of ΔE_c in a crystal, the induced inhomogeneous linewidth is

$$\begin{aligned} \frac{\partial\omega}{\partial E_c} &= \frac{\alpha \sin(2\varphi - 2\varphi_0)}{2g_\perp} \frac{\mu_B}{\hbar} B_0 \\ \Gamma_{inh} &\sim \Gamma_{min} + \left|\frac{\partial\omega}{\partial E_c}\right| \Delta E_c \end{aligned} \tag{5.14}$$

where Γ_{min} is the minimal linewidth reached at $\varphi = \varphi_0$.

The inhomogeneity in electric field is possibly due to charge compensation or to local deformations of the crystal that modify the electric field E_c felt by the spin. We will see in Chapter 8 that crystal deformations at the interface between the Niobium superconducting metal and the $CaWO_4$ substrate due to differential thermal contractions cause strain shifts. Indeed, those materials have roughly two orders of magnitude difference in their thermal expansion coefficient at cryogenic temperature [YB71; Whi62]. The lattice strain induces a modification of the local E_c in opposite direction for the two type of Ca^{2+} sites as it changes the relative distance with the neighboring Oxygen atoms. Therefore, all the spins in the strained crystal region have their frequency shifted in the same direction.

Prior to this thesis, the spectroscopy of Erbium ions was studied by Marianne Le Dantec on this very same sample but using ID-ESR. In the results shown in Figure 5.4, we see that the erbium ions line varies a lot in linewidth and amplitude with the field angle φ. By fitting $\Gamma_{inh}(\varphi)$ with Equation 5.14, the parameters were extracted: $\Delta E_c = 32.0 \pm 0.6$ kV/cm, $\varphi_0 = 31 \pm 0.2\,^\circ$ and $\alpha = (11 \pm 0.6) \times 10^{-6}(\text{V/cm})^{-1}$. In particular, it allows to determine $\Gamma_{inh,0} = \Gamma_{inh}(\varphi_0)/2\pi = 1.0 \pm 0.2$ MHz. In Section 7.1.3, we will revisit the linewidth measurements using FD-ESR.

5.2.2 Energy relaxation

Once excited out of their thermal equilibrium, spins relax by exchanging energy with thermal baths: either the lattice vibration bath (non-radiative relaxation) or the electromagnetic bath (radiative relaxation). Those competing relaxation processes are taken into account in the spin dynamics (Section 3.2.3). As discussed in Section 3.2.2.2, the spin radiative

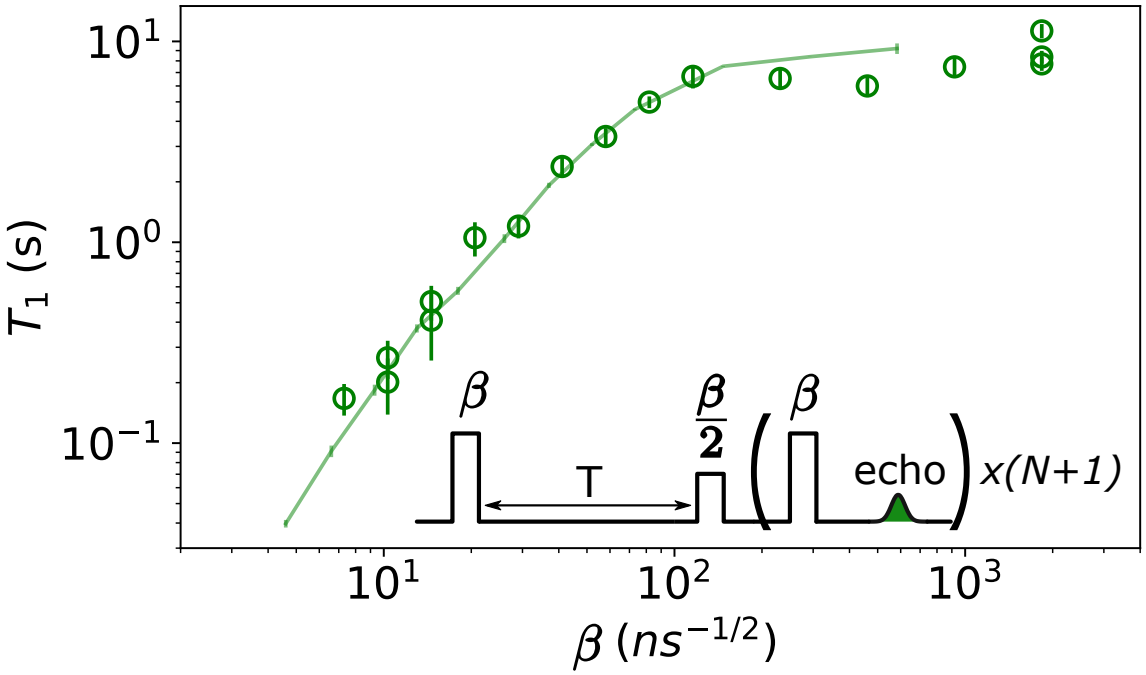

Figure 5.5: **Er^{3+} relaxation time with ID-ESR from** [Le 22] T_1 for various excitation pulse amplitude β realized with the inversion recovery sequence followed by a CPMG sequence [Alb+20], illustrated here, in order to enhance the measurement SNR.

relaxation rate Γ_R is completely dominated by the Purcell effect due to the coupling with the resonator. The spin non-radiative relaxation rate Γ_{NR} depends on the spin coupling with the crystal phonons. Indeed, the lattice vibration interacts with the spin magnetic moment through spin-orbit coupling. At non zero magnetic field, the crystal field ground state Z_1 hybridization with higher energy level such as Z_2 allows the lattice vibration to interact with the spin magnetic moment. Moreover, for REI isotopes with nuclear spin, the hyperfine coupling splits the spin states $|e\rangle$ and $|g\rangle$ into multiplets and opens up relaxation through various possible transitions

$$|e, m_I\rangle \rightarrow \begin{array}{l} |g, m_I\rangle \\ |g, m_I - 1\rangle \\ |g, m_I + 1\rangle \end{array} \quad (5.15)$$

The spins with a nuclear spin moment m_I that allows those additional relaxation channel relax faster in the lattice vibrations, with $\Gamma_{NR} \propto (I(I-1) - m_I^2)$.

Prior to this thesis, Erbium ions relaxation was studied by Marianne Le Dantec on this very same sample but using ID-ESR with inversion recovery sequence. This competition between radiative and non-radiative relaxation was observed in the dependence of the measured T_1 with the excitation pulse amplitude β. Indeed, the spins contributing to the signal g_0, and therefore Γ_R, depends on the pulse amplitude. One can distinguish the low amplitude regime, for which $\Gamma_R > \Gamma_{NR}$ and T_1 strongly varies with β, from the high amplitude regime, for which $\Gamma_R < \Gamma_{NR}$ and T_1 tends to saturate. The crossover between those two regime is visible in Figure 5.5 and is quantitatively reproduced by simulations. In Section 7.2, we will see a related effect by studying the excitation strength dependence of the fluorescence curves.

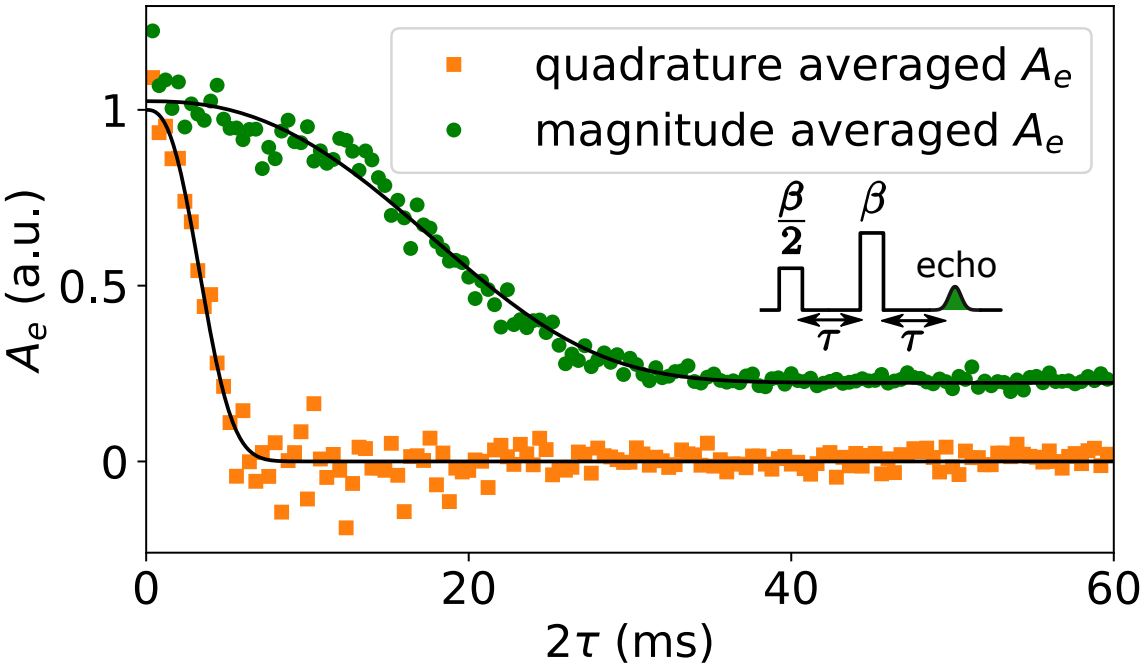

Figure 5.6: **Er^{3+} coherence time with ID-ESR from** [Le 22] Echo amplitude A_e as a function of 2τ. In orange, the data has been averaged on a single quadrature and was fitted with: $A_e = Ae^{-(2\tau/T_{2,q})^{x_q}}$, yielding $T_{2,q} = 4.0 \pm 0.1$ ms, $x_q = 2.6 \pm 0.2$. In green, the data has been averaged on the field magnitude and was fitted with: $A_e = \sqrt{Ae^{-2(2\tau/T_{2,m})^{x_m}} + C}$, yielding $T_{2,m} = 23.2 \pm 0.5$ ms and $x_m = 2.4 \pm 0.1$.

5.2.3 Coherence times

The homogeneous linewidth Γ_2 can be measured by recording the decay of a Hahn echo amplitude as a function of the inter-pulse delay τ. This decay is caused by the spins interaction with their dynamically-evolving environment.

In the sample studied in this thesis, the paramagnetic impurities are so dilute that interactions between them are negligible. Interactions with the nuclear spins of the ^{183}W atoms in the vicinity are however relevant. They lead to two distinct effects :

- Electron Spin Echo Envelope Modulation (ESEEM): the oscillation of the most proximal nuclear spins trigger a modulation of the ion spin frequency
- Spectral Diffusion (SD): the nuclear spins exchange energy in flip-flop interactions that trigger fluctuations in the ion spin frequency. This is the dominant decoherence phenomenon in our sample.

Prior to this thesis, Erbium ions coherence time was studied by Marianne Le Dantec on this very same sample but using ID-ESR. On the one hand, ESEEM has been reported by changing τ in small steps of $\sim 1\,\mu$s around $\tau \approx 100\,\mu$s. On the other hand, the spin coherence time has been studied by varying τ up to a few tens of ms. The results, presented in Figure 5.6, show different coherence time according to the data averaging procedure. When the data is average along one quadrature $\langle X \rangle$, the fit yields a coherence time of $T_{2,q} = 4$ ms, a value below the theoretical prediction for $Er^{3+} : CaWO_4$ [Kan+22]. However, when the signal is averaged in magnitude $\langle \sqrt{X^2 + Y^2} \rangle$, the fit yields a coherence time of $T_{2,m} = 23.2$ ms. We attribute the difference between those two coherence times to field fluctuations that randomizes the echo phase. In Chapter 9, we will demonstrate a method to detect spin echoes with FD and observe similar Erbium coherence times.

Chapter 6

Experimental system

This thesis focuses on ESR spectroscopy measurements performed with REIs in $CaWO_4$. We study a sample characterized prior to this thesis. In this chapter, we describe the Scheelite crystal of $CaWO_4$ as well as the resonator design. We then describe the experimental setups.

6.1 Scheelite sample

6.1.1 Sample growth and properties

6.1.1.1 Sample preparation

Our sample is a piece of $CaWO_4$ cut from a crystal boule grown with the Czochralski method [Bra04]. This crystal was produced in the Walther-Meißner-Institut by Andreas Erb and Jean-Côme Lanfranchi, and is described in detail here [EL13]. It was made for particle detection applications, and therefore was prepared with ultra pure materials: $CaCO_3$ with purity of 99.999% and WO_3 with purity of 99.998%. Nevertheless, the crystal contains a low residual concentration of paramagnetic impurities, which are detected in this work.

X-ray diffraction was used to prepare a sample in the shape of a rectangular slab, with a thickness of 0.5 mm and a plane surface with dimensions $3 \times 6\,\mathrm{mm}^2$ approximately within the (a,b) plane. A second X-ray characterization done on the sample showed that the surface makes an angle $\theta_c = 87\,^\circ$ with the c axis, and that the sample short edge makes an angle $\varphi_c = 47^\circ$ with the a-axis. Those figures are known within a precision of $\pm 2^\circ$ (Figure 6.1). In the following, except when explicitly mentioned, we consider the sample surface as corresponding to the (a, b)-plane.

6.1.1.2 ESR characterization

The sample was first characterized with a commercial ESR spectrometer by Sylvain Bertaina, from Aix-Marseille Université. Paramagnetic impurities were detected in a wide variety of magnetic field amplitude and angle. In Figure 6.2, we can see many peaks, each one associated with a spin species resonance. The peak position in B_0 and its evolution with the field orientation is an indication of the spin parameters, and thus can allow to recognize the corresponding paramagnetic element. Many different experimental parameters can influence the signal (resonator frequency, temperature, excitation power...) which means that all the spins present in the sample are not necessarily detected. However, the chosen parameters here are suited to detect REI impurities.

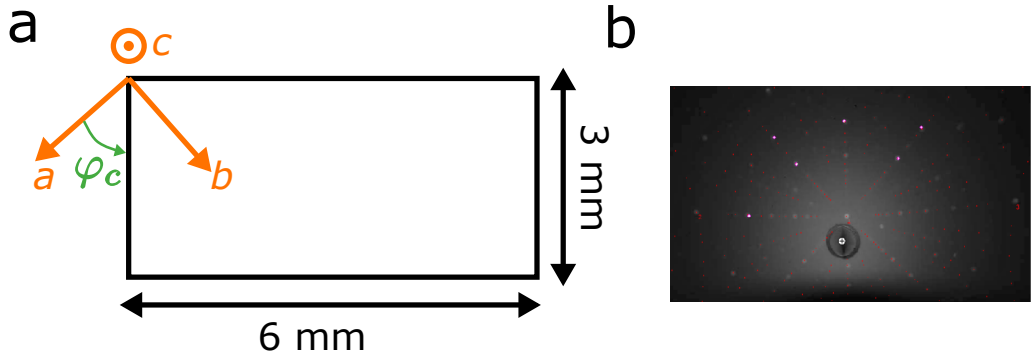

Figure 6.1: **Sample dimensions and orientation. a** Schematic of the rectangular shape sample. The sample surface corresponds approximately with the (a, b)-plane and its small edge makes an angle φ_c with the a-axis. **b** X-ray diffraction picture with in red a fit that allows to determine: $\theta_c = 87\,^\circ$ and $\varphi_c = 47\,^\circ$

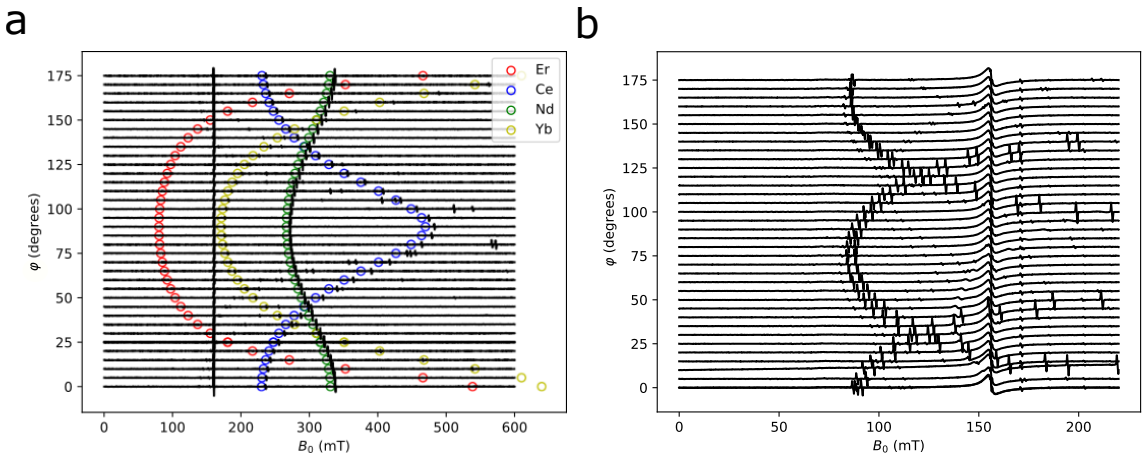

Figure 6.2: **ESR spectroscopy at a frequency $\omega_0/2\pi = 9.63$ GHz and temperature $T = 8$ K. a**. $B_0 \in [0, 600]$ mT varies the (a, c)-plane. 4 Kramers ions are identified with colors: Erbium (red), Cerium (blue), Neodymium (green) and Ytterbium (yellow). A strong signal associated to Iron ions is detected at $B_0 \approx 160$ mT. Unknown peaks evolve in pairs. **b**. $B_0 \in [0, 225]$ mT varies in the (a, b)-plane. Kramers ions peaks are harder to detect as the spin coupling is mediated by the smaller $g_{\|}$ in this configuration. The iron line is still visible at $B_0 \approx 160$ mT. Unknown peaks evolve in pairs.

The spectra in Figure 6.2a was recorded with B_0 varying in the (a, c)-plane. Thanks to our knowledge of the REI impurities **g**-tensor, we are able to recognize four of them: Er^{3+},Ce^{3+},Nd^{3+},Yb^{3+}.

The spectra in Figure 6.2b were recorded with B_0 varying in the (a, b)-plane. This time, the REI impurities are expected to have a constant resonant field due to the $S4$ symmetry of the Ca^{2+} substitution site (see Chapter 5). Those impurities are in fact hardly visible here due to their weak coupling to the oscillating field in the c axis (Er^{3+} is for instance expected at $B_0 \approx 80$ mT). We observe other lines which do not obey the $S4$ symmetry and evolve with the field orientation in groups of peaks. Some of these lines may be associated with Er^{3+} in non-$S4$ symmetry due to charge compensation occurring in the nearest neighboring Ca^{2+} sites [GM64]. Another feature of those two spectra is a strong and narrow line at $B_0 = 160$ mT ($g \approx 4.3$), which consists in 4 closely spaced line when measured at higher resolution, and which is attributed to the middle Kramers doublet of Fe^{3+} [GKT78].

This characterization not only gives an insight of the paramagnetic species present in

Er^{3+}	Ce^{3+}	Yb^{3+}	Nd^{3+}	Fe^{3+}
0.7	2.7	38	12	11

Table 6.1: **Absolute concentration of detected ions**. Values in part per billion (ppb) with an uncertainty of 20%.

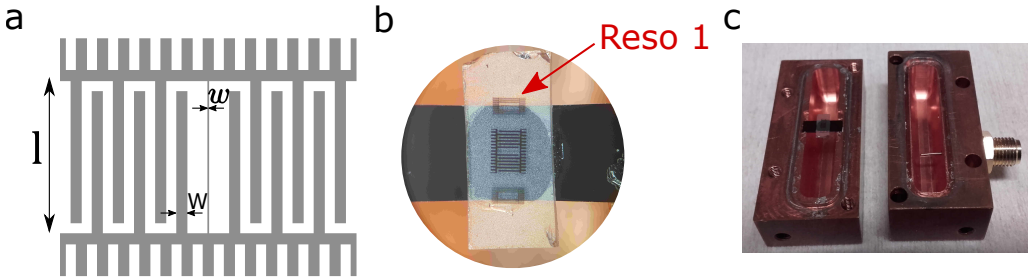

Figure 6.3: **Picture of our sample.** **a**, schematic of the resonator design showing its geometrical parameters l, w and W **b**, picture of the sample glued with Silicon grease on a high resistivity Silicon chip to hold it in the 3D box. The resonator manipulated in this thesis is "Reso 1". **c**, picture of the sample put in the copper box. We can see the pin that penetrates in the box.

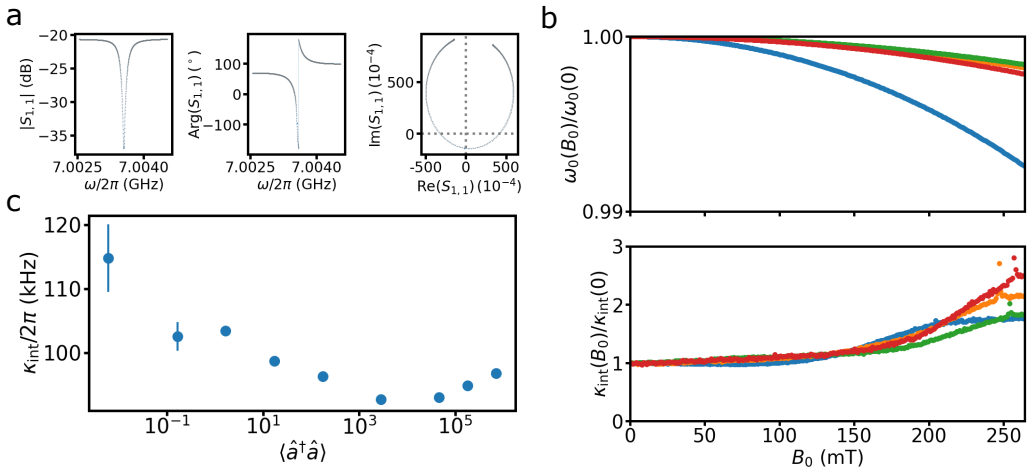

Figure 6.4: **Resonator characterization**. **a**, "Reso 1" characterization with $S_{11}(\omega)$ (dots) and the corresponding fit (line) in setup 1 at $\langle\hat{a}^\dagger\hat{a}\rangle \approx 7 \times 10^5$ and $B_0 = 60$ mT. **b**, top panel: relative shift in ω as a function of B_0 for four test resonators with the same type of design as patterned on our sample. Bottom panel: relative shift in κ_{int} as a function of B_0 for the same resonators. **c**, power dependence of the resonator "reso 1" inner loss rate κ_{int} at $B_0 = 60$ mT. The errorbars are deduced from the fit.

the sample but also enables to compute their concentration. Indeed, the spins relative concentration can be extracted from those spectra after a renormalization by the experimental parameters and the isotope abundance. Additionally, the absolute concentration of Er^{3+} was determined thanks to the ID-ESR measurements reported in [Le +21]. Altogether, those sets of experiments give access to the Kramers ions concentration, which are summarized in Table 6.1. The very low concentration of Er^{3+} in this sample is of interest for long spin coherence times [Le +21].

6.1.2 Resonator characterization

For our experiments, a superconducting lumped-element resonator is fabricated on top of the sample surface. It consists in two interdigitated electrodes (the capacitive part)

connected by a narrow wire (the inductive part). The resonator is characterized by its geometric properties, visible in Figure 6.3a: the wire width w and length l, the fingers width W and the number of fingers N_{fingers}. Those parameters were adjusted to reach the targeted frequency $\omega_0/2\pi \approx 7$ GHz. Although 3 resonators were patterned on our sample, only one of them is used in this thesis since it is the only one with a resonance frequency within the SMPDs frequency range. This resonator, named "reso 1" in Figure 6.3b as in [Le 22], has the following characteristics: $w = 2\mu$m, $l = 630\mu$m, $W = 10\mu$m and $N_{\text{fingers}} = 8$. Microwave simulations were conducted using Ansys HFSS software in order to develop the resonator design and to compute its impedance, yielding $Z_0 = 35\,\Omega$. The resonator simulations and fabrications were done by Marianne Le Dantec. More details can be found in Appendix B and in [Le 22].

As shown in Figure 6.3c, the sample is put in a 3D copper box and cooled at millikelvin temperature in a dilution cryostat. The resonator is coupled to the measurement line through a pin protruding in the cavity. This type of coupling enables to tune the resonator coupling to the lines κ_c. This coupling can be changed by modifying the sample position in the box, the size of the pin, the box resonance frequency...

Before any ESR experiment, the first step is to characterize the resonator. This is done in a continuous wave measurement where we measure for each resonator the reflection coefficient $S_{11}(\omega)$ using a Vector Network Analyser. The measurement is then fitted by Equation 3.18, as is shown in Figure 6.4a. The resonator characteristics vary with the magnetic field amplitude, in particular due to it's out of plane component that triggers vortexes in the superconductor, changing ω_0 and κ_{int}. The resonator is patterned in Niobium and can withstand magnetic fields applied parallel to the surface, as can be seen in Figure 6.4b where we measure 4 test resonators up to ~ 250 mT. At $B_0 = 140$ mT, the highest field applied for ESR measurements in this thesis, we have a $\sim 20\%$ increase in κ_{int} and a shift in frequency of a few MHz. As we will focus on Erbium ions in this thesis, "reso 1" characterization is done at $B_0 = 60$ mT, close to the $I = 0$ Erbium resonance. It is well established that the internal losses of superconducting resonators also depend on the power at which they are measured due to the presence of a bath of two-level systems which brings additional absorption at low powers, but gets saturated at high powers. Therefore, we characterize in setup 1 the internal loss rate evolution according to the probing power, corresponding to intra-resonator average photon number $\langle \hat{a}^\dagger \hat{a} \rangle$, and present the result in Figure 6.4d. In both setups, we extract the resonator characteristics at $\langle \hat{a}^\dagger \hat{a} \rangle \approx 1$:

- **setup 1**: $\omega_0/2\pi = 7.0035$ GHz, $\kappa_c/2\pi = 130$ kHz and $\kappa_{\text{int}}/2\pi = 100$ kHz
- **setup 2**: $\omega_0/2\pi = 6.999$ GHz, $\kappa_c/2\pi = 300$ kHz and $\kappa_{\text{int}}/2\pi = 60$ kHz

Those parameters will be used in this thesis to perform simulations and fits.

The resonator characteristics differ from one setup to the other, likely due to different experimental conditions. Since the experiments in setup 2 were done after the ones in setup 1, the Niobium film has likely oxidized in between the two sets of experiment which explains a reduction in $\omega_0/2\pi$ in setup 2. Each setup has its own sample holder in which we put differently the sample in order to have it strongly coupled to the microwave line, yielding the difference in κ_c. Eventually, the magnetic field out of plane component depends on the sample position relative to the coils, specific to each setup.

6.2 Experimental setups

We now describe the experimental setups used in this thesis. Two different setups mounted in two different cryostats were operated during this thesis, with their description visible in Figure 6.5 and Figure 6.6. Here, we describe the experimental principle in common for the two setups as well as their few differences.

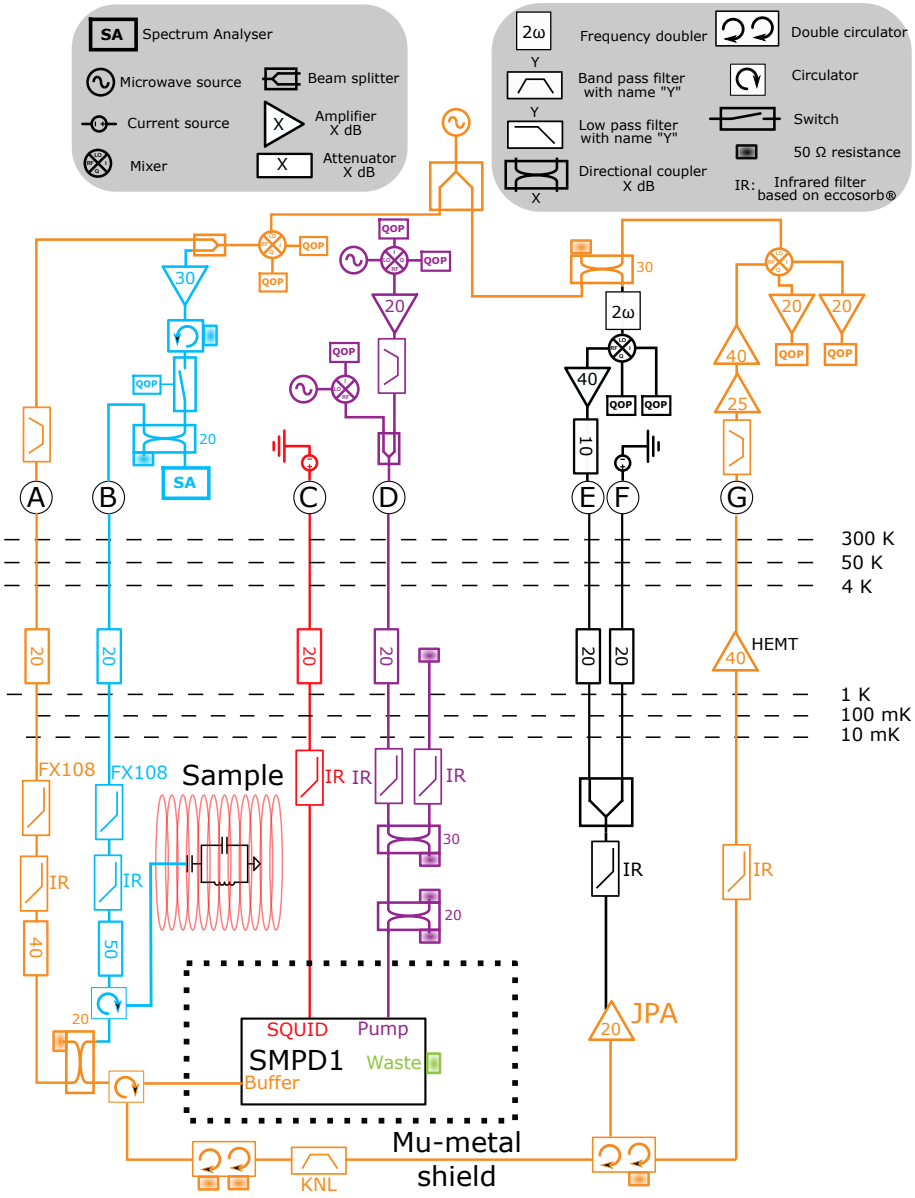

Figure 6.5: **Microwave setup 1.** Schematic of setup 1 microwave components where the label from A to G distinguish the room temperature setup (top part) from the cryogenic setup (bottom part). The microwave lines are colored accordingly to their corresponding detection step. The sample is inserted in a coil (red) to produce B_0. A device name is associated to each filter to help readers to find their characteristics.

6.2.1 Microwaves setup for ESR experiment

Experimentally, to shape the microwave pulses as well as to acquire the spin signal, we use electronic devices to convert analog to digital and digital to analog signal. This kind of device have a typical bandwidth of ~ 200 MHz and therefore cannot be directly used to shape and acquire a field at a frequency in the GHz range. To overcome this practical issue, we use I/Q mixers to perform a modulation/demodulation procedure, where I and Q stands for the 2 field quadratures at the mixer. The quadrature acquisition is done on I and Q, which can be related to the echo natural quadrature X and Y if the amplification is calibrated. For the modulation, a Local Oscillator (LO) converts the pulse sequence generated at an Intermediate Frequency (IF) $\omega_{\text{IF}}/2\pi = 100$ MHz into a signal at the required frequency $\omega/2\pi$. In order to preserve the signal phase, demodulation is done with

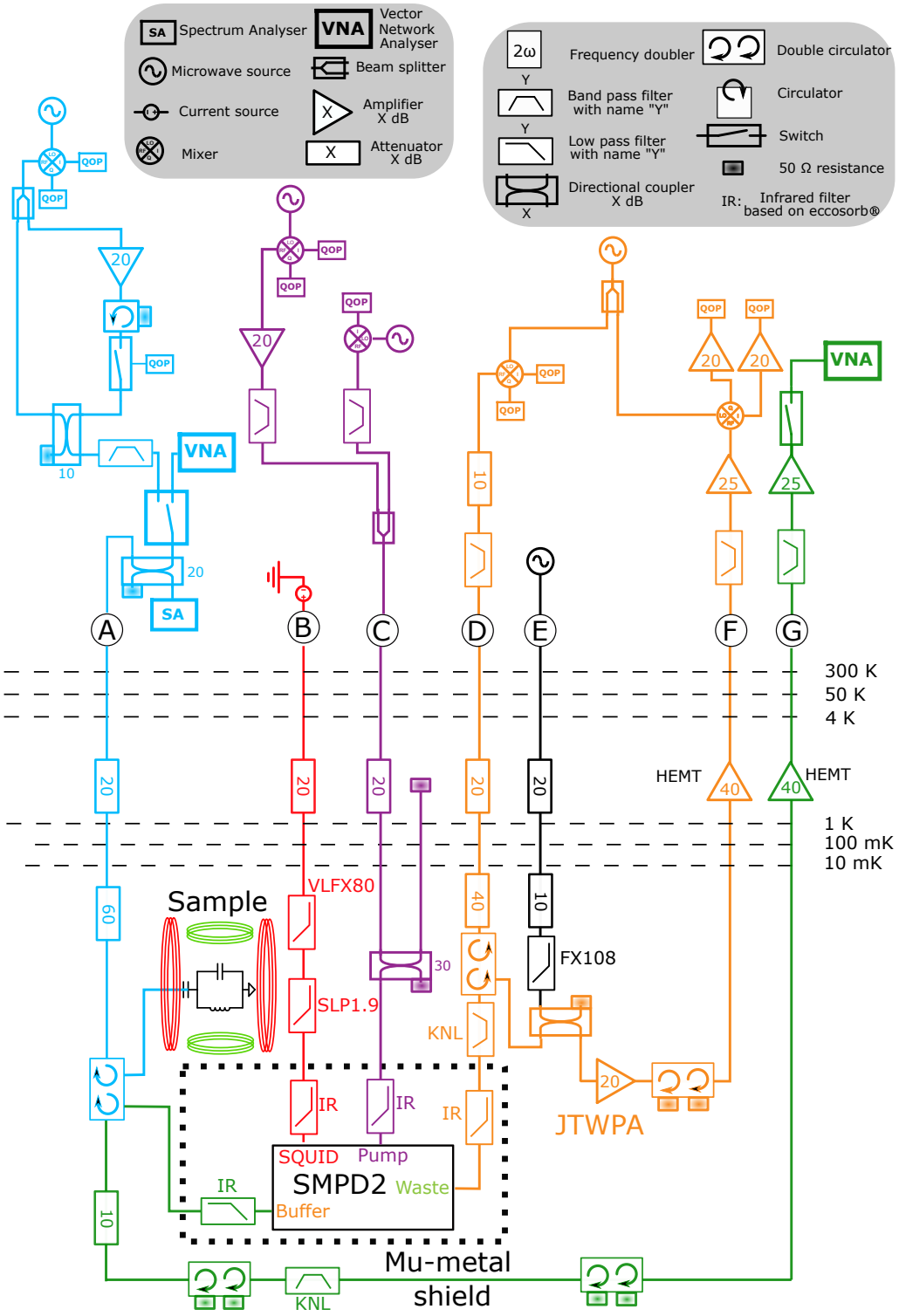

Figure 6.6: **Microwave setup 2.** Schematic of setup 2 microwave components where the label from A to G distinguish the room temperature setup (top part) from the cryogenic setup (bottom part). The microwave lines are colored accordingly to their corresponding detection step. The sample is inserted inside two Helmotz coils (red and green) that can generate a field in any desired direction within the (a, b)-plane. A device name is associated to each filter to help readers to find their characteristics.

the same LO than the corresponding pulse modulation: in ID-ESR it corresponds to the spin excitation pulses that will trigger the spin echo, whereas in FD-ESR it corresponds to the read out pulse sent to a SMPD port. To control our whole experiment, we operate a Quantum Orchestration Platform (QOP) made by Quantum Machine® that acts as a pulse generator of both analog and digital signal as well as an acquisition apparatus. The QOP is based on a Fast Programmable Gate Array, which allows to have quick feedback on the experiment status. This is in particular needed to perform the conditional SMPD reset.

In the dilution cryostat, all the microwave components are cooled down to a temperature of ~ 10 mK. However, the electromagnetic field is not necessarily thermalized at ~ 10 mK since it is directly connected through the microwave lines to higher temperature stages. In order to keep the field thermal population as low as possible, we put attenuators in the input lines and circulators in the output lines. In the lines where we use strong pulses, such as the SMPD pump line, we use directional couplers and $50\,\Omega$ impedance to damp the field without warming up the cryostat. Moreover, we insert filters to let through only the frequency of interest. In particular, we filter out the infrared field known to trigger quasi particles excitation within the superconductor. As amplifiers typically emit permanently photons at their output, the line used for spin excitation that is amplified is connected to the cryostat through a switch that allows the connection only during excitation pulse. A good thermalization of the lines is particularly critical for the SMPD, as it is directly related to its dark counts rate.

The signal collected in the cryostat is amplified through a full amplification chain before its acquisition, typically consisting in a parametric amplifier, a High Electron Mobility Transistor (HEMT) and low noise amplifiers at room temperature.

The sample is inserted in coils to produce the static field B_0. As this field would be detrimental to the SMPD, The SMPD and the sample are spatially separated and connected through a microwave cable. In addition, the SMPD sample holder is put in a Mu-metal shield.

In the figures Figure 6.5 and Figure 6.6, the colors are associated to the ESR detection steps:

- Spin excitation: we generate a pulse sequence at frequency $\omega_0/2\pi$ and send it to the sample. A Spectrum Analyser (SA) allows to measure the pulse amplitude before the cryostat input.
- Buffer frequency tuning: we pass a DC current to tune the buffer frequency on resonance, or out of resonance, with the spins.
- SMPD mode conversion and qubit reset: during the SMPD detection step we generate the pump tone at frequency $\omega_p/2\pi$ to convert an incoming photon into a qubit excitation, while during the SMPD reset step we generate a qubit π pulse at frequency $\omega_q/2\pi$.
- **Parametric amplification**: we send a microwave tone to the parametric amplifier to amplify the signal with a quantum limited noise.
- Spin detection: for FD-ESR, we send a read out pulse to a SMPD port, then amplify and acquire it to observe the qubit state. For ID-ESR, we directly amplify the echo coming from the spin

6.2.2 Setup 1

The setup 1 full description is visible in Figure 6.5. This setup allows to perform both FD-ESR and ID-ESR, as the sample is connected to the SMPD and a parametric amplifier.

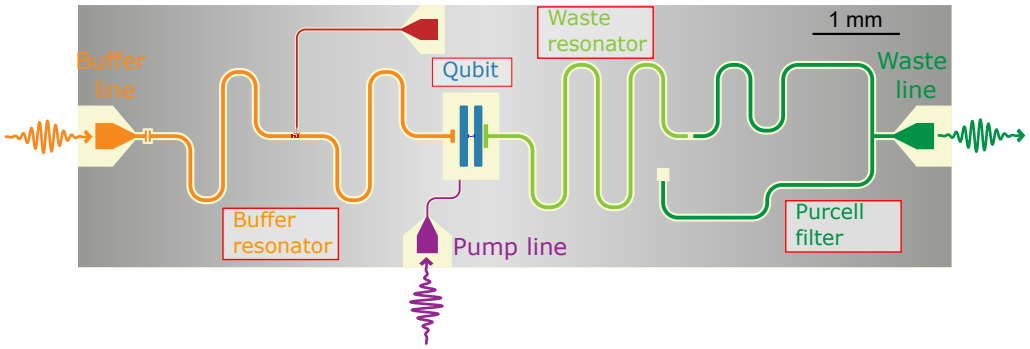

Figure 6.7: **SMPD1.** Picture of the SMPD1 chip with its various elements: the buffer resonator connected to the buffer line (orange), the buffer's SQUID line (red), the qubit (blue), the pump line (violet) and the waste resonator connected to the waste line through a Purcell filer (green).

For FD-ESR, the SMPD buffer frequency is tuned on resonance with the spins to detect the spin signal while for ID-ESR, it is tuned out of resonance to simply reflect the spin signal. The SMPD read out is performed through the buffer resonator. In this setup, the coil is a simple solenoid, therefore the angle φ cannot be varied, and all the measurements are done at $\varphi = \varphi_c = 47\,^\circ$.

In setup 1, SMPD1 comes from a first generation of SMPD made of Aluminum on Silicon with a design shown in Figure 6.7. Each SMPD element, described in Section 4.2.2.2, is visible here. In addition, there is a resonator called Purcell filter that couples the waste resonator with the external lines, which limits the qubit effective coupling to this line and therefore its Purcell relaxation rate.

The SMPD1 figures of merit are:

- **Dark Count rate**: $\alpha = 1500 \pm 200\,\text{counts/s}$
- **Conversion efficiency**: $\eta_{\text{SMP}D} = 0.45$
- **Duty cycle**: $\eta_{\text{dc}} = 0.58$

The SMPD1 was fabricated by Emanuele Albertinale. More details can be found in [Alb21].

In setup 1, we have exclusively studied Er^{3+}:$CaWO_4$. Using this setup, we have detected the spin fluorescence signal for various excitation strength and reproduced it using simulations (Section 7.2). Thanks to the possibility to do measurements both in ID-ESR and FD-ESR, we have quantitatively compared the SNR of those two detection methods used for spin detection in similar spin excitation conditions (Section 7.3). We have measured spin frequency shifts caused by mechanical strain and driven a small spin sub-ensemble into coherent oscillations (Section 8.2.3). Eventually, we have compared the SNR of the two detection methods for spin echo detection (Section 9.3).

6.2.3 Setup 2

The setup 2 full description is visible in Figure 6.6. In this setup, we can perform only FD-ESR (since there is no parametric amplifier after the SMPD). The SMPD read out is done through the waste resonator. The sample is put within two Helmotz coils that can generate a field in an arbitrary direction in the (a, b)-plane.

In setup 2, SMPD2 comes from the second generation of SMPD, made of Tantalum on Sapphire for all its elements except from the Josephson junctions, still made of Aluminum. This change in material is meant to increase the qubit T_1 [Pla+21], that indeed improved from $T_{1,\text{setup1}} \approx 7\,\mu\text{s}$ in 1^{st} generation of SMPD to $T_{1,\text{setup2}} \approx 15\,\mu\text{s}$ in the 2^{nd} generation.

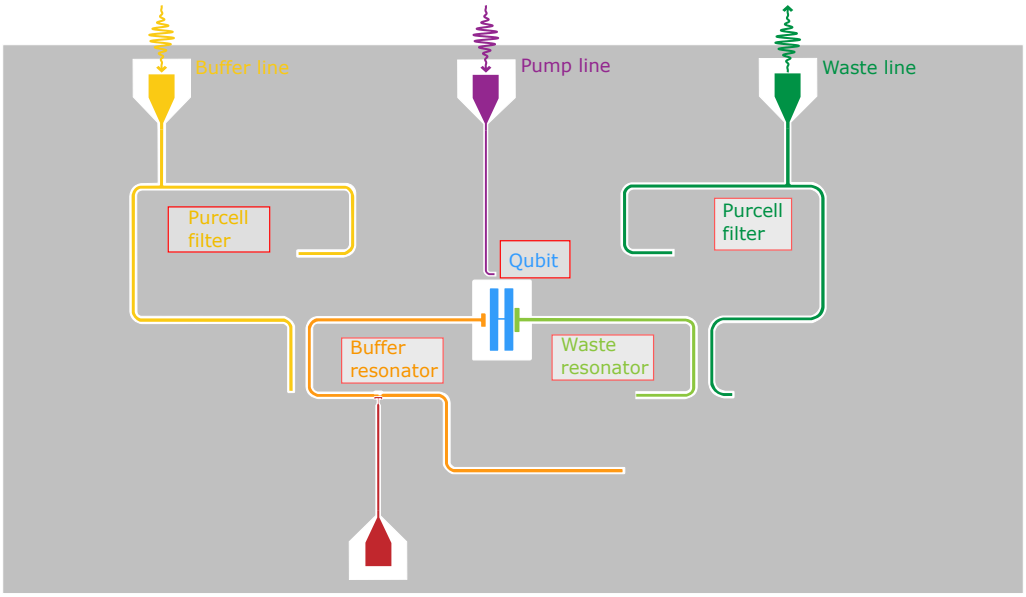

Figure 6.8: **SMPD2.** Picture of the SMPD2 chip with its various elements: the buffer resonator connected to the buffer line thorugh a Purcell filter (orange), the buffer's SQUID line (red), the qubit (blue), the pump line (violet) and the waste resonator connected to the waste line through a Purcell filer (green).

As can be seen in Figure 6.8, the SMPD chip has also an additional Purcell filter fabricated in front of the buffer line. Eventually, the SMPD sample holder has evolved to improve the chip thermalization and to incorporate the infrared filters.

The SMPD2 figures of merit are:

- **Dark count rate**: $\alpha = 500 \pm 200\,\text{counts/s}$
- **Conversion efficiency**: $\eta_{\text{SMPD}} = 0.4$
- **Duty cycle**: $\eta_{\text{dc}} = 0.78$

The SMPD2 has the particularity to have a pump frequency $\omega_{\text{p}}/2\pi = 6.990$ GHZ very close to the buffer frequency $\omega_{\text{b}}/2\pi = 6.999$ GHz. In consequence of this frequency collision, part of the pump photons likely leaks towards the buffer and contributes to the value of α. This phenomenon is particularly visible when the resonator frequency decreases, as is visible at high values of magnetic field in the large range spectroscopy shown in Section 7.1.

The SMPD 2 was fabricated by Léo Balembois. More details can be found in article and PhD manuscript to be published soon.

In setup 2, we have measured large-scale FD-ESR spectra showing signal from a wide variety of spin species and we have noticed the interest of the fluorescence curve in spin characterization (Section 7.1). We have observed again the spin frequency shifts caused by mechanical strain and studied its dependence with the static field angle (Section 8.1). We have examined a spin sub-ensemble coherent oscillation dependence with the magnetic field (Section 8.2). Eventually, we have characterized the spin coherence times using FD-ESR (Section 9.1 and Section 9.2).

6.3 Typical experimental spin signal

Here, we describe typical ESR measurements and introduce the interesting physical quantities.

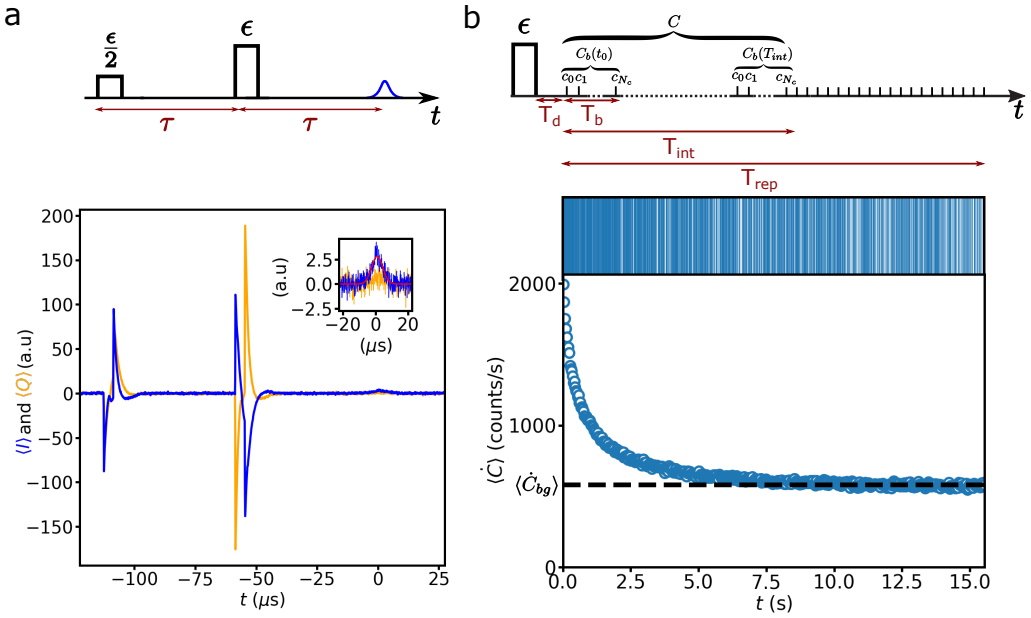

Figure 6.9: **ID-ESR and FD-ESR curves a**, ID-ESR sequence representation and typical experimental curve with the two quadratures (I in blue, Q in orange) plotted in arbitrary unit, showing a spin echo at $t = 0$. In the inset, zoom on the echo with a gaussian fit (red) yielding the echo mode. **b**. FD-ESR sequence representation and typical experimental data. Top panel: manipulation sequence to detect spin fluorescence where we send at $t = 0$ an excitation pulse of strength ϵ (black rectangle), wait a dead time T_{d}, then we cycle the SMPD over a time T_{rep} (vertical bars). The SMPD clicks are treated (quantities on top) over various time (arrows at the bottom) as binned click probability or as integrated counts. Middle panel: SMPD clicks (vertical bars) following a spin excitation pulse, where we see a higher click probability just after the pulse. Bottom panel: averaged count rate $\langle \dot{C} \rangle$ that relaxes down to $\langle \dot{C}_{bg} \rangle$ (dashed line).

6.3.1 Inductive detection

A typical spin echo trace detected with ID-ESR following a Hahn echo sequence, as well as a schematic of the pulse sequence, is shown in Figure 6.9a.

For pulses of amplitude β and duration Δt, we define the pulse strength as $\epsilon = \beta \times \Delta t$, which gives an excitation sequence: $\epsilon/2_X - \tau - \epsilon_Y - \tau -$ echo. We detect the quadratures I and Q during the whole sequence. Since in most ID-ESR experiment the gain in the amplification chain between the sample and the detection apparatus is not calibrated, we cannot relate the signal amplitude to an absolute echo field amplitude. Therefore, the resulting quadratures are plotted in arbitrary unit. The curves clearly show the 2 excitation pulses as strong signals separated in time by $\tau = 50\,\mu$s. In addition, a zoom around $t = 0$ shows the spin echo, mostly appearing in the I quadrature.

As the signal presented here has been averaged over several iterations, the spin polarization depends on the time duration during which we let the spins relax before iterating the experiment, namely the pulse sequence repetition rate T_{rep}. So as to have a large signal, T_{rep} should be large compared to the spin relaxation time T_1.

In order to extract a quantity proportional to the number of contributing spin, we integrate the spin echo along the echo mode $u(t)$. A Gaussian fit allows to extract $u(t)$ and then to perform the integration Equation 4.3.1.1. The resulting quantity $\langle \hat{I}_e \rangle$ is proportional to the spin echo $\langle \hat{X}_e \rangle$, although in most ID-ESR experiment $\langle \hat{I}_e \rangle$ is also computed in arbitrary unit as the amplification chain is not calibrated. However, we will see in Section 7.3.1.1 that the SMPD allows to measure the number of photons in the echo

mode, and so gives access to the echo absolute amplitude.

6.3.2 Fluorescence detection

A typical spin fluorescence trace following an excitation pulse applied at $t = 0$, as well as a schematic of the signal treatment, is shown in Figure 6.9b.

As detailed in Section 3.3.2.1 and Section 4.2, we detect with FD-ESR the photons emitted by the spins following an excitation pulse sequence (for instance, a single pulse, as shown in Figure 6.9b). After reflecting on the spin resonator sample, the pulse reaches the SMPD input, which strongly perturbs its operation during a certain time. We find empirically that the SMPD recovers after a dead-time $T_\mathrm{d} = 50\,\mu$s, which is negligibly short compared to the fluorescence timescales that we are considering here. In this thesis, all the FD measurements are taken after this dead time.

The SMPD click output c_j, which is either 0 or 1, of cycle j at cycle time t_j shows an excess of photons following the pulse, which decays over a characteristic time T_charac. The SMPD clicks are coarse grained in bins of N_c cycles, corresponding to a bin time T_b, to compute a binned click probability $C_\mathrm{b}(t) = 1/N_\mathrm{c} \sum_{t \leq t_j \leq t+T_b} c_j$. The grain size is chosen depending on the signal such that $T_\mathrm{b} \ll T_\mathrm{charac}$.

From that, we deduce the count rate $\dot{C} = C_\mathrm{b}(t) N_\mathrm{c}/T_\mathrm{b}$. The signal is averaged over several iterations, yielding $\langle \dot{C} \rangle$. The SMPD cycle keeps on going for the whole duration T_rep between two successive pulse sequence. The average count rate relaxes down to the background rate $\langle \dot{C_\mathrm{bg}} \rangle = \langle \dot{C}(t = T_\mathrm{rep}) \rangle$.

To extract a single value from a spin fluorescence curve, we sum the counts over an integration time T_int to obtain the integrated counts $\langle C \rangle = \sum_{0 \leq t_j \leq T_\mathrm{int}} \langle C_\mathrm{b}(t_j) \rangle$. The choice of the integration time T_int is important to optimize the signal-to-noise ratio, as will be detailled in Section 7.3.

However, since part of the photons integrated are dark counts, $\langle C \rangle$ is not directly proportional to the contributing spin number. The background contributions can be subtracted in order to get

$$\langle C_\mathrm{spin} \rangle = \sum_{0 \leq t_j \leq T_\mathrm{int}} \langle C_\mathrm{b}(t_j) \rangle - \langle \dot{C_\mathrm{bg}} \rangle T_\mathrm{int}, \tag{6.1}$$

a quantity proportional to the spin number. One should keep in mind that the background subtraction also removes the contribution of spins that have not reached steady-state at $t = T_\mathrm{rep}$.

Chapter 7

Fluorescence detection as a high sensitivity spectroscopy method

In this chapter, we present FD-ESR spectroscopy measurements of the Scheelite sample. Using the signal from Er^{3+}, we provide a quantitative analysis of the fluorescence curves. We also compare the SNR of ID-ESR and FD-ESR and find a significant sensitivity improvement for small numbers of excited spins.

7.1 Spin spectroscopy using fluorescence detection

Here we report the first large scale spectra done with FD-ESR where several spin species are detected. This result confirms the potential application of FD-ESR to characterize a large variety of spin species.

7.1.1 Spectroscopy over a large range of magnetic field

In a first set of experiments, we perform FD-ESR on the Scheelite sample over a magnetic field range of ≈ 90 mT, at $\varphi = 37°$. For each value of B_0, we apply an excitation pulse and record the subsequent integrated number of counts. The procedure is repeated 50 times to average the signal, resulting in a $\langle C(B_0) \rangle$ curve shown in Figure 7.1. Since the small B_0 out-of plane component is expected to shift the resonator frequency, we adapt every 0.5 mT the pulse frequency and the SMPD detection frequency. Among the lines visible in this spectrum, we attribute some of them to known spin species.

We can attribute some lines to the Ytterbium ion: the two peaks at $B_0 = 87.5$ mT and $B_0 = 95.4$ mT correspond to the $m_I = -5/2$ and $m_I = -3/2$ transitions of $^{173}Yb^{+3}$, the peak at $B_0 = 101.01$ mT corresponds to the $m_I = -1/2$ transition of $^{171}Yb^{+3}$ and the peak at $B_0 = 127.75$ mT corresponds to the Ytterbium line $I = 0$. The other transitions of the $^{173}Yb^{+3}$ isotopes are not visible, likely due to the polarization of the ground-state manifold at 10 mK. Since we observe two transitions, their relative amplitude gives access to the spins effective temperature T_{eff} using Equation 5.12. To properly compare those peaks, we subtract to the spin signal the dark count rate $\alpha = 330$ counts/s, computed by averaging $\dot{C}$ over a magnetic range without spin signal $B_0 \in [50.5, 51.5]$ mT to mitigate the background fluctuations. Also, as detailed below, the two transitions have different relaxation times, each longer than $T_{\text{rep}} = 2$ s, that need to be taken into account to properly compare the peaks amplitude. All in all, we compute $T_{\text{eff}} = 40$ mK.

Similarly, we can associate two lines to the Erbium ion: one small amplitude peak at $B_0 = 52.15$ mT is the $m_I = -1/2$ transition of $^{167}Er^{+3}$ and a large amplitude peak at $B_0 = 59.75$ mT is the $I = 0$ transition. The other transitions of the $^{167}Er^{+3}$ isotopes are not visible, again likely due to the polarization of the ground-state manifold.

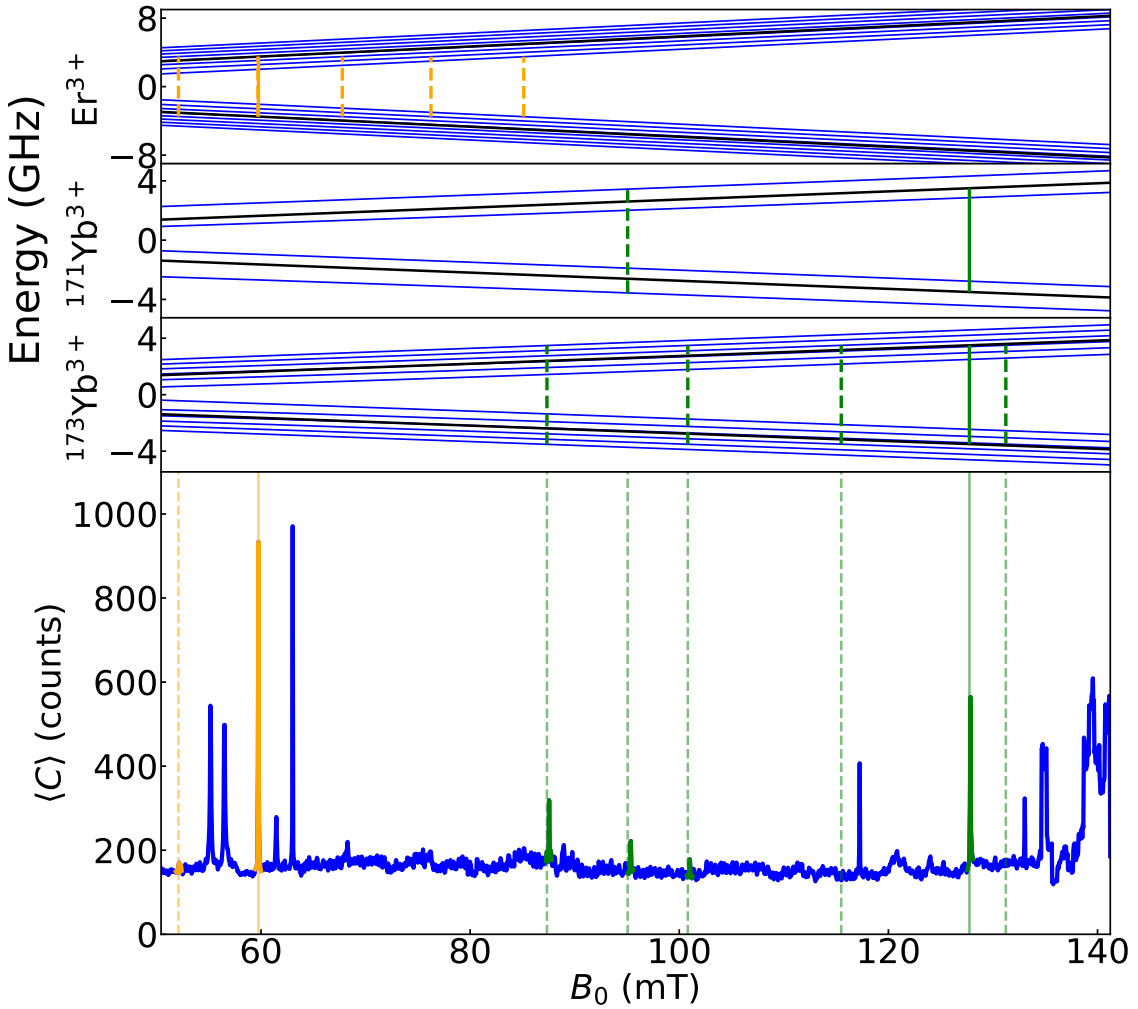

Figure 7.1: **Large B_0 range spectroscopy (setup 2).** In the bottom panel is plotted the integrated counts $\langle C \rangle$ over a time $T_{\text{int}} = 450$ ms as a function of B_0, varying between 50.5 to 141 mT by step of 0.05 mT with $\varphi = 37°$. The excitation pulse has an amplitude $\beta = 117\,\text{ns}^{-1/2}$ and duration $\Delta t = 5\,\mu s$, with a repetition time $T_{\text{rep}} = 2$ s. Every 0.5 mT, we calibrate the pulse frequency and SMPD detection frequency to follow the shift in the resonator frequency due to B_0. The acquisition of this spectrum took 68h. In the top panel is plotted the computed energy levels of Er^{3+}, $^{171}Yb^{3+}$ and $^{173}Yb^{3+}$ according to B_0, with (blue) and without (black) nuclear spin hyperfine interaction. The corresponding transition at $\omega_0/2\pi$ are vertical bars, filled when $I = 0$ and dashed when $I \neq 0$. The bars are prolonged up to the data, where the colors (orange for Er^{3+}, green for Yb^{3+}) and the position in B_0 allow to recognize the transitions.

We use the Er^{+3} line $I = 0$ to calibrate our coils, given its known gyromagnetic tensor as well as the sample orientation. We then check that the position of the Yb^{3+} line $I = 0$ coincides with the theoretical expectations to better than 10^{-1} mT, thus validating our coil calibration procedure.

In addition to the Er^{3+} and Yb^{3+} peaks, several other lines are observed. One of them is close to the value expected for Fe^{3+} ($g \simeq 4.3$). However, several considerations prevent us from attributing this peak to Fe^{3+}. First, we observe only one line, instead of the expected 4 closely spaced lines. Second, the $g = 4.3$ line is generally attributed to the middle Kramers doublet of Fe^{3+}, which should not be populated at all at a temperature close to 10 mK.

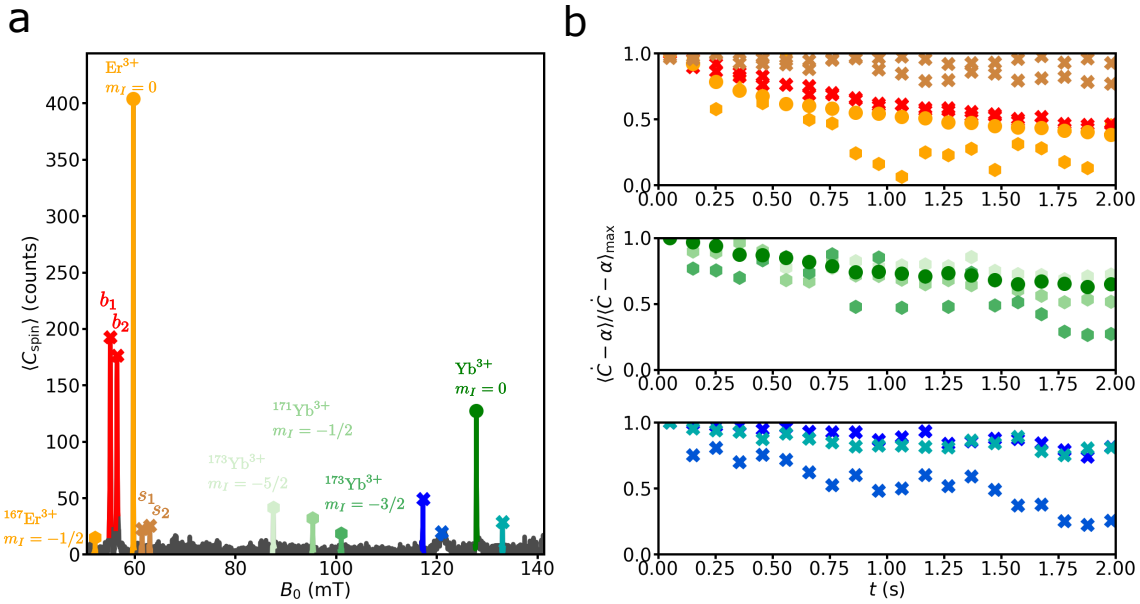

Figure 7.2: **Spectroscopy with background removal and peaks fluorescence curve (setup 2).** Same data than Figure 7.1 **a**, $\langle C_{\text{spin}} \rangle$ as a function of B_0, with the background rate $\langle C_{bg} \rangle$ averaged over the time window $[1.6 : 2]$ s. The peaks colors allow to recognize the fluorescence curves, associated to various maker shape (circle for $I = 0$, hexagon for $I \neq 0$, crosses for unknown peaks). The peaks attributed are labeled. **b**, normalized fluorescence curves with dark count subtracted for each colored peak in the spectrum. Top panel: fluorescence curves of the 6 peaks at low B_0: in orange is Er^{3+} with circle (hexagon) for $I = 0$ ($I \neq 0$), in red are two peaks labeled b_1 and b_2 with a fluorescence curve similar than Er^{3+} with $I = 0$, and in brown are two peaks labeled s_1 and s_2 with a slow relaxation rate compared to Er^{3+}. Middle panel: fluorescence curves of the Yb^{3+} peaks with circle (hexagon) for $I = 0$ ($I \neq 0$). The hyperfine peaks are recognizable through their various shade. Bottom panel: fluorescence curves of the 3 remaining unknown peaks.

The spectrum Figure 7.1 shows a large instability at $B_0 > 135$ mT. We understand it as due to the frequency proximity at high B_0 between the SMPD buffer resonance, that is shifted downward with B_0 along with the sample resonator by up to 1.5 MHz, and the SMPD pump, as discussed in Section 6.2.3.

In order to distinguish clearly the meaningful spin peaks from the background fluctuations, we have subtracted in Figure 7.2a at each B_0 the background contribution, as explained in Section 6.3.2. In cases where the spins have not entirely decayed at a time T_{rep}, this background-subtraction procedure effectively removes part of the signal and therefore affects the peak height. Because the fluorescence decay time depends on the spin species, this can result in a drastic change in the relative peak amplitude. This is clearly visible when comparing Figure 7.1 and Figure 7.2a.

In addition to the peak position and height, FD-ESR spectroscopy automatically gives access to the shape of the fluorescence decay curve, which bears a number of information about the spin properties that are not readily available in ID-ESR. Indeed, as explained in Section 3.3.3, this shape in the most general case depends non-trivially on the pulse excitation power, and on the spin radiative and non-radiative relaxation rates. Nevertheless, as explained in Section 5.2.2, in the high-power limit the long-time decay is dominated by the non radiative spin-lattice relaxation. It is thus worthwhile to examine the various fluorescence curves of each species to access this non radiative relaxation rate. They are plotted in Figure 7.2b with the dark count rate α subtracted to each of them. We have chosen to organize these data in 3 groups :

- Top panel shows the 6 low-field lines in the Er^{3+} region. On the Erbium, we observe that the relaxation of the $m_I = -1/2$ line of $^{167}Er^{3+}$ is faster than the $I = 0$, as expected from the spin-lattice relaxation (Section 5.2.2). A pair of peaks, in red in the figure and called in the following b_1 and b_2, shows a fluorescence decay very similar as the Er^{3+} line $I = 0$, which indicates that they might be related to Erbium. They could come from Er^{3+} ions with a specificity in their local environment that breaks the $S4$ symmetry, such as a charge compensation. The other pair of peaks, in brown in the figure and called in the following s_1 and s_2, have a very slow relaxation rate that explains why their amplitude is strongly reduced by the background removal procedure. Since transition metal ions have usually lower spin-lattice relaxation rates than REI, it is possible that these peaks originate from transition metal ion paramagnetic species.

- Middle panel shows the Yb^{3+} lines. The decay rate of the $I = 0$ line is similar to the decay rate of the $^{173}Yb^{3+}$ line $m_I = -5/2$ and the $^{171}Yb^{3+}$ line $m_I = -1/2$. On the other hand, the ^{173}Yb line $m_I = -3/2$ has a faster relaxation. This behavior is consistent with the so-called hyperfine effect in the REI spin-lattice relaxation (see Section 5.2.2).

- Bottom panel shows the 3 last unknown peaks. Two of them, among which the peak close to the expected Fe^{3+} peak, have a rather slow relaxation rate close to the s_1 and s_2 peaks relaxation rate, therefore we also suggest that they come from transition metal ion spins. On the other end, the last peak has a relaxation rate similar than the Er^{3+} line $I = 0$ and the Yb^{3+} line $I = 0$, suggesting a possible REI origin.

7.1.2 Rotation pattern spectroscopy

In Figure 7.3, we show a rotation pattern measured with FD-ESR where we vary the field amplitude B_0 and orientation φ both without and with background subtraction, plotting respectively $\langle C \rangle$ and $\langle C_{\text{spin}} \rangle$. The peaks position angular dependence gives access to the spin species gyromagnetic factor in the (a, b)-plane. We observe that some peaks have their mean B_0 field position independent of φ; they obey the $S4$ symmetry that is expected for paramagnetic ions replacing a Ca^{2+} ion. On the other hand, the position of some other peaks is seen to strongly depend on φ, revealing that they do not follow $S4$ symmetry. We also see some spikes appearing rarely and randomly; we attribute them to a rare and sudden change in the SMPD properties, such as at $\varphi = 26\,^\circ$ and $B \approx 53$ mT, possibly due to fluctuations of the properties of the transmon qubit. We take the rotation pattern in a magnetic range with $B_0 < 91$ mT to avoid reaching a coil quenching current. We notice larger fluctuations and a rise in background at high magnetic field, again likely due to the frequency collision between the pump and the buffer, as the buffer frequency is shifted downward by up to 1.2 MHz (Section 6.2.3).

Among the $S4$-symmetric peaks, we retrieve the Er^{3+} lines $I = 0$ and $m_I = -1/2$, as well as the ^{173}Yb with $m_I = -5/2$ peak. If the peaks mean position remain fixed, their amplitude and width appear to be strongly dependent on φ. The φ-dependent linewidth is explained by the effect of the inhomogeneously distributed charged impurity background, as explained in Section 5.2.1.2. This linewidth modulation also partly explains the observed peak amplitude dependence on φ. Another effect comes into play: the coupling constant g_0, hence the radiative rate Γ_R and also the integrated number of counts $\langle C \rangle$, depend on φ. The linewidth evolution of the Er^{3+} line $I = 0$ is detailed in Section 7.1.3.

The pair of peaks on each side of the $I = 0$ Erbium at $\varphi \approx 37\,^\circ$ are also visible in this spectrum, showing a strong dependence of their resonance field with φ. The peaks b_1 and b_2 increase in field resonance as φ decreases and get too high in field resonance to be seen when $\varphi < 0$. At the angles $\varphi < 0$, another pair of peaks appear and decrease in field

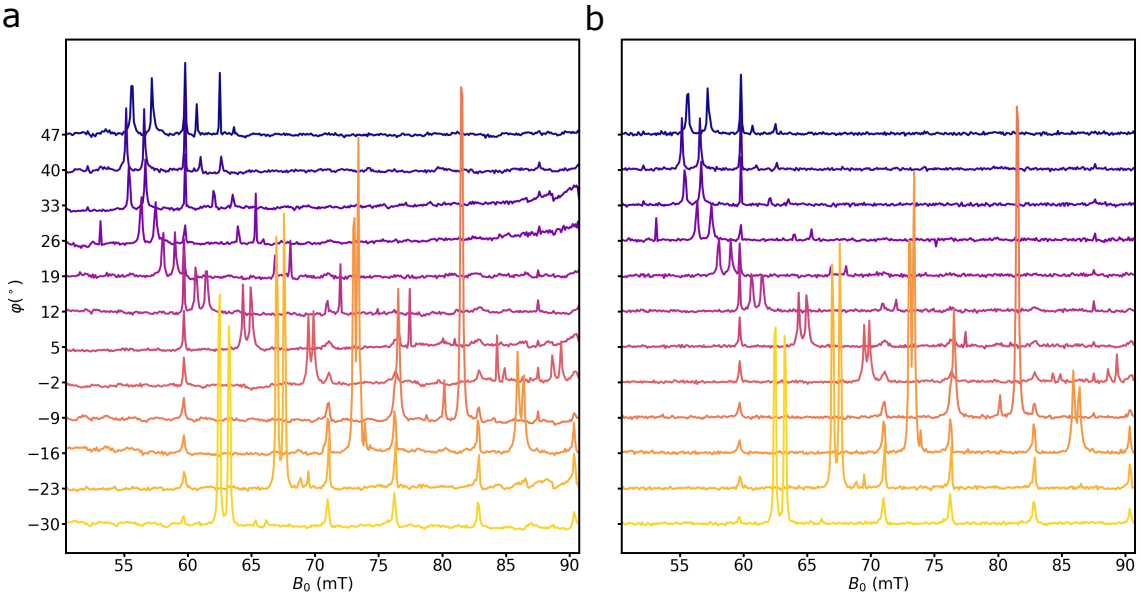

Figure 7.3: **Rotation pattern spectroscopy, with varying B_0 and φ (setup 2). a**, integrated counts $\langle C \rangle$ over a time $T_{\text{int}} = 450$ ms as a function of B_0, varying between 50.5 to 90.8 mT by step of 0.1 mT, and φ, varying between $-30\,^\circ$ to $47\,^\circ$ by step of $7\,^\circ$. The excitation pulse has $\beta = 58\,\text{ns}^{-1/2}$ and $\Delta t = 3\,\mu s$, with a repetition time $T_{\text{rep}} = 5$ s. Every 2 mT, we calibrate the pulse frequency and SMPD detection frequency to follow the shift in the resonator frequency due to B_0. The acquisition of this rotation pattern took 100 h. **b**, same data with background subtraction, plotting $\langle C_{\text{spin}} \rangle$. The background rate $\langle C_{\text{bg}} \rangle$ is defined for each magnetic field parameter as the mean value of $\langle C \rangle$ over the time window $[4, 5]$ s.

resonance as φ decreases. Those two pairs of peaks have a similar amplitude modification as we subtract the background, indicating similar decay time. A possible explanation of those two pairs of peaks is that they arise from a replacement a Tungsten atom close to the Erbium ion, for instance by a vacancy. This modification would give rise to two pairs of ESR line showing an approximate $90\,^\circ$ symmetry with one another [MG67].

We observe 4 peaks at $B_0 \in [70.4, 75.6, 82.1, 89.6]$ mT that obey the $S4$ symmetry, that we name in the following l_i with $i \in [1, 2, 3, 4]$.$The se peaks are only visible for \varphi \in [-30, 12]\,^\circ$, which explains that they do not appear in Figure 7.1. Note however that, due to the limited range of our scan, we cannot exclude that related extra peaks can be found at higher B_0.

To illustrate once again the interest of the access to the spin fluorescence curve, we single out in Figure 7.4a the spectrum with background subtracted at $\varphi = -2\,^\circ$. We compute the experiment dark count rate $\alpha = 430$ counts/s using the average rate in the field range $B_0 \in [50.5 : 58.5]$ mT where no peaks are visible. We associate the lines visible in the spectrum in three groups and plot their fluorescence curves after subtracting α, yielding the curves visible in Figure 7.4b:

- Top panel: we plot together the peaks previously seen in Figure 7.1. We recognize the Er^{3+} line $I = 0$ at $B_0 \approx 59.8$ mT, the pair of peaks b_1 and b_2 at $B_0 \approx 70$ mT and the $^{173}Yb^{3+}$ line $m_I = -5/2$. We find again a striking similarity in the Erbium fluorescence curve with the b_1 and b_2 fluorescence curves, whereas the $^{173}Yb^{3+}$ relaxes slower.

- Middle panel: we plot together the peaks at $B_0 \in [70.4, 75.6, 82.1, 89.6]$ mT that we believe to belong to the same spin species. A natural hypothesis would be that the 4 peaks arise due to the hyperfine coupling of a paramagnetic species with a

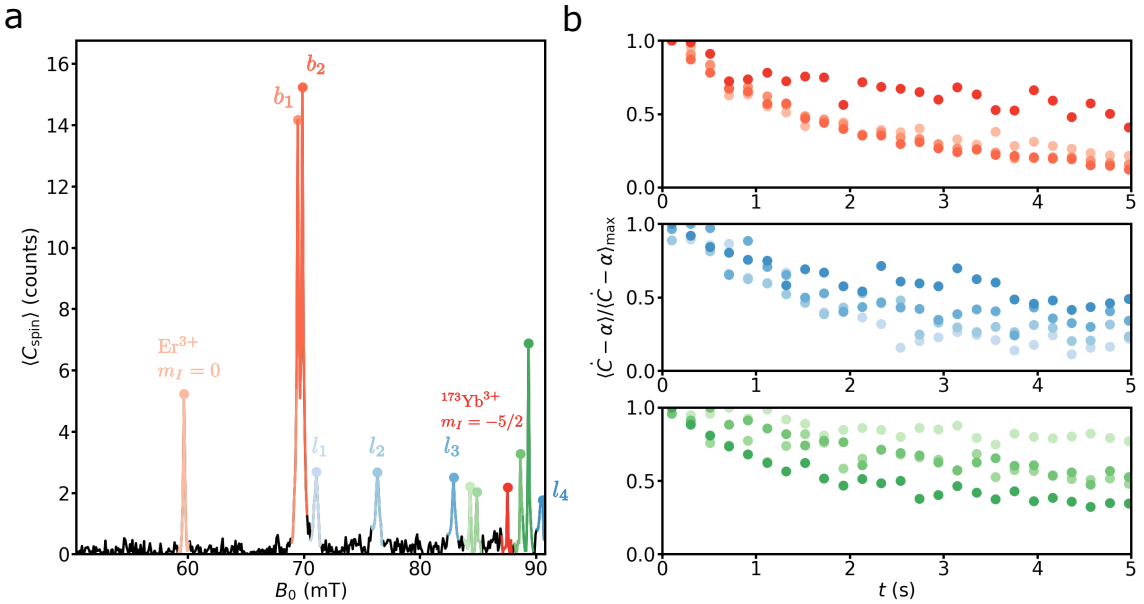

Figure 7.4: **Spectroscopy at $\varphi = -2\,^\circ$ and peaks fluorescence curves (setup 2).** Same data than Figure 7.3 **a**, $\langle C_{\text{spin}} \rangle$ as a function of B_0 at $\varphi = -2\,^\circ$, also visible in Figure 7.3b. The peaks color and shade allow to recognize the fluorescence curves. The peaks attributed are labeled. **b**, normalized fluorescence curves with dark count subtracted for each colored peak in the spectrum to compare their relaxation shape. Top panel: fluorescence curves of the 4 peaks seen in the previous spectrum: Er^{3+} line $I = 0$,^{173}Yb line $m_I = -5/2$, b_1 and b_2 lines. Middle panel: fluorescence curves of the peaks l_i with $i \in [1, 2, 3, 4]$. Bottom panel: fluorescence curves of the remaining unknown peaks.

nuclear spin. Several observations are however not entirely consistent with this attribution. First, all 4 peaks have approximately the same amplitude, whereas one would expect some differences due to polarization of the manifold ground state at thermal equilibrium. Also, from the hyperfine effect in spin-lattice relaxation, one would expect the relaxation of peaks l_2 and l_3 to be faster than peak l_1, whereas we observe the opposite. We finally note that peak l_1 relaxes even faster than Er^{3+}, and thus shows an appreciable spin-lattice coupling, possibly indicating a REI origin.

- Bottom panel: we plot together the remaining unknown peaks. The fluorescence curve gives additional information on each line, however we cannot conclude on their source.

The recognition of all the peaks requires additional work that falls out of the scope of this thesis, but the information within this rotation pattern is a proof of the characterization possibility of the FD-ESR method.

Note that in the spectrum, spikes may arise due to random events leading to qubit excitation over long times. Such event is visible in Figure 7.5 where we have plotted two successive count rate traces, with one showing a clear sudden spike reaching $\dot{C} \approx 15000$ counts/s and relaxing over a time scale of the order 1 s. This kind of even possibly arises due to some high-energy particle impact on the chip.

To sum up all the spectroscopic information we have on this sample, we compare this rotation pattern to one measured prior to this thesis using the ID-ESR. As can be seen in Figure 7.6a, FD-ESR and ID-ESR angular dependence spectra show very similar features: both show peaks with a S4 symmetry such as the Er^{3+} line $I = 0$ as well as lines varying with the field orientation like the pair of peaks b_1 and b_2 as well as s_1 and s_2. This similarity confirms that FD-ESR yields the same spectroscopic information than ID-ESR.

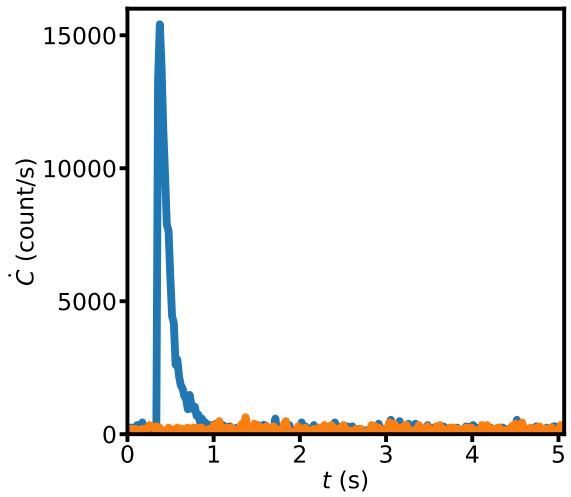

Figure 7.5: **Single shot count rate curves at $B_0 = 53.1$ mT and $\varphi = 26\,^\circ$ (setup 2).** Two successive single shot traces of $\dot{C}$ as a function of time, where one curve (blue) shows a strong peak uncorrelated from the spin excitation pulse happening at $t = 0$.

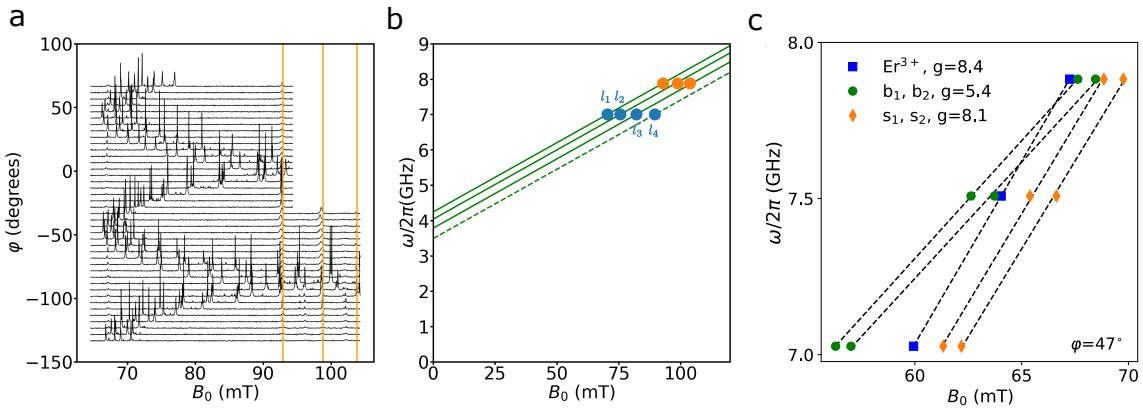

Figure 7.6: **Rotation pattern with ID-ESR and study of peaks properties. a**, ID-ESR rotation pattern measured prior to this thesis at $\omega/2\pi = 7.88$ GHz (figure taken from [Le 22]). **b**, l_i peaks resonance at 7.88 GHz (orange dots) and at 7 GHz (blue dots). A linear extrapolation (green) yields an effective gyromagnetic factor $\gamma = 39$ GHz/T and a Zero Field Spitting (ZFS) of about 4 GHz. **c**, resonant field of the peaks around the Er^{3+} measured with ID-ESR at difference frequencies, with $\varphi = 47\,^\circ$ (figure taken from [Le 22]). Linear extrapolations (dashed line) yield the spins g-factor as well as a their ZFS.

In addition, the comparison of those spectra allows to characterize in more details the 4 high-field peaks l_i with $i \in [1, 2, 3, 4]$, with 3 of them also visible in the ID-ESR spectrum. We compare their resonant magnetic field at two different frequencies in Figure 7.6b and extract a gyromagnetic factor $\gamma = 39$ GHz/T and a Zero Field Splitting (ZFS) of ~ 4 GHz. The peaks around Er^{3+} have been measured at various frequency in [Le 22], as is visible in Figure 7.6c, allowing to compute their g-factor. We notice that the peaks b_1 and b_2 have a ZFS of ~ 2.8 GHz, which is unexpected for Er^{3+} with a charge compensation. We cannot conclude in term of those peak attribution to a spin system.

7.1.3 Spectroscopy of Erbium ions

In the following of this thesis, we concentrate on Er^{3+} line $I = 0$ in order to extract a comprehensive set of data that could be compared to the ID-ESR data presented in Section 5.2 in order to conclude on the interest of FD-ESR.

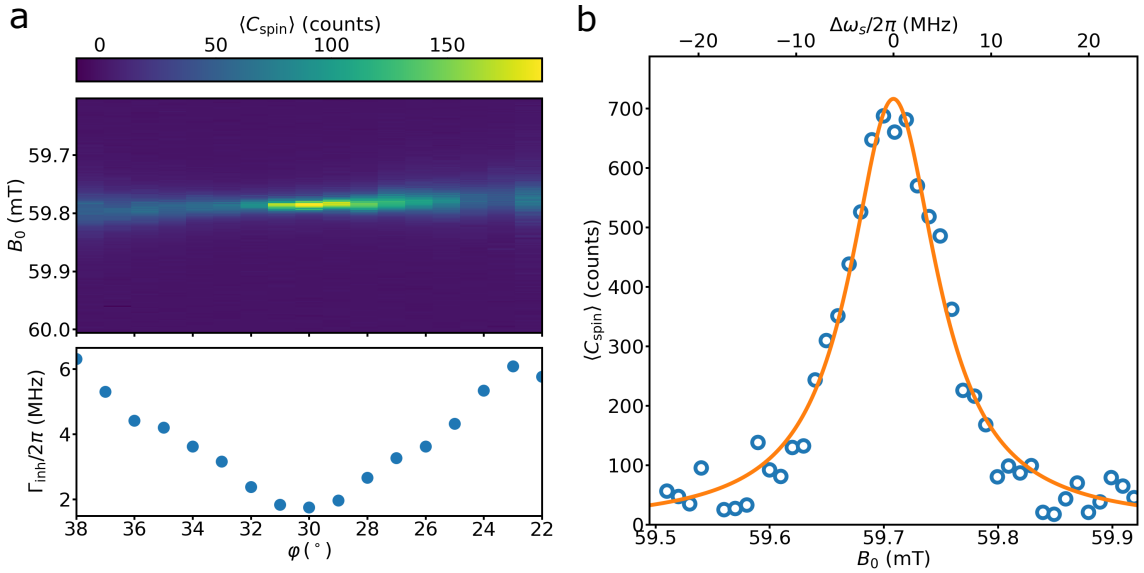

Figure 7.7: **Er^{3+} line $I = 0$. a**, Er^{3+} spectroscopy in setup 2. Top panel: color maps of $\langle C_{\text{spin}} \rangle$ as a function of B_0 and φ, with the excitation pulse parameters: $T_{\text{int}} = 0.45$ s, $T_{\text{rep}} = 5$ s, $\Delta t = 3\,\mu$s and $\beta = 58\,\text{ns}^{-1/2}$. It shows a minimum in linewidth and maximum in signal amplitude at $\varphi_0 = 30\,°$. Bottom panel: Γ_{inh} evolution with φ extracted using a Lorentzian fit. **b**, Er^{3+} spectroscopy in setup 1. $\langle C_{\text{spin}} \rangle$ (blue dots) as a function of B_0 at φ_c, with the excitation pulse parameters: $T_{\text{int}} = T_{\text{rep}} = 8.6$ s, $\Delta t = 4\,\mu$s and $\beta = 52\,\text{ns}^{-1/2}$. The Loretzian fit (orange line) yields $\Gamma_{\text{inh}}/2\pi = 10.8$ MHz.

In setup 2, we characterize the Er^{3+} line $I = 0$ angular dependence by varying the magnetic field orientation close to φ_0, with the result visible in Figure 7.7a. We find the expected values of $\Gamma_{\text{inh}}/2\pi < 2$ MHz at $\varphi_0 = 30°$, an angle interesting to explore the physics of Erbium ions as it maximizes the signal. In the following of this thesis, experiments performed in setup 2 are typically done with $\varphi = 30°$ and $B_0 = 59.79$ mT corresponding to the middle of the line, except when stated otherwise.

In setup 1, the Erbium spectroscopy is done with the magnetic field fixed orientation $\varphi = \varphi_c = 47°$ showing a linewidth of $\Gamma_{\text{inh}}/2\pi = 10.8$ MHz, as illustrated in Figure 7.7b. In this setup also we use the Erbium main line to calibrate our coil. In the following of this thesis, experiments performed in setup 1 is done with $B_0 = 59.73$ mT, except when stated otherwise.

7.2 Simulation of the Erbium fluorescence

As discussed earlier, the spin relaxation curve detected with FD-ESR is a complex signal that contains valuable information on the spins (characteristic relaxation time, curve shape, curve amplitude...). Here, we compare quantitatively the measured fluorescence curves and the model discussed in Section 3.3.3 in the case of the $I = 0$ line of Er^{3+}. The comparison is discussed in detail for various pulse excitation parameters in setup 1, and applied to a single fluorescence curve in setup 2.

7.2.1 Fluorescence at various excitation strengths in setup 1

In setup1, we measure fluorescence curves varying the excitation pulse amplitude β and duration Δt over a wide range, summarized in Table 7.1. It corresponds to detecting the fluorescence curve at various pulse strength, defined as $\epsilon = \beta \times \Delta t$. Because of the saturation of our amplifiers, we are limited to an upper-bound in β, which is why we also

label	β ($\mathrm{ns}^{-1/2}$)	Δt (μs)	T_{rep} (s)	ϵ ($\mathrm{ns}^{1/2}$)
a	1.23	4	0.43	4.9×10^3
b	1.46	4	0.43	5.9×10^3
c	1.95	4	0.43	7.8×10^3
d	2.46	4	0.43	9.8×10^3
e	3.48	4	0.43	1.4×10^4
f	4.63	4	0.86	1.9×10^4
g	9.25	4	2.15	3.7×10^4
h	13.06	4	6.03	5.2×10^4
i	26.06	4	8.61	1.0×10^5
j	52	4	18.90	2.1×10^5
k	246	1	18.90	2.5×10^5
l	246	5	18.90	1.2×10^6
m	246	9	18.90	2.2×10^6
n	246	13	18.90	3.2×10^6
o	246	17	18.90	4.2×10^6

Table 7.1: **Excitation pulse conditions**. We vary the pulse amplitude β (the values are deduced after the calibration of A_{dB}) over the range available in our setup (a to j). To keep increasing the excitation strength ϵ at saturation of amplitude, we vary the pulse duration (k to o).

increase Δt to keep increasing ϵ. However, the effect of β and Δt on spin dynamics is not equivalent, for instance due to power broadening as shown in Figure 3.7. We therefore also simulate the high-ϵ pulse (k to o) with a fixed $\Delta t = 4\,\mu$s but varying the β to check that that our results are consistent no matter the way to increase ϵ, as detailed below.

For each excitation condition, the repetition time T_{rep} was carefully chosen such that the count rate relaxes down to an apparent steady-state, meaning that we collect roughly all the photons coming from the spins. The data are shown in Figure 7.8. Qualitatively, we observe that the number of counts and the characteristic decay time increase with the pulse strength. We also see that the shape of the curves deviates significantly from a single exponential.

To perform quantitative predictions of the fluorescence curves based on Equation 3.33, only two parameters are unknown : the attenuation of the lines A_{dB} and the total spin detection efficiency η. We proceed in two steps. First, we calibrate A_{dB} by fitting the time-dependence of the normalized fluorescence curves. Then, we obtain η by computing the number of counts predicted, using the fact that the Er^{3+} concentration is known.

The other parameters used in the simulation are:

- the resonator characteristics $\omega_0/2\pi = 7.0035$ GHz, $\kappa_{\mathrm{c}}/2\pi = 130$ kHz and $\kappa_{\mathrm{int}}/2\pi = 100$ kHz,
- the non-radiative relaxation rate $\Gamma_{\mathrm{NR}} = 0.15\,s^{-1}$,
- the repetition time T_{rep},
- the pulse amplitude at the resonator input β,
- the spin distribution in frequency $\rho(\Delta\omega)$. We use the measured Er^{3+} Lorentzian line and truncate it in a range $\Delta\omega/2\pi \in [-575 : 575]$ kHz as shown in Figure 3.11a, considering that the resonator frequency is at the line center and that spins out of this simulated frequency range wouldn't significantly contribute. To perform the simulation, we sample this distribution with a 2 kHz step size.

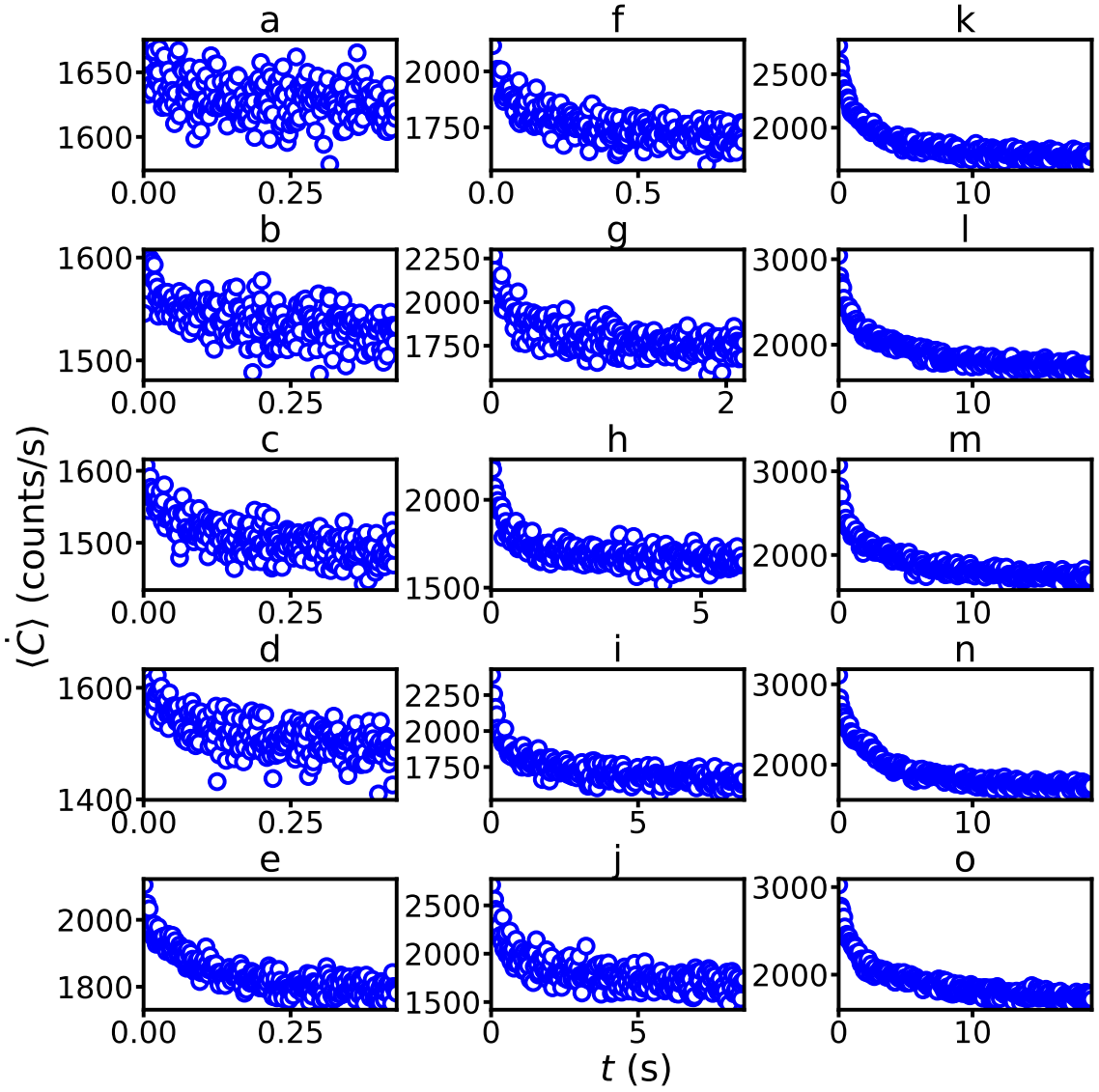

Figure 7.8: **Fluorescence data curves at various ϵ (setup 1).** Count rate $\langle \dot{C} \rangle$ as a function of time t following an excitation pulse with various strength ϵ. We adapt T_{rep} to measure the fluorescence down to an apparent steady rate. Each curve label is associated to ϵ in Table 7.1.

- the spin distribution in coupling $\rho(g_0)$. We use the coupling distribution shown in Figure 3.11b. To perform the simulation, we sample this distribution with $g_0/2\pi \in [4 : 800]$ Hz in step of 27.5 Hz.

The simulation computes the final value of $\langle S_Z \rangle$ following the excitation pulse for a given coupling g_0 and detuning $\Delta\omega$; using Equation 3.33, we thus obtain the fluorescence curve (see Section 3.3.3).

7.2.1.1 Calibration of the line attenuation

An important unknown parameter is the attenuation in the microwave lines A_{dB}, such that

$$\beta = 10^{A_{\text{dB}}/20} \beta_{\text{SA}} \tag{7.1}$$

with β the pulse amplitude reaching the sample for a given pulse amplitude β_{SA} measured with the Spectrum Analyzer at the cryostat input.

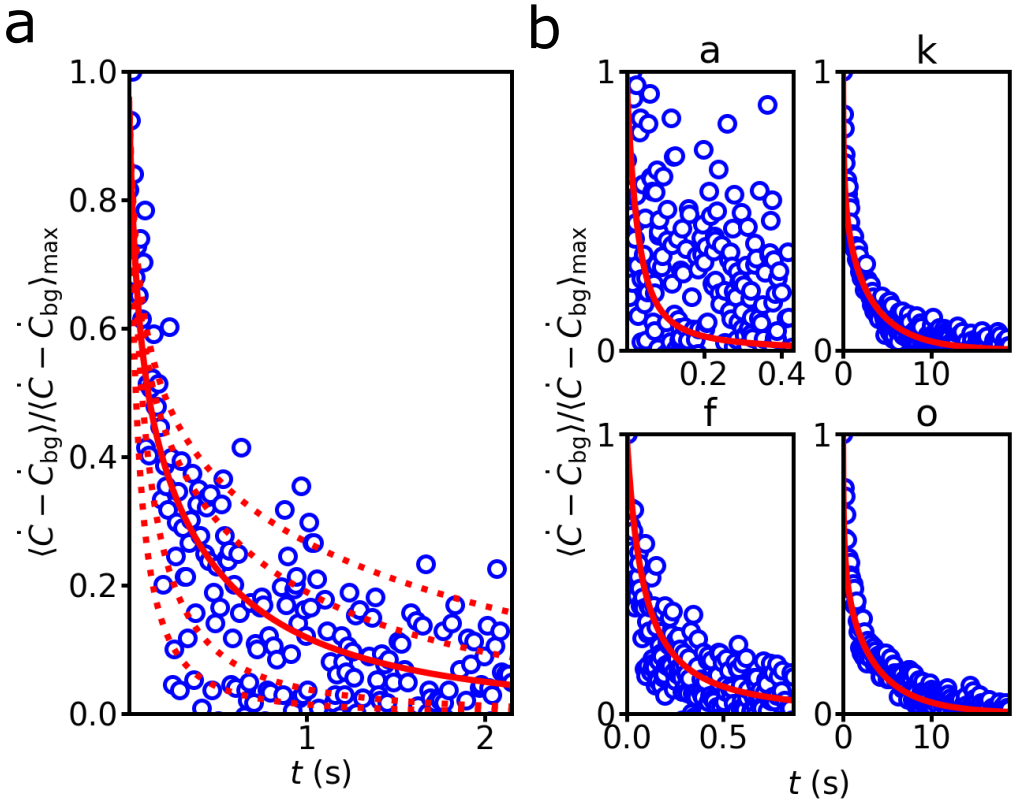

Figure 7.9: **Normalized fluorescence curves for data and simulation (setup 1).** **a**, Normalized fluorescence curve with background subtracted for the data with $\beta_{SA} = 1.5 * 10^5\,\mathrm{ns}^{-1/2}$ (blue dots) and several simulation curves (red lines) with varying excitation pulse amplitude, yielding a fitting amplitude of $\beta = 9.25\,\mathrm{ns}^{-1/2}$ (solid line). **b**, Normalized relaxation curve with background subtracted for data (blue) and their corresponding simulation (red) based on the calibration of the line attenuation.

We use the dependence of the fluorescence curve shape on β to determine the attenuation that matches best our data. This adjustment is shown in Figure 7.9a. Here, we compare a single normalized fluorescence curve to the result of the simulation (also normalized), for several values of attenuation. The best match is obtained for $A_{dB} = -85$ dB. Such an attenuation is indeed compatible with the setup as shown in Figure 6.5, which includes 70 dB of fixed attenuation at low temperatures, ≈ 10 dB in cables (both at room-temp and low-temp), yielding a likely total 5 dB attenuation in filters, circulators, and connectors.

Based on this calibrated attenuation, we have done the simulations that correspond to the other experimental data and find a very good agreement in the curve shape, as can be seen in Figure 7.9b. This good agreement therefore validates the value of input line attenuation obtained.

7.2.1.2 Calibration of the detection efficiency

Now that the line attenuation has been determined, we obtain η by comparing the measured number of counts to the simulation predictions. To remove the experimental background as accurately as possible, we subtract the last data point in each fluorescence curve, and we do the same treatment in the simulation. We then compare the integrated number of counts in the data and in the simulation. The result is shown in Figure 7.10 top panel, where we observe a similar increase in number of counts with ϵ up to a saturation value at

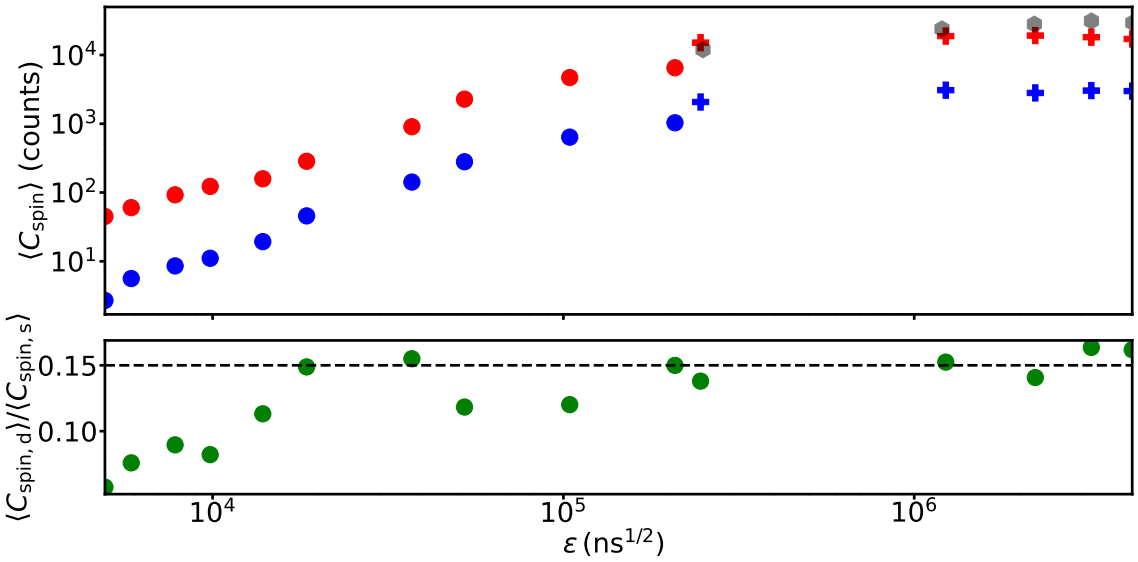

Figure 7.10: **Comparison of data and simulation integrated counts (setup 1). a**, Integrated counts with background subtracted for data (blue) and simulation (red) at various pulse strength ϵ. We also plot the simulation results at high-ϵ keeping the pulse duration fixed $\Delta t = 4\,\mu$s and varying the amplitude β only (black hexagons). **b**, ratio of counts in data $\langle C_{\mathrm{spin,d}} \rangle$ over simulation $\langle C_{\mathrm{spin,s}} \rangle$ as a function of ϵ (green dots). The ratio is roughly stable at high-ϵ at $\eta = 0.15$ (black dashed line) that we take as our measurement efficiency.

high-ϵ. This saturation is well reproduced in the simulations of the same strength ϵ with a fixed Δt and a varying β. We interpret this saturation as being due to the non-radiative relaxation of spins far from the wire that therefore won't contribute to the signal. This explanation is supported by the saturation in the decay characteristic time, detailed below.

We notice that the simulated predictions are consistently larger than the measured counts. We plot the ratio of data over simulation in Figure 7.10 bottom panel, and find that it is constant over a large range of ϵ values, at least in the high-ϵ limit. In the low-ϵ regime however, this ratio is observed to decrease. This phenomenon is due to an extra broadening of the spin resonance for the most strongly coupled spins due to mechanical strain, and will be explained and investigated in more details in Chapter 8. Therefore, we believe the detection efficiency corresponds to the ratio of photon number of at high ϵ, namely $\eta = 0.15$.

This overall efficiency $\eta = \eta_{\mathrm{reso}}\eta_{\mathrm{line}}\eta_{\mathrm{dc}}\eta_{\mathrm{SMPD}}$ decomposes into several efficiency contributions, some of which we have measured:

- the resonator collection efficiency $\eta_{\mathrm{reso}} = \kappa_{\mathrm{c}}/(\kappa_{\mathrm{c}} + \kappa_{\mathrm{int}}) = 0.55$,
- the SMPD duty cycle $\eta_{\mathrm{dc}} = 0.58$,
- the SMPD detection efficiency $\eta_{\mathrm{SMPD}} = 0.45$.

Thus, we deduce that the transmission in the line efficiency is $\eta_{\mathrm{line}} \approx 1$. Even though we would expect small losses in the cables and resonators between the sample and the SMPD, this result makes sense regarding the various uncertainty sources such as the Er^{3+} concentration known with 20% uncertainty or the resonator impedance Z_0 computed in a microwave simulation that doesn't take into account kinetic inductance.

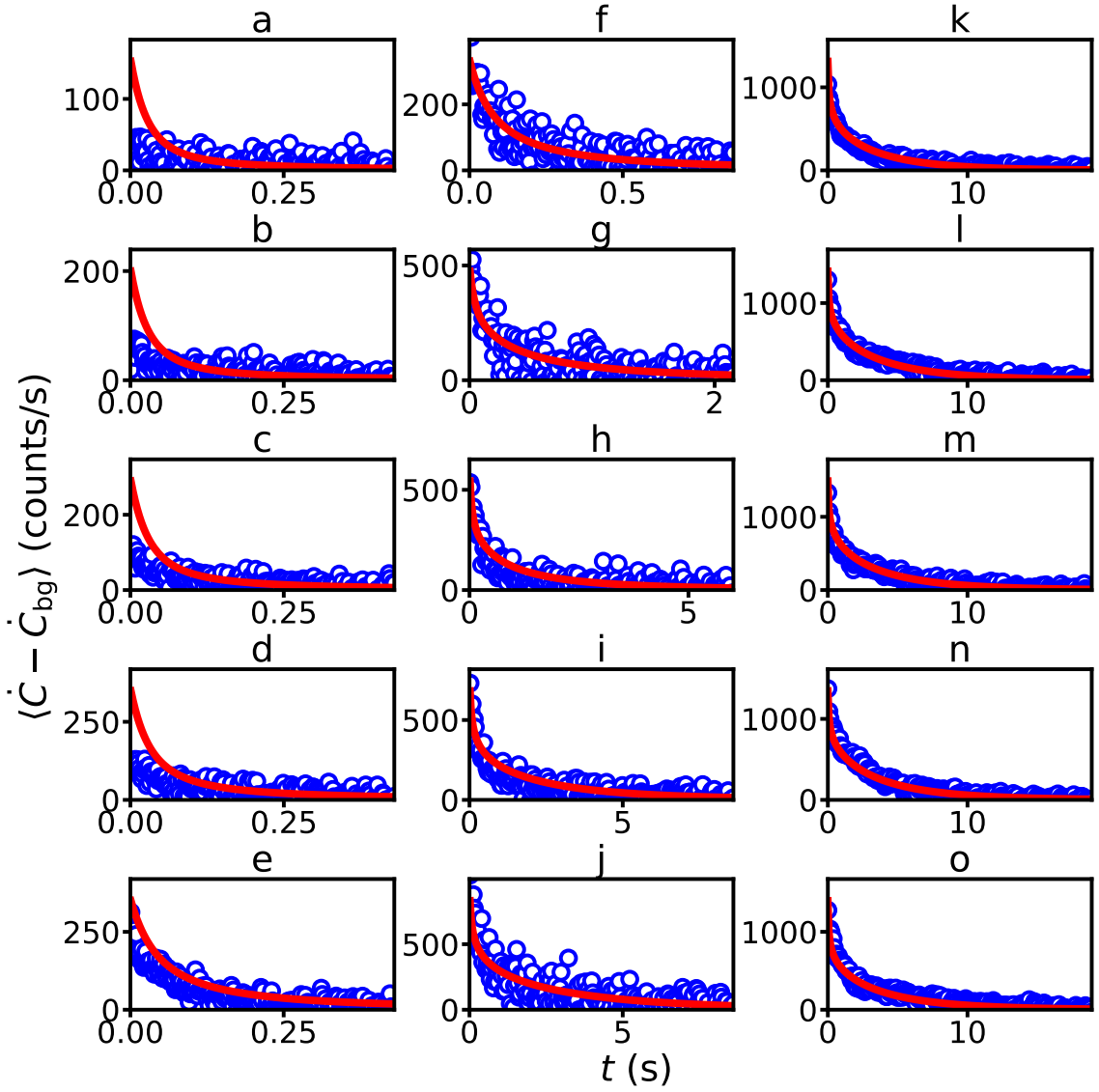

Figure 7.11: **Fluorescence data curves reproduced with simulations (setup 1).** Fluorescence curve with background subtracted of data (blue dots), reproduced with simulations (red line) using the calibration of $A_{\mathrm{dB}} = -85$ dB and $\eta = 0.15$, for various pulse strength ϵ.

7.2.1.3 Data to simulation comparison

Eventually, the calibration of A_{dB} and η allows to compare the data and the simulation over the whole range of ϵ, as is shown in Figure 7.11. The agreement is quantitative over a large range of ϵ despite the non-trivial dependence of the fluorescence curve shapes, which supports the validity of the fluorescence modeling described in Section 3.3.3. As explained earlier, the discrepancy at low ϵ is attributed to strain broadening, and will be explored in Chapter 8.

Using this set of data and simulations, we have computed the fluorescence characteristic relaxation time T_{charac}, defined as $\langle \dot{C}(t = T_{\mathrm{charac}}) \rangle = \langle \dot{C}(t = 0) \rangle \times e^{-1}$. In the results shown in Figure 7.12, the decay time T_{charac} increases with ϵ until it saturates at high ϵ due to the crossover between radiative and non-radiative relaxations, as observed with ID-ESR in Figure 5.5. Nonetheless, here we observe also a saturation at low ϵ that happens at $T_{\mathrm{charac}} \approx 200$ ms in the data and at $T_{\mathrm{charac}} \approx 50$ ms in the simulation. We attribute this

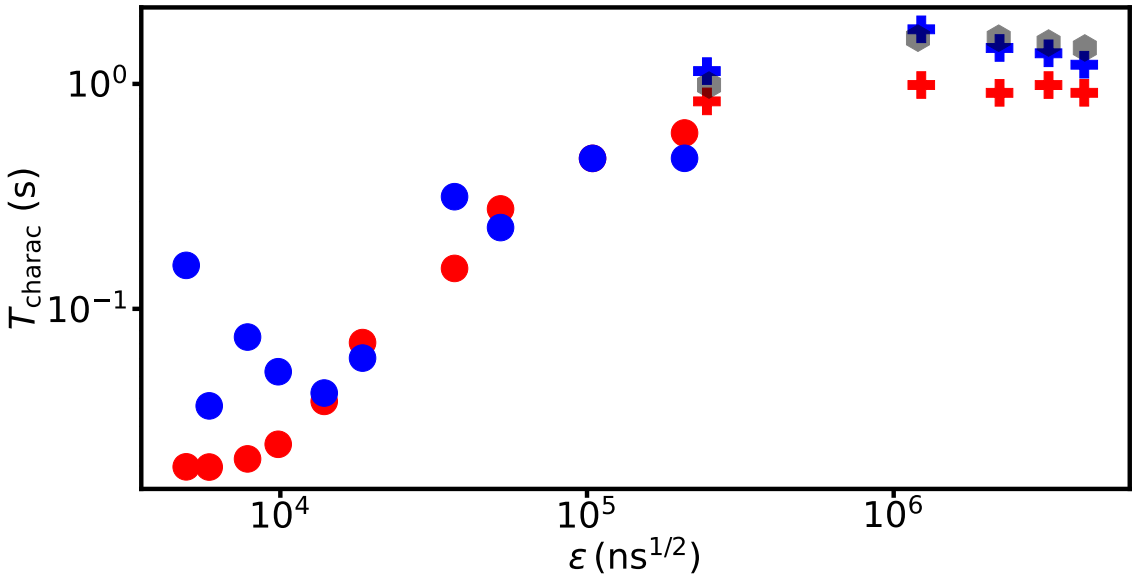

Figure 7.12: **Characteristic relaxation time in data and simulation (setup 1).** Fitted characteristic relaxation time T_{charac} as a function of pulse strength ϵ for data (blue) and simulation (red). The fit is also done on the simulations at high-ϵ keeping the pulse duration fixed $\Delta t = 4\,\mu$s and varying the amplitude β only (black hexagons).

difference in the low ϵ characteristic times to strain effect that shifts the frequency of the highly coupled spins away from the resonator frequency.

7.2.2 Fluorescence in setup 2

In setup 2, we apply the same simulation procedure to calibrate the line attenuation and the detection efficiency, using the comparison with data at a single value of pulse excitation strength. In this setup, the field orientation $\varphi = \varphi_0$ is taken different than in setup 1, changing the spin distributions. We use simulation parameters corresponding to this setup configuration:

- the resonator characteristics $\omega_0/2\pi = 6.999$ GHz, $\kappa_c/2\pi = 300$ kHz and $\kappa_{\text{int}}/2\pi = 60$ kHz,
- the non-radiative relaxation rate $\Gamma_{\text{NR}} = 0.15\,s^{-1}$,
- the repetition time $T_{\text{rep}} = 15$ s,
- the pulse amplitude at the resonator input β,
- the spin distribution in frequency $\rho(\Delta\omega)$, visible in Figure 7.13a, where we truncate the line in a range $\Delta\omega/2\pi \in [-950 : 950]$ kHz and take a 3 kHz step size
- the spin distribution in coupling $\rho(g_0)$, visible in Figure 7.13b. We couldn't fit the data with the simulation using the coupling distribution deduced from the current flowing in the resonator wire, likely due the line narrower linewidth that makes the distribution more sensitive to strain. In order to mimic the strain effect, we introduce in the coupling distribution a progressive cut-off $\rho(g_0) \propto 1/g_0^6$ at high coupling for $g_0 > 350$ Hz, taking $g_0/2\pi \in [4 : 800]$ Hz with a finer sampling at high g_0.

We obtain a good fit of the data for an attenuation $A_{\text{dB}} = 90$ dB. Such attenuation is reasonable considering the setup shown in Figure 6.6, which includes 80 dB of fixed attenuation at low temperatures and ≈ 10 dB for the cables, circulators, and connectors.

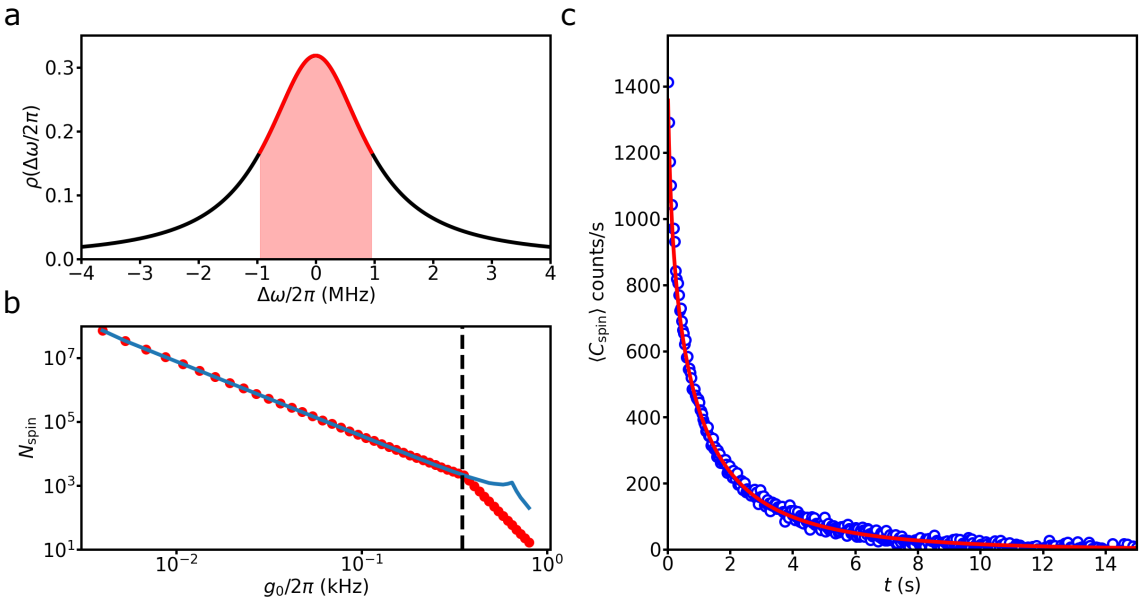

Figure 7.13: **Data to simulation comparison (setup 2). a**, normalized frequency distribution with the Er^{3+} line at $\varphi = 30\,^\circ$ (black) and frequency range considered in the simulations (red surface). **b**, distribution in number of spin N_{spin} as a function of coupling g_0, with the distribution deduced from the current flowing in the resonator wire (blue line) and the distribution used here (red histogram), showing a cut-off at $g_0/2\pi = 350$ Hz (black dashed line). **c**, fluorescence comparison of data (blue dots) and simulation (red line) at $\epsilon = 5.0 \times 10^4\,\text{ns}^{1/2}$ yielding $A_{\text{dB}} = 90$ dB and $\eta = 0.1$.

Computing the ratio of data counts to the simulation prediction, we obtain $\eta = 0.1$ that comes from the successive efficiencies:

- the resonator collection efficiency $\eta_{\text{reso}} = 0.83$
- the SMPD duty cycle $\eta_{\text{dc}} = 0.78$
- the SMPD detection efficiency $\eta_{\text{SMPD}} = 0.4$

From this, we deduce $\eta_{\text{line}} \approx 0.4$. A possible explanation of the difference with the value in setup 1 is the presence of an infrared filter in between the sample and the SMPD that might add losses.

7.3 Signal-to-Noise Ratio (SNR) experimental comparison for spin detection

A strong motivation for developing the FD-ESR detection method is its potential to improve the detection sensitivity compared to the usual ID-ESR, as explained in Section 4.3. In order to quantitatively conclude on this SNR comparison, one needs to use the same spin excitation conditions. In this chapter, we present a study of SNR for both ID-ESR and FD-ESR in identical excitation conditions realized in setup 1, demonstrating a clear advantage to FD-ESR in the detection of a low number of highly coupled spins.

7.3.1 Measurement procedure

The computation of a detection scheme SNR requires to determine both its mean value and its variance. The most direct way to proceed is to acquire many single shot data and

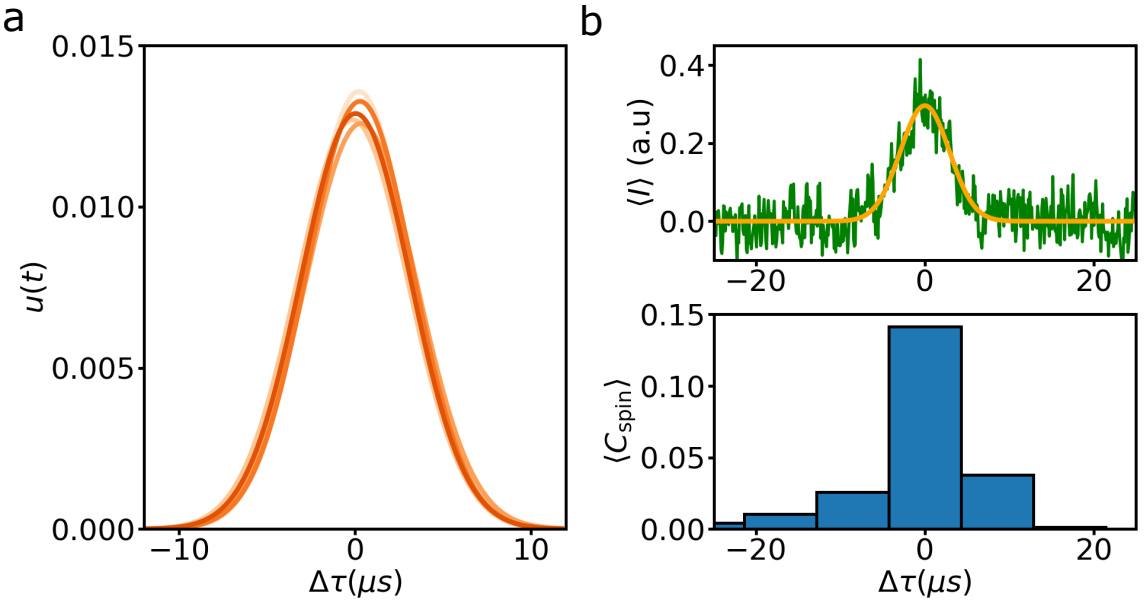

Figure 7.14: **Echo mode characterization a**, normalized temporal mode $u(t)$ fitted on echo measured at various $\epsilon \in [3.9 \times 10^4, 7.8 \times 10^4, 1.6 \times 10^5, 3.1 \times 10^5, 6.2 \times 10^5]\,\mathrm{ns}^{1/2}$ (darker shade of orange). **b**, echo measured with quadrature detection or photon detection with the same excitation conditions. Top panel: echo detected with quadrature detection (green) and fit of its temporal mode with a Gaussian (orange line). Bottom panel: echo detected directly with the SMPD, where each blue bar is the average number of count with background subtracted during a single SMPD detection cycle.

to extract from each of them the quantity of interest. The distribution of this quantity bears directly the signal mean value and variance. We compute the SNR of both ID-ESR and FD-ESR on a wide range of excitation pulse parameters.

7.3.1.1 Inductive detection SNR

In the case of ID-ESR, the quantity of interest is the integrated echo amplitude in a Hahn echo sequence: $\epsilon/2_X - \tau - \epsilon_Y - \tau -$ echo.

As explained in Section 4.3.1.1, the echo is integrated over its corresponding temporal mode $u(t)$. We have verified that the echo emission mode is independent of the excitation pulse power. For that, we record echoes for a large range of ϵ and fit their temporal dependence with a Gaussian-shaped function $u(t)$, normalized such that $\int |u(t)|^2 = 1$. The result in Figure 7.14a shows that the shape is independent of ϵ, as expected.

Because the echo amplitude is obtained after a complex chain of amplification, filtering, and mixing, it is not straightforward to convert the detected output signal into the dimensionless field amplitude at the output of the resonator, which is the quantity of interest. Fortunately, this conversion is enabled by the presence of the SMPD in the setup. In that goal, we measure a Hahn echo in the exact same conditions, first with amplification and quadrature detection, and then with the SMPD, yielding the emitted echo energy in absolute units. The data are shown in Figure 7.14b. A low excitation amplitude was purposely chosen in order not to saturate either the JPA or the SMPD. We detect the echo with the SMPD, correct with the known SMPD efficiency η_{SMPD} and the proportion of the echo that happens in the SMPD detection time, and obtain an echo number of photons $\langle X_\mathrm{e} \rangle^2 = 0.42$ in the given excitation conditions. We therefore deduce the calibration of the integrated homodyne voltage in absolute units and express in the following the integrated echo X_e in its natural unit.

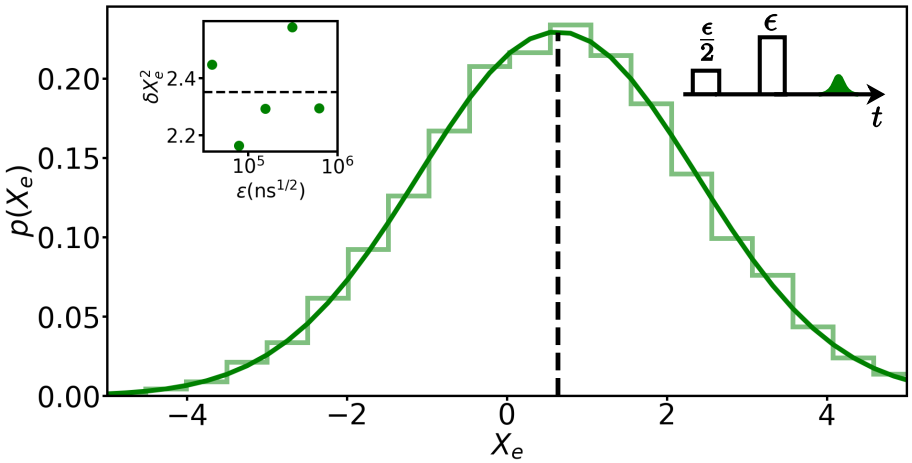

Figure 7.15: **ID-ESR histogram.** Distribution of integrated spin echo in natural unit for $\epsilon = 7.8 \times 10^4\,\mathrm{ns}^{1/2}$ (green histogram) and its Gaussian fit (green line) that yields $\langle X_e \rangle = 0.6$ (black vertical dashed line) and $\delta X_e^2 = 2.45$. The right inset represents the Hahn echo sequence (black rectangle) and the signal in the integrated echo (green). The left inset shows the standard deviation of similar distributions taken at various ϵ yielding a mean value of $\overline{\delta X_e^2} = 2.35$ (black horizontal dashed line).

We now turn to the SNR measurements. At a given ϵ, single shot measurements of the echo have been performed many times (~ 1000 iterations) in order to determine the distribution of X_e. As shown in Figure 7.15, the resulting histogram can be fitted by a gaussian to extract its mean value $\langle X_e \rangle$ and its variance δX_e^2. Such distributions were measured for various ϵ to check that, as expected since the signal is integrated over the same mode, the variance remains roughly constant at $\overline{\delta X_e^2} = 2.35 \pm 0.2$, as can be seen in Figure 7.15. As explained in Section 4.3.2, the expected variance in the echo mode can be written as

$$\overline{\delta X_e^2} = \delta X_{\mathrm{vacuum}}^2 + \delta X_{\mathrm{JPA}}^2 + \frac{\delta X_{\mathrm{HEMT}}^2}{G_{\mathrm{JPA}}} \tag{7.2}$$

with $\delta X_{\mathrm{vacuum}}^2 = 1/4$ the mode vacuum fluctuations, $\delta X_{\mathrm{JPA}}^2 = 1/4$ the minimal fluctuations added by the JPA and $\delta X_{\mathrm{HEMT}}^2 / G_{\mathrm{JPA}} = 0.15$ the fluctuations added by the HEMT. The HEMT contribution was measured separately, by measuring the variance with the JPA turned off. The measured fluctuation $\overline{\delta X_e^2}$ thus is larger than expected. This is likely due in part to the neglect of losses between the SMPD and the JPA in our model, which leads to an over-estimation of the conversion factor between the output voltage and the echo dimensionless amplitude. In the following SNR measurements, we consider that $\overline{\delta X_e^2}$ is constant, and we only measure $\langle X_e \rangle$ as it is much faster.

7.3.1.2 Fluorescence detection SNR

We now turn to the FD-ESR SNR. We measure the single shot fluorescence trace many times (up to $\sim$ 10000 iterations) following a single pulse excitation of strength ϵ and integrate the number of counts for each iteration over a time T_{int} with the background subtracted.

It's worth to mention that the background rate $\langle \dot{C}_{\mathrm{bg}} \rangle$ is averaged over all the iterations at a given ϵ before subtraction, in order to minimize the added noise due to background fluctuations. The SNR varies with the integration time T_{int} as can be seen in Figure 7.16a where the SNR dependence with T_{int} is plotted for two values of ϵ with one order of magnitude difference. In both case, the SNR increases at low T_{int}, as we integrate more of the spin signal, and then starts to reduce at high T_{int}, as the added fluctuations typically

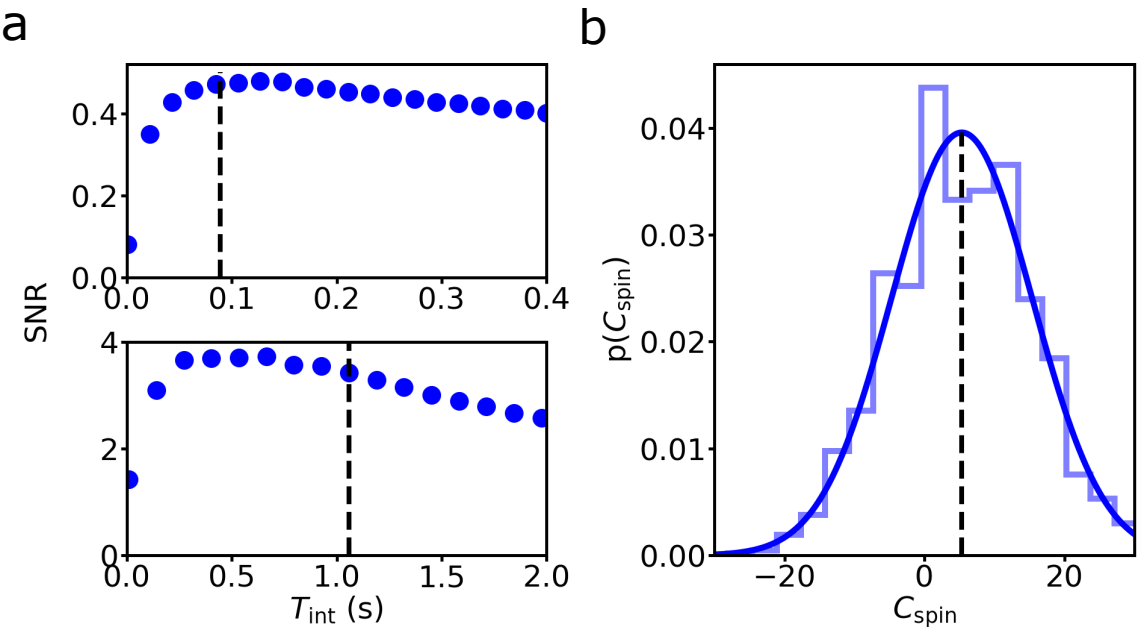

Figure 7.16: **FD-ESR SNR dependence with T_{int} and histogram. a**, SNR in FD-ESR as a function of T_{int} for $\epsilon = 1.6 \times 10^4\,\mathrm{ns}^{1/2}$ (top) and $\epsilon = 2.9 \times 10^5\,\mathrm{ns}^{1/2}$ (bottom). The vertical dashed lines correspond to T_{charac}. **b**, distribution of integrated counts with background removed for $\epsilon = 9.3 \times 10^3\,\mathrm{ns}^{1/2}$ (histogram) and its Gaussian fit (blue line) that yields $\langle C_{spin} \rangle = 5$ counts (black vertical dashed line) and $\delta C^2 = 100$.

due to dark count overcomes the gain in signal. We observe in those data that T_{charac} is close to the optimal integration time. This result was verified for all the excitation parameters, therefore in the following we use $T_{int}(\epsilon) = T_{charac}(\epsilon)$ to compute the SNR. The resulting histogram is fitted with a Gaussian to extract the signal mean value $\langle C_{spin} \rangle$ and its variance δC^2, as is shown in Figure 7.16b.

We reproduce the fluorescence curves measured at each ϵ with the master equation simulation described in Section 7.2. The noise is modeled with Equation 4.24 with $\alpha = 1500$ counts/s and $\eta = 0.15$. We compare the SNR measured and simulated in Figure 7.17. For low to medium values of ϵ, we find a good agreement between both curves which confirms the validity of the Poissonian description of the noise. However, we can see at high ϵ the onset of some discrepancy. This is confirmed by looking at the ratio $\delta C^2 / \langle C \rangle$, which increases noticeably above the value of 1 expected for the Poisonian noise. This increase in the noise is unexpected and presently not understood. In particular, this increase in noise is not visible with ID-ESR at similar ϵ, as is visible in Figure 7.15. One possible hypothesis is the onset of super-radiant fluctuations. More work is needed to investigate the validity of this idea.

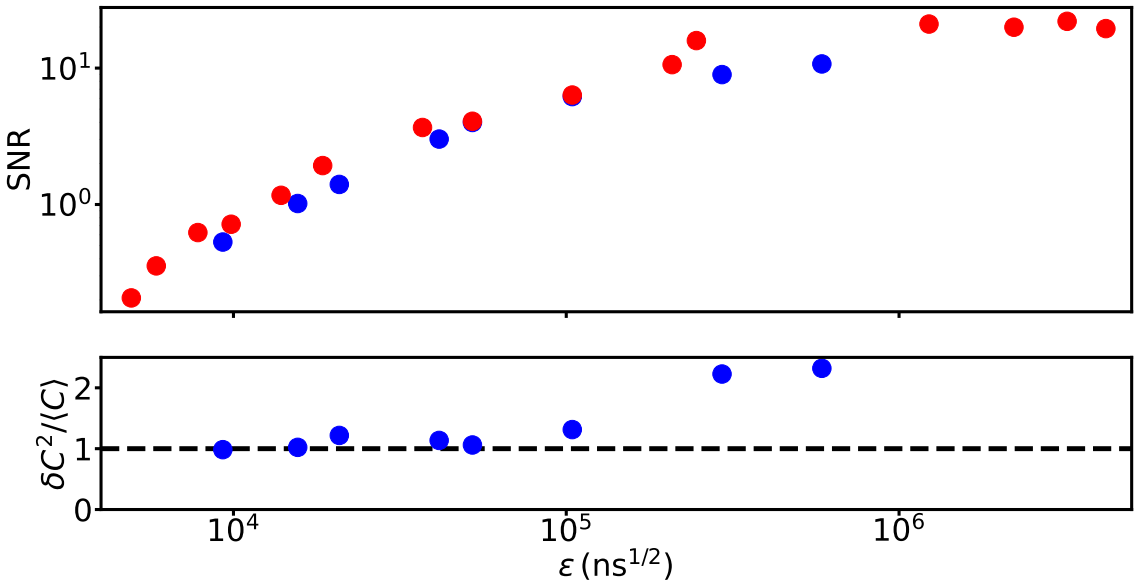

Figure 7.17: **FD-ESR comparison of data and simulation SNR.** Top panel: FD-ESR SNR as a function of ϵ in the data (blue) and in the simulation (red). Bottom panel: ratio in the data of the variance δC^2 over the mean value $\langle C\rangle$ (blue dots), expected to be equal to 1 for a Poissonian distribution (black dashed line).

7.3.2 Comparison

T_{rep} (s)	$\epsilon\,(\mathrm{ns}^{1/2})$
0.87	9.8×10^3
0.87	2.0×10^4
1.75	3.9×10^4
4.30	7.8×10^4
14.00	1.6×10^5
17.30	3.1×10^5
17.30	6.2×10^5

Table 7.2: **ID pulse conditions**.

T_{rep} (s)	$\epsilon\,(\mathrm{ns}^{1/2})$	T_{charact} (s)
0.87	9.3×10^3	0.044
0.87	1.6×10^4	0.089
1.75	2.1×10^4	0.138
4.30	4.2×10^4	0.257
12.15	5.2×10^4	0.330
17.23	1.0×10^5	0.510
17.23	2.9×10^5	1.060
20.72	5.9×10^5	1.157

Table 7.3: **FD pulse conditions.**

We now turn to the comparison between ID-ESR and FD-ESR. The measurements are done at various excitation pulse conditions ϵ and T_{rep} for a fixed $\Delta t = 4\,\mu$s, with values summarized in Table 7.2 with $\tau = 50\,\mu$s for ID-ESR and in Table 7.3 for FD-ESR. To have quantitative comparison, the two detection methods must be applied to detect the same contributing spins. In ID-ESR, we consider that the echo signal comes mostly from spins that see the sequence $\pi/2_X - \tau - \pi_Y - \tau -$ echo whereas in FD-ESR, we consider that the fluorescence mostly comes from spin that see a π pulse. Therefore, we compare the two detection methods with the same pulse strength ϵ for the second pulse in the Hahn echo and for the single pulse. The comparison results are plotted in Figure 7.18.

We start by comparing the signal mean value and fluctuations of these two detection methods. In order to compare quantities with the same unit, the top panels plot the number of photons in the signal and in the fluctuations for each detection method. We see in Figure 7.18a that the number of photon carrying the signal increases with ϵ for both detection methods. It makes sense since the number of contributing spins also increases with ϵ. As expected from the discussion in Section 4.3, the number of detected photon is much larger in FD-ESR than in ID-ESR, by a factor as large as 10^3 for the lowest pulse excitation power. The ratio of the signals in FD-ESR and ID-ESR, $\langle C\rangle/\langle X_e\rangle$, is shown

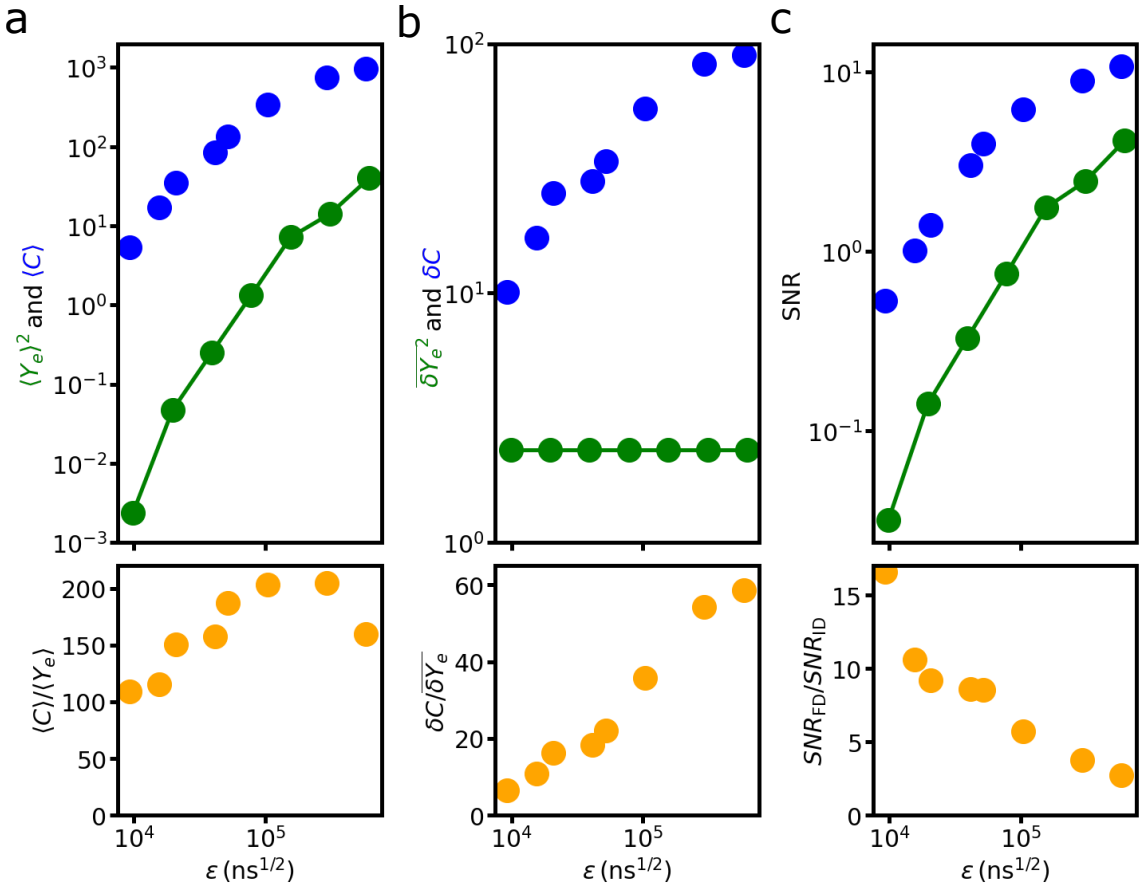

Figure 7.18: **Comparison of ID-ESR and FD-ESR a**, top panel: amount of photon detected using ID (green dots) and FD (blue dots) as a function of ϵ. We linearly interpolate the values obtained with ID (green line) to allow comparison with FD. Bottom panel: signal ratio of FD over ID as a function of ϵ. **b**, top panel: fluctuation of photon number detected using ID (green dots) and FD (blue dots) as a function of ϵ. We linearly interpolate the values obtained with ID (green line) to allow comparison with FD. Bottom panel: standard deviation ratio of FD over ID as a function of ϵ. **c**, top panel: spin detection SNR using ID (green dots) and FD (blue dots) as a function of ϵ. We linearly interpolate the values obtained with ID (green line) to allow comparison with FD. Bottom panel: SNR ratio of FD over ID as a function of ϵ.

to vary moderately with ϵ. In term of fluctuations, we observe in Figure 7.18b that the FD-ESR detection method sees δC^2 increase with ϵ as it depends on the amount of photon detected, whereas ID-ESR has a constant noise at $\overline{\delta X_e^2}$. The ratio of the noise $\langle \delta C \rangle / \langle \delta X_e \rangle$ varies more appreciably, due to the noise increase with ϵ in FD-ESR.

We then compare in Figure 7.18c the SNR of ID-ESR and FD-ESR. All over the range of ϵ studied here, we have a bigger SNR with FD-ESR than with ID-ESR. Although there might be ESEEM effect reducing the effective spin echo signal, we don't expect to have more than 50% change in the amplitude detected with ID-ESR, as will be visible in the ESEEM curve shown in Chapter 9. Therefore, we can conclude that fluorescence detection indeed increases the sensitivity of ESR in the experimental parameters explored during this thesis. A clear trend of reduction of this SNR gain is visible as we increase ϵ. From previous discussion about mean value and fluctuation evolution with ϵ, we understand that this reduction of SNR gain is largely due to the increase in the fluctuations of FD-ESR at high ϵ. At the opposite, the gain in sensitivity increases at low ϵ with a measured gain of up to a factor 16. Moreover, it is meaningful to note that δC is dominated by the detector

dark counts, which can be reduced without limit with better SMPD properties; whereas δX_e is almost limited by vacuum fluctuations and can thus not be much reduced. Our results therefore confirm that FD-ESR can be more sensitive than ID-ESR, in the limit of small number of spins with sufficiently large radiative relaxation rate. The limit of single spin detection has even been reached very recently in an experiment very similar to the one presented in this thesis, as will be reported in the thesis of Z.Wang and L.Balembois.

Chapter 8

Spectroscopy and coherent dynamics of strained Erbium ions

In this chapter, we present further data on the Er^{3+} spectroscopy at low-power. Line broadening and shifts are observed, which we attribute to strain in the substrate caused by the differential thermal contractions of the metal thin-film and the crystal. Coherent oscillations are observed in the tails of the spectrum.

8.1 Strain induced resonance frequency shift

8.1.1 Correlations between resonance frequency and relaxation time

The FD-ESR spectra discussed in Chapter 7 were obtained at high excitation pulse strength; we now measure the erbium spectrum at much lower strength such that only the most strongly coupled spins contribute to the fluorescence signal. The high/low-ϵ comparison is shown in Figure 8.1. Here, the angle was $\varphi = 30\,^\circ$ for both spectra, and the spectra were normalized to facilitate the comparison. We observe that the low-ϵ line is much broader than the high-ϵ line that we will call the spin "main line" in the following. In the same figure, we also show the effective decay time $T_{1,\text{eff}}$, using an exponential decay fit, of the fluorescence curves for the low-ϵ spectrum as a function of B_0. Although we know that the fluorescence relaxation isn't exponential, $T_{1,\text{eff}}$ appears as a good approximation of the curve decay time at low-ϵ, as is shown in the inset of Figure 8.1. We observe that $T_{1,\text{eff}}$ strongly depends on B_0; in particular, it is longer with $T_{1,\text{eff}} \approx 0.2$ s at the center of the spin main line while it is shorter with $T_{1,\text{eff}} \approx 0.05$ s in the tails of the spectrum. This indicates a correlation between frequency shift and the radiative relaxation rate of the spin. Another confirmation of this correlation is acquired by treating the high-ϵ data differently: we integrate the signal over various integration time down to $T_{\text{int}} = 0.05$ s, thereby enhancing the contribution of the most strongly coupled spins which contribute more to the short-time fluorescence. As expected, the lineshape is affected by this short-time integration (see Figure 8.1), and some amount of broadening becomes visible as in the low-ϵ spectra.

Such correlation between the spins coupling and their resonance has been seen before with donors in silicon measured by a superconducting resonator [Pla+18], and here we observe it also for REIs in Scheelite. It is explained by strain induced shifts in the spin resonance, resulting from differential thermal contraction between the metal and the substrate as the sample is cooled down to 10 mK. In our system, we know that Niobium has 2 orders of magnitude larger thermal expansion coefficient than $CaWO_4$. The mechanical deformation in such conditions is simulated using a finite element simulation software that yields the strain $\boldsymbol{\epsilon}$-tensor. The result is shown in Figure 8.2, where we plot the cross section below the resonator wire either with the spatial distribution of the radiative

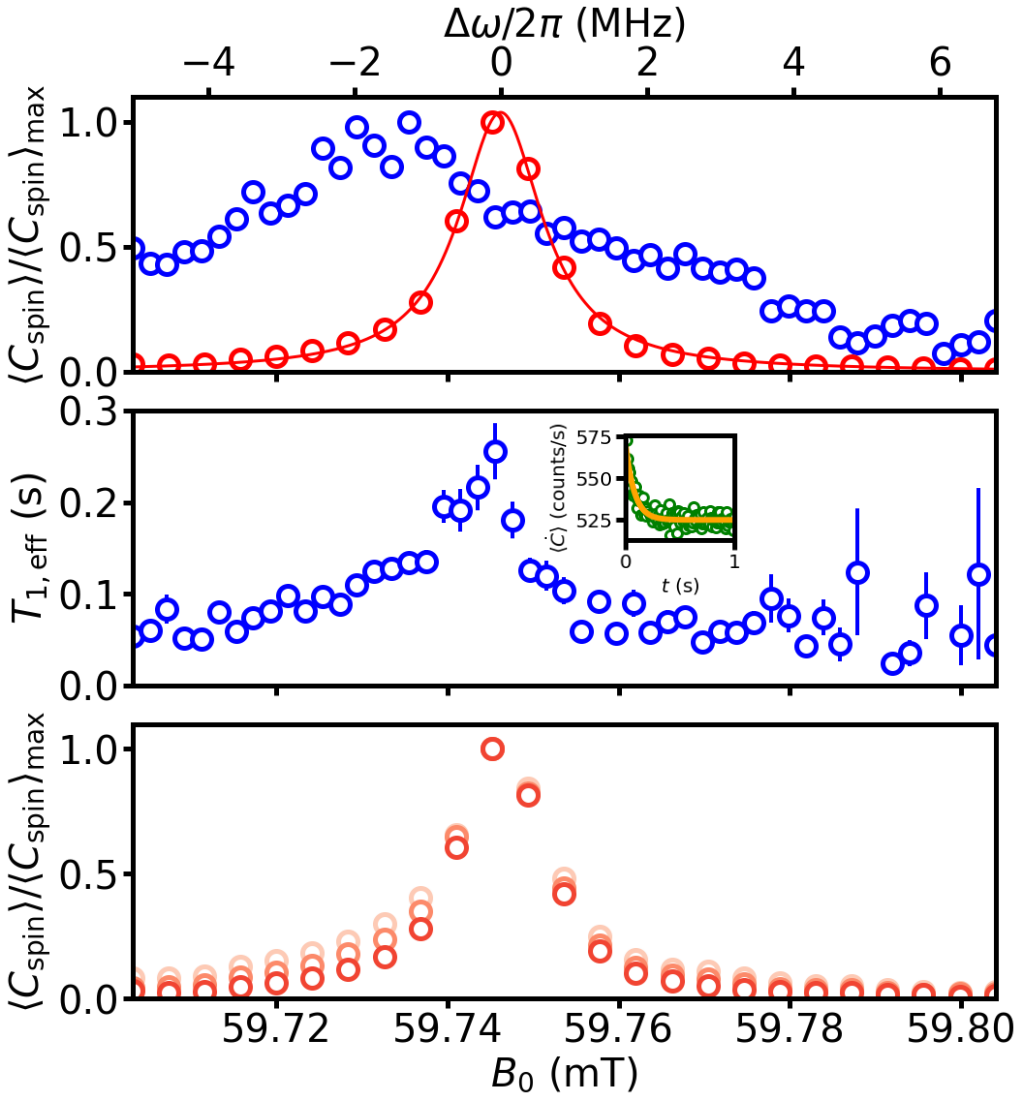

Figure 8.1: **Spectroscopy at high and low strength showing strain asymmetry (setup 2)**. Top panel: Normalized spectroscopy taken at $\varphi_0 = 30°$ with high excitation pulse strength ($\epsilon = 3.5 \times 10^5\,\mathrm{ns}^{1/2}$, $T_{\mathrm{int}} = 0.75$ s, $T_{\mathrm{rep}} = 3$ s, red dots) and at low strength ($\epsilon = 5.8 \times 10^3\,\mathrm{ns}^{1/2}$, $T_{\mathrm{int}} = 0.05$ s, $T_{\mathrm{rep}} = 1$ s, blue dots). The red line is a Lorentzian fit yielding $\Gamma_{\mathrm{inh}}/2\pi = 1.4$ MHz. The frequency axis (top axis) is defined centered on the main line. Middle panel: on the low-ϵ data, effective relaxation time $T_{1,\mathrm{eff}}$ fitted with a single exponential on the relaxation curve as a function of B_0. The error bars are deduced from the fit. In the inset is plotted the relaxation curve (green dots) fitted with an exponential (orange) at $B_0 = 59.723$ mT. Bottom panel: on the high-ϵ data, normalized spectroscopy varying T_{int} from dark to light reds: $[0.75, 0.2, 0.05]$ s.

relaxation time $T_{\mathrm{R}} = 1/\Gamma_{\mathrm{R}}$ or with the hydrostatic strain $\epsilon = \sqrt{\epsilon_{x,x}^2 + \epsilon_{y,y}^2 + \epsilon_{z,z}^2}$. We see that the region where the strain is large coincides with the short radiative relaxation time, typically $T_{\mathrm{R}} < 0.07$ s. As strain is unavoidably associated with a change in the crystal field parameters, it appears plausible that strain leads to changes in the **g**-tensor, although a quantitative modeling of the strain to frequency shift coefficients is unfortunately not available and beyond the scope of this work.

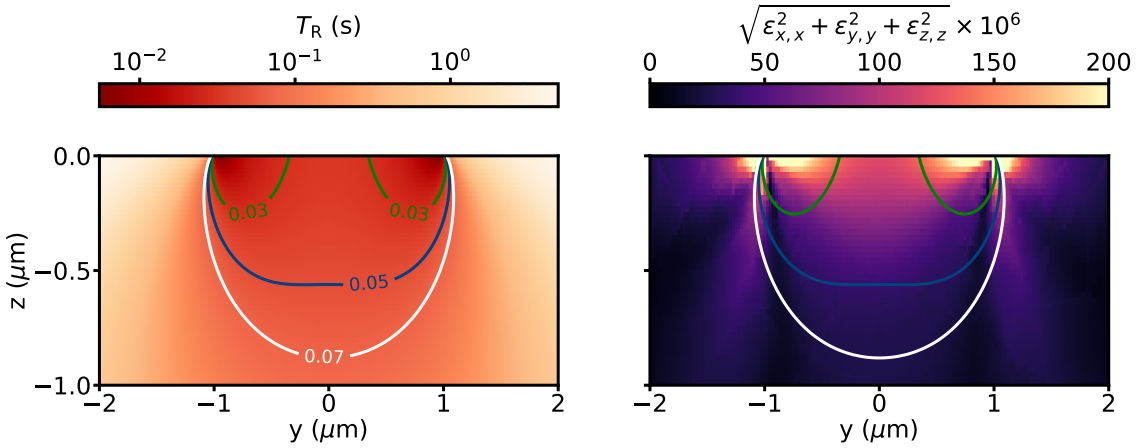

Figure 8.2: **Cross section of T_R and strain**. Left: Spatial dependence of the radiative relaxation time T_R. On both plot the contours show the position where $T_R = 0.03$ s (green), $T_R = 0.05$ s (blue), $T_R = 0.07$ s (white). Right: Spatial dependence of the simulated hydrostatic strain amplitude $\sqrt{\epsilon_{x,x}^2 + \epsilon_{y,y}^2 + \epsilon_{z,z}^2}$, rescaled by a factor 10^6.

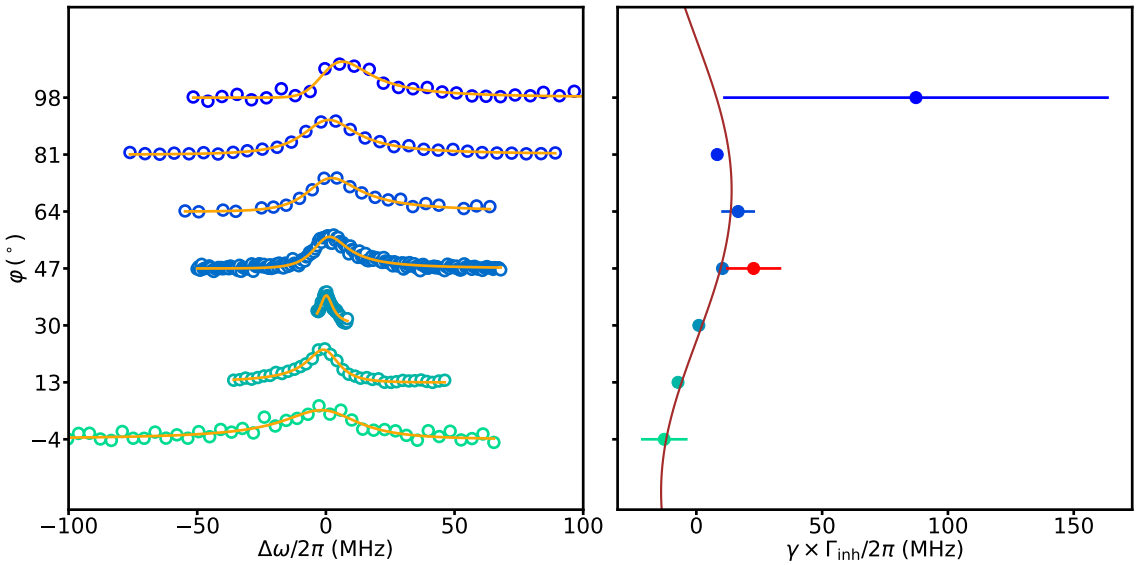

Figure 8.3: **Angular dependence of the line asymmetry.** Left panel: normalized spectra taken at various φ (blue dots). The excitation pulse parameters (ϵ, T_{rep}) vary from spectrum to spectrum in order to have some signal. The integration time is taken fixed at $T_{int} = 0.05$ s. The orange lines are fits done with Equation 8.1. Right panel: fitted asymmetry parameter $\gamma \times \Gamma_{inh}$ as a function of φ for setup 2 (blue dots) and for setup 1 (red dot, detailed in Section 8.2.3). The error bars are 1σ deduced from the fit. The brown line is a fit on the data from setup 2 except from the point at $\varphi = 98°$, using Equation 5.14 that yields $\varphi_0 = 26\,°$ and a typical electric field modulation due to the strain $\Delta E_c = 25$ kV/cm.

8.1.2 Line asymmetry dependence with the field orientation

In order to collect more data on the strain effect, we measure low-ϵ spectra at various field orientation φ in Figure 8.3a. It is worth to mention that the spin coupling g_0 depends on φ, and therefore the pulse excitation parameters ϵ and T_{rep} are adapted to have enough signal while keeping ϵ as low as possible. In all spectra, the integration time is fixed at $T_{int} = 0.05$ s to observe mostly the highly coupled spins. The strained lines appear to

be quite asymmetric, and the sign of this asymmetry depends on φ. To extract more quantitative information, we fit the lines with a skewed Lorentzian model

$$f(\Delta\omega) = \frac{A}{1+4(\frac{\Delta\omega}{\Gamma_{\text{inh}}})^2}(1+\text{erf}[\frac{\gamma\Delta\omega}{\Gamma_{\text{inh}}}]) \tag{8.1}$$

where $\text{erf}(x)$ is the error function defined as

$$\text{erf}(x) = \frac{2}{\sqrt{\pi}}\int_0^x e^{-t^2}dt. \tag{8.2}$$

This fit allows to extract the skewness in frequency $\gamma \times \Gamma_{\text{inh}}$ dependence with φ, visible in Figure 8.3b. We observe that the skewness goes to zero at $\varphi_{0,\text{skewness}}$. We fit this dependence using Equation 5.14 and extract the typical electric field modulation due to strain $\Delta E_c = 25$ kV/cm and the symmetry axis at $\varphi_{0,\text{skewness}} = 26\,°$, close to $\varphi_0 = 30\,°$.

A qualitative understanding of the strain effect on the spins was discussed in Section 5.2.1.2. To summarize the arguments here, the Er^{3+} inhomogeneous linewidth is dominated by the crystal electric field inhomogeneity E_c. Although a global electric field would affect similarly the two Ca^{2+} sites and enlarge the linewidth, the strain modifies the local E_c in opposite directions for the two sites and shifts the spin frequency in the same direction, causing asymmetry.

8.2 Coherent oscillations of Erbium ions

The correlation of the spin resonance with its coupling g_0 allows to address a sub-ensemble of spins with a rather homogeneous coupling, by setting the magnetic field on the side of the main line. Because the coupling is better defined, one may expect to observe coherent oscillations with a well-defined Rabi angle; in this section, we report such measurements.

8.2.1 Coherent oscillations varying pulse duration

To select a spin sub-ensemble, we choose a value of B_0 that is far enough from the main line to have a relative homogeneity in g_0 but staying in a range where we have enough signal. Based on the spectra in Figure 8.1a, we set $B_0 = 59.7$ mT and realize a Rabi measurement by varying the excitation pulse duration Δt. The resulting signal, visible in Figure 8.4a, shows an increase in amplitude with Δt as well as a damped oscillation. The curve is fitted with

$$f(\Delta t, \beta) = A\sin^2(\Omega_{\text{R0}}\Delta t/2)e^{-\Delta t/T_{c,1}} + B(1-e^{-\Delta t/T_{c,2}}) \tag{8.3}$$

where a Rabi oscillation damped with a characteristic time $T_{c,1}$ is superposed with an exponential increase of characteristic time $T_{c,2}$. This fit allows to extract from the Rabi frequency $\Omega_{\text{R0}} = 4g_{0,\text{eff,R}}\sqrt{\kappa_c}\beta/\kappa$ the effective coupling $g_{0,\text{eff,R}}/2\pi = 350$ Hz.

The damping of the Rabi oscillations may have several origins. It could originate from the inhomogeneous broadening, or from residual inhomogeneity of the coupling constant, or it could also be caused by the spin coupling to proximal nuclear spins (the same effect that causes ESEEM). Using simulations, we tested the simplest hypothesis of inhomogeneous broadening as well as inhomogeneous broadening combined with a coupling distribution modeled by a Gaussian centered on $g_{0,\text{eff,R}}$ with a given width. In order to compare the data with the simulations, since we cannot quantitatively know the number of strained spins, we normalize the Rabi oscillation curves and plot them together in Figure 8.4b. Several Gaussian width in the coupling distribution have been tried without success in reproducing the data, therefore it appears that this simple model is not sufficient. Therefore, either the distribution in coupling constant has a non-Gaussian shape (which is likely), or the coupling to the nuclear spins cannot be neglected.

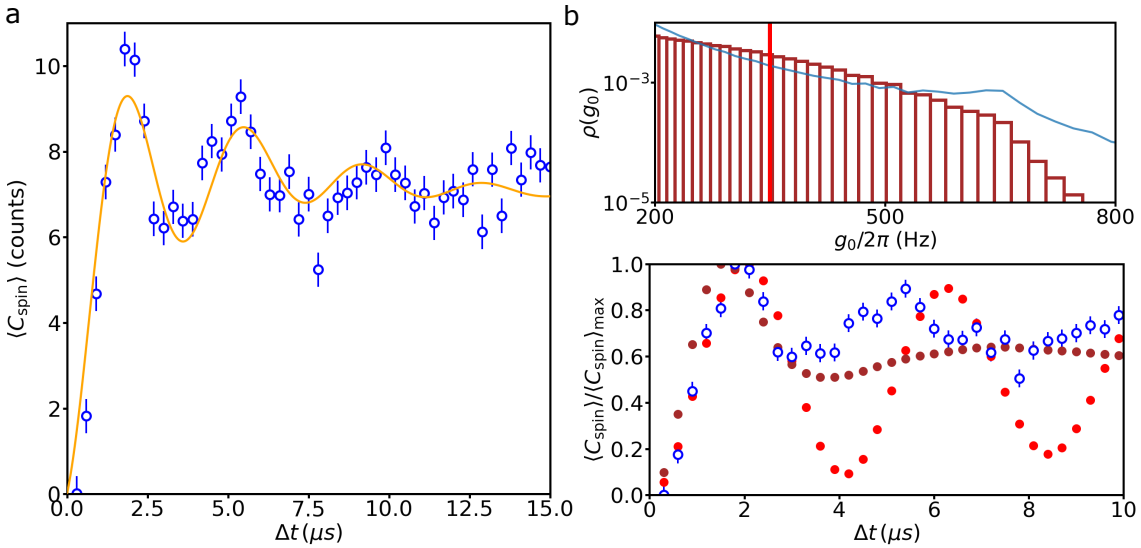

Figure 8.4: **Rabi oscillations varying the pulse duration**. **a**, Rabi oscillations (blue dots) measured by varying the pulse duration Δt with field parameters $\varphi = 30\,^\circ$ and $B_0 = 59.70$ mT and with pulse parameters $\beta = 10\,\mathrm{ns}^{-1/2}$, $T_{\mathrm{int}} = T_{\mathrm{rep}} = 0.25$ ms. The solid line is a fit using Equation 8.3 that yields $g_{0,\mathrm{eff,R}} = 350$ Hz. Error bars are 1σ statistical. **b**, Top panel: coupling distribution $\rho(g_0)$ used for the simulations. For the red simulation, a single value of $g_0 = 350$ Hz is used to simulate a perfectly homogeneous coupling whereas for the brown simulation, a distribution of $\rho(g_0)$ that combines the known spatial distribution of coupling (blue, deduce from Figure 3.11b) and a gaussian distribution centered around $g_0 = 350$ Hz is used to simulate some inhomogeneity in coupling. Bottom panel: the same data normalized (blue dots) plotted together with the normalized simulation (red and brown).

8.2.2 Rabi frequency dependence on the magnetic field

We explore how the contributing spins effective coupling evolves with the magnetic field B_0, using two different methods to determine this quantity. The first method consists in fitting the Rabi oscillations obtained at various B_0 on the side of the main line to determine $g_{0,\mathrm{eff,R}}$, with the plots visible in Figure 8.5a. As we get further away from the main line, we see that the Rabi frequency increases, indicating that $g_{0,\mathrm{eff,R}}$ increases, and the amount of signal decreases, indicating that less spins contribute. The other way to extract the effective coupling is to fit the relaxation curves with an exponential decay of a characteristic time dominated by the radiative relaxation: $T_{1,\mathrm{eff}} = \kappa/4g_{0,\mathrm{eff,r}}^2$. In Figure 8.5b, we perform a fit on the average of all the relaxation curves taken at a given field B_0 and see the same effect than in the Rabi oscillation: the signal relax faster and has a smaller amplitude farther from the main line.

Eventually in Figure 8.5c, we plot the effective coupling for the 2 fitting methods and find that they have a similar dependence with B_0 but have different values, with $g_{0,\mathrm{eff,r}} = 1.53 g_{0,\mathrm{eff,R}} \pm 0.05$. Using the simulations shown in Figure 8.4 (brown), we apply the same fitting procedure to extract the spin coupling and find $g_{0,\mathrm{eff,r,simu}} = 1.38 g_{0,\mathrm{eff,R,simu}}$, in a rather good agreement with the experimental result. The plateau reached far from the main line might be due to a large region where the coupling is rather uniform but where the strain varies, or maybe also to the limited detection sensitivity of our measurement that might not detect the signal from the few higher coupled spins.

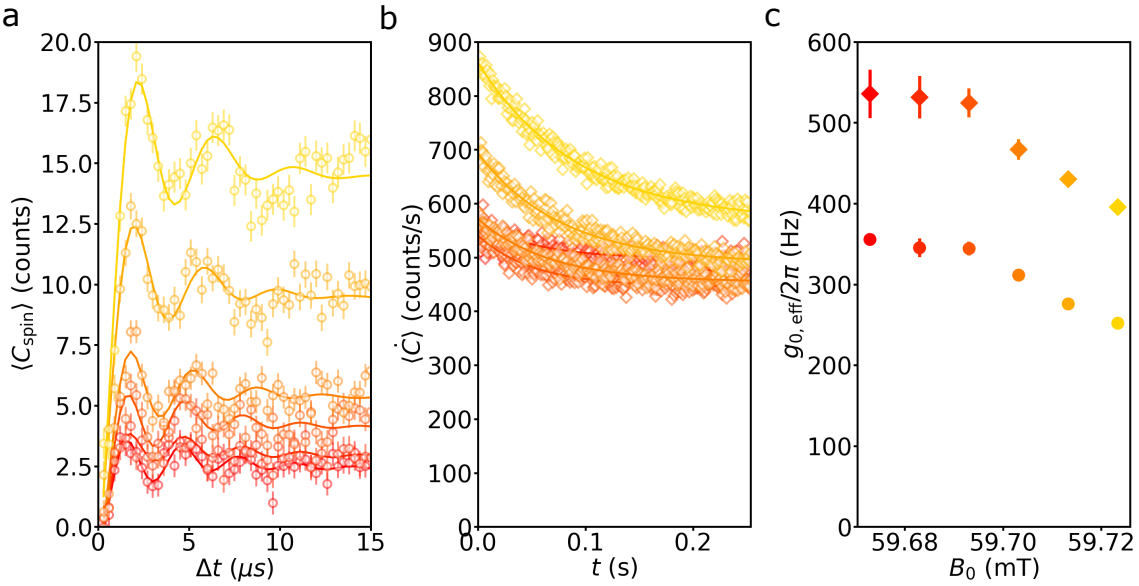

Figure 8.5: **Rabi oscillations at various B_0 (setup 2).** Data measured by varying the pulse duration Δt at various field amplitude from $B_0 = 59.673$ mT (red) to $B_0 = 59.723$ (yellow) by step of 0.01 mT, with the parameters $\varphi = 30\,°$, $\beta = 11.5\,\mathrm{ns}^{-1/2}$ and $T_{\mathrm{int}} = 0.075$ s and $T_{\mathrm{rep}} = 0.25$ s. **a**, Rabi oscillations (dots) fitted using Equation 8.3 (solid lines) to get $g_{0,\mathrm{eff,R}}$. **b**, fluorescence curves at each B_0 averaged over all Δt (hexagons) and exponential fits yielding $g_{0,\mathrm{eff,r}}$. **c**, effective spin coupling $g_{0,\mathrm{eff}}$ as a function of B_0, fitted with the Rabi oscillation (dots) and the relaxation curves (hexagons). The error bars are 1σ deduced from the fits.

8.2.3 Consistency with setup 1 measurements

We report in this part similar measurements done in setup 1 that show the effect of strain as well as coherent oscillations of a spin sub-ensemble.

8.2.3.1 Asymmetry in the Erbium line

We measure the Er^{3+} line at low-ϵ and high-ϵ in setup 1, with results visible in Figure 8.6a. We observe that the high-ϵ spectrum is symmetrical, with a Lorentzian shape, while the low-ϵ spectrum has a strong asymmetry, fitted with Equation 8.1 that yields a skewness consistent with the measurement at the same φ done in setup 2, as can be seen in Figure 8.3.

We plot in Figure 8.6a the effective $T_{1,\mathrm{eff}}$ as a function of B_0 for the low-ϵ spectrum. We find again that there is a longer relaxation time $T_{1,\mathrm{eff}} \approx 0.1$ s in the main line than on the tails where it goes down to $T_{1,\mathrm{eff}} \approx 0.03$ s. The values of $T_{1,\mathrm{eff}}$ are noticeably smaller than for setup 2, as expected due to the difference in the resonator properties κ_{c} and κ_{int} as well as due to the the field orientation, which gives the maximum spin coupling g_0 when aligned with the wire at φ_c.

8.2.3.2 Coherent oscillations varying pulse duration or pulse amplitude

To select a spin sub-ensemble with a relatively homogeneous coupling, we set the field at $B_0 = 59.88$ mT. In Figure 8.6b, we observe coherent oscillations induced by varying the pulse duration Δt and we fit the data with

$$f(\Delta t) = A\sin^2(\Omega_{\mathrm{R0}}\Delta t/2)e^{-\Delta t/T_{c,1}} + B(1 - e^{-\Delta t/T_{c,2}}) + C(1 - e^{-\Delta t/T_{c,3}}) \qquad (8.4)$$

consisting in a Rabi oscillation damped in a characteristic time $T_{c,1}$ superposed with two exponential of characteristic times $T_{c,2}$ ans $T_{c,3}$. The fit allows to extract the effective

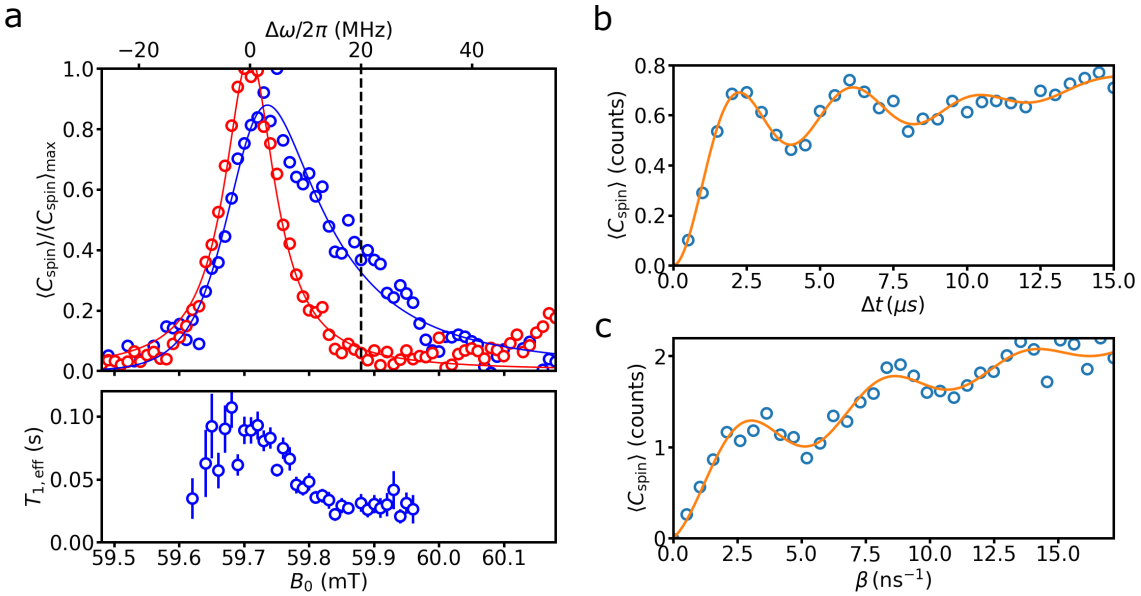

Figure 8.6: **Strain effect and coherent oscillations (setup 1). a**, spectra taken with $\varphi = 47\,^\circ$. Top panel: Normalized spectroscopy at high excitation strength ($\epsilon = 2.1 \times 10^5\,\mathrm{ns}^{-1/2}$, $T_{\mathrm{int}} = 3$ s, $T_{\mathrm{rep}} = 8.6$ s, red dots) and at low excitation strength ($\epsilon = 1 \times 10^4\,\mathrm{ns}^{-1/2}$, $T_{\mathrm{int}} = 0.05$ s, $T_{\mathrm{rep}} = 0.52$ s, blue dots). The high-ϵ data are fitted with a Lorentzian yielding $\Gamma_{\mathrm{inh}}/2\pi = 11$ MHz (red line) while the low-ϵ data are fitted with Equation 8.1 yielding $\gamma \times \Gamma_{\mathrm{inh}}/2\pi = 22.8$ MHz. The black dashed line is the field amplitude used to detect Rabi oscillations. The frequency axis (top axis) is defined centered on the main line. Bottom panel: Effective relaxation time $T_{1,\mathrm{eff}}$ fitted with an exponential decay on the low-ϵ fluorescence data. Only the values where the signal is large enough to extract the fit are plotted. The error bars are 1σ deduced from the fit. **b**, coherent oscillations at $B_0 = 59.88$ mT and $\varphi = 47\,^\circ$ varying the pulse duration Δt (blue dots) with the pulse parameters $\beta \approx 6.5\,\mathrm{ns}^{-1/2}$, $T_{\mathrm{int}} = 0.05$ s, $T_{\mathrm{rep}} = 0.2$ s. The orange line is a fit, using Equation 8.4, that yields $g_{0,\mathrm{eff,R}} = 470$ Hz **c**, coherent oscillations at $B_0 = 59.88$ mT and $\varphi = 47\,^\circ$ varying the pulse amplitude β (blue dots) with the pulse parameters $\Delta t = 4\,\mu$s, $T_{\mathrm{int}} = 0.05$ s, $T_{\mathrm{rep}} = 0.1$ s. The orange line is a fit, using Equation 8.3 with $\Delta t = 4\,\mu$s, that yields $g_{0,\mathrm{eff,R}} = 570$ Hz.

coupling $g_{0,\mathrm{eff,R}} = 470$ Hz. The fit with two exponentials, yielding $T_{c,2} \approx 2.5\,\mu$s and $T_{c,3} \approx 70\,\mu$s, appears as an indication that the non oscillating part of the signal comes from spins with a coupling $g_0 < g_{0,\mathrm{eff,Rabi}}$, whose contribution keeps increasing as Δt increases.

At the same value of B_0, we induce coherent oscillations by varying the pulse amplitude β at fixed $\Delta t = 4\,\mu s$, as shown in Figure 8.6c. The data is fitted with Equation 8.3, which yields an effective coupling $g_{0,\mathrm{eff,R}} = 570$ Hz. We notice that the increase of signal fitted by the exponential is qualitatively different for the two Rabi measurements: when varying Δt the signal saturates after a few Rabi oscillations, whereas when vary β the signal keeps increasing. We understand this difference as being due to the power broadening described in Section 3.3.2.1: as the excitation power increases, the detuned spins contributes more and more to the total signal.

In conclusion, the study of strain effects on Er^{3+} in $CaWO_4$ and the possibility of driving a small ensemble of spins into coherent oscillations appear as a proof of the interest of FD-ESR high sensitivity. In the curves presented in Figure 8.6, we can distinguish a signal of the order ~ 0.1 photon, which corresponds to ~ 10 spins contributing provided the calibrated SMPD efficiency. Therefore, this detection method is very promising for reaching the limit of single spin detection, as it was measured in the Quantronics group

following the results presented in this thesis. Articles and the PhD manuscript of Zhiren Wang are to be published soon about this result.

Chapter 9

Fluorescence detection of spin echoes

In order to fully characterize the spin dynamics, FD-ESR needs to be able to detect spin echoes. Although we have seen in Chapter 7 that direct echo detection is possible, this echo detection method wouldn't yield the FD-ESR sensitivity gain proven in the same chapter. Indeed the amount of signal detected in the echo mode is limited, as discussed in Section 4.3, and the photon shot noise in FD-ESR would limit its sensitivity even for an ideal SMPD.

In this chapter, we report the detection of spin echoes using FD-ESR by adding a restoring pulse to the Hahn echo sequence. Using this detection method, we characterize the Er^{3+} coherence properties. Eventually, we check that, in identical excitation pulse conditions, FD-ESR using restored Hahn echo sequence is more sensitive than ID-ESR for the detection of spin echo.

9.1 Method for the fluorescence detection of spin echo

9.1.1 Restoring the spin echo

As seen in Section 3.3, the fluorescence signal is proportional to the spin longitudinal component $\langle S_Z \rangle$. In order to detect a spin echo using the spin fluorescence, we need to convert the transverse magnetization appearing at the echo time $\langle S_X \rangle$ into a longitudinal one; this is achieved by a $\pi/2$ rotation. Therefore, the ideal FD spin echo sequence consists of 3 pulses $\pi/2_X - \tau - \pi_Y - \tau - \pi/2_\Phi$, which consists in a Hahn echo sequence followed by a restoring $\pi/2$ pulse with phase Φ, followed by microwave fluorescence detection. The echo is expected to appear as a modulation of the number of counts as a function of Φ.

The measurements in Figure 9.1a shows the integrated counts according to Φ with the background removed. This set of data is acquired in setup 1 using high-ϵ pulses with the magnetic field $B_0 = 59.73$ mT set at the middle of the Er^{3+} main line in order to maximize the signal. The measurements consist in 3 different pulse sequences:

- $\epsilon/2_X - \tau - \epsilon_X - \tau - \epsilon/2_\Phi$: the projection modulates the signal according to Φ, with a projection towards the excited state when $\Phi = \pi$.
- $\epsilon/2_X - \tau - \epsilon_Y - \tau - \epsilon/2_\Phi$: the projection modulates the signal according to Φ, with a projection towards the excited state when $\Phi = 0$.
- $\epsilon/2_X - 2\tau - \epsilon/2_\Phi$: the signal is independent from Φ. This appears as a proof that the modulation comes from the spin echo.

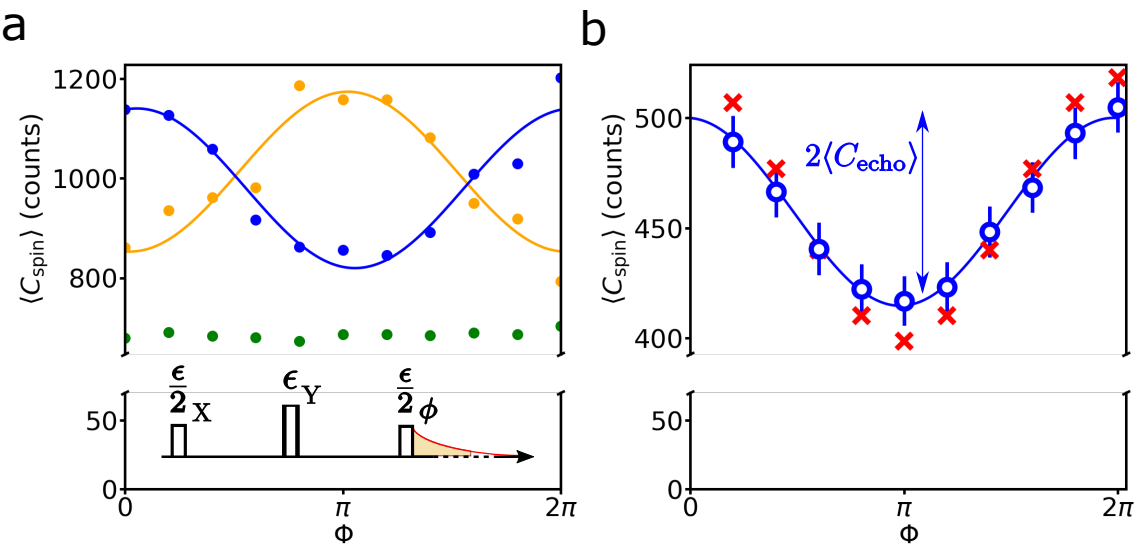

Figure 9.1: **Restoration of spin echo**. **a**, in setup 1, $\langle C_{\text{spin}}\rangle$ as a function of the restoring pulse phase Φ for 3 different pulse sequence: $\epsilon/2_X - \tau - \epsilon_Y - \tau - \epsilon/2_\Phi$ (blue dots), $\epsilon/2_X - \tau - \epsilon_X - \tau - \epsilon/2_\Phi$ (orange dots), and $\epsilon/2_X - 2\tau - \epsilon/2_\Phi$ (green dots). The solid lines are fits with Equation 9.1 that yields $C_{\text{incoh}} = 980$ counts, $C_{\text{echo}} = 160$ counts, $\Phi_0 = 0.05\pi$ (blue curve) and $C_{\text{incoh}} = 1010$ counts, $C_{\text{echo}} = 160$ counts, $\Phi_0 = 0.98\pi$ (orange curve). The experiment parameters are: $B_0 = 59.73$ mT, $\tau = 50\,\mu$s, $\epsilon = 2.1 \times 10^5$ ns$^{1/2}$, $T_{\text{rep}} = T_{\text{int}} = 6.9$ s. **b**, in setup 2, $\langle C_{\text{spin}}\rangle$ as a function of the restoring pulse phase Φ with $\epsilon/2_X - \tau - \epsilon_X - \tau - \epsilon/2_\Phi$ (blue dots) and a fit with Equation 9.1 (blue line) that yields $C_{\text{incoh}} = 460$ counts, $C_{\text{echo}} = 43$ counts, $\Phi_0 = 0.02\pi$. The experiment parameters are: $B_0 = 59.744$ mT, $\varphi = 30\,^\circ$, $\epsilon = 1.4 \times 10^5$ ns$^{1/2}$, $T_{\text{rep}} = T_{\text{int}} = 1.52$ s. The red cross are simulations considering an efficiency $\eta = 0.094$ that matches the number of incoherent photons $\langle C_{\text{incoh}}\rangle$ from the data. We represent $2\langle C_{\text{echo}}\rangle$ with a double arrow.

The modulation can be fitted with a cosine function

$$f(\Phi) = C_{\text{incoh}} + C_{\text{echo}} \cos(\Phi + \Phi_0) \tag{9.1}$$

where C_{incoh} are counts due to incoherent photons, C_{echo} is the signal modulation due to coherent photons resulting from the projection of the echo on the Z axis and Φ_0 is the signal modulation phase depending on the second pulse phase. As we observe a signal modulation with Φ only in the presence of a spin echo, we confirm that this 3 pulses method allows to detect spin echoes with FD-ESR. The presence of the incoherent background in the data of Figure 9.1a is likely due to the spin coupling g_0 inhomogeneity.

To test this hypothesis, we use our simulation tool to model the 3-pulse echo data. Other data are taken in setup 2 using high-ϵ pulses with the magnetic field amplitude $B_0 = 59.744$ mT in order to sit at the middle of the Er^{3+} main line. The field orientation $\varphi = 30\,^\circ$ maximizes the signal amplitude. To compare the simulations with the data, we adjust the efficiency $\eta = 0.094$ to match the incoherent background (the difference with the value reported in Section 7.2.2 is possibly due to a difference in the SMPD calibration). Then, in Figure 9.1b, we observe that the modulation is well reproduced by the simulation; in particular the amplitude is close to the measured value. The slight residual discrepancy in amplitude may be due to ESEEM oscillations, which are not taken into account in the simulation (see below). Overall, the agreement is satisfactory, and confirms our understanding of the echo signal, in particular that the incoherent background is caused by the large Rabi frequency inhomogeneity in this experiment, and would likely vanish in an experiment where well-defined Rabi rotations are applied.

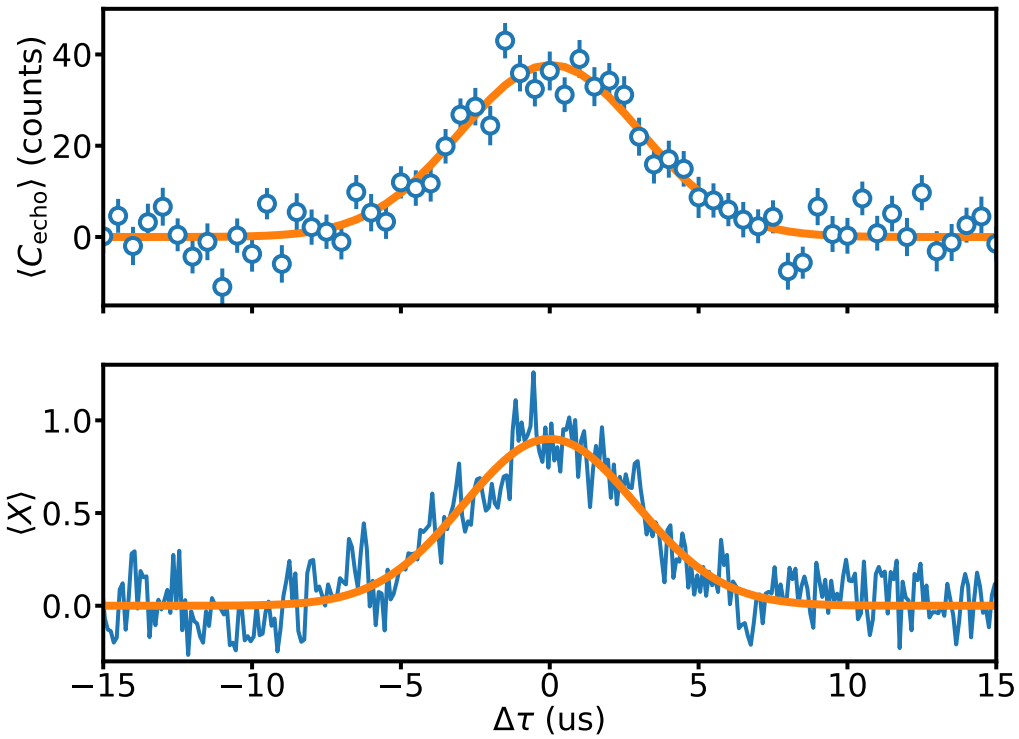

Figure 9.2: **Echo shape detection.** Top panel: in setup 2, $\langle C_{\text{echo}} \rangle$ as a function of the restoring pulse time $\Delta\tau$: $\epsilon/2_X - \tau - \epsilon_Y - \tau + \Delta\tau - \epsilon/2_{X/-X}$. The experiment parameters are: $B_0 = 59.744$ mT, $\tau = 1$ ms, $\varphi = 30\,°$, $\epsilon = 2.9 \times 10^4\,\text{ns}^{1/2}$, $T_{\text{rep}} = T_{\text{int}} = 1.52$ s. Error bars are 1σ statistical. Bottom panel: in setup 1, field quadrature in natural unit as a function of time $\Delta\tau$ centered around the echo following a Hahn echo sequence: $\epsilon/2_X - \tau - \epsilon_Y - \tau -$ echo. The experiment parameters are: $B_0 = 59.73$ mT, $\tau = 50\,\mu$s, $\epsilon = 1.9 \times 10^4\,\text{ns}^{1/2}$, $T_{\text{rep}} = 7.5$s. The solid lines are gaussian fits of the echo mode.

In the following, we use the pulse sequence: $\epsilon/2_X - \tau - \epsilon_Y - \tau - \epsilon/2_\Phi$. In order to extract a quantity proportional to the spin echo amplitude, we define the FD echo amplitude as

$$\langle C_{\text{echo}} \rangle = \frac{\langle C(\Phi = 0) \rangle - \langle C(\Phi = \pi) \rangle}{2}. \tag{9.2}$$

Therefore we have to apply twice the 3 pulse sequence to extract $\langle C_{\text{echo}} \rangle$, hence the division by a factor 2 to correspond to the amount of signal extracted by one sequence. This procedure appears as an analogy of phase cycling in ID echo detection, where the echo emerges successively aligned (in analogy with $\langle C(0) \rangle$) and anti-aligned (in analogy with $\langle C(\pi) \rangle$) with one quadrature. The quantity $2\langle C_{\text{echo}} \rangle$ is represented in Figure 9.1b with a double arrow.

9.1.2 Spin echo shape detection

To further confirm that the signal we get with $\langle C_{\text{echo}} \rangle$ corresponds to the spin echo, we measure the echo shape with FD-ESR. We apply a sequence $\epsilon/2_X - \tau - \epsilon_Y - \tau + \Delta\tau - \epsilon/2_{X/-X}$ and we plot $\langle C_{\text{echo}} \rangle$ as a function of the restoring pulse time position $\Delta\tau$. This measurement is compared to the echo shape detected using ID-ESR in Figure 9.2. We indeed see a similar echo shape with the two detection methods. The echo mode is fitted with a gaussian $f(\Delta\tau) = Ae^{-2\Delta\tau^2/T_e^2}$ that yields similar echo duration for the two detection methods, with $T_{\text{e,FD}} = 6.1\,\mu$s and $T_{\text{e,ID}} = 5.8\,\mu$s.

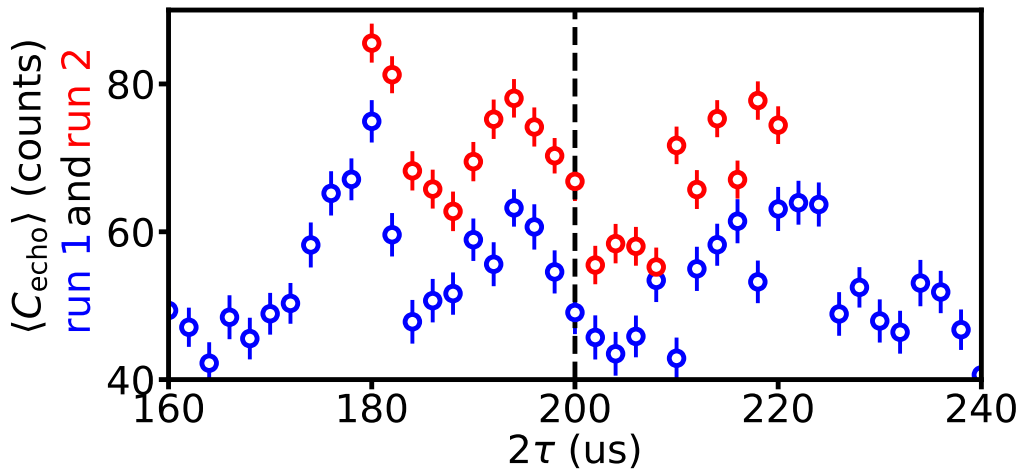

Figure 9.3: **Detection of ESEEM.** In setup 2, we plot $\langle C_{\text{echo}} \rangle$ as a function of the inter-pulse time τ with 1 μs time step for two successive runs with different SMPD calibration, with run 1 (blue) and run 2 (red). The vertical dashed line corresponds to the value of $\tau = 100\,\mu$s used in Figure 9.1b. The experiment parameters are: $B_0 = 59.744$ mT, $\varphi = 30\,°$, $\epsilon = 2.9 \times 10^4\,\text{ns}^{1/2}$, $T_{\text{rep}} = T_{\text{int}} = 1.52$ s.

9.2 Characterization of Erbium coherent properties

In this part, we use the restored Hahn echo sequence to characterize the erbium spin dynamics with FD-ESR. We first detect the ESEEM effect and then measure the spin coherence time using two different protocols that correspond to single quadrature detection and to echo field magnitude detection. All the data shown in this part are taken in setup 2 at high-ϵ, with $B_0 = 59.744$ mT and $\varphi = 30\,°$.

9.2.1 Electron Spin Echo Envelope Modulation (ESEEM)

In order to see ESEEM, we vary the delay τ in the restoring pulse sequence by small time steps of 1 μs. In Figure 9.3, we observe a reproducible modulation of $\langle C_{\text{echo}} \rangle$ in two successive runs. The difference in signal amplitude is likely explained by difference in the SMPD calibration. Note that the ESEEM may explain the residual discrepancy between simulations and data visible in Figure 9.1b since the value $\tau = 100\,\mu$s is not at a maximum of the ESEEM modulation. A detailed understanding of this ESEEM signal is possible [SJ01; Le 22] but was not attempted, as it was not the goal of this study.

9.2.2 Coherence times

9.2.2.1 Measurement in quadrature

To measure the spin coherence time, we detect $\langle C_{\text{echo}} \rangle$ as a function of τ at longer time scales than for the ESEEM measurements. We observe in the data shown in Figure 9.4 the decay of $\langle C_{\text{echo}} \rangle$. We fit this decay with a stretched exponential

$$\langle C_{\text{echo}}(\tau) \rangle = A e^{-(2\tau/T_{2,\text{q}})^{x_\text{q}}} \tag{9.3}$$

where $T_{2,\text{q}}$ is the characteristic decay time and x_q the stretching exponent. The fit yields $T_{2,\text{q}} = 3.6$ ms and exponent $x_\text{q} = 1.7$, in good agreement with the coherence time detected with ID in quadrature, as presented in Figure 5.6. Indeed, the quantity $\langle C_{\text{echo}} \rangle$ is sensitive only to the echo amplitude along the axis X, in analogy with the ID quadrature detection. This brings further confirmation that $\langle C_{\text{echo}} \rangle$ is indeed proportional to $\langle S_X \rangle$ and can be used for Hahn echo detection.

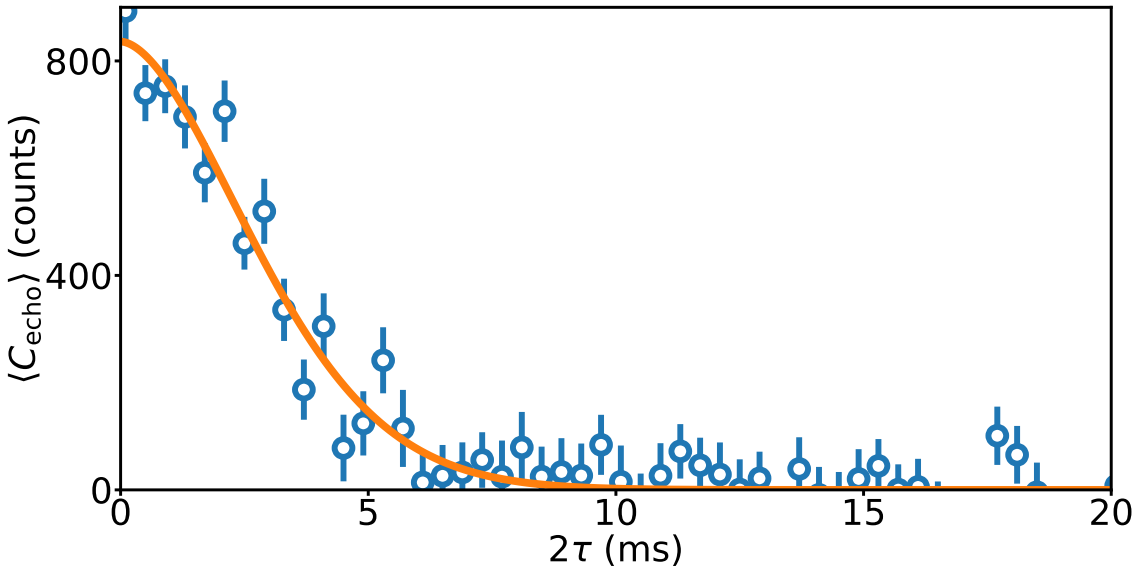

Figure 9.4: **Erbium coherence time in quadrature**. In setup 2, $\langle C_{\text{echo}} \rangle$ as a function of the delay 2τ with 0.2 ms time step (blue dots). The solid line is a fit done with Equation 9.3, yielding a time constant $T_{2,\text{q}} = 3.6\,\text{ms}$ and exponent $x_\text{q} = 1.7$. The experiment parameters are: $B_0 = 59.744$ mT, $\varphi = 30\,°$, $\epsilon = 2.9 \times 10^5\,\text{ns}^{1/2}$, $T_\text{rep} = T_\text{int} = 8.16$ s. Error bars are 1σ statistical.

9.2.2.2 Measurement in amplitude

As explained in Section 5.2.3, the actual erbium spin coherence time, as caused by the ^{183}W spectral diffusion, is significantly longer than the $T_{2,\text{q}} = 3.6$ ms measured using quadrature-sensitive detection, which was found to be limited by B_0 noise. In ID-ESR, it is possible to access the intrinsic coherence time T_2 ms using magnitude averaging [Le +21]. We now explain that it is also possible to perform an analog of magnitude averaging in FD-ESR, enabling us to retrieve the $T_2 \approx 20$ ms coherence time measured in Figure 5.6. The derivation of the equations used here is available in Appendix C.

We start with a model that describes how the magnetic field noise affects the measurements. We attribute the difference of $T_2 \neq T_{2,\text{q}}$ to flux fluctuations in the echo phase $\delta\Phi$ (due to magnetic field noise) that randomize the echo phase once $2\tau > T_{2,\text{q}}$. To model this effect, we describe the integrated counts as

$$C(\Phi, \delta\Phi, \tau) = C_\text{incoh} + C_\text{echo} \cos(\Phi + \delta\Phi) \text{e}^{-(2\tau/T_2)^2} \tag{9.4}$$

where the intrinsic spin coherence time is assume to decay with a Gaussian shape and $\delta\Phi$ is a random variable that follows a gaussian distribution whose standard deviation is $2\sqrt{2}\tau/T_{2,\text{g}}$, such that the probability to have $\delta\Phi = m$ is

$$p(\delta\Phi = m, \tau) = \frac{T_{2,\text{g}}}{\sqrt{\pi} 4\tau} e^{-\frac{(mT_{2,\text{g}})^2}{2(2\sqrt{2}\tau)^2}} \tag{9.5}$$

Experimentally, we have to perform the measurement with a finite number of phases Φ. We derive the result of this model for the fluctuations σ, taken over discrete values of phase $\Phi \in [0, \pi/2, \pi, 3\pi/2]$ and the random phase $\delta\Phi$, yielding

$$\sigma = \sqrt{\text{Var}(C_\text{incoh}) + \frac{C_\text{echo}^2 \text{e}^{-2(2\tau/T_2)^2}}{2}}. \tag{9.6}$$

We readily see that the evolution of this quantity allows to extract the characteristic time T_2.

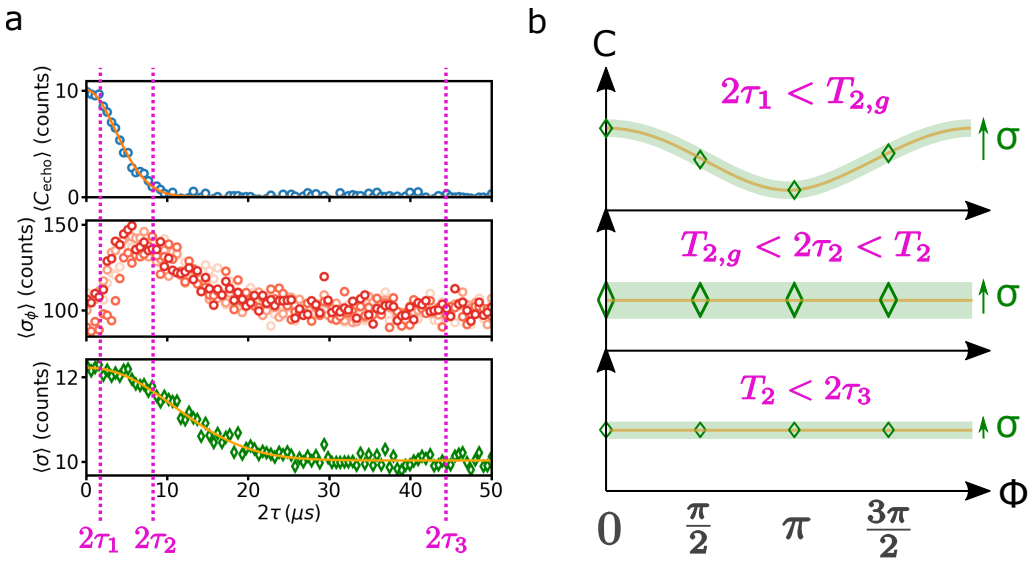

Figure 9.5: **Simulation of the coherent signal evolution**. **a**, we simulate 1000 iterations of $C(\Phi, \delta\Phi, \tau)$ based on the Equation 9.4 with $C_0 = 100$ counts, $C_{\text{echo}} = 10$ counts, $T_{2,\text{g}} = 4$ ms and $T_2 = 20$ ms. The number of counts follows a Poissonian distribution. In the top panel, we plot $\langle C_\text{e} \rangle$ as a function of 2τ (blue circle) with a fit using Equation 9.3 (orange line) that yields $T_{2,\text{q}} = 3.94$ ms and $x_\text{q} = 2.04$. In the middle panel, we plot the variance for each angle σ_Φ with $\Phi \in [0, \pi/2, \pi, 3\pi/2]$ (various shade of red) as a function of 2τ. In the bottom panel, we plot $\langle \sigma \rangle$, the fluctuations over the angles Φ for each iteration then averaged over all the iterations, as a function of 2τ (green diamond) and its fit with Equation 9.7 (orange line) that yields $T_{2,\text{m}} = 20.08$ ms and $x_\text{m} = 1.99$. The vertical magenta dashed line represents 3 different times $2\tau_1 < T_{2,\text{g}}$, $T_{2,\text{g}} < 2\tau_2 < T_2$ and $T_2 < 2\tau_3$. **b**, Sketch of the number of counts C as a function of the restoring pulse angle Φ at 3 different times $2\tau_1$, $2\tau_2$, $2\tau_3$ as shown in figure a. The orange line represents $\langle C \rangle$ and the green width σ_Φ the standard deviation at each angle. The diamonds show the values of $\Phi \in [0, \pi/2, \pi, 3\pi/2]$ used to compute σ, schematically represented with an arrow.

We numerically implement this model with a sample of 1000 iterations of the random variable $\delta\Phi$ and considering a Poissonian distribution of the the total number of counts, with $T_{2,\text{g}} = 4$ ms and $T_2 = 20$ ms. In Figure 9.5a, we show the evolution of 3 quantities:

- C_{echo}, the echo amplitude in one quadrature decays with a characteristic time $T_{2,\text{q}}$, fitted with Equation 9.3 yielding $T_{2,\text{q}} = 3.94$ ms and $x_\text{q} = 2.04$.

- σ_Φ, the variance of a given phase Φ over the random phase $\delta\Phi$ increases up to $2\tau = T_{2,\text{g}}$ and then decreases.

- σ, the variance over the phase Φ and the random phase $\delta\Phi$ decays with a characteristic time fitted with the equation:

$$\langle \sigma \rangle = \sqrt{A e^{-2(2\tau/T_{2,m})^{x_m}} + B} \tag{9.7}$$

  yielding $T_{2,\text{m}} = 20.08$ ms and $x_\text{m} = 1.99$. This confirms that σ is the right quantity to consider in order to extract T_2.

In Figure 9.5b, we consider the integrated counts C as a function of Φ at 3 different times $[2\tau_1, 2\tau_2, 2\tau_3]$ to illustrate the phenomenon that explains the evolution of these quantities:

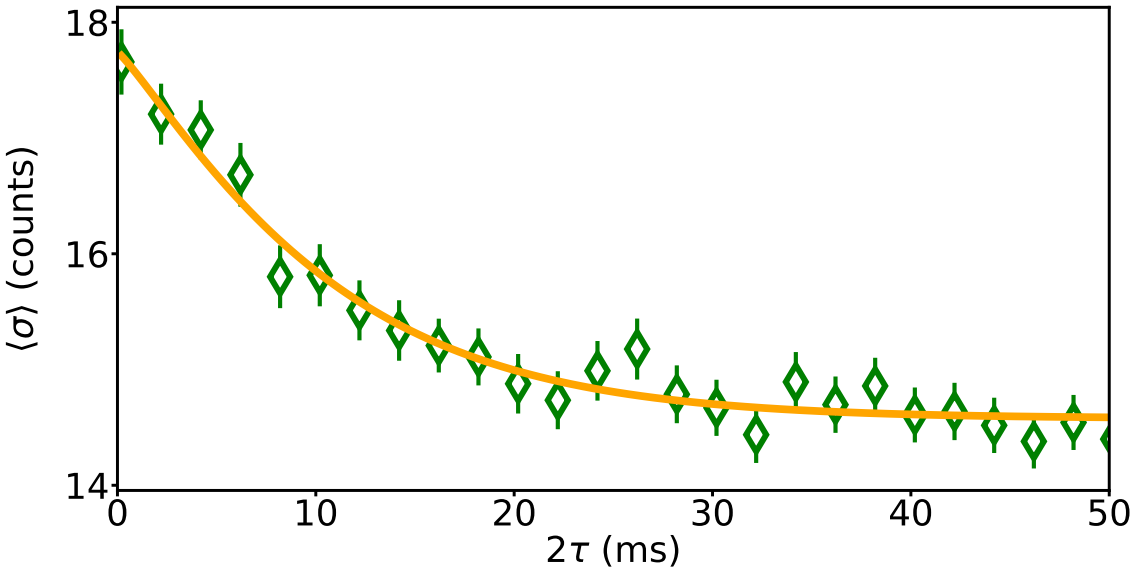

Figure 9.6: **Erbium coherence time in magnitude**. In setup 2, standard deviation $\langle\sigma\rangle$ computed over $\Phi \in [0, \pi/2, \pi, 3\pi/2]$ averaged then over 950 iterations as a function of the delay 2τ (green diamond). The solid line is a fit using Equation 9.6 yielding $T_{\mathrm{m}} = 19.0\,\mathrm{ms}$ and exponent $x_{\mathrm{m}} = 1.13$. The experiment parameters are: $B_0 = 59.744$ mT, $\varphi = 30\,^\circ$, $\epsilon = 2.9 \times 10^4\,\mathrm{ns}^{1/2}$, $T_{\mathrm{rep}} = 1.52$ s, $T_{\mathrm{int}} = 0.55$ s. Error bars are 1σ statistical.

- At $2\tau_1 < T_{2,\mathrm{g}}$, the echo happens along a given phase and contributes to σ by the difference in the average signal of each phase Φ.
- At $T_{2,\mathrm{g}} < 2\tau < T_2$, the echo happens with a random phase and therefore acts as an effective increase in the fluctuations at each phase. The echo still contributes to σ.
- At $T_2 < 2\tau$, the echo is suppressed and doesn't contribute anymore to σ.

We now experimentally realize this measurement procedure. We measure the integrated counts for $\Phi \in [0, \pi/2, \pi, 3\pi/2]$ as a function of τ. Because of fluctuations in the setup, typically due to the air conditioner, a slow fluctuation prevented us from taking the variance at a given τ over the many iterations done during the measurement. To minimize the impact of slow drifts, we found it is better to compute first σ at a given τ for a single iteration and then average it over many iterations. The result, presented in Figure 9.6, shows a decay with 2τ that is fitted with Equation 9.7 to extract $T_{2,\mathrm{m}} = 19.0$ ms and $x_{\mathrm{m}} = 1.13$. The stretched exponent is however not the one expected for spectral diffusion, as shown in Figure 5.6. We believe this is due to the low SNR of these measurements.

9.3 Signal-to-Noise Ratio (SNR) experimental comparison for spin echo detection

We now compare the SNR of ID-ESR and FD-ESR for echo spin detection in identical excitation conditions. We use setup 1 with $B_0 = 59.73$ mT and apply a relatively low-ϵ pulse, namely $\epsilon = 9.8 \times 10^3\,\mathrm{ns}^{1/2}$, within the regime where FD-ESR has proven a gain in sensitivity to detect spins in Section 7.3. Histograms are acquired following procedures similar as the ones detailed in Section 7.3:

- ID-ESR: we measure the integrated echo amplitude with the pulse sequence $\epsilon/2_X - \tau - \epsilon_Y - \tau -$ echo over 4000 iterations. It is expressed in its natural unit thanks to the echo photon number calibration discussed in Section 7.3.1.1.

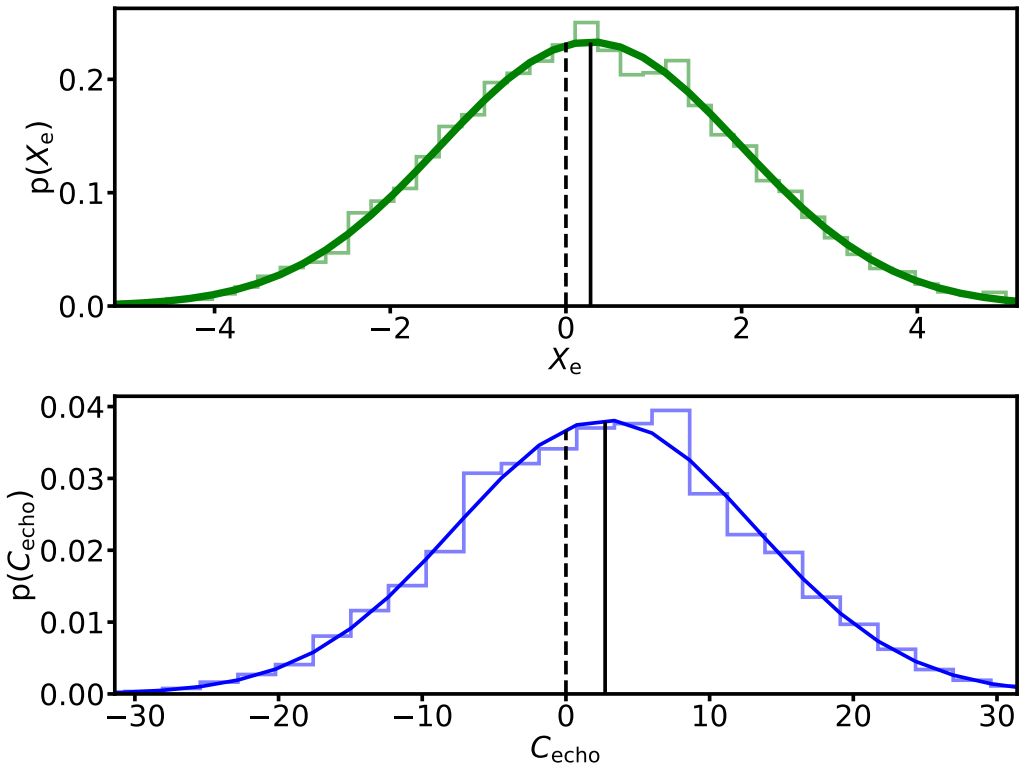

Figure 9.7: **Histogram comparison between ID and FD for echo detection (setup 1).** Histograms of echo detection with ID (green, 4000 iterations) and FD (blue, 4000 iterations) taken in the same conditions with $\epsilon = 9.8 \times 10^3\,\mathrm{ns}^{1/2}$, $\tau = 50\,\mu$s and $T_{\mathrm{rep}} = 0.43$ s with their gaussian fits (solid lines). The solid black line show the distributions mean value while the dashed black line shows the 0. Graphs are aligned on 0 in horizontal axis and are 6 standard deviation large.

- FD-ESR: we measure C_{echo} using 2 successive pulse sequences: $\epsilon/2_X - \tau - \epsilon_Y - \tau - \epsilon/2_X$ and $\epsilon/2_X - \tau - \epsilon_Y - \tau - \epsilon/2_{-X}$. We repeat the measurement over 9000 iterations.

Here we are directly comparing the same echo using the two detection methods. The result is shown in Figure 9.7, where the histograms are plotted to allow a visual comparison of the SNR: the x axis is centered on 0 and its scale is 6 times the distribution standard deviation for each histogram. The center of the histogram, corresponding to the measurement mean value, is further away from 0 for FD than for ID, which is an indication of the FD gain in sensitivity. This is confirmed by the SNR computation yielding $\mathrm{SNR}_{\mathrm{ID}} = 0.08$ and $\mathrm{SNR}_{\mathrm{FD}} = 0.13$.

We assume that the number of spins contributing to the echo corresponds to the variation of the observable $\langle S_z \rangle$ under the first pulse in the Hahn echo sequence. We perform the simulation of this pulse for the conditions used here, yielding $N_{\mathrm{spin}} = 320$ spins. Given the measured SNR values, we deduce the detection sensitivity for the two methods:

- In ID-ESR, the sensitivity if 1200 [Spins/$\sqrt{\mathrm{Hz}}$]
- In FD-ESR, the sensitivity is 750 [Spins/$\sqrt{\mathrm{Hz}}$]

The FD sensitivity is not as good as the record in ID-ESR [Ran+20a], but this likely due differences in the resonator design. In Z. Wang thesis, a sensitivity of 0.5 [Spins/$\sqrt{\mathrm{Hz}}$] is reached with single pulse FD-ESR, thanks to an optimized SMPD and resonator design, giving access to single-spin measurements

In conclusion of this chapter, we have proven that we can detect spin echoes using FD-ESR with a sensitivity gain compared ID-ESR. We also have proposed and performed a method to access the spin intrinsic coherence time in the presence of magnetic noise in analogy to magnitude averaging in ID-ESR.

Chapter 10

Conclusion

Fluorescence detection as a widely applicable high sensitivity spin detection method

In this thesis, we investigated an Electron Spin Resonance (ESR) spectroscopy method based on Fluorescence Detection (FD), recently proposed in [Alb+21]. The results presented here show that FD-ESR can reach a higher sensitivity than the usual Inductive Detection (ID) ESR while preserving all the ESR detection possibilities.

We applied FD-ESR to Rare Earth Ions (REI) in Scheelite using a Single Microwave Photon Detector (SMPD) device, at millikelvin temperature. The experiment used a superconducting resonator magnetically coupled to the resonant spin ensemble in order to manipulate and detect the spin signal. We reported large-scale FD-ESR spectra showing signal from a wide variety of spin species, proving the generality of this detection method. As FD gives immediately access to the spin fluorescence, it calls for a better understanding of the spin relaxation curve. Focusing on Erbium ions, we modeled the spin ensemble dynamics as the sum of single spin contribution and performed simulations that quantitatively reproduce the fluorescence signal over three orders of magnitude in excitation pulse strength. The comparison of ID and FD in similar spin excitation conditions confirmed a sensitivity gain with FD for spin detection, reaching a factor 16 at the lowest excitation strength explored. This higher sensitivity allowed us to measure the frequency shifts caused by mechanical strain on a small spin sub-ensemble and to study its dependence with the static field angle. Thanks to the spin sub-ensemble coupling homogeneity, we observed spin coherent oscillations. Although FD is sensitive to incoherent photons, we used a three-pulse sequence to perform FD of Hahn echoes. We characterized the spin coherence time using FD, and demonstrated a method to access the spin intrinsic coherence time even in the presence of magnetic field noise. Eventually, we show that there is also a sensitivity gain with FD compared to ID for echo detection.

Perspectives for future experiments

Considering the wide variety of spin signal detected in our Scheelite sample using FD-ESR, it would be interesting to explore even larger field parameters to push forward the paramagnetic impurities characterization. Moreover, some peaks not yet attributed to spin species could be better known through these wider range spectra. As the fluorescence curves show that some spins have a decay time way longer than the REIs, and therefore were not properly measured given the experimental parameters used in this thesis, we could better characterize those peaks by increasing the experiment repetition time.

The FD-ESR characterization could be implemented to other kind of sample than Scheelite. It would be straight forward to apply it to other kind of crystal on which

we can pattern a superconducting resonator. Another appealing application would be the characterization of materials deposited on top of the resonator. That way, we could characterize other type of spin species not embedded in a crystal using FD-ESR, opening the way for applications in chemistry [Sen90].

Our data call for a better modeling of the behavior of REIs under strain. Even though our simulations reproduced quantitatively most of the data presented in this thesis, the strain effect remained elusive to it. It would be interesting to explore the **g**-tensor dependence with strain in order to implement it in our simulations.

The Signal-to-Noise Ratio (SNR) study described in this thesis explores a parameter range where FD always gives a sensitivity gain compared to ID. However, the gain seriously reduced at high excitation strength, and one would expect a SNR crossover at even higher pulse strength. It would be interesting to reach that regime where ID is more sensitive than FD and describe further the conditions where the crossover happens. For characterization applications, it would be of great interest to be able to know which detection method to use in order to maximize the detection sensitivity according to the characteristics of the spin system under study.

Eventually, our experiment sensitivity could be even more enhanced. The resonator design could be modified to increase the spin coupling, for instance by shrinking the wire width. The SMPD device dark counts could be reduced by increasing the working frequency or by narrowing the resonator bandwidth. The magnetic field could be applied on the crystal c-axis, so that spin like Erbium ions with $g_{\mathrm{perp}} > g_{\mathrm{para}}$ gets even more coupled to the resonator. All in all, by implementing such modifications, the single spin sensitivity for Erbium detection in a Scheelite sample has already been reached in our group, as will be reported in the theses of Z. Wang and L. Balembois.

Appendix A

Simulations

In the following we describe the set of equations implemented in a python code to numerically simulate the spin ensemble dynamics coupled to a cavity. The simulation is valid in the low-ensemble-cooperativity regime. In this regime, the dynamics of each spin packet is simulated independently, and the ensemble result is obtained by simply summing each spin packet contribution weighted by its density.

A.1 Single spin evolution

The simulation is performed by considering separately each spin packet j, characterized by its frequency detuning from the resonator $\Delta\omega_j$, and its coupling $g_{0,j}$. This yields a relaxation rate

$$\Gamma_{1,j} = \Gamma_{\mathrm{R,j}} + \Gamma_{\mathrm{NR}} = \frac{g_{0,j}^2}{\frac{\kappa}{4} + \Delta\omega_j} + \Gamma_{\mathrm{NR}}. \tag{A.1}$$

with the contributions of the Purcell radiative rate $\Gamma_{\mathrm{R,j}}$, that depends on the cavity total loss rate κ, and a non-radiative rate Γ_{NR} considered homogeneous over the spin ensemble.

Initialization

The simulation takes into account the finite repetition time by initializing the spin packet as follows. It is assumed that at the end of the coherent evolution in the previous sequence, the spin packet is fully un-polarized, $\langle S_{z,j} \rangle = 0$. Then, after a waiting time T_{rep}, the polarization at the beginning of the sequence should be

$$\langle S_{Z,j}(t=0) \rangle = \frac{1}{2}(e^{-\Gamma_{1,j} T_{\mathrm{rep}}} - 1). \tag{A.2}$$

which we thus consider as the initialization of the spin packet at the beginning of the computation.

Excitation pulse field

The dynamics depends on the drive field, which consists of a sequence of pulses of amplitude $\beta(t)$. We take into account the cavity filtering of these pulses by first computing the time-dependent intra-cavity field $\alpha(t)$, using

$$\frac{d\alpha}{dt} = -\frac{\kappa}{2}\alpha - \sqrt{\kappa_c}\beta \tag{A.3}$$

with κ_{c} the cavity coupling rate to the microwave lines. Note that here, we neglect the modifications of the intra-cavity field caused by spin absorption; this corresponds to the

low-ensemble-cooperativity hypothesis (or equivalently, in magnetic resonance terms, the neglect of radiation damping).

Spin dynamics

The spin packet j dynamics under the influence of the resonator intra cavity field α is then computed as

$$\dot{\boldsymbol{S}}_j = \begin{pmatrix} \langle \dot{\hat{S}}_{X,j} \rangle \\ \langle \dot{\hat{S}}_{Y,j} \rangle \\ \langle \dot{\hat{S}}_{Z,j} \rangle \end{pmatrix} = \begin{pmatrix} 0 & \Delta\omega_j & 0 \\ -\Delta\omega_j & 0 & 2g_{0,j}\alpha \\ 0 & 2g_{0,j}\alpha & 0 \end{pmatrix} \boldsymbol{S} \; - \begin{pmatrix} \Gamma_2 \\ \Gamma_2 \\ \Gamma_{\mathrm{R,j}} + \Gamma_{\mathrm{NR}} \end{pmatrix} \boldsymbol{S} \tag{A.4}$$

with Γ_2 the spin decoherence rate considered homogeneous over the spin ensemble.

Case 1: spin induction detection

If we want to compute the inductively emitted spin-echo, we then obtain the intracavity field considering the spin contribution

$$\frac{d\alpha}{dt} = -\frac{\kappa}{2}\alpha - \sqrt{\kappa_c}\beta + ig_{0,j}\langle S_{-,j} \rangle. \tag{A.5}$$

Case 2: spin fluorescence detection

To simulate the spin radiative energy relaxation, we compute the spin dynamics at a time $t > T_{\mathrm{empty}}$ following the excitation pulse sequence such that $\alpha(t = T_{\mathrm{empty}}) = 0$. The spin relaxes exponentially as it generates an intracavity field:

$$|\alpha_j|^2(t) = \frac{\Gamma_{\mathrm{R,j}}}{\kappa} \frac{1 + 2S_{Z,j}(t = T_{\mathrm{empty}})}{2} e^{-(\Gamma_{1,j})t}. \tag{A.6}$$

Field emitted in the line

The intracavity field induces a field emitted in the microwave line:

$$\alpha_{\mathrm{out,j}} = \sqrt{\kappa_{\mathrm{c}}}\alpha_j \tag{A.7}$$

A.2 Spin ensemble signal

Case 1: spin induction detection

The contributions from all the spin packets are coherent during the echo, yielding

$$\langle \alpha_{\mathrm{out}} \rangle(t) = \frac{\kappa_{\mathrm{c}}}{\kappa} 2i \sum_j g_{0,j}\rho(\Delta\omega_j) d\Delta\omega_j \rho(g_{0,j}) dg_{0,j} \langle S_{-,j} \rangle(t). \tag{A.8}$$

where $\rho(\Delta\omega_j)$ is the spin frequency density at $\Delta\omega_j$ and $\rho(g_{0,j})$ is the spin coupling density at $g_{0,j}$, such that for a total of N_{spin} we have

$$N_{\mathrm{spin}} = \sum_j \rho(\Delta\omega_j) d\Delta\omega_j \rho(g_{0,j}) dg_{0,j}. \tag{A.9}$$

Case 2: spin fluorescence detection

The total fluorescence signal is the sum of the contributions from all the spin packets, that writes at time $t > T_{\text{empty}}$

$$\langle \alpha^{\dagger}_{\text{out}} \alpha_{\text{out}} \rangle (t) = \sum_j \rho(\Delta\omega_j) d\Delta\omega_j \rho(g_{0,j}) dg_{0,j} \langle \alpha^{\dagger}_{\text{out},j} \alpha_{\text{out},j} \rangle (t) \tag{A.10}$$

Appendix B

Resonator fabrication

B.1 Microwave simulations

Microwave simulations were conducted using Ansys HFSS software in order to predict the resonator frequency for a given resonator design. The simulator solves the system electromagnetic eigenmodes and yields the corresponding mode frequency $\omega/2\pi$ and quality factor $Q_c = \omega/\kappa_c$. The resonance frequency is targeted around 7 GHz for a few reasons: this frequency is high enough to have the spins polarized at a temperature of $T = 10$ mK since $\hbar\omega \gg k_B T$, this frequency is small enough so that a relatively small field $B_0 \approx 100$ mT allows to set the REI ions on resonance with the resonator, and it corresponds to a frequency in the detection range of our SMPDs. The various elements taken into account in the simulations are:

- the copper box
- the antenna, coupled to a $50\,\Omega$ line
- a silicon piece meant to hold the sample
- the $CaWO_4$ sample
- the resonator

All copper elements and the resonator are taken as perfect conductors. The silicon relative permittivity at cryogenic temperature is taken as $\epsilon_{Si} = 11.5$ [Kru+06]. For $CaWO_4$, the relative permittivity is anisotropic, with $\epsilon_{a,b} = 11.7 \pm 0.1$ and $\epsilon_{a,b} = 9.5 \pm 0.2$ [TA75].

The simulation tool solves Maxwell equations and gives the spatial distribution of electromagnetic quantities for 1 Joule of energy in the eigenmode, as presented in Figure B.1b. From those quantities, we can compute the resonator impedance and find $Z_0 = 35 \pm 2\,\Omega$.

B.2 Fabrication recipe

The 2D superconducting resonator was made out of Niobium (Nb), a superconductor material with $T_c = 9.2$ K and a bulk critical magnetic field $B_c = 0.2$ T. The resonator fabrication steps done in a clean room are the following:

- **Substrate cleaning**: 5' in acetone bath with ultrasounds, 1' in isopropanol (IPA) bath with ultrasounds, then rinse in another bath of IPA for 30" and blow dry. The sample is put on a hot plate at 115 °C for 5' to evaporate any residual water.
- **Metal deposition**: sputter of a 50 ± 3 nm thick Niobium layer. To avoid metal deposition on the sample sides, it is surrounded by silicon pieces.

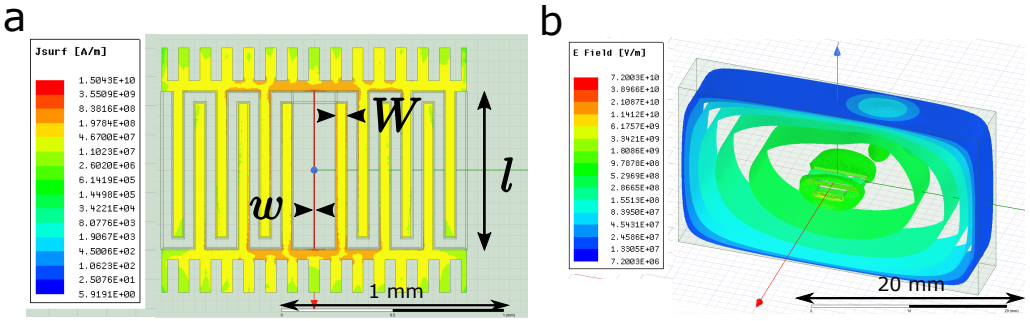

Figure B.1: **Microwave simulations a** Simulation result showing the resonator design with its geometrical parameters: the wire width w, the wire length l and the capacitive fingers width W. The colors represent in logarithmic scale the surface current when 1 J of energy is injected in the resonator resonance mode. **b** Picture of the whole simulation result with colors representing the electric field in the box when 1 J of energy is in injected in the box fundamental mode.

- **Resist coating**: Clean of the Niobium surface with 3' in acetone while moving the chip with tweezers, twice 30" in IPA in two different bath, 3' on a 110 °C hot plate. Cover the sample with nLOF2020 resist: 4" at 8000 rpm (rotations per minute) acceleration 4000, then 60" at 4000 rpm acceleration 1000. Baking for 90" on hot plate at 110 °.
- **Optical lithography**: Exposure done with the lithography machine Heidelberg µMLA: dose 45 mJ/cm2 and defoc 5. The nLOF is a negative resist such that only the exposed parts stay.
- **Resist development**: post exposition bake of 90" on hot plate at 110 °, 1' in MF319 before rinsing for 1' in water.
- **Dry etching**: Reactive ion etching: base pressure of 12 µbar, 10 sccm (standard cubic centimeters per minute) of Ar, 20 sccm of SF6 and 50 W of power. To avoids border effect in the etching, the sample is surrounded by silicon pieces. A laser reflectometry indicates when the niobium is etched, in 39", to which we add an overetch time of 11".
- **Resist removal**: 15' in remover P1331 at $50 - 60°$, rinse in two successive bath of water for 30". Last cleaning step with 3' in acetone then twice 30" in IPA.

In such a fabrication process, we expect to have some uncontrolled parameters influencing the resulting resonator frequency. In order to target a frequency, we have patterned 3 resonators with various geometrical dimensions to increase the probability to have one of them in a convenient frequency range.

Appendix C

Measuring spin coherence time in the signal fluctuations

In this chapter, we derive the equation Equation 9.6 used to describe the evolution of the signal fluctuations $\sigma(\tau) = \sqrt{\mathrm{Var}(C(\Phi, \delta\Phi, \tau))}$.

In our model, we express the signal as

$$C(\Phi, \delta\Phi, \tau) = C_{\mathrm{incoh}} + C_{\mathrm{echo}} \cos(\Phi + \delta\Phi) \mathrm{e}^{-(2\tau/T_2)^2} \tag{C.1}$$

where T_2 is the intrinsic spin coherence time (which we assume to decay with a Gaussian shape) and $\delta\Phi$ is a random variable that follows a gaussian distribution whose standard deviation is $2\sqrt{2}\tau/T_{2,\mathrm{g}}$, such that the probability to have $\delta\Phi = m$ writes as

$$p(\delta\Phi = m, \tau) = \frac{T_{2,\mathrm{g}}}{\sqrt{\pi} 4\tau} e^{-\frac{(mT_{2,\mathrm{g}})^2}{2(2\sqrt{2}\tau)^2}} \tag{C.2}$$

C.1 Evolution of C_{echo}

We first consider how the signal evolves once averaged over the random variable $\delta\Phi$:

$$\begin{aligned}
\langle C(\Phi, \delta\Phi, \tau) \rangle_{\delta\Phi} &= C_{\mathrm{incoh}} + \frac{C_{\mathrm{echo}} T_{2,\mathrm{g}} \mathrm{e}^{-(2\tau/T_2)^2}}{\sqrt{\pi} 4\tau} \int_{\infty}^{\infty} \cos(\Phi + x) e^{-\frac{(mT_{2,\mathrm{g}})^2}{2(2\sqrt{2}\tau)^2}} dx \\
&= C_{\mathrm{incoh}} + \frac{C_{\mathrm{echo}} T_{2,\mathrm{g}} \mathrm{e}^{-(2\tau/T_2)^2}}{\sqrt{\pi} 4\tau} \mathrm{Re}\left(\int_{\infty}^{\infty} e^{-i(\Phi+x)} e^{-\frac{(mT_{2,\mathrm{g}})^2}{2(2\sqrt{2}\tau)^2}} dx \right) \\
&= C_{\mathrm{incoh}} + C_{\mathrm{echo}} \mathrm{e}^{-(2\tau/T_2)^2} \cos(\Phi) e^{-(\frac{2\tau}{T_{2,\mathrm{g}}})^2}
\end{aligned} \tag{C.3}$$

We find the expression for $C_{\mathrm{echo}}(\tau)$:

$$\begin{aligned}
C_{\mathrm{echo}}(\tau) &= \frac{\langle C(0, \delta\Phi, \tau) \rangle_{\delta\Phi} - \langle C(\pi, \delta\Phi, \tau) \rangle_{\delta\Phi}}{2} \\
&= C_{\mathrm{echo}} \mathrm{e}^{-(2\tau/T_2)^2} e^{(\frac{2\tau}{T_{2,\mathrm{g}}})^2}
\end{aligned} \tag{C.4}$$

$C_{\mathrm{echo}}(\tau)$ decays in a characteristic time shorter than T_2, as measured in Figure 9.4, that we fit with the equation

$$\langle C_{\mathrm{echo}}(\tau) \rangle = A \mathrm{e}^{-(2\tau/T_{2,\mathrm{q}})^{x_{\mathrm{q}}}}, \tag{C.5}$$

yielding a coherence time $T_{2,\mathrm{q}}$ and a stretching coefficient x_{q} in quadrature detection.

C.2 Evolution of σ

To find a quantity that decays with a characteristic time T_2, we are interested in the overall signal fluctuations over $\delta\Phi$ and Φ, expressed in the variance:

$$\sigma^2 = \mathrm{Var}(C_{\mathrm{incoh}}) + \mathrm{Var}(C_{\mathrm{echo}}\cos(\Phi+\delta\Phi)\mathrm{e}^{-(2\tau/T_2)^2}) \tag{C.6}$$

To compute the coherent contribution to the variance, we start by deriving:

$$\begin{aligned}\langle (C_{\mathrm{echo}}\cos(\Phi+\delta\Phi)\mathrm{e}^{-(2\tau/T_2)^2})^2\rangle_{\delta\Phi} &= \frac{C_{\mathrm{echo}}^2 T_{2,\mathrm{g}}\mathrm{e}^{-2(2\tau/T_2)^{x_2}}}{\sqrt{\pi}4\tau}\int_\infty^\infty \cos^2(\Phi+x)e^{-\frac{(mT_{2,\mathrm{g}})^2}{2(2\sqrt{2}\tau)^2}}dx \\ &= \frac{C_{\mathrm{echo}}^2 T_{2,\mathrm{g}}\mathrm{e}^{-2(2\tau/T_2)^2}}{2\sqrt{2\pi}2\tau}\int_\infty^\infty e^{-\frac{(mT_{2,\mathrm{g}})^2}{2(2\sqrt{2}\tau)^2}} + \cos(2(\Phi+x))e^{-\frac{(mT_{2,\mathrm{g}})^2}{2(2\sqrt{2}\tau)^2}}dx \\ &= \frac{C_{\mathrm{echo}}^2\mathrm{e}^{-2(2\tau/T_2)^2}}{2}(1+\cos(2\Phi)e^{-4(\frac{2\tau}{T_{2,\mathrm{g}}})^2})\end{aligned} \tag{C.7}$$

Average in the continuum limit

By averaging over Φ in the continuum limit we obtain:

$$\mathrm{Var}(C_{\mathrm{echo}}\cos(\Phi+\delta\Phi)\mathrm{e}^{-(2\tau/T_2)^2}) = \frac{C_{\mathrm{echo}}^2\mathrm{e}^{-2(2\tau/T_2)^2}}{2}. \tag{C.8}$$

Coming back to σ, it yields

$$\sigma = \sqrt{\mathrm{Var}(C_{\mathrm{incoh}}) + \frac{C_{\mathrm{echo}}^2\mathrm{e}^{-2(2\tau/T_2)^2}}{2}}. \tag{C.9}$$

Average with discrete phases

Let's consider the average over $\Phi \in [0, \pi/2, \pi, 3\pi/2]$. Then we have:

$$\begin{aligned}\sum_\Phi \langle C_{\mathrm{echo}}\cos(\Phi+\delta\Phi)\mathrm{e}^{-(2\tau/T_2)^2}\rangle_{\delta\Phi} &= 0, \\ \sum_\Phi \langle (C_{\mathrm{echo}}\cos(\Phi+\delta\Phi)\mathrm{e}^{-(2\tau/T_2)^2})^2\rangle_{\delta\Phi} &= \frac{C_{\mathrm{echo}}^2\mathrm{e}^{-2(2\tau/T_2)^2}}{2}.\end{aligned} \tag{C.10}$$

Coming back to σ, it yields

$$\sigma = \sqrt{\mathrm{Var}(C_{\mathrm{incoh}}) + \frac{C_{\mathrm{echo}}^2\mathrm{e}^{-2(2\tau/T_2)^2}}{2}}. \tag{C.11}$$

The evolution of σ is fitted with

$$\langle\sigma\rangle = \sqrt{A\mathrm{e}^{-2(2\tau/T_{2,m})^{xm}} + B} \tag{C.12}$$

yielding a coherence time $T_{2,\mathrm{m}}$ and a stretching coefficient x_m in magnitude detection.

Appendix D

Carbon footprint

During my PhD, I have participated to initiatives to reduce the laboratory environmental footprint. In this chapter, I detail the carbon footprint of Quantronics research group. It is a work that I have done with the support of Lucille Zribi, who did the carbon footprint of another research laboratory named "Laboratoire des Sciences du Climat et de l'Environnement" (LSCE), and Hélène le Sueur, researcher in Quantronics.

D.1 Motivations

It all start with an observation: every year, humankind emits more Greenhouse Gas (GG). The integrated emissions have already caused a temperature rise of more than 1°, and this rise is accelerating. According to the IPCC, this climate change is triggering catastrophies, with dire human impacts. A simple climate change causality chain is proposed in Figure D.1.

We are concerned in many ways by this phenomenon. On the one hand because it is in our interest, because we are suffering from it and we will only suffer more in the near future. Even if we are not hit yet, we want to react and find a way to help in empathy for the others not as lucky as us. On the hand we have a responsibility, because our research emits GG and because, as scientists, we have a specific role to play in the much needed society change. It is also a matter of continuing our passionate research: constraints will gradually appear to reduce emissions throughout society, and research fields that have not taken it into account might face serious troubles.

Scientists are getting involved to mitigate the climate change: through individual choices that allow them to be in line with their values but also through collective responses that ignit change at a wider scale. In particular, scientists in France have gatherer into an association and a research group to promote the reduction of research GG emissions [lab].

Even if we are willing to curb our GG emissions, where to start? In Quantronics, we have realized our carbon footprint to quantify our emissions in order to undertake then the right actions to efficiently reduce our GG emissions. Furthermore, the carbon footprint allows to have a support for discussions and debates within the whole SPEC laboratory.

D.2 Method

The carbon footprint computation principle is straightforward: we gather all the data associated to our research activities, then find in reference databases the most relevant emission factor and realize the product of the two figures. This computation is represented in Figure D.2

There is a choice to make in term of scope for our carbon footprint, with a balance between considering all the relevant GG emission sources and the amount of work it

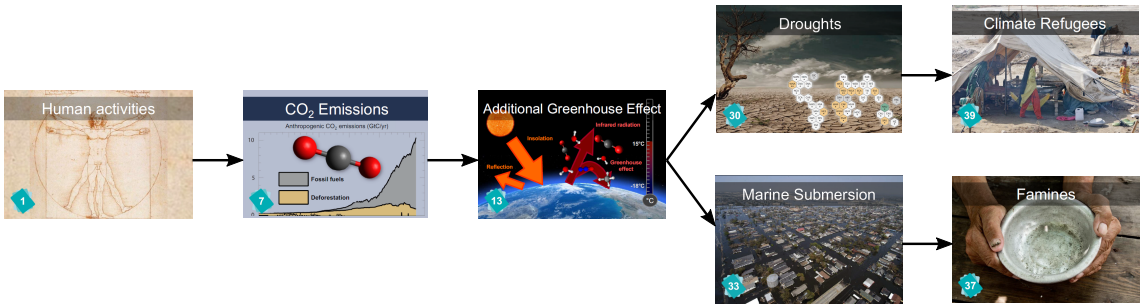

Figure D.1: **Climate change.** Simplified causality chain of the ongoing climate change. We believe that scientists have a specific role to play to mitigate it, by reducing the impact of their research and participating to a much needed societal change. Pictures are from [RIN].

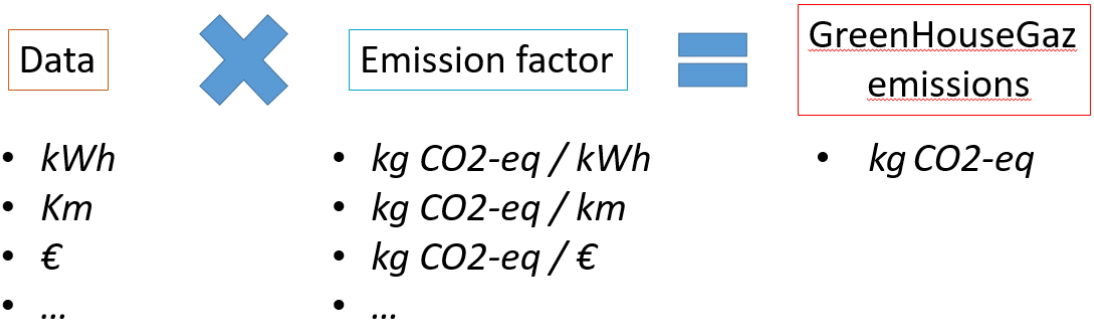

Figure D.2: **Carbon footprint method.** Carbon footprint computation principle: after collecting the relevant data in our laboratory, expressed in various units, we use emission factors from reference databases to convert it into an equivalent mass of CO_2.

represents. Based on the work of Lucille Zribi, we have chosen the few emission sources that were relevant in the case of LSCE carbon footprint:

- the buying of equipments
- the transportation
- the energy consumption
- the laboratory buildings fabrication

The carbon footprint has been realized at the relatively small scale of Quantronics to have an easy access to the data. However, it would be desirable to realize the carbon footprint at a wider scale such as the SPEC laboratory to take into account a larger audience and to propose actions at a larger scale. This is the first carbon footprint done in Quantronics, so we decided to realize it for the year 2019, before the impact of COVID on our research.

D.3 Results

The overall result of Quantronics carbon footprint for the year 2019, shown in Figure D.3, is 16 tonsCO_2-eq/person $\times$ year. This figure can be compared to France average carbon footprint of around 10 tonsCO_2-eq/person $\times$ year, showing that our activity emits GG significantly. In term of emission target, the Paris agreement aims at 2 tonsCO_2-eq/person$\times$

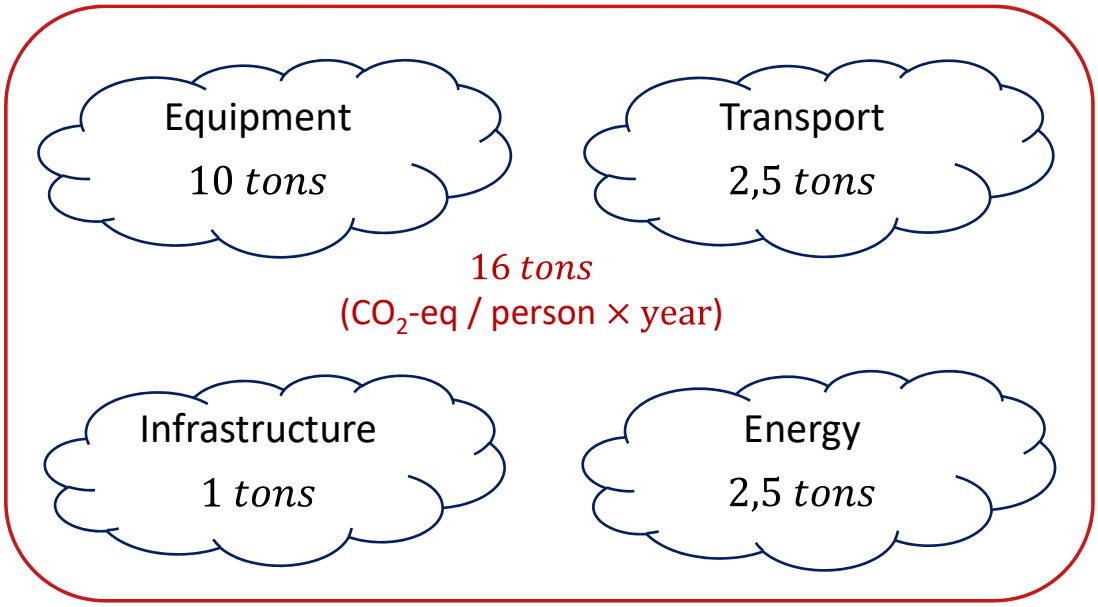

Figure D.3: **Quantronics carbon footprint results.** Results of Quantronics carbon footprint done for the year 2019. The total footprint of 16 tonsCO_2-eq/person × year is split into 4 types of emission source: equipment (10 tonsCO_2-eq/person × year), transport (2.5 tonsCO_2-eq/person × year), energy (2.5 tonsCO_2-eq/person × year), infrastructure (1 tonsCO_2-eq/person × year).

year by the year 2050. To convert this overall figure into concrete actions, one need to have a closer look to how it decomposes.

The larger GG emission source is the buying of our equipment, with 10 tonsCO_2-eq/person × year. However, this figure has a very high uncertainty. Indeed, the emission factor expressed in kgCO_2-eq / € that we are using are very generic, with label such as "laboratory device". In principle, if this factor is representative of the average emission of devices in a laboratory and if the set of data is spread over a large number of devices, then the result should be by and large relevant. But more than half of the money spent to buy equipment in the year 2019 by Quantronics was for a single dilution cryostat, for which we have no idea if the emission factor "laboratory device" is relevant.

The GG emission of transportation is around 2.5 tonsCO_2-eq/person × year. For transportation, we have taken into account the dayly commuting as well as the travel for conferences, and found a very interesting result: close to 90% of the transportation emissions are due to travel for conferences, and almost 100% of this travel emissions are due to the use of planes. This is understandable provided the very large number of kilometers traveled for conferences (around 14000 km per person in average for the year 2019, even though there is a large disparity from researcher to researcher), as well as provided that plane and train are the main two options to go to conferences and that the emission factor of train (in France, $\sim 0.005\,\mathrm{kgCO_2\text{-}eq}$ / km) is way smaller than the one of plane ($\sim 0.2\,\mathrm{kgCO_2\text{-}eq}$ / km).

The GG emission of energy consumption is also around 2.5 tonsCO_2-eq/person × year. We consider here both the electrical consumption as well as the heating done with gas,

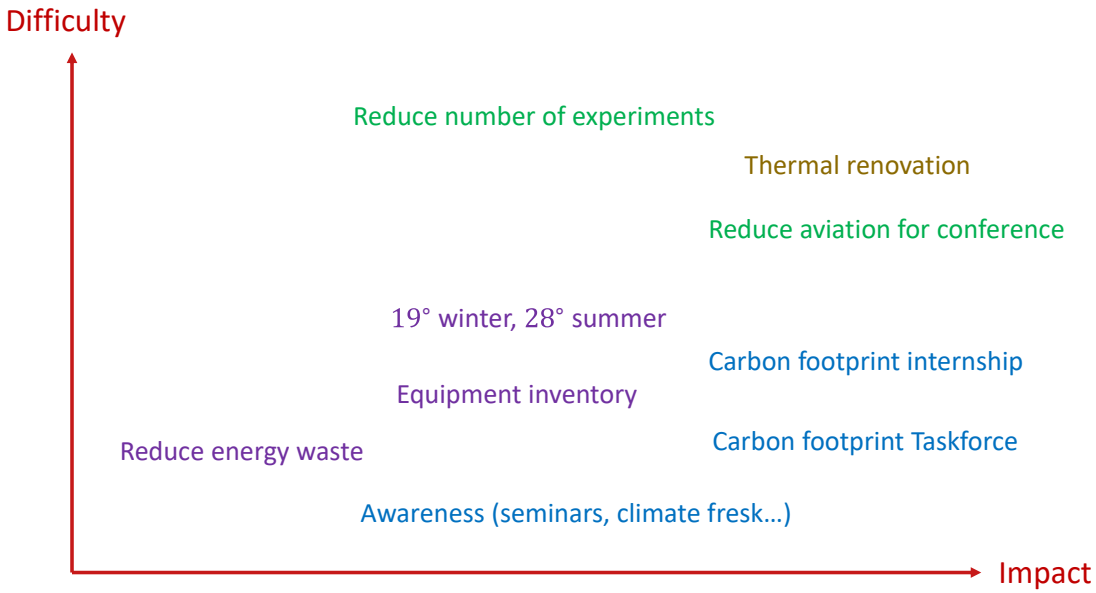

Figure D.4: **Actions to reduce our carbon footprint.** Graph representing the impact in term of emission reduction and the difficulty to set up of various actions. The propositions have colors to distinguish different type of actions: awareness, practice, investment, research intensity.

both giving a similar result close to 1.25 tonsCO_2-eq/person $\times$ year. It is worth to keep in mind that this was obtained considering France electrical production that has relatively low emissions ($\sim 0.05\,kgCO_2$-eq / kWh). The electrical consumption has been measured for the whole SPEC laboratory ($\sim$ 2 GWh for the year 2019) and divided equally between its members, yielding to $\sim$ 13 MWh / person.

Eventually, the building fabrication GG emission, spread over 50 years by convention, corresponds to 1 tonsCO_2-eq/person $\times$ year, with $\sim$ 1250 tonsCO_2-eq emitted for its fabrication.

D.4 Propositions

Based on this analysis, we can put forward a few propositions to curb our emissions.

First, we should keep improving our knowledge of our carbon footprint. We have advocated for the realization of an internship within SPEC laboratory dedicated to perform the carbon footprint of the whole laboratory. This proposition has been accepted already, and an internship aims at realizing the carbon footprint of SPEC for the year 2022. This ongoing work calls for refining the work, using for instance tools from Labo 1p5 [lab]. Also, it is crucial to have carbon footprints done over the years to have access to the emissions trend.

Second, this work has been the opportunity to get the laboratory involved about this issue. In particular, a carbon footprint task force has been set up to organize the reduction of our emission.

Eventually, based on the carbon footprint results, we propose a few concrete propositions that aim at reducing our laboratory emissions, such as:

- performing an equipment inventory over the whole SPEC laboratory and organizing the sharing of equipment
- monitoring the electrical consumption at refined scale, to find and reduce the significant waste
- setting the temperature within the building at more reasonable values, such as 19° in winter and 28° in summer
- reducing the use of plane to travel to conferences

These propositions would have an impact on various aspect of our professional life: comfort, investment, research intensity... This raises the big question of how to debate, to decide and to enforce decisions that impact our professional life.

Bibliography

[AB12] A. Abragam and B. Bleaney. *Electron paramagnetic resonance of transition ions*. Oxford: Oxford University Press, 2012 (cit. on pp. 9, 21).

[Abh+22] Nandita Abhyankar et al. "Recent advances in microresonators and supporting instrumentation for electron paramagnetic resonance spectroscopy". In: *Review of Scientific Instruments* 93.10 (Oct. 2022), p. 101101 (cit. on pp. 9, 21).

[Abr11] Anatole Abragam. *The principles of nuclear magnetism*. Repr. 32. Oxford: Oxford Univ. Pr, 2011 (cit. on pp. 9, 21).

[Alb+20] B. Albanese et al. "Radiative cooling of a spin ensemble". In: *Nature Physics* 16.7 (July 2020), pp. 751–755 (cit. on p. 64).

[Alb+21] Emanuele Albertinale et al. "Detecting spins by their fluorescence with a microwave photon counter". In: *Nature* 600.7889 (Dec. 2021), pp. 434–438 (cit. on pp. 10, 14, 22, 25, 50, 119).

[Alb21] Emanuele Albertinale. "Measuring spin fluorescence with a microwave photon detector". PhD thesis. Paris-Saclay, 2021 (cit. on pp. 10, 22, 74).

[Ber+07] S. Bertaina et al. "Rare-earth solid-state qubits". In: *Nature Nanotechnology* 2.1 (Jan. 2007), pp. 39–42 (cit. on p. 60).

[Ber+09] S. Bertaina et al. "Spin-Orbit Qubits of Rare-Earth-Metal Ions in Axially Symmetric Crystal Fields". In: *Physical Review Letters* 103.22 (Nov. 2009), p. 226402 (cit. on pp. 13, 23).

[BHP73] W. G. Breiland, C. B. Harris, and A. Pines. "Optically Detected Electron Spin Echoes and Free Precession in Molecular Excited States". In: *Physical Review Letters* 30.5 (Jan. 1973), pp. 158–161 (cit. on pp. 11, 23).

[Bie+16] A. Bienfait et al. "Controlling spin relaxation with a cavity". In: *Nature* 531.7592 (Mar. 2016), pp. 74–77 (cit. on pp. 10, 22, 37, 38).

[Bil+22] Eric Billaud et al. "Microwave fluorescence detection of spin echoes". In: (2022) (cit. on pp. 11, 14, 23, 25).

[Bla+21] Alexandre Blais et al. "Circuit quantum electrodynamics". In: *Reviews of Modern Physics* 93.2 (May 2021), p. 025005 (cit. on p. 50).

[Blo46] F. Bloch. "Nuclear Induction". In: *Physical Review* 70.7-8 (Oct. 1946), pp. 460–474 (cit. on pp. 9, 21).

[Bra04] C.D. Brandle. "Czochralski growth of oxides". In: *Journal of Crystal Growth* 264.4 (Mar. 2004), pp. 593–604 (cit. on p. 67).

[Cas] M.A Castellanos Beltran. "Development of a Josephson parametric amplifier for the preparation and detection of nonclassical states of microwave fields". PhD thesis (cit. on p. 49).

[Cav82] Carlton M. Caves. "Quantum limits on noise in linear amplifiers". In: *Physical Review D* 26.8 (Oct. 1982), pp. 1817–1839 (cit. on p. 49).

[EL13] Andreas Erb and Jean-Côme Lanfranchi. “Growth of high-purity scintillating CaWO4 single crystals for the low-temperature direct dark matter search experiments CRESST-II and EURECA”. In: *CrystEngComm* 15.12 (2013), p. 2301 (cit. on p. 67).

[Enr71] Bernal G. Enrique. “Optical Spectrum and Magnetic Properties of Er $^{3+}$ in CaWO $_4$”. In: *The Journal of Chemical Physics* 55.5 (Sept. 1971), pp. 2538–2549 (cit. on pp. 13, 23).

[Flu] Emmanuel Flurin. “The Josephson mixer : a swiss army knife for microwave quantum optics”. PhD thesis (cit. on p. 49).

[GC85] C. W. Gardiner and M. J. Collett. “Input and output in damped quantum systems: Quantum stochastic differential equations and the master equation”. In: *Physical Review A* 31.6 (June 1985), pp. 3761–3774 (cit. on p. 35).

[GK05] C. C. Gerry and Peter Knight. *Introductory quantum optics*. Cambridge, UK ; New York: Cambridge University Press, 2005 (cit. on p. 47).

[GKT78] R M Golding, M Kestigian, and C W Tennant. “EPR of high-spin Fe $^{3+}$ in calcium tungstate, CaWO $_4$”. In: *Journal of Physics C: Solid State Physics* 11.24 (Dec. 1978), pp. 5041–5049 (cit. on p. 68).

[GM64] C. G. B. Garrett and F. R. Merritt. “PMR SPECTRA OF Nd $^{3+}$ IN COMPENSATED AND UNCOMPENSATED CaWO $_4$”. In: *Applied Physics Letters* 4.2 (Jan. 1964), pp. 31–32 (cit. on pp. 60, 68).

[Gru+97] A. Gruber et al. “Scanning Confocal Optical Microscopy and Magnetic Resonance on Single Defect Centers”. In: *Science* 276.5321 (June 1997), pp. 2012–2014 (cit. on pp. 10, 21).

[Hah50] E. L. Hahn. “Spin Echoes”. In: *Physical Review* 80.4 (Nov. 1950), pp. 580–594 (cit. on p. 21).

[HM62] H. A. Haus and J. A. Mullen. “Quantum Noise in Linear Amplifiers”. In: *Physical Review* 128.5 (Dec. 1962), pp. 2407–2413 (cit. on p. 49).

[HR06] S. Haroche and J.-M. Raimond. *Exploring the quantum: atoms, cavities and photons*. Oxford ; New York: Oxford University Press, 2006 (cit. on pp. 10, 22, 34, 38, 47).

[JL05] Bernard Jacquier and Guokui Liu. *Spectroscopic properties of rare earths in optical materials*. 83. Berlin Tsinghua: Springer Tsinghua University Press, 2005 (cit. on p. 58).

[JM12] B. Julsgaard and K. Mølmer. “Reflectivity and transmissivity of a cavity coupled to two-level systems: Coherence properties and the influence of phase decay”. In: *Physical Review A* 85.1 (Jan. 2012), p. 013844 (cit. on p. 39).

[Kan+22] Shun Kanai et al. “Generalized scaling of spin qubit coherence in over 12,000 host materials”. In: *Proceedings of the National Academy of Sciences* 119.15 (Apr. 2022), e2121808119 (cit. on pp. 60, 65).

[Kie66] A. Kiel. “Theory of Electric Shifts of the Optical and Magnetic Resonance Properties of Paramagnetic Ions in Crystals”. In: *Physical Review* 148.1 (Aug. 1966), pp. 247–256 (cit. on pp. 16, 28, 62).

[Kra30] HA Kramers. “General theory of paramagnetic rotation in crystals”. In: *Proc. Acad. Sci. Amsterdam* 33 (1930), p. 959 (cit. on pp. 13, 23, 58).

[Kru+06] J. Krupka et al. “Measurements of Permittivity, Dielectric Loss Tangent, and Resistivity of Float-Zone Silicon at Microwave Frequencies”. In: *IEEE Transactions on Microwave Theory and Techniques* 54.11 (Nov. 2006), pp. 3995–4001 (cit. on p. 125).

[lab] 1.5 labo. *Labo 1p5* (cit. on pp. 129, 132).

[Le +21] Marianne Le Dantec et al. “Twenty-three–millisecond electron spin coherence of erbium ions in a natural-abundance crystal”. In: *Science Advances* 7.51 (Dec. 2021), eabj9786 (cit. on pp. 10, 13, 18, 22, 23, 30, 69, 113).

[Le 22] Marianne Le Dantec. “Electron spin dynamics of erbium ions in scheelite crystals, probed with superconducting resonators at millikelvin temperatures”. PhD thesis. 2022 (cit. on pp. 10, 13, 14, 22, 23, 25, 40, 61, 63–65, 70, 85, 112).

[Les+20] Raphaël Lescanne et al. “Irreversible Qubit-Photon Coupling for the Detection of Itinerant Microwave Photons”. In: *Physical Review X* 10.2 (May 2020), p. 021038 (cit. on pp. 10, 22, 50).

[MG67] W. B. Mims and R. Gillen. “Local Electric Fields and the Paramagnetic Resonance of Charge-Compensated Sites in (Ca, Ce)WO4”. In: *The Journal of Chemical Physics* 47.9 (Nov. 1967), pp. 3518–3532 (cit. on pp. 60, 83).

[Mim64] W. B. Mims. “Electric Field Effects in Spin Echoes”. In: *Physical Review* 133.3A (Feb. 1964), A835–A840 (cit. on p. 60).

[Mim65] W. B. Mims. “Electric Field Shift in Paramagnetic Resonance for Four Ions in a Calcium Tungstate Lattice”. In: *Physical Review* 140.2A (Oct. 1965), A531–A535 (cit. on pp. 16, 28, 62).

[OMG88] E van Oort, N B Manson, and M Glasbeek. “Optically detected spin coherence of the diamond N-V centre in its triplet ground state”. In: *Journal of Physics C: Solid State Physics* 21.23 (Aug. 1988), pp. 4385–4391 (cit. on pp. 11, 23).

[Pla+18] J. J. Pla et al. “Strain-Induced Spin-Resonance Shifts in Silicon Devices”. In: *Physical Review Applied* 9.4 (Apr. 2018), p. 044014 (cit. on pp. 11, 16, 23, 28, 101).

[Pla+21] Alexander P. M. Place et al. “New material platform for superconducting transmon qubits with coherence times exceeding 0.3 milliseconds”. In: *Nature Communications* 12.1 (Dec. 2021), p. 1779 (cit. on p. 74).

[Pol06] Martin Polovka. “EPR spectroscopy: A tool to characterize stability and antioxidant properties of foods”. In: *Journal of Food and Nutrition Research* 45.1 (2006), pp. 1–11 (cit. on pp. 9, 21).

[PTP46] E. M. Purcell, H. C. Torrey, and R. V. Pound. “Resonance Absorption by Nuclear Magnetic Moments in a Solid”. In: *Physical Review* 69.1-2 (Jan. 1946), pp. 37–38 (cit. on pp. 9, 21).

[Rab+38] I. I. Rabi et al. “A New Method of Measuring Nuclear Magnetic Moment”. In: *Physical Review* 53.4 (Feb. 1938), pp. 318–318 (cit. on pp. 9, 21).

[Ran+20a] V. Ranjan et al. “Electron spin resonance spectroscopy with femtoliter detection volume”. In: *Applied Physics Letters* 116.18 (May 2020), p. 184002 (cit. on pp. 10, 22, 116).

[Ran+20b] V. Ranjan et al. “Pulsed electron spin resonance spectroscopy in the Purcell regime”. In: *Journal of Magnetic Resonance* 310 (Jan. 2020), p. 106662 (cit. on pp. 14, 27).

[RIN] Cedric RINGENBACH. *Climate fresk* (cit. on p. 130).

[Riz+22] R. Rizzato et al. “Polarization Transfer from Optically Pumped Ensembles of N- V Centers to Multinuclear Spin Baths”. In: *Physical Review Applied* 17.2 (Feb. 2022), p. 024067 (cit. on pp. 10, 21).

[Sen90] N. Senesi. “Application of Electron Spin Resonance (ESR) Spectroscopy in Soil Chemistry”. In: *Soil Restoration*. Ed. by B. A. Stewart, Rattan Lal, and B. A. Stewart. Vol. 17. New York, NY: Springer New York, 1990, pp. 77–130 (cit. on p. 120).

[SJ01] A. Schweiger and Gunnar Jeschke. *Principles of pulse electron paramagnetic resonance*. Oxford, UK ; New York: Oxford University Press, 2001 (cit. on p. 112).

[Sli55] Charles P. Slichter. “Spin Resonance of Impurity Atoms in Silicon”. In: *Physical Review* 99.2 (July 1955), pp. 479–480 (cit. on pp. 9, 21).

[Sto14] N.J Stone. “TABLE OF NUCLEAR MAGNETIC DIPOLE AND ELECTRIC QUADRUPOLE MOMENTS”. In: *INDC International Nuclear Data Committee* (Feb. 2014) (cit. on p. 60).

[TA75] J. S. Thorp and E. A. E. Ammar. “The dielectric constants of CaWO4, Nd/CaWO4 and Gd/CaWO4”. In: *Journal of Materials Science* 10.6 (June 1975), pp. 918–922 (cit. on p. 125).

[VT99] Theodore Van Duzer and C. W. Turner. *Principles of superconductive devices and circuits*. 2nd ed. Upper Saddle River, N.J: Prentice Hall, 1999 (cit. on p. 33).

[Wal+06] Herbert Walther et al. “Cavity quantum electrodynamics”. In: *Reports on Progress in Physics* 69.5 (May 2006), pp. 1325–1382 (cit. on pp. 10, 22).

[Wei83] M. Weissbluth. *Atoms and Molecules Student Edition*. New York: Academic Press, 1983 (cit. on p. 57).

[WF16] Jörg Wrachtrup and Amit Finkler. “Single spin magnetic resonance”. In: *Journal of Magnetic Resonance* 269 (Aug. 2016), pp. 225–236 (cit. on pp. 9, 21).

[Whi62] G.K White. “Thermal expansion of vanadium, niobium, and tantalum at low temperatures”. In: *Cryogenics* 2.5 (Sept. 1962), pp. 292–296 (cit. on p. 63).

[Xia+04] M. Xiao et al. “Electrical detection of the spin resonance of a single electron in a silicon field-effect transistor”. In: *Nature* 430.6998 (July 2004), pp. 435–439 (cit. on pp. 9, 21).

[YB71] B. Yates and A. C. Bailey. “The low-temperature anisotropic thermal expansion of calcium tungstate”. In: *Journal of Low Temperature Physics* 4.1 (Jan. 1971), pp. 117–125 (cit. on p. 63).

[Yin+13] Chunming Yin et al. “Optical addressing of an individual erbium ion in silicon”. In: *Nature* 497.7447 (May 2013), pp. 91–94 (cit. on pp. 10, 21).

[Yos+96] Tetsuhiko Yoshimura et al. “In vivo EPR detection and imaging of endogenous nitric oxide in lipopolysaccharide-treated mice”. In: *Nature Biotechnology* 14.8 (Aug. 1996), pp. 992–994 (cit. on pp. 9, 21).

université PARIS-SACLAY | ÉCOLE DOCTORALE Physique en l'Île-de-France (PIF)

Titre : Spectroscopie de résonance de spin électronique des ions de terres rares dans la scheelite détectée par fluorescence micro-ondes, à une température de l'ordre du millikelvin

Mots clés : résonance magnétique, résonance de spin électronique, circuits supraconducteurs, fluorescence, ions de terres rares

Résumé : La spectroscopie de Résonance de Spin Electronique (ESR) est une méthode de caractérisation applicable à une grande variété de systèmes de spin. Cette méthode, généralement basée sur la Détection Inductive (ID) de l'écho de spin, a une faible sensibilité, permettant seulement la détection de grands ensembles de spin. Améliorer la sensibilité tout en gardant la variété des possibilités d'application est souhaitable pour caractériser les propriétés des petits ensembles de spin.

Cette thèse explore une nouvelle méthode de détection ESR : la Détection par Fluorescence (FD) - récemment développée dans le groupe Quantronics. Nous l'appliquons à la spectroscopie des ions de terres rares dans la scheelite en utilisant un dispositif de détection de photons à micro-ondes unique, à une température de l'ordre du millikelvin. L'expérience utilise un résonateur supraconducteur couplé magnétiquement à l'ensemble de spin résonnant, afin de manipuler et de détecter le signal de spin. Nous présentons des spectres FD-ESR à grande échelle montrant le signal d'une grande variété d'espèces de spin, ce qui indique la généralité de cette méthode de détection. Comme la FD donne un accès immédiat à la fluorescence de spin, elle appelle une meilleure compréhension de la courbe de relaxation de spin.

En nous concentrant sur les ions Erbium, nous modélisons la dynamique de l'ensemble des spins comme la somme des contributions des spins individuels et nous effectuons des simulations qui reproduisent quantitativement le signal de fluorescence sur trois ordres de grandeur de la force de l'impulsion d'excitation. La comparaison de l'ID et de la FD dans des conditions similaires d'excitation de spin confirme un gain de sensibilité avec la FD pour la détection de spin, atteignant un facteur 15 à la plus faible force d'excitation explorée. Cette plus grande sensibilité nous permet de mesurer les décalages de fréquence causés par une contrainte mécanique sur un petit sous-ensemble de spin, et d'étudier sa dépendance avec l'angle du champ statique. Grâce à l'homogénéité du couplage du sous-ensemble de spin, nous observons des oscillations cohérentes de spin. Bien que la FD soit sensible aux photons incohérents, nous utilisons une séquence de trois impulsions pour réaliser la FD des échos de Hahn. Nous caractérisons le temps de cohérence du spin en utilisant la FD, et nous démontrons une méthode pour contourner la limitation du temps de cohérence du spin due au bruit du champ magnétique. Enfin, nous montrons qu'il y a également un gain de sensibilité avec la FD par rapport à l'ID pour la détection des échos.

université PARIS-SACLAY | ÉCOLE DOCTORALE Physique en l'Île-de-France (PIF)

Title : Electron spin resonance spectroscopy of rare earth ions in scheelite detected by microwave fluorescence at millikelvin temperature

Keywords : magnetic resonance, electron spin resonance, superconducting circuits, fluorescence, rare earth ions

Abstract: Electron Spin Resonance (ESR) spectroscopy is a characterization method applicable to a wide variety of spin systems. This method, usually based on the Inductive Detection (ID) of spin echo, has a low sensitivity, restricting the detection to large spin ensembles. Improving the sensitivity while keeping the generality of application is desirable to characterize small spin ensemble properties.

This thesis explores a new ESR detection method Fluorescence Detection (FD) - recently developed in Quantronics group. We apply it to the spectroscopy of rare earth ions in Scheelite using a Single Microwave Photon Detector device, at millikelvin temperature. The experiment uses a superconducting resonator magnetically coupled to the resonant spin ensemble, in order to manipulate and detect the spin signal. We report large-scale FD-ESR spectra showing signal from a wide variety of spin species, proving the generality of this detection method. As FD gives immediately access to the spin fluorescence, it calls for a better understanding of spin relaxation curve.

Focusing on Erbium ions, we model the spin ensemble dynamics as the sum of single spin contribution and perform simulations that quantitatively reproduce the fluorescence signal over three orders of magnitude in excitation pulse strength. The comparison of ID and FD in similar spin excitation conditions confirms a sensitivity gain with FD for spin detection, reaching a factor 15 at the lowest excitation strength explored. This higher sensitivity allows us to measure the frequency shifts caused by mechanical strain on a small spin sub-ensemble, and to study its dependence with the static field angle. Thanks to the spin sub-ensemble coupling homogeneity, we observe spin coherent oscillations. Although FD is sensitive to incoherent photons, we use a three-pulse sequence to perform FD of Hahn echoes. We characterize the spin coherence time using FD, and demonstrate a method to get around the limitation in spin coherence time due to magnetic field noise. Eventually, we show that there is also a sensitivity gain with FD compared to ID for echo detection.